



**PhD COURSE IN “CIVIL ENGINEERING, ARCHITECTURE,  
ENVIRONMENTAL AND TERRITORY PROTECTION”**

**CURRICULUM: “MEASURES AND INFRASTRUCTURES FOR ENVIRONMENTAL AND  
TERRITORY PROTECTION”**

XV Cycle - New Series (2014-2016)

**UNIVERSITY OF SALERNO  
DEPARTMENT OF CIVIL ENGINEERING**

**PhD Thesis in:**

**VULNERABILITY ANALYSIS OF BUILDINGS IN  
AREAS AFFECTED BY SLOW-MOVING  
LANDSLIDES AND SUBSIDENCE PHENOMENA**

**(ANALISI DELLA VULNERABILITÀ DI EDIFICI IN AREE  
AFFETTE DA FRANE A CINEMATICA LENTA E  
FENOMENI DI SUBSIDENZA)**

2016/2017

**Eng. GIANFRANCO NICODEMO**

Supervisor:

Prof. Eng. Settimio FERLISI

Coordinator:

Prof. Eng. Ciro FAELLA

Co-supervisors:

Dr. Eng. Dario PEDUTO

Dr. Eng. Giovanni GULLÀ



---

VULNERABILITY ANALYSIS OF BUILDINGS IN AREAS AFFECTED BY  
SLOW-MOVING LANDSLIDES AND SUBSIDENCE PHENOMENA

---

Copyright © 2017 Università degli Studi di Salerno – via Giovanni Paolo II, 132 –  
84084 Fisciano (SA), Italy – web: [www.unisa.it](http://www.unisa.it)

Proprietà letteraria, tutti i diritti riservati. La struttura ed il contenuto del presente volume non possono essere riprodotti, neppure parzialmente, salvo espressa autorizzazione. Non ne è altresì consentita la memorizzazione su qualsiasi supporto (magnetico, magnetico-ottico, ottico, cartaceo, etc.).

Benché l'autore abbia curato con la massima attenzione la preparazione del presente volume, Egli declina ogni responsabilità per possibili errori ed omissioni, nonché per eventuali danni dall'uso delle informazione ivi contenute.

Finito di stampare il 10/04/2017



*To my Family*



# INDEX

INDEX.....	i
Index of figures.....	iii
Index of tables .....	xix
ABSTRACT .....	xxi
SOMMARIO .....	xxiii
ACKNOWLEDGEMENTS .....	xxv
About the author.....	xxv
1 Introduction.....	1
2 Analysed phenomena and their consequences in urban areas .....	4
2.1 Subsidence.....	4
2.2 Slow-moving landslides.....	6
2.3 Consequences induced by subsidence or slow-moving landslides .....	9
3 Analysis and prediction of the damage to buildings.....	13
3.1 Consequence analysis .....	13
3.2 Damage classification .....	16
3.3 Damageability criteria.....	20
3.4 Fragility and vulnerability curves .....	31
4 The DInSAR techniques.....	35
4.1 Synthetic aperture radar (SAR).....	36
4.2 Principles of SAR Interferometry.....	40
4.3 DInSAR multipass alghoritms .....	41
4.4 DInSAR applications to subsidence phenomena and slow- moving landslides.....	44
5 The proposed procedures.....	52
5.1 Empirical procedure for the analysis and prediction of the damage to buildings in subsiding areas .....	52
5.2 Empirical procedure for the analysis and prediction of the damage to buildings in slow-moving landslide-affected areas..	55
5.3 Procedure for the analysis and prediction of the damage to buildings via numerical approach .....	57
6 Analysis and prediction of the damage to buildings in subsiding areas: case studies in The Netherlands .....	60

6.1	Study area and available dataset .....	60
6.1.1	Geological setting .....	61
6.1.2	DInSAR dataset .....	65
6.1.3	Buildings damage survey .....	69
6.2	Results .....	72
6.2.1	Analysis at medium scale .....	72
6.2.2	Analysis at large scale .....	76
6.2.3	Analysis at detailed scale .....	84
6.3	Validation of the empirical fragility curves .....	89
7	Analysis and prediction of the damage to buildings in slow-moving landslide-affected areas .....	103
7.1	The selected study areas .....	103
7.2	The Lungro case study .....	107
7.2.1	Geological and geomorphological setting .....	108
7.2.2	DInSAR dataset .....	112
7.2.3	Building damage survey .....	116
7.2.4	Results .....	120
7.3	The Verbicaro case study .....	128
7.3.1	Geological and geomorphological setting .....	129
7.3.2	DInSAR dataset .....	131
7.3.3	Building damage survey .....	134
7.3.4	Results .....	136
8	Numerical analysis of building damage .....	144
8.1	Model description .....	144
8.2	Parametric analysis .....	147
8.3	Results .....	157
9	Discussion and Conclusions .....	166
	References .....	172
APPENDIX A		
	Validation of PSInSAR data accuracy: cross-comparison with leveling data .....	205
APPENDIX B		
	Reliability assessment of the cumulative log-normal distribution function using the Kolmogorov-Smirnov (K-S) goodness-of-fit test .....	210
APPENDIX C		
	Result of the numerical analysis in terms of damage exhibited by the masonry walls of a building subjected to differential settlements .....	214



## INDEX OF FIGURES

Figure 2.1	Proposed landslide velocity scale and probable destructive significant (Cruden and Varnes, 1996).....	7
Figure 2.2	Geotechnical schematization of landslide given by Leroueil et al., 1996: (a) scheme for landslide characterization, (b) material involved and (c) different stages of slope movements.....	8
Figure 3.1	Framework for landslide risk management (from Fell et al., 2008) .....	14
Figure 3.2	Schematic illustration of building damage associated with various types of subsidence movement, some of which may occur together (from Cooper, 2008).....	17
Figure 3.3	Definition of building deformation: a) settlement, differential settlement; b) relative deflection, deflection ratio, c) tilt, relative rotation (after Burland, 1995).....	20
Figure 3.4	Weightless, elastic beam of unit thickness adopted by Burland and Wroth (1974) to model the behavior of superstructures undergoing settlements in the foundation system .....	23
Figure 3.5	a) Relationship between $\Delta/L_{crit}$ and $L/H$ for rectangular beams deflecting due to combined bending and shear (neutral axis in the middle). b) Relationship $\Delta/L_{crit}$ between and $L/H$ for rectangular beams defecting due to combined bending and shear (neutral axis at the bottom) (after Burland and Wroth, 1974).....	24
Figure 3.6	Interaction diagram relating angular distortion and horizontal strain for different categories of damage (from Boscardin and Cording, 1989).....	25
Figure 3.7	Effect of $\epsilon_h$ on $\Delta/L$ (after Burland, 1995).....	27
Figure 3.8	Damage chart for a point loaded beam with $L/H = 1$ , $E/G = 2.6$ and the neutral axis in the bottom of the beam (hogging mode of deformation) (after Burland, 1995) .....	27

Figure 3.9(a) Damage distribution, (b) fragility curves and (c) vulnerability curves for M4 building type, according to EMS-98 (from Saeidi et al., 2009).....	33
Figure 4.1 Illustration of the SAR acquisition geometry (from Moreria et al., 2013) .....	37
Figure 4.2 The available SAR sensors, the archives and the achievable resolution (modified after Peduto et al., 2015).....	38
Figure 5.1 Flowchart of the proposed empirical procedure for the analysis and prediction of the damage to buildings in subsidence-affected areas.....	53
Figure 5.2 Flowchart of the proposed empirical procedure for the analysis and prediction of damages to buildings affected by slow-moving landslides .....	56
Figure 5.3 Flowchart of the proposed procedure for the analysis and prediction of the damage to building via numerical approach .....	58
Figure 6.1 The study area: a) area analyzed for investigating factors predisposing to ground settlements at medium scale; b) the study area at large scale and c) the study area at detailed scale .....	61
Figure 6.2 Geological map of The Netherlands (from van der Meulen et al., 2013) .....	62
Figure 6.3 GeoTop modelling workflow: a) borehole descriptions subdivided into lithostratigraphical, lithofacies and lithological units; b) 2D interpolation of the basal surface of each lithostratigraphical unit; c) 3D interpolation of lithofacies and lithology within each lithostratigraphical unit (modified from van der Meulen et al., 2013) .....	63
Figure 6.4 a) GeoTop model; b) example of geological cross-section and c) probability of occurrence of organic soil along the A–A' profile sketched in a) (extracted from the portal of the Geological Survey of the Netherland – DINOloket).....	63
Figure 6.5 Geological setting of the study area: a) land cover; b) cumulative thickness of soft soils (organic and clayey); c) cumulative thickness of sandy soils, and d) geological cross-	

	section along the A–A' profile sketched in a) (extracted from the portal of the Geological Survey of the Netherland – DINOloket).....	64
Figure 6.6	Distribution of PSI data provided by the TerraSAR-X radar sensor projected along the vertical direction: PSI data on ascending orbit a) on top of the buildings and b) at ground level.....	67
Figure 6.7	Distribution of PSI data provided by the TerraSAR-X radar sensor projected along the vertical direction: PSI data on descending orbit a) on top of the buildings and b) at ground level.....	68
Figure 6.8	Building fact-sheet: (Section 1) location area and building information; (Section 2) background data related to the geological context and PSI velocities; (Section 3) some photos of the field survey and damage severity levels.....	70
Figure 6.9	Map of surveyed building aggregates distinguished according to the recorded equivalent damage level and foundation type; b) distribution (in percentage) of foundation types and equivalent damage levels in the surveyed area.....	71
Figure 6.10	a) Map of surveyed single building distinguished according to the recorded equivalent damage level and foundation type; b) distribution (in percentage) of damage levels according to building foundation type.....	72
Figure 6.11	Map of cumulative settlements in the period 2009–2014 using TerraSAR-X data at ground level along the vertical direction on a) ascending and b) descending orbit.....	74
Figure 6.12	Correlation between cumulative settlements derived by high-resolution TerraSAR-X data at ground level and geological information: maps of spatial distribution of cumulative settlements on a) ascending and c) descending orbit; cross-section along the A–A' profile of the cumulative settlements on b) ascending and d) descending orbit in the period 2009–2014; e) map of spatial distribution and f) cross-section along the A–A' profile of soft soils (organic and clayey); h) geological cross-section along the A–A' profile and g)	

	probability of occurrence of soft soil (organic and clayey) extracted from the portal of the Geological Survey of the Netherland – DINOLOket.....	75
Figure 6.13	3D view of the study area at large scale with spatial distribution of PSI vertical velocities at ground level and on top of the buildings.....	76
Figure 6.14	Analysis of high-resolution PSI data at large scale: a) moving and not moving building aggregates and b) moving and not moving areas/roads surrounding the buildings.....	78
Figure 6.15a	Spatial distribution of different possible scenarios resulting from the correlation analysis between moving and not moving PSI data located on top of the building aggregates and on area/roads surrounding the buildings .....	79
Figure 6.15b	Description of different possible scenarios resulting from the correlation analysis between moving and not moving PSI data located on top of the building aggregates and on area/roads surrounding the buildings.....	80
Figure 6.16	Analysis of high-resolution PSI data at large scale: a) distribution of TerraSAR-X data on top of building aggregates; b) map of cumulative settlements and c) map of settlement gradients derived from TerraSAR-X data (period 2009–2014).....	81
Figure 6.17	Analysis of high-resolution PSI data at large scale: a) cumulative settlements and b) settlement gradients along the A-B profile sketched in Figure 6.16a) and b).....	82
Figure 6.18	Maximum settlement gradients and related equivalent damage levels for building aggregates with a) shallow and b) piled foundations .....	83
Figure 6.19	Analysis of high-resolution PSI data at detailed scale: a) map of cumulative settlements and damage severity recorded in 2015 damage surveys; b) scheme of differential settlement assessment on the single building.....	84
Figure 6.20	Damage level vs. differential settlements for buildings with c) shallow and d) piled foundations.....	85

Figure 6.21	Class frequency of the different levels of damage severity recorded to single buildings with a) shallow and c) piled foundations .....	86
Figure 6.22	Results of PSI-derived differential settlements and damage survey relationship for single buildings at detailed scale: empirical fragility curves generated by using the log-normal distribution for single buildings with a) shallow and b) piled foundations .....	88
Figure 6.23	a) Zaanstad and b) Dordrecht study areas: geological setting and cross-sections along the A-A' profile sketched in a) and B-B' profile sketched in b) (extracted from the portal of the Geological Survey of the Netherland – DINOloket). Spatial distribution of the available foundation type on the investigated areas: north a_1) and south a_2) neighborhood of the Municipality of Zaanstad; central portion b_1) of the Municipality of Dordrecht.....	90
Figure 6.24	Spatial distribution (on ascending and descending orbit) of high-resolution TerraSAR-X data on top of the buildings projected along the vertical direction (period 2009-2015) for the investigated north (a_1) and south (a_2) neighborhood of Zaanstad Municipality and central portion (b_1) of Dordrecht Municipality.....	92
Figure 6.25	Map of surveyed buildings distinguished according to the recorded damage severity for the investigated north (a_1) and south (a_2) neighborhood of Zaanstad Municipality and central portion (b_1) of Dordrecht Municipality .....	93
Figure 6.26	Some photos of damage recorded on the building facades during the field survey in Zaanstad and Dordrecht Municipality .....	94
Figure 6.27	Damage level vs. differential settlements for buildings with a) shallow and b) piled foundations in Zaanstad and Dordrecht Municipality .....	95
Figure 6.28	Empirical fragility curves generated by using the log-normal distribution for single buildings with a) shallow and b) piled foundations in Zaanstad and Dordrecht Municipality .....	96

Figure 6.29	Empirical fragility curves generated by using the log-normal distribution with a fixed value of standard deviation for single buildings in Schiedam Municipality with a) shallow and b) piled foundations and single buildings in Zaanstad and Dordrecht Municipality with c) shallow and d) piled foundations.....	98
Figure 6.30	Empirical fragility curves derived from the combination of the Schiedam, Zaanstad and Dordrecht case studies for single buildings with a) shallow and b) piled foundations .	101
Figure 6.31	Empirical vulnerability curves for single masonry building with piled foundations.....	102
Figure 7.1	Flowchart for the identification of the vulnerable areas at small scale.....	105
Figure 7.2	Map of municipalities of the Cosenza Province in which fall: vulnerable areas, not vulnerable areas or stable urban centres .....	106
Figure 7.3	The Lungro study area .....	107
Figure 7.4	Geological map of Lungro study area (modified from Antronico et al., 2014).....	109
Figure 7.5	Landslide inventory map of Lungro area (modified from Antronico et al., 2014).....	110
Figure 7.6	Map of typified landslide in Lungro urban area (modified from Gullà et al., 2017a) .....	111
Figure 7.7	DInSAR data distribution over the study area: a) ENVISAT DInSAR benchmarks on ascending orbit for the period 2003-2010 and b) COSMO-SkyMed DInSAR benchmarks on ascending orbit for the period 2012-2014 .....	114
Figure 7.8	Comparison between ENVISAT and COSMO-SkyMed data in terms of a) percentage of covered buildings and b) number of coherent PS per building.....	115
Figure 7.9	Building fact-sheet filled in for a masonry building located in the historic center of the Lungro municipality .....	118
Figure 7.10	Building fact-sheet filled in for a reinforced concrete building located in the new developed area of the Lungro municipality.....	118

Figure 7.11	Map of surveyed buildings distinguished according to the recorded level of damage severity (for the legend of typified landslides, refer to Table 7.1) .....	119
Figure 7.12	Distribution of the building damage severity on basis the building typology.....	119
Figure 7.13	Distribution of the building damage severity on basis the typified landslides (for the legend of typified landslides, refer to Table 7.1).....	120
Figure 7.14	Monitoring of building damage evolution over the time via DInSAR data. The example refers to a reinforced concrete building located on the boundary of an active roto-traslational slide .....	121
Figure 7.15	Sketch of computation of DInSAR-derived differential settlement ( $\Delta$ ) for each building.....	122
Figure 7.16	Damage severity level vs. differential settlements for a) reinforced concrete and b) masonry buildings located on different typified landslides within Lungro area (for the legend of typified landslides, refer to Table 7.1) .....	123
Figure 7.17	Class frequency of occurrence for each damage level suffered by masonry buildings for a given range of differential settlement.....	124
Figure 7.18	Empirical fragility curves obtained via the adoption of the log-normal distribution function for masonry buildings within the Lungro urban area.....	125
Figure 7.19	Empirical vulnerability curve for masonry buildings within the Lungro urban area.....	126
Figure 7.20	The Verbicaro study area.....	128
Figure 7.21	Landslide inventory map of Verbicaro area. Legend: 1) scarp of active landslide; 2) active roto-translational slide; 3) active complex landslide; 4) active landsliding area; 5) scarp of dormant landslide; 6) dormant roto-translational slide; 7) dormant complex landslide; 8) stabilized dormant complex landslide; 9) active landsliding area.....	130

Figure 7.22	Spatial distribution of DInSAR data provided by ENVISAT radar sensor in the period 2003-2010 on a) descending and b) ascending orbit for Verbicaro urban area.....	132
Figure 7.23	Spatial distribution of DInSAR data provided by COSMOSky-med radar sensor in the period 2012-2014 on a) descending and b) ascending orbit for Verbicaro urban area .....	133
Figure 7.24	Map of surveyed buildings distinguished according to the recorded damage severity based on data collected in 2014 via fact-sheets for both b) reinforced concrete and c) masonry buildings. (for the legend of landslides inventory, refer to Figure 7.19) .....	135
Figure 7.25	Distribution of damage severity according to landslide typology for a) reinforced concrete and b) masonry buildings .....	136
Figure 7.26	Distribution of damage severity for a) reinforced concrete and b) masonry buildings according to their position with respect to the landslide-affected areas .....	137
Figure 7.27	Damage level vs. maximum cumulative settlement ( $\delta_{max}$ ) distinguished for a) reinforced concrete and b) masonry buildings according to their position with respect to the landslide-affected areas .....	138
Figure 7.28	Damage level vs. differential settlement for a) reinforced concrete and b) masonry buildings.....	139
Figure 7.29	Empirical fragility curves obtained via the adoption of the log-normal distribution function for a) reinforced concrete and b) masonry buildings within the Verbicaro urban area .....	140
Figure 7.30	Empirical vulnerability curve for masonry buildings within the Verbicaro urban area.....	142
Figure 8.1	a) 3D view and b) foundation level of the modelled masonry building.....	145
Figure 8.2	a) Idealization of the equivalent frame of the masonry wall in the case of a regular arrangement of the openings; b) schematization of the failure mechanisms of the masonry	



	panel: banding-rocking b1, shear sliding b2 and diagonal cracking b3 (modified from Lagomarsino et al., 2012) .....	146
Figure 8.3	2D view of the four exterior walls of the modelled structure by TReMuri software masonry.....	147
Figure 8.4	Flowchart of the carried out analysis using the parametric approach.....	148
Figure 8.5	Example of calculation of the soil-foundation stiffness using the model proposed by Gazetas, 1991.....	151
Figure 8.6	3D view of the structure and layout of the imposed differential settlements at the foundation level for the four considered deformation modes: a) bilinear left; b) bilinear right; c) sagging; d) hogging.....	153
Figure 8.7	Damage evolution of the wall P1 to the building M1 resting on medium/ hard clay (S1_2), during the progressive increase of the differential settlements from 0 to 50 cm for different deformation modes: a) bilinear left; b) bilinear right; c) sagging; d) hogging.....	154
Figure 8.8	a) scheme of the drift ratio b) Moment-Curvature relationship.....	156
Figure 8.9	Fragility curves for masonry building resting on S2_1 (medium/hard clay): M1 affected by differential settlement with a) bilinear left/right and b) sagging/hogging deformation modes; M2 affected by differential settlement with c) bilinear left/right and d) sagging/hogging deformation modes.....	159
Figure 8.10	M1 vs M2 fragility curves for bi-linear displacement patterns (left and right) on different soil types: a) S1= soft soil; b) S2_1= soft clay; c) S2_2= medium/hard clay; d) S3_1= loose sand; e) S3_2= dense sand .....	160
Figure 8.11	M1 vs M2 fragility curves for sagging and hogging displacement patterns on different soil types: a) S1= soft soil; b) S2_1= soft clay; c) S2_2= medium/hard clay; d) S3_1= loose sand; e) S3_2= dense sand .....	161
Figure 8.12	Comparison between the fragility curves obtained for M1 building resting on different soils types subjected to different	

	deformation modes: a) bilinear left; b) bilinear right; c) sagging and d) hogging. Legend: LSi = ith damage limit state; S1= soft soil; S2_1= soft clay; S2_2= medium/hard clay; S3_1= loose sand; S3_2= dense sand.....	164
Figure 8.13	Comparison between the fragility curves obtained for M2 building resting on different soils types subjected to different deformation modes: a) bilinear left; b) bilinear right; c) sagging and d) hogging. Legend: LSi = ith damage limit state; S1= soft soil; S2_1= soft clay; S2_2= medium/hard clay; S3_1= loose sand; S3_2= dense sand.....	165
Figure A.1	Map of topographic leveling benchmarks provided by Schiedam municipality (period 2004-2014).....	206
Figure A.2	Spatial distribution of ascending and descending orbit TerraSAR-X PS-InSAR data projected along the vertical direction (period 2009-2014) located on top of the buildings .....	206
Figure A.3	PSInSAR-leveling contingency table with indication of the correct (green cells) and incorrect (red cells) rates .....	207
Figure A.4	Comparison between settlements derived from PSInSAR and leveling measurements in the period 2009-2014.....	209
Figure B.1	$D_{max}$ estimation for the K-S goodness-of-fit test of the log-normal distribution function used for the generation of fragility curves for buildings with a) shallow and b) piled foundations within the Schiadam area.....	211
Figure B.2	$D_{max}$ estimation for the K-S goodness-of-fit test of the log-normal distribution function used for the generation of fragility curves for masonry buildings within the Lungro area .....	213
Figure C.1	Deformation modes considered for the parametric analysis: a) bilinear left; b) bilinear right; c) sagging; d) hogging .....	214
Figure C.2	Damage evolution of the exterior (Pi, P2, P3, P4) and interior (P5, P6, P7, P8) walls of the masonry building M1 resting on soft soil (S1), during the progressive increase of the differential settlements from 0 to 50 cm applied with a bi-linear trend and a maximum value in the left corner .....	215

Figure C.3 Damage evolution of the exterior (P<sub>i</sub>, P<sub>2</sub>, P<sub>3</sub>, P<sub>4</sub>) and interior (P<sub>5</sub>, P<sub>6</sub>, P<sub>7</sub>, P<sub>8</sub>) walls of the masonry building M1 resting on soft soil (S1), during the progressive increase of the differential settlements from 0 to 50 cm applied with a bi-linear trend and a maximum value in the right corner...216

Figure C.4 Damage evolution of the exterior (P<sub>i</sub>, P<sub>2</sub>, P<sub>3</sub>, P<sub>4</sub>) and interior (P<sub>5</sub>, P<sub>6</sub>, P<sub>7</sub>, P<sub>8</sub>) walls of the masonry building M1 resting on soft soil (S1), during the progressive increase of the differential settlements from 0 to 50 cm applied according to a sagging configuration .....217

Figure C.5 Damage evolution of the exterior (P<sub>i</sub>, P<sub>2</sub>, P<sub>3</sub>, P<sub>4</sub>) and interior (P<sub>5</sub>, P<sub>6</sub>, P<sub>7</sub>, P<sub>8</sub>) walls of the masonry building M1 resting on soft soil (S1), during the progressive increase of the differential settlements from 0 to 50 cm applied according to a hogging configuration .....218

Figure C.6 Damage evolution of the exterior (P<sub>i</sub>, P<sub>2</sub>, P<sub>3</sub>, P<sub>4</sub>) and interior (P<sub>5</sub>, P<sub>6</sub>, P<sub>7</sub>, P<sub>8</sub>) walls of the masonry building M1 resting on soft clay (S2\_1), during the progressive increase of the differential settlements from 0 to 50 cm applied with a bi-linear trend and a maximum value in the left corner .....219

Figure C.7 Damage evolution of the exterior (P<sub>i</sub>, P<sub>2</sub>, P<sub>3</sub>, P<sub>4</sub>) and interior (P<sub>5</sub>, P<sub>6</sub>, P<sub>7</sub>, P<sub>8</sub>) walls of the masonry building M1 resting on soft clay (S2\_1), during the progressive increase of the differential settlements from 0 to 50 cm applied with a bi-linear trend and a maximum value in the right corner...220

Figure C.8 Damage evolution of the exterior (P<sub>i</sub>, P<sub>2</sub>, P<sub>3</sub>, P<sub>4</sub>) and interior (P<sub>5</sub>, P<sub>6</sub>, P<sub>7</sub>, P<sub>8</sub>) walls of the masonry building M1 resting on soft clay (S2\_1), during the progressive increase of the differential settlements from 0 to 50 cm applied according to a sagging configuration .....221

Figure C.9 Damage evolution of the exterior (P<sub>i</sub>, P<sub>2</sub>, P<sub>3</sub>, P<sub>4</sub>) and interior (P<sub>5</sub>, P<sub>6</sub>, P<sub>7</sub>, P<sub>8</sub>) walls of the masonry building M1 resting on soft clay (S2\_1), during the progressive increase of the differential settlements from 0 to 50 cm applied according to a hogging configuration .....222

Figure C.10	Damage evolution of the exterior (P <sub>i</sub> , P <sub>2</sub> , P <sub>3</sub> , P <sub>4</sub> ) and interior (P <sub>5</sub> , P <sub>6</sub> , P <sub>7</sub> , P <sub>8</sub> ) walls of the masonry building M1 resting on medium/ hard clay (S <sub>2_2</sub> ), during the progressive increase of the differential settlements from 0 to 50 cm applied with a bi-linear trend and a maximum value in the left corner.....	223
Figure C.11	Damage evolution of the exterior (P <sub>i</sub> , P <sub>2</sub> , P <sub>3</sub> , P <sub>4</sub> ) and interior (P <sub>5</sub> , P <sub>6</sub> , P <sub>7</sub> , P <sub>8</sub> ) walls of the masonry building M1 resting on medium/ hard clay (S <sub>2_2</sub> ), during the progressive increase of the differential settlements from 0 to 50 cm applied with a bi-linear trend and a maximum value in the right corner .....	224
Figure C.12	Damage evolution of the exterior (P <sub>i</sub> , P <sub>2</sub> , P <sub>3</sub> , P <sub>4</sub> ) and interior (P <sub>5</sub> , P <sub>6</sub> , P <sub>7</sub> , P <sub>8</sub> ) walls of the masonry building M1 resting on medium/ hard clay (S <sub>2_2</sub> ), during the progressive increase of the differential settlements from 0 to 50 cm applied according to a sagging configuration.....	225
Figure C.13	Damage evolution of the exterior (P <sub>i</sub> , P <sub>2</sub> , P <sub>3</sub> , P <sub>4</sub> ) and interior (P <sub>5</sub> , P <sub>6</sub> , P <sub>7</sub> , P <sub>8</sub> ) walls of the masonry building M1 resting on medium/ hard clay (S <sub>2_2</sub> ), during the progressive increase of the differential settlements from 0 to 50 cm applied according to a hogging configuration .....	226
Figure C.14	Damage evolution of the exterior (P <sub>i</sub> , P <sub>2</sub> , P <sub>3</sub> , P <sub>4</sub> ) and interior (P <sub>5</sub> , P <sub>6</sub> , P <sub>7</sub> , P <sub>8</sub> ) walls of the masonry building M1 resting on loose sand (S <sub>3_1</sub> ), during the progressive increase of the differential settlements from 0 to 50 cm applied with a bi-linear trend and a maximum value in the left corner .....	227
Figure C.15	Damage evolution of the exterior (P <sub>i</sub> , P <sub>2</sub> , P <sub>3</sub> , P <sub>4</sub> ) and interior (P <sub>5</sub> , P <sub>6</sub> , P <sub>7</sub> , P <sub>8</sub> ) walls of the masonry building M1 resting on loose sand (S <sub>3_1</sub> ), during the progressive increase of the differential settlements from 0 to 50 cm applied with a bi-linear trend and a maximum value in the right corner ..	228
Figure C.16	Damage evolution of the exterior (P <sub>i</sub> , P <sub>2</sub> , P <sub>3</sub> , P <sub>4</sub> ) and interior (P <sub>5</sub> , P <sub>6</sub> , P <sub>7</sub> , P <sub>8</sub> ) walls of the masonry building M1 resting on loose sand (S <sub>3_1</sub> ), during the progressive increase	

	of the differential settlements from 0 to 50 cm applied according to a sagging configuration .....	229
Figure C.17	Damage evolution of the exterior (P <sub>i</sub> , P <sub>2</sub> , P <sub>3</sub> , P <sub>4</sub> ) and interior (P <sub>5</sub> , P <sub>6</sub> , P <sub>7</sub> , P <sub>8</sub> ) walls of the masonry building M1 resting on loose sand (S <sub>3_1</sub> ), during the progressive increase of the differential settlements from 0 to 50 cm applied according to a hogging configuration .....	230
Figure C.18	Damage evolution of the exterior (P <sub>i</sub> , P <sub>2</sub> , P <sub>3</sub> , P <sub>4</sub> ) and interior (P <sub>5</sub> , P <sub>6</sub> , P <sub>7</sub> , P <sub>8</sub> ) walls of the masonry building M1 resting on dense sand (S <sub>3_2</sub> ), during the progressive increase of the differential settlements from 0 to 50 cm applied with a bi-linear trend and a maximum value in the left corner .....	231
Figure C.19	Damage evolution of the exterior (P <sub>i</sub> , P <sub>2</sub> , P <sub>3</sub> , P <sub>4</sub> ) and interior (P <sub>5</sub> , P <sub>6</sub> , P <sub>7</sub> , P <sub>8</sub> ) walls of the masonry building M1 resting on dense sand (S <sub>3_2</sub> ), during the progressive increase of the differential settlements from 0 to 50 cm applied with a bi-linear trend and a maximum value in the right corner...	232
Figure C.20	Damage evolution of the exterior (P <sub>i</sub> , P <sub>2</sub> , P <sub>3</sub> , P <sub>4</sub> ) and interior (P <sub>5</sub> , P <sub>6</sub> , P <sub>7</sub> , P <sub>8</sub> ) walls of the masonry building M1 resting on dense sand (S <sub>3_2</sub> ), during the progressive increase of the differential settlements from 0 to 50 cm applied according to a sagging configuration .....	233
Figure C.21	Damage evolution of the exterior (P <sub>i</sub> , P <sub>2</sub> , P <sub>3</sub> , P <sub>4</sub> ) and interior (P <sub>5</sub> , P <sub>6</sub> , P <sub>7</sub> , P <sub>8</sub> ) walls of the masonry building M1 resting on dense sand (S <sub>3_2</sub> ), during the progressive increase of the differential settlements from 0 to 50 cm applied according to a hogging configuration .....	234
Figure C.22	Damage evolution of the exterior (P <sub>i</sub> , P <sub>2</sub> , P <sub>3</sub> , P <sub>4</sub> ) and interior (P <sub>5</sub> , P <sub>6</sub> , P <sub>7</sub> , P <sub>8</sub> ) walls of the masonry building M2 resting on soft soil (S <sub>1</sub> ), during the progressive increase of the differential settlements from 0 to 50 cm applied with a bi-linear trend and a maximum value in the left corner .....	235
Figure C.23	Damage evolution of the exterior (P <sub>i</sub> , P <sub>2</sub> , P <sub>3</sub> , P <sub>4</sub> ) and interior (P <sub>5</sub> , P <sub>6</sub> , P <sub>7</sub> , P <sub>8</sub> ) walls of the masonry building M2 resting on soft soil (S <sub>1</sub> ), during the progressive increase of	

	the differential settlements from 0 to 50 cm applied with a bi-linear trend and a maximum value in the right corner ..	236
Figure C.24	Damage evolution of the exterior (P <sub>i</sub> , P <sub>2</sub> , P <sub>3</sub> , P <sub>4</sub> ) and interior (P <sub>5</sub> , P <sub>6</sub> , P <sub>7</sub> , P <sub>8</sub> ) walls of the masonry building M2 resting on soft soil (S <sub>1</sub> ), during the progressive increase of the differential settlements from 0 to 50 cm applied according to a sagging configuration .....	237
Figure C.25	Damage evolution of the exterior (P <sub>i</sub> , P <sub>2</sub> , P <sub>3</sub> , P <sub>4</sub> ) and interior (P <sub>5</sub> , P <sub>6</sub> , P <sub>7</sub> , P <sub>8</sub> ) walls of the masonry building M2 resting on soft soil (S <sub>1</sub> ), during the progressive increase of the differential settlements from 0 to 50 cm applied according to a hogging configuration .....	238
Figure C.26	Damage evolution of the exterior (P <sub>i</sub> , P <sub>2</sub> , P <sub>3</sub> , P <sub>4</sub> ) and interior (P <sub>5</sub> , P <sub>6</sub> , P <sub>7</sub> , P <sub>8</sub> ) walls of the masonry building M2 resting on soft clay (S <sub>2_1</sub> ), during the progressive increase of the differential settlements from 0 to 50 cm applied with a bi-linear trend and a maximum value in the left corner .....	239
Figure C.27	Damage evolution of the exterior (P <sub>i</sub> , P <sub>2</sub> , P <sub>3</sub> , P <sub>4</sub> ) and interior (P <sub>5</sub> , P <sub>6</sub> , P <sub>7</sub> , P <sub>8</sub> ) walls of the masonry building M2 resting on soft clay (S <sub>2_1</sub> ), during the progressive increase of the differential settlements from 0 to 50 cm applied with a bi-linear trend and a maximum value in the right corner ..	240
Figure C.28	Damage evolution of the exterior (P <sub>i</sub> , P <sub>2</sub> , P <sub>3</sub> , P <sub>4</sub> ) and interior (P <sub>5</sub> , P <sub>6</sub> , P <sub>7</sub> , P <sub>8</sub> ) walls of the masonry building M2 resting on soft clay (S <sub>2_1</sub> ), during the progressive increase of the differential settlements from 0 to 50 cm applied according to a sagging configuration .....	241
Figure C.29	Damage evolution of the exterior (P <sub>i</sub> , P <sub>2</sub> , P <sub>3</sub> , P <sub>4</sub> ) and interior (P <sub>5</sub> , P <sub>6</sub> , P <sub>7</sub> , P <sub>8</sub> ) walls of the masonry building M2 resting on soft clay (S <sub>2_1</sub> ), during the progressive increase of the differential settlements from 0 to 50 cm applied according to a hogging configuration .....	242
Figure C.30	Damage evolution of the exterior (P <sub>i</sub> , P <sub>2</sub> , P <sub>3</sub> , P <sub>4</sub> ) and interior (P <sub>5</sub> , P <sub>6</sub> , P <sub>7</sub> , P <sub>8</sub> ) walls of the masonry building M2 resting on medium/hard clay (S <sub>2_2</sub> ), during the progressive	

	increase of the differential settlements from 0 to 50 cm applied with a bi-linear trend and a maximum value in the left corner.....	243
Figure C.31	Damage evolution of the exterior (P <sub>i</sub> , P <sub>2</sub> , P <sub>3</sub> , P <sub>4</sub> ) and interior (P <sub>5</sub> , P <sub>6</sub> , P <sub>7</sub> , P <sub>8</sub> ) walls of the masonry building M2 resting on medium/hard clay (S <sub>2_2</sub> ), during the progressive increase of the differential settlements from 0 to 50 cm applied with a bi-linear trend and a maximum value in the right corner .....	244
Figure C.32	Damage evolution of the exterior (P <sub>i</sub> , P <sub>2</sub> , P <sub>3</sub> , P <sub>4</sub> ) and interior (P <sub>5</sub> , P <sub>6</sub> , P <sub>7</sub> , P <sub>8</sub> ) walls of the masonry building M2 resting on medium/hard clay (S <sub>2_2</sub> ), during the progressive increase of the differential settlements from 0 to 50 cm applied according to a sagging configuration.....	245
Figure C.33	Damage evolution of the exterior (P <sub>i</sub> , P <sub>2</sub> , P <sub>3</sub> , P <sub>4</sub> ) and interior (P <sub>5</sub> , P <sub>6</sub> , P <sub>7</sub> , P <sub>8</sub> ) walls of the masonry building M2 resting on medium/hard clay (S <sub>2_2</sub> ), during the progressive increase of the differential settlements from 0 to 50 cm applied according to a hogging configuration .....	246
Figure C.34	Damage evolution of the exterior (P <sub>i</sub> , P <sub>2</sub> , P <sub>3</sub> , P <sub>4</sub> ) and interior (P <sub>5</sub> , P <sub>6</sub> , P <sub>7</sub> , P <sub>8</sub> ) walls of the masonry building M2 resting on loose sand (S <sub>3_1</sub> ), during the progressive increase of the differential settlements from 0 to 50 cm applied with a bi-linear trend and a maximum value in the left corner .....	247
Figure C.35	Damage evolution of the exterior (P <sub>i</sub> , P <sub>2</sub> , P <sub>3</sub> , P <sub>4</sub> ) and interior (P <sub>5</sub> , P <sub>6</sub> , P <sub>7</sub> , P <sub>8</sub> ) walls of the masonry building M2 resting on loose sand (S <sub>3_1</sub> ), during the progressive increase of the differential settlements from 0 to 50 cm applied with a bi-linear trend and a maximum value in the right corner...	248
Figure C.36	Damage evolution of the exterior (P <sub>i</sub> , P <sub>2</sub> , P <sub>3</sub> , P <sub>4</sub> ) and interior (P <sub>5</sub> , P <sub>6</sub> , P <sub>7</sub> , P <sub>8</sub> ) walls of the masonry building M2 resting on loose sand (S <sub>3_1</sub> ), during the progressive increase of the differential settlements from 0 to 50 cm applied according to a sagging configuration .....	249

Figure C.37	Damage evolution of the exterior (Pi, P2, P3, P4) and interior (P5, P6, P7, P8) walls of the masonry building M2 resting on loose sand (S3_1), during the progressive increase of the differential settlements from 0 to 50 cm applied according to a hogging configuration .....	250
Figure C.38	Damage evolution of the exterior (Pi, P2, P3, P4) and interior (P5, P6, P7, P8) walls of the masonry building M2 resting on loose sand (S3_2), during the progressive increase of the differential settlements from 0 to 50 cm applied with a bi-linear trend and a maximum value in the left corner .....	251
Figure C.39	Damage evolution of the exterior (Pi, P2, P3, P4) and interior (P5, P6, P7, P8) walls of the masonry building M2 resting on dense sand (S3_2), during the progressive increase of the differential settlements from 0 to 50 cm applied with a bi-linear trend and a maximum value in the right corner ..	252
Figure C.40	Damage evolution of the exterior (Pi, P2, P3, P4) and interior (P5, P6, P7, P8) walls of the masonry building M2 resting on dense sand (S3_2), during the progressive increase of the differential settlements from 0 to 50 cm applied according to a sagging configuration .....	253
Figure C.41	Damage evolution of the exterior (Pi, P2, P3, P4) and interior (P5, P6, P7, P8) walls of the masonry building M2 resting on dense sand (S3_2), during the progressive increase of the differential settlements from 0 to 50 cm applied according to a hogging configuration .....	254



## INDEX OF TABLES

Table 2.1	Landslide classification based on type of movements and involved materials (Varnes, 1978).....	6
Table 3.1	Classification of visible damage to walls with particular reference to ease of repair of plaster and brickwork masonry (from Burland, 1977).....	19
Table 3.2	Relations between maximum absolute/differential settlement and angular distortion (after Skempton and MacDonald, 1956).....	22
Table 3.3	Limiting values of the angular distortion causing architectonic and structural damage (after Skempton and MacDonald, 1956).....	22
Table 3.4	Relations between category of damage and limiting tensile strain (after Boscardin & Cording, 1989).....	26
Table 3.5	Damage Criteria (modified from Finno et al., 2005).....	30
Table 4.1	Applications of DInSAR technique to subsidence in analysis at different scale (modified after Arena, 2014).....	46
Table 4.2	Applications of DInSAR technique to landslide in analysis at different scale (modified after Arena, 2014).....	50
Table 6.1	Main features of the TerraSAR-X datasets (processed by PSI technique) used for the analysis.....	65
Table 6.2	Main PSI measurement precision.....	66
Table 6.3	Median and standard deviation parameters of the lognormal distribution function used for each damage levels and distinguished according to the foundation type.....	87
Table 6.4	Median and standard deviation parameters of the lognormal distribution function used for each damage levels and distinguished according to the foundation type for the union of the Zaastad and Dordrecht case studies.....	97
Table 6.5	Differences between the probabilities of reaching or exceeding a particular damage level $D_i$ for different intensity values of	

	the differential settlements derived from the empirical fragility curves showed in figure 6.29.....	99
Table 7.1	Main features of the typified landslides in Lungro urban area (modified from Gullà et al., 2017a).....	112
Table 7.2	Main features of the Envisat and Cosmo-SkyMed datasets used for the analysis in Lungro area.....	113
Table 7.3	Median and standard deviation parameters used to derive the fragility functions for each damage levels for masonry buildings within the Lungro urban area.....	125
Table 7.4	Main features of the Envisat and Cosmo-SkyMed datasets used for the analysis in Verbicaro area .....	131
Table 7.5	Median and standard deviation parameters used to derive the fragility functions for each damage levels for reinforced concrete and masonry buildings within the Verbicaro urban area .....	141
Table 8.1	Masonry mechanical parameters (from M.C. n. 617 – NTC/2008).....	149
Table 8.2	Soil elastic properties .....	150
Table 8.3	Thresholds of the damage limits states .....	156
Table 8.4	Median $\mu$ and standard deviation $\beta$ parameters of the lognormal distribution function used for each damage limits states and distinguished according to the deformation mode and soil type.....	162
Table A.1	Results of the PSInSAR-leveling contingency table .....	208
Table B.1	Results of K-S test of derived fragility curves for buildings with shallow and piled foundations within the Schiadam area .....	211
Table B.2	Results of K-S test of derived fragility curves for masonry buildings within the Lungro area.....	212

## ABSTRACT

Slow-moving landslides and subsidence phenomena yearly induce huge damages both direct (on structures and/or infrastructures with them interacting) and indirect (corresponding to the associated economic losses). For this reason, studies aimed at analyzing and predicting the aforementioned damages are of great interest for Scientific Community and Authorities in charge of identifying the most suitable strategies for the land-use planning and management of urban areas affected by slow-moving landslides and subsidence phenomena.

However, carrying out the activities related to the pursuit of those goals is not straightforward since it usually requires high costs due to the great amount of data to be collected for setting up reliable forecasting models as well as the development of proper procedures that take into account *i)* the identification and quantification of the exposed elements; *ii)* the definition and estimation of an intensity parameter; *iii)* the prediction of the damage severity level (generally associated with the attainment of a certain limit state).

In this PhD Thesis some original procedures are proposed. In particular, on the basis of empirical and numerical methods, fragility and vulnerability curves are generated in order to predict the damage to buildings in subsidence- and slow-moving landslide-affected areas.

The proposed empirical procedures, based on the joint use of DInSAR data (provided from the processing of images acquired by Synthetic Aperture Radar via Differential Interferometric techniques) and information on damages suffered by buildings (recorded and classified during in situ surveys), were tested on case studies in The Netherlands, affected by subsidence phenomena, and in Calabria Region (southern Italy) for slow-moving landslide-affected areas.

The procedure based on the adoption of a numerical method was applied on a structural model representative of a single building.

With reference to subsidence phenomena, the analyses were carried out for a densely urbanized municipality following a multi-scale approach. In particular, at *medium scale*, the subsiding areas that are most prone to ground surface settlements along with their spatial distribution and rates, were preliminarily detected. The above ground surface settlements (here

considered as subsidence intensity parameter) combined with the results of an extensive damage survey on masonry buildings, allowed first retrieving, at *large-scale* (on building aggregates) and at *detailed scale* (on single buildings), the relationships between cause (settlements/differential settlements) and effect (damage severity level); then, empirical fragility curves were generated for structurally independent single buildings. These latter were validated via their comparison with fragility curves generated, with reference to two others densely urbanized municipalities, for buildings with similar structural typology (masonry) and foundation type (shallow or deep). Finally, fragility and vulnerability curves for masonry buildings were generated by using the entire database of damages.

As for slow-moving landslides, the analyses were carried out at *large scale*. In particular, the joint use of DInSAR and damage surveys data allowed analyzing the consequences induced on the buildings (either of masonry or reinforced concrete) with shallow foundations by retrieving the cause-effect relationships and generating empirical fragility and vulnerability curves.

Finally, the numerical analyses carried out on a structural model representative of a single masonry building, allowed to go in-depth in the different aspects contributing to the onset and development of building damages as well as to quantify the uncertainties inherent to the addressed issue.

The obtained results highlight the huge potential of the fragility and vulnerability curves generated according to the proposed procedures that, once further calibrated/validated and jointly used with a continuous monitoring of the intensity parameter via conventional (e.g., inclinometers, GPS, topographic leveling) and/or innovative (e.g., SAR images processed via DInSAR techniques) systems, can be valuably used as tools for the analysis and prediction of the damage to buildings for land-use planning and urban management purposes in subsidence- and slow-moving landslide-affected areas.

## SOMMARIO

Le frane a cinematica lenta e i fenomeni di subsidenza causano annualmente ingenti danni sia diretti (su strutture e/o infrastrutture con essi interagenti) che indiretti (quali si configurano le associate perdite di natura economica). Per tale ragione, gli studi volti ad analizzare e a prevedere i predetti danni sono di indubbio interesse per le Comunità e gli Enti impegnati nella individuazione delle più idonee strategie di pianificazione e di gestione delle aree urbanizzate affette dai suddetti fenomeni.

Tuttavia, lo svolgimento delle attività connesse al perseguimento dei predetti obiettivi è tutt'altro che agevole in quanto richiede costi elevati, dovuti alla grande quantità di dati da acquisire per la generazione di modelli previsionali affidabili, nonché lo sviluppo di procedure che contemplino *i)* l'identificazione e la quantificazione degli elementi esposti, *ii)* la definizione e la stima di un parametro di intensità e *iii)* la previsione del livello di severità del danno (generalmente associato al raggiungimento di uno stato limite).

La presente Tesi di Dottorato propone alcune procedure originali che, sulla base di metodi empirici e numerici, conducono alla generazione di curve di fragilità e vulnerabilità quali strumenti di previsione del danno a edifici in aree affette da frane a cinematica lenta e fenomeni di subsidenza.

Le procedure empiriche proposte, basate sull'integrazione congiunta di dati DInSAR (ovvero derivanti dalla elaborazione di immagini acquisite da radar ad apertura sintetica montati su piattaforme satellitari mediante tecniche interferometriche differenziali) e sul danno subito da edifici (a sua volta classificato sulla base degli esiti di rilievi in sito dei quadri fessurativi esibiti dalle facciate), sono state testate con riferimento a casi di studio dei Paesi Bassi, affetti da fenomeni di subsidenza, e della Regione Calabria (Italia meridionale), interessati da frane a cinematica lenta.

La procedura basata sull'impiego di metodi numerici è stata, invece, applicata su un modello strutturale rappresentativo di un edificio singolo.

Con riferimento ai fenomeni di subsidenza, le attività svolte con un approccio multi-scalare hanno consentito preliminarmente di rilevare (a *media scala*) le aree che risultano essere maggiormente predisposte a cedimenti dovuti a fenomeni di subsidenza. La conoscenza della distribuzione spaziale e della entità di tali cedimenti è stata, poi, combinata con i risultati di un esteso rilievo del danno agli edifici in muratura di un'area comunale in modo da *i*) risalire – sia a *grande scala* (su aggregati di edifici) che a *scala di dettaglio* (singoli edifici) – alle relazioni funzionali che si stabiliscono tra causa (cedimenti assoluti/differenziali) ed effetti (livello di severità del danno) e *ii*) generare per singoli edifici strutturalmente indipendenti curve di fragilità su base empirica. Le curve di fragilità così calibrate sono state, poi, validate operandone un confronto con curve di fragilità generate, con la medesima procedura, per altre due aree comunali caratterizzate dalla presenza di edifici con la stessa tipologia strutturale e fondale (superficiale o profonda). Si è, infine, provveduto alla generazione di curve di fragilità e di vulnerabilità di edifici in muratura utilizzando l'intero campione di dati a disposizione. Per quanto riguarda le frane a cinematica lenta, le analisi sono state svolte esclusivamente a *grande scala*, dove l'uso congiunto dei dati DInSAR e del rilievo del danno a edifici in cemento armato e in muratura con fondazioni superficiali ha consentito, ancora una volta, di risalire alle relazioni causa-effetto e di generare curve di fragilità e di vulnerabilità su base empirica.

Infine, l'analisi numerica effettuata su un modello strutturale rappresentativo di un singolo edificio in muratura con fondazioni superficiali ha consentito di approfondire il ruolo esercitato da alcuni fattori nella generazione e nello sviluppo del danno nonché di quantificare le incertezze che intervengono nel problema esaminato.

I risultati ottenuti evidenziano l'enorme potenzialità delle curve di fragilità e vulnerabilità ottenute che, laddove ulteriormente calibrate e validate, possono essere impiegate congiuntamente con tecniche di monitoraggio in continuo dei parametri d'intensità – sia di tipo convenzionale (quali, ad esempio, inclinometri, GPS, livellazione topografica) che innovative (come quelle derivanti dall'elaborazione di immagini satellitari mediante tecniche DInSAR) – per la messa a punto di modelli previsionali utili alla pianificazione territoriale e alla gestione di aree urbane affette da frane a cinematica lenta e fenomeni di subsidenza.

## ACKNOWLEDGEMENTS

*The value of the knowledge is not the learning of many facts  
but the training of the mind to think.*

*(Albert Einstein)*

In primo luogo desidero ringraziare di cuore il *Prof. Ing. Settimio Ferlisi*, a cui va la mia profonda riconoscenza e gratitudine per avermi dato l'opportunità di svolgere questo importante percorso formativo che mi ha permesso di approfondire temi assolutamente originali, guidandomi e indirizzandomi nelle attività svolte e nella stesura del presente elaborato sempre con grande attenzione e precisione e parole di incoraggiamento e di conforto.

Un ringraziamento particolare lo rivolgo al *Dott. Ing. Dario Peduto*, per avermi fatto intravedere le potenzialità del tema di ricerca affondato, la possibilità di vivere entusiasmanti esperienze di ricerca all'estero e la qualità del tempo che mi ha dedicato, guidandomi con i suoi preziosi suggerimenti nelle attività da svolgere sempre con il sorriso e l'allegria che lo contraddistinguono.

Un sentito ringraziamento va al *Dott. Ing. Giovanni Gullà*, per tutto il materiale fornito, gli utili consigli nell'approfondire i temi di ricerca affondati e la sua grande disponibilità e professionalità mostratami durante questi anni. Ringrazio tutto il CNR-IRPI di Cosenza, in particolare il *Dott. Luigi Borrelli*, per le lunghe giornate di campo condivise.

Ringrazio il CNR-IREA di Napoli, in particolare il *Dott. Ing. Gianfranco Fornaro* e il *Dott. Ing. Diego Reale*, per il tempo dedicato all'elaborazione dei dati, la sempre interessante interazione e la disponibilità in chiarimenti e approfondimenti.

Ringrazio tutto il gruppo della Società SkyGeo (Delft, Olanda), in particolare il *Dr. Ing. Jos Maccabiani* e il Bureau de Recherches Géologiques et Minières - BRGM (Orléans, Francia), nella persona del *Dr. Ing. Gilles Grandjean*, per avermi dato la possibilità di svolgere parte

della mia attività di Ricerca all'estero in ambienti fortemente stimolanti e professionali.

Ringrazio tutto il gruppo del Laboratorio di Geotecnica “*Giuseppe Sorbino*” a partire dal *Prof. Ing. Leonardo Cascini*, il *Prof. Ing. Michele Calvello* e il *Prof. Ing. Sabatino Cuomo*, i Tecnici, i Dottorandi e gli Assegnisti con i quali ho condiviso questa indimenticabile esperienza.

Ringrazio il *Dr. Ing. Caterina Negulescu* e *Prof. Ing. Olga Christina Mavrouli*, in qualità di revisori del presente elaborato di Tesi.

Ringrazio la mia Famiglia, mia madre *Antonia*, mio padre *Pietro* e mio Fratello *Mario*, a cui dedico questo elaborato finale con affetto ed infinita gratitudine.



## ABOUT THE AUTHOR

**Gianfranco Nicodemo** graduated in June 2013 in Civil Engineering - Structures and Constructions - at the University of Salerno with 110/110 cum laude. In December 2013 he passed the admission exam for the PhD course in Civil Engineering, Architecture, Environmental and Territory Protection (XV cycle- New Series) at the University of Salerno. During the PhD Course he developed his research on vulnerability analysis of buildings affected by slow-moving landslides and subsidence phenomena via the joint use of damage surveys and remote sensing data. To deepen these themes, he carried out part of his study and research activities abroad at SkyGeo company in Delft, The Netherlands and at BRGM in Orléans, France; stage period at CNR-IRPI of Cosenza and CNR -IREA of Naples, Italy; attended several courses within the PhD Course, among which the LARAM International School on "LAndslide Risk Assessment and Mitigation". Some of the obtained result have been already published on both International and National journals and presented in Conference.

**Gianfranco Nicodemo** si laurea nel Giugno 2013 in Ingegneria Civile – Strutture e Costruzioni – presso l'Università degli Studi di Salerno con voti 110/110 e lode. Nel dicembre 2013 supera l'esame di ammissione al Corso di Dottorato di Ricerca in Ingegneria Civile, Edile-Architettura, Ambiente e del Territorio (XV ciclo - Nuova Serie) presso l'Università degli Studi di Salerno. Durante il Corso di Dottorato sviluppa ricerche incentrate sull'analisi della vulnerabilità di edifici in aree affette da frane a cinematica lenta e fenomeni di subsidenza attraverso l'uso congiunto di rilievi del danno al costruito e dati di telerilevamento satellitare. Allo scopo di approfondire tali tematiche, svolge parte dell'attività di studio e ricerca all'estero presso la società SkyGeo a Delft in Olanda e il BRGM a Orléans in Francia; periodi di stage e ricerca presso il CNR-IRPI di Cosenza e il CNR-IREA di Napoli oltre a seguire numerosi corsi tra cui la Scuola Internazionale LARAM. Alcuni risultati ad oggi conseguiti, sono stati oggetto di pubblicazioni su riviste internazionali e nazionali, nonché in contributi di atti di Convegni.



# 1 INTRODUCTION

Slow-moving landslides and subsidence phenomena are widespread all over the world and their existence is often associated to consequences to facilities with them interacting, such as: the break of underground utilities (e.g. sewers, water and gas distribution pipelines, etc.), interruption of transport infrastructure (e.g. roads and railways) with related economic losses, cracking and/or tilting of buildings until the attainment of serviceability or ultimate limit states.

Therefore, studies aimed at analyzing and predicting the damages to facilities in subsidence- and slow-moving landslide-affected areas have become a relevant issue for both the scientific and the technical communities involved in identifying the most suitable strategies for the land-use planning and urban management.

However, the above studies usually require huge data collection on the phenomena at hand (e.g. extent and intensity parameters) and the exposed elements (stiffness/strength of constituting materials, state of maintenance, damage, value).

As for the former, displacement patterns (and rates) experienced by single (or set of) facilities located in (or in the proximity of) subsidence- and slow-moving landslide-affected areas may derive – in addition to the conventional monitoring techniques (i.e. inclinometers, GPS, topographic leveling) – from the processing of images acquired by Synthetic Aperture Radar (SAR) sensors via Differential Interferometric (DInSAR) techniques. These latter, in the last decades were successfully tested in a wide range of applications. They proved effective for monitoring structures/infrastructures on unstable slopes and subsidence areas. Moreover, the availability of SAR archives spanning a long time interval (more 20 years) with high spatial coverage and accuracy favoured an increasing interest of the Scientific Community towards the above techniques.

This PhD Thesis is aimed at providing helpful tools (i.e. fragility and vulnerability curves) for the analysis and prediction of the damage to buildings in areas affected by slow-moving landslides or subsidence phenomena. This goal is pursued first through the development of

innovative empirical procedures based on the joint use of DInSAR data and building damage surveys; then, a numerical approach is adopted in order to address the issues concerning the use of empirical fragility curves as well as to account for uncertainties into models that can support a better understanding of the different factors contributing to the occurrence and development of building damages.

In particular, Chapter 2 offers an overview of the main features of the phenomena at hand (i.e., subsidence and slow-moving landslides), their diffusion all over the world and related consequences in urban areas.

Chapter 3 deals with the relevance of the consequence analysis in processes aimed at quantifying the risk to buildings; the main damageability criteria offered by the scientific literature are also provided along with the newly proposed probabilistic approaches for the analysis and prediction of the damage to buildings.

Chapter 4 focuses on DInSAR techniques with a description of their basics, limitations and potential; the most relevant applications to subsidence and slow-moving landslides, available in scientific literature, are also synthesized.

Chapter 5 presents the proposed innovative procedures for the generation, via empirical and numerical approaches, of fragility and vulnerability curves of buildings in areas affected by slow-moving landslides and subsidence phenomena.

Chapter 6 is devoted to the application of the proposed multi-scale empirical procedure for subsidence-affected areas on some case studies in The Netherlands. In particular, referring to an area of about 15 km<sup>2</sup> including the cities of Rotterdam and Schiedam, the role played by the factors predisposing to ground displacements is first investigated *at medium scale* in order to map the areas where damages to the built-up environment are most likely to be found or expected. Then, focusing on a smaller area of about 2 km<sup>2</sup> represented by a neighborhood of Schiedam, the preliminary identification *at large scale* of different possible scenarios for the exposed elements allows distinguishing possible ground displacements and related effects on either buildings or infrastructure and utilities. The relationship retrieved between cause (settlements) and effect (equivalent damage level) with reference to building aggregates provide an overview on their behavior depending on the foundation typology in which more detailed analyses need to be carried out. The analysis *at detailed scale* on a portion of the neighborhood of Schiedam on structurally independent single buildings allows deriving the empirical

relationships between differential settlements suffered by the structures and relative damage levels, in turn used to generate the fragility curves for single buildings with shallow and piled foundations. The obtained empirical fragility curves for buildings with the same structural typology and foundation type are validated with reference to two other densely urbanized municipalities located in the northern (Zaanstad) and southern (Dordrecht) part of The Netherlands. For these two case studies, fragility curves representative of the building response in terms of damage severity levels are generated based on a larger sample dataset.

Chapter 7 deals with the application of the proposed procedure for the analysis, *at large scale*, of building damage induced by slow-moving landslides located in Calabria region (southern Italy). On two test sites, preliminarily selected through an analysis performed at small scale on the whole territory of northern sector of Calabria region (Cosenza Province), empirical fragility and vulnerability curves are derived via a proper combination of DInSAR and damage survey data.

Chapter 8 presents the results in terms of analytical fragility curves obtained via numerical simulations carried out on single masonry buildings subjected to differential settlements. The parametric analysis allows investigating the role played by some factors on the building response in terms of damage severity levels and their effects on the trend of fragility curves.

Finally, in Chapter 9 a discussion on the obtained results and some remarks on further improvements of the adopted methodological approach are provided for a proper use of proposed tools in the analysis and prediction of damages to buildings induced by slow-moving landslides and subsidence phenomena.

## **2 ANALYSED PHENOMENA AND THEIR CONSEQUENCES IN URBAN AREAS**

In many parts of the world, a wide spectrum of dangers related to either natural processes or human activities, or complex combinations of both, causes severe damages to exposed facilities (e.g., roads, embankments, subsurface infrastructure and housing) resulting in economic losses of billions of dollars per year (Holzer, 2009, Bucx et al., 2015). This is the case of subsidence phenomena and slow-moving landslides whose huge detrimental consequences are expected to grow in the near future due to the increase of the demographic pressure and the effects of climate changes (EEA, 2012). Therefore, studies aimed at both detecting slow-moving- and subsidence-affected areas and predicting the related damages to exposed facilities are of great interest for authorities in charge of the land-use planning and management of urban systems. The related activities call for a deep knowledge of both phenomena (e.g. extent and intensity) and exposed facilities, as well as the interaction among them. In this regard, this Chapter offers an insight into the above phenomena and their effects on urbanized areas.

### **2.1 SUBSIDENCE**

Subsidence occurs in many parts of the world, particularly in densely populated deltaic regions (Poland, 1984; Barends et al., 1995), and refers to ground surface displacements – with prevailing vertical component (i.e., settlements).

Most of the major subsidence-affected areas developed in the past half century, starting largely during World War II and continuing since then, with accelerated rates due to the increasing use of groundwater as well as of oil and gas (Strozzi et al., 2001). Over 150 areas of contemporary subsidence are known (UNESCO), some with as much subsidence as 10 m in countries such as Mexico (Booker et al., 1985; Bell, 1994; Ovando-Shelley et al., 2003; López-Quiroz et al., 2009), and the United States

(Allen and Mayuga, 1969; Ireland et al., 1984; Prokopovich, 1983); up to 5 m in cities like Tokyo and Niigata in Japan (Konogai et al., 2012; Okumura et al., 1969), from 1 to 3 m in Shanghai, China (Shi et al., 2008), Bangkok, Thailand (Phien-wej et al., 2005) or Bologna (Modoni et al., 2013); under 0.5 m in Venice, Italy (Ricceri, 2007; Tosi et al., 2013), and many more areas of subsidence are likely to develop in the next few decades as a result of accelerated exploitation of natural resources in order to meet the demands of increasing population and industrial development in many developed countries of the world (Barendas et al., 1995).

The subsidence can be induced by natural, anthropogenic or mixed causes.

The subsidence of natural origin is associated to tectonic movements, sea level rise, consolidation processes or physically/chemically-induced decay of mechanical soil properties (Ericson et al., 2006; Holzer et al., 2009).

The subsidence of anthropogenic origin generally relates to water exploitation (for industrial and human needs) and mining activities. In the former case, the magnitude and the surface distribution of induced settlements are mainly influenced by the stratigraphy of soil deposits and related compressibility parameters (concerning both primary and secondary consolidation stages), hydraulic boundary conditions, withdrawal characteristics (Syvitski et al., 2009; Holzer et al., 2009); whereas for mining – which can lead to sudden sinking or slow settlements – the main influencing factors are (Jones and Bellamy, 1973): seam thickness, depth of working, mine geometry, total amount of mining, angle of draw, seam inclination, geological conditions, time, direction and rate of advance of the face and method of working.

Another cause of anthropogenic subsidence – widely studied over the years due to the potentially induced damages on adjacent and overlying services and structures – is the tunneling. In such a case, the displacements caused by tunneling are mainly depending on (Peck, 1969): *i*) the ground and groundwater conditions; *ii*) the tunnel depth and diameter and *iii*) the construction details.

Finally, as for the subsidence induced by mixed causes, one can mention the hydro-compaction of loosely deposited sediments, oxidation and shrinkage of organic deposits, or the development of sinkholes in karstic terrain.

## 2.2 SLOW-MOVING LANDSLIDES

Landslides are natural dangers whose inherent complexity required and still requires many endeavours from the scientific community. According to Cruden (1991) the landslide corresponds to any “*movements of a mass of rock, debris or earth down a slope*” activated or triggered by causes that can be either external or internal (Terzaghi 1950). Several classification systems have been proposed in the scientific literature; among them, the most widely adopted by both scientific and technical communities are those proposed by Skempton (1953), Varnes (1958), Hutchinson (1968), Blong (1973), Varnes (1978), Hutchinson (1988), Cruden and Varnes (1996), Leroueil et al., (1996), Hungr et al., (2001) and Hungr et al. (2014). They are mainly based on the characteristics of involved soils/rocks, morphometrical and kinematical (type of movement) aspects, the stage of movement.

Varnes’ classification (1978), for instance, first distinguishes the involved materials among “rock” (a hard or firm mass that was intact and in its natural place before the initiation of movement), “earth” (material in which 80% or more of the particles are smaller than 2 mm) and “debris” (contains a significant proportion of coarse material, 20% to 80% of particles are greater than 2 mm and the remaining are smaller than 2 mm). Then, the author considers five types of movements (Table 2.1), namely: falls, topples, slides (rotational and translational), lateral spreads and flows; an additional class, including the complex movements, is used to define any combination of more than one type of movement.

**Table 2.1 Landslide classification based on type of movements and involved materials (Varnes, 1978).**

TYPE OF MOVEMENT		TYPE OF MATERIAL		
		BEDROCK	ENGINEERING SOILS	
			Predominantly coarse	Predominantly fine
FALLS		Rock fall	Debris fall	Earth fall
TOPPLES		Rock topple	Debris topple	Earth topple
SLIDES	ROTATIONAL	Rock slide	Debris slide	Earth slide
	TRANSLATIONAL			
LATERAL SPREADS		Rock spread	Debris spread	Earth spread
FLOWS		Rock flow (deep creep)	Debris flow (soil creep)	Earth flow
COMPLEX		Combination of two or more principal types of movement		



The knowledge/prediction of the maximum value of the velocity attained by the displaced mass during the post-failure stage (Leroueil et al., 1996) allows separating the landslides in two main categories. In particular, according to Cruden and Varnes (1996), it is possible to discriminate fast- from slow-moving landslides. The authors individuate seven velocity classes; similarly to the Mercalli's scale that is based on the descriptions of the local effects of an earthquake, each of them is associate to a destructive significance (Figure 2.1). As for “slow-moving landslides” – namely, the category addressed in this Thesis – typical velocity values does not exceed 1.8 m/hr (velocity classes from 1 to 4); whereas “fast-moving landslides” are characterised by maximum velocity values larger than 1.8 m/hr (velocity classes from 5 to 7).

Velocity Class	Description	Velocity (mm/sec)	Typical Velocity	Probable Destructive Significance
7	Extremely Rapid	$5 \times 10^3$	5 m/sec	Catastrophe of major violence; buildings destroyed by impact of displaced material; many deaths; escape unlikely
6	Very Rapid	$5 \times 10^1$	3 m/min	Some lives lost; velocity too great to permit all persons to escape
5	Rapid	$5 \times 10^{-1}$	1.8 m/hr	Escape evacuation possible; structures; possessions, and equipment destroyed
4	Moderate	$5 \times 10^{-3}$	13 m/month	Some temporary and insensitive structures can be temporarily maintained
3	Slow	$5 \times 10^{-5}$	1.6 m/year	Remedial construction can be undertaken during movement; insensitive structures can be maintained with frequent maintenance work if total movement is not large during a particular acceleration phase
2	Very Slow	$5 \times 10^{-7}$	15 mm/year	Some permanent structures undamaged by movement
	Extremely SLOW			Imperceptible without instruments; construction POSSIBLE WITH PRECAUTIONS

Figure 2.1 Proposed landslide velocity scale and probable destructive significant (Cruden and Varnes, 1996).

Leroueil et al. (1996) stressed both the importance of an accurate geotechnical characterization of slope instabilities for their appropriate classification, and their stage of movement. Schematically, this takes the form of a 3-D matrix (Figure 2.2a) in which the three axes refer to the type of material (Figure 2.2b), the type of movement and the stage of movement. For instance, considering a slide in brittle fine-grained soils

(Figure 2.2c), the first stage of movement (*pre-failure*) includes all the deformation processes leading to failure.

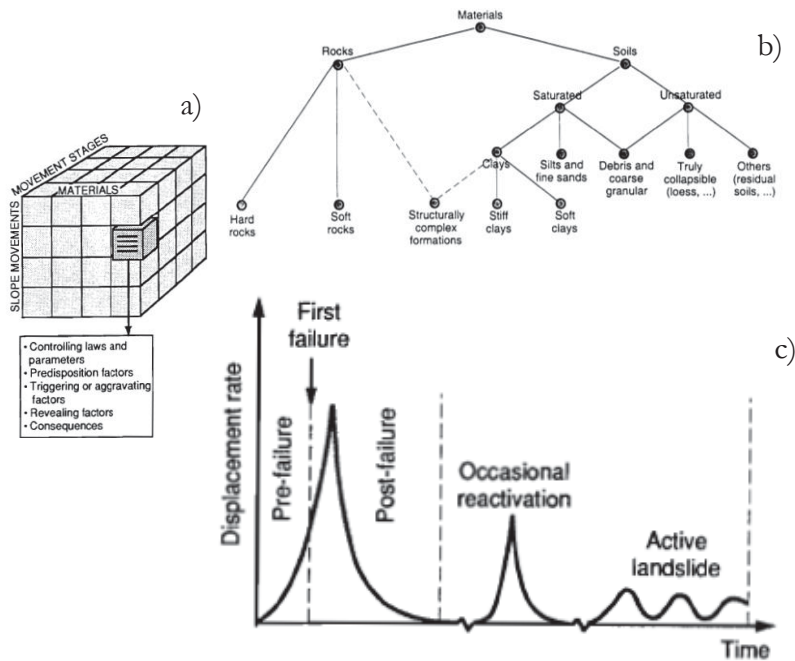


Figure 2.2 Geotechnical schematization of landslide given by Leroueil et al., 1996: (a) scheme for landslide characterization, (b) material involved and (c) different stages of slope movements.

These processes determine a relatively small displacement rate that increases when approaching failure, as a consequence of the gradual (progressive) formation of a shear zone in the soil mass. Once these processes are completed, the *failure* comes about and the soil mass moves along the generated continuous shear zone until a new equilibrium configuration is reached. In this *post-failure stage*, the velocity of soil mass first increases and then decreases. The last stage of movement corresponds to the *reactivation*; in this stage, the soil mass (moving along one or several pre-existing shear zones) can exhibit *active* or *occasional reactivation* styles. In particular, active (slow-moving) landslides show seasonal variations (Figure 2.2c) of the rate of movement that are controlled, both in the accelerating and decelerating phases, by pore-

water pressure fluctuations strictly correlated, in turn, to the net rainfall regime and/or snowmelt. The occasional reactivations (Figure 2.2c) refer to episodic movements that are not controlled by the seasonal fluctuations of the pore-water pressures and must be related to a different specific and episodic triggering factors (e.g., an earthquake). Slow-moving landslides are diffused in many geological and geomorphological contexts over the world. Within the Italian territory, many areas from the north to the south of the country are affected by slow-moving landslides, as testified by well-documented case studies in the scientific literature. Many of these slope instabilities are classified as earth slides (Bertini et al., 1986; Cotecchia, 1989; Cascini et al., 1992a,b; 1994; Lanzo and D'Elia, 1997; Gulla et al., 2003; Tommasi et al., 2006) or earth flows (Angeli et al., 1989; Pellegrino et al., 2004; Iovine et al., 2006), but also examples of complex landslides can be found (Cotecchia, 2006; Agostini, 2013; Antronico et al., 2013, 2014; Gulla, 2017a).

### **2.3 CONSEQUENCES INDUCED BY SUBSIDENCE OR SLOW-MOVING LANDSLIDES**

Subsidence and slow-moving landslides may cause different consequences to facilities with them interacting, such as: the break of underground utilities (e.g. sewers, water and gas distribution pipelines, etc.), interruption of transport infrastructures (e.g. roads and railways) with consequent high cost of maintenances, but also cracking and tilting of buildings. Generally, their occurrence does not cause injured and/or killed people; however, relevant economic losses and damage to both cultural heritages and environmental assets can be recorded.

As for subsidence phenomena, the associated economic losses equal millions of dollars per year, as highlighted by Swiss Re (2011) for the European countries. In the United Kingdom, for example, figures from the Association of British Insurers (ABI) indicate that subsidence-induced building damage entailed economic losses for about £500 millions over the summer seasons of 1975–1976, up to £400 millions in 2003 (Professional Broking, 2007). In France, the economic losses increased by more than 50% within two decades since 1990, with an average cost for the affected regions of € 340 million per year (Swiss RE, 2011).

In Northern European countries – as Netherlands, Sweden, Norway, Denmark – the presence of weak and compressible fine-grained soil deposits that include continuous or discontinuous layers of organic clays and peats, namely soft soils, predisposes to the occurrence of subsidence phenomena. As a consequence, buildings resting on them can suffer from absolute/differential settlements that may cause damages of different severity, eventually affecting the aesthetics or compromising either the functionality or even the stability of the superstructures with significant economic losses. For this reason, since the 11<sup>th</sup> century piled foundations – mainly on wood – started to be used and millions of these are now still in service (Klaassen et al., 2012). However, in the last decades buildings founded on wooden piles posed an urging problem due to wood decaying (e.g. associated with fungi or bacteria attack) that may negatively affect the proper behaviour of the foundation system. Therefore, in many cases homeowners have to bear high costs to adopt appropriate measures for maintaining, repairing or replacing one or more piles or even the whole foundation system in order to prevent the increase of the damage severity level on the superstructure. For instance, it is estimated that in The Netherlands the cost of foundation repairs equals about € 60,000 per household that – on average – represents 10-30 % of the house global value (Klaassen et al., 2015).

In Italy, different urban areas are affected by subsidence phenomena mainly induced by water exploitation (ISPRA, 2006); however, an economic estimate of related losses is not available.

Subsidence consequences are also recorded in other Continents. In the United States, for instance, the National Research Council (1991) estimated that annual costs deriving from flooding and structural damage caused by subsidence exceeded US\$125 million. In Shanghai (China), the phenomenon caused economic losses summing up to more than US\$13 billion (China Daily, Feb. 14, 2007).

It is worth highlighting that, the total cost of subsidence could be probably significantly larger than the current estimations considering that its assessment is normally a difficult task, especially when the phenomenon is induced from different concurrent causes that can make it difficult the individuation of the role played by each of them in the assessment of real costs (Galloway et al., 1999).

As regard landslides, the available information on related economic losses are generally referred to all types of landslides phenomena. For instance, the annual economic losses in Italy, Austria, Switzerland and

France are estimated as US\$ 1–5 billion while United States exceed USD 3.5 billion (Kjekstad and Highland 2009). A separate economic estimation for landslides types (fast or slow-moving) is not available. However, as above mentioned, slow-moving landslides cause consequences to structure and infrastructures with them interacting. In Italy there are several examples of damages to facilities induced by slow-moving landslides, among which: the case of Ancona city, located in central-eastern Italy, where the reactivation of a landslide damaged or completely destroyed 280 buildings, for a total of 865 dwellings, two hospitals and relevant infrastructures (Crescenti et al., 1983); the landslide that affected the urban area of Camerata Picena (AN) with about thirty buildings severely damaged as along with roads (Iovine et al., 2006); many cases in Calabria region (southern Italy), as the landslide that occurred in the little town of San Pietro in Guarano where many buildings, including primary and secondary schools, were severely damaged and later demolished (Cascini et al., 1992a,b; 1994; 2006); Cavallerizzo, where about thirty buildings were severely damaged or destroyed; Ianò, neighborhood of the Catanzaro Province, where the reactivation of the landslide in February 2010 caused relevant damage to buildings, infrastructure and productive activities (Gullà et al., 2014); the municipalities of Lungro (Antronico et al., 2013, 2014; Gullà et al., 2017a) and Verbicaro (Nicodemo et al., 2014; Ferlisi et al., 2015), both suffering from slow-moving landslides which caused damages to the existing facilities located in the historic centres and new developed areas. Mansour et al. (2011) reviewed more than 50 case-histories of slow-moving landslides that caused damages of different severity to facilities in many Countries of the world such as: Canada (Clementino et al., 2008; Moore et al., 2006), USA (Esser, 2000), Australia (Jworchan et al., 2008), New Zealand (Gillon and Saul, 1996), United Kingdom (Nichol and Lowman, 2000), Switzerland (Bonnard et al., 2008), Greece (Topal and Akin, 2008), China (Zhou, 2000), Japan (Fujisawa et al., 2007), Malaysia (Malone et al., 2008).

The case-histories reported in the scientific literature show that damages induced to facilities may depend on several factors related to the features of the slope instability at hand (governing the intensity parameter values) and the exposed facility (including its position within the landslide-affected area); focusing on buildings, onset and propagation of cracks on the superstructures are mainly due to differential displacements at the foundation level whose rates are controlled by soil mass movements in

the reactivation stage, often underestimated in decision making processes (SafeLand Deliverable 2.5, 2011). Therefore, developing methods to analyze and predict the slow-moving-landslide-induced damages to buildings is of particular concern to adequately assess the tolerability/acceptability of differential displacements in order to plan the most suitable mitigation strategies.

### **3 ANALYSIS AND PREDICTION OF THE DAMAGE TO BUILDINGS**

The analysis of consequences to buildings in subsidence- and slow-moving landslide-affected areas has become a relevant issue for scientists/technicians and stakeholders/policy makers in charge of the land-use planning and urban system management, as already outlined in the previous Chapter. Carrying out the related activity mainly relates to the scale of the analysis and generally requires: *i*) the quantitative estimation of some relevant parameters (describing the ground and foundation movement) whose variation leads to the damage occurrence and development, *ii*) the availability of damage classification systems; *iii*) the choice of the most adequate methodology for the damage analysis and prediction.

All these issues are addressed in this Chapter where, after a brief introduction on the relevance of the consequence analysis for the quantification of the risk to the exposed buildings, the main damageability criteria provided by the scientific literature along with the newly proposed probabilistic approaches are discussed.

#### **3.1 CONSEQUENCE ANALYSIS**

The analysis of consequences induced to exposed elements by natural dangers (UNEP, 1997) is a relevant step of the risk management, as specifically highlighted by Fell et al. (2008) for landslide phenomena (Figure 3.1).

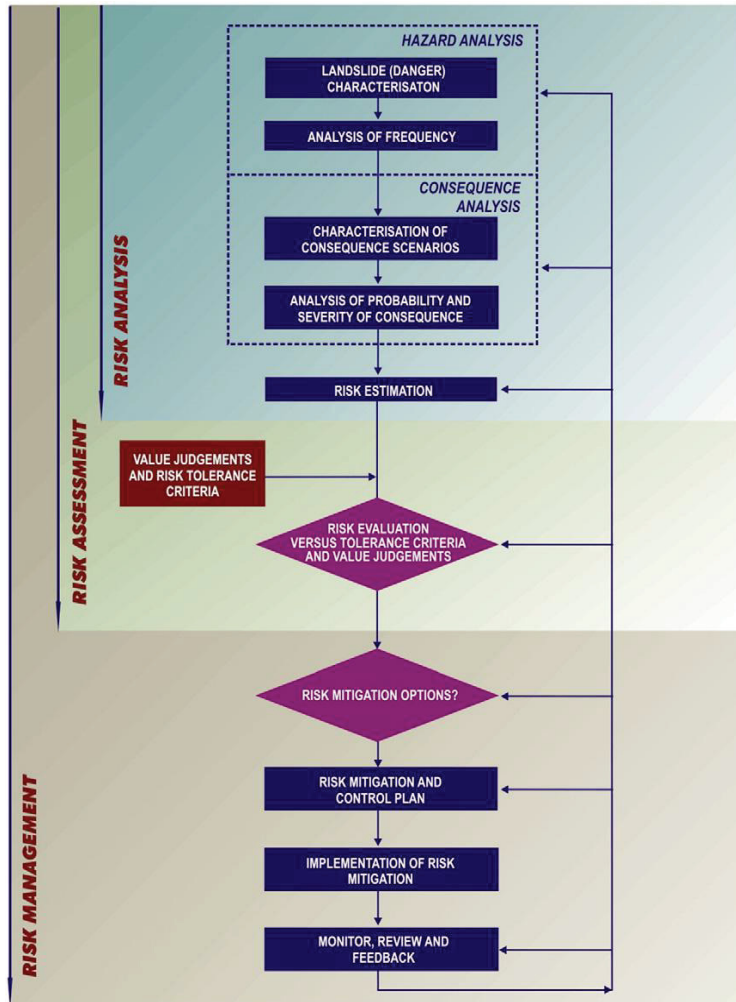


Figure 3.1 Framework for landslide risk management (from Fell et al., 2008).

According to the Authors, the risk management includes analysing, evaluating and mitigating the risk. Within the risk analysis, the analysis of consequences is comprised of two sequential steps that, respectively, deal with the identification/quantification of the exposed elements and the estimation of their vulnerability.

For slow-moving landslides and subsidence phenomena (to which the framework of Figure 3.1 might be easily adapted), the exposed elements are mainly represented by facilities (e.g. buildings, roads, etc.) with them



interacting. Focusing on buildings, the first step involves detecting and classifying them on the basis of reliable information (concerning the age of construction, structural and foundation typologies, occupancy type, number of floors, etc.) to be collected via image processing and field surveys (Remondo et al. 2005; van Westen 2004). Anyway, carrying out these activities depends on the scale of work. In analyses at medium scale (1:100,000 to 1:25,000), in order to overcome the difficulties associated with time consuming data collection and related inherent uncertainties (van Westen 2004), the use of aggregated levels (e.g. groups of buildings characterized by relative homogeneity of structural type) is recommended (Cascini et al. 2013a); whereas, at large (1:25,000 to 1:5,000) and detailed ( $> 1:5,000$ ) scales single buildings can be accounted for (Cascini et al. 2013a; Corominas et al. 2014; Ferlisi et al. 2007; Maquaire et al. 2004; Palmisano et al. 2016; Peduto et al. 2016d; van Westen et al. 2008). Once the elements at risk are recognized and mapped, the elements could be also monetarily quantified (e.g. in terms of monetary value or replacement cost) (Amatruda et al. 2004; Blahut et al. 2014).

The vulnerability is generally defined as the expected degree of loss of a given element or set of elements within an area actually or potentially affected by a hazard of a given intensity (Varnes 1984; Léone et al. 1996; Fell and Hartford 1997; Buckle et al. 2000; Remondo et al. 2008; Bonachea et al. 2009). Focusing on the so-called “physical vulnerability” (Corominas et al., 2014) – which refers to buildings, utilities and infrastructures – it can be expressed in terms of the extent of damage or the cost of recovery as a result of a given event. Its estimation depends on several factors related to both the intensity of the dangerous event (e.g. for slow-moving landslides the volume of the displaced mass, its kinematics and related displacements; for subsidence phenomena the subsiding areas, displacement patterns and rates) and the exposed facilities (type structural system, geometry, material properties, state of maintenance and adopted design codes).

However, gathering this relevant information is not an easy task due to the existence of several sources of uncertainties, in turn related to (Glade 2003): the peculiarities of factors that predispose/trigger a given phenomenon; the spatial distribution of the intensity parameter and its temporal variability; the vulnerability value that might change from one facility to another even for similar danger intensity; the lack of

comprehensive databases of physical damage and its change (if any) over the time.

In the next sections the classification systems of the damage suffered by buildings due to the ground movements along with the methods mostly adopted in geotechnical engineering practice or newly developed for damage forecasting purposes are presented.

### **3.2 DAMAGE CLASSIFICATION**

Many structures, especially old buildings but even modern ones resting on badly-designed foundations, are prone to the damage induced by slow-moving landslides or subsidence phenomena. Accordingly, they represent sensitive recording devices for detecting and mapping both kind of instability phenomena with a better understanding of the mechanisms and magnitudes of movements causing settlements.

Generally, case studies reported in technical and scientific literature show that subsidence and slow-moving landslide can affect the buildings in different ways. In general, the severity of the damage to the superstructures mainly controlled by the structural typology as well as by the soil-footing relative stiffness. For instance, a masonry building resting on high deformable shallow footings can be affected by ground movements more than a reinforced concrete building with very stiff shallow footings.

Furthermore, it must be taken into account that – in some situations – vertical components of the ground displacements may coexist with horizontal ones; moreover, concave upward bending (hogging) or convex bending (sagging) mode of deformation (Figure 3.2) must be properly considered. Each movement type – including footing extension or support loss (Figure 3.2) – generates peculiar (incremental) stress states on a given building which mainly concentrate on corners, doors and windows where cracks first originates (National Coal Board, 1975; The Institution of Structural Engineers, 1994).

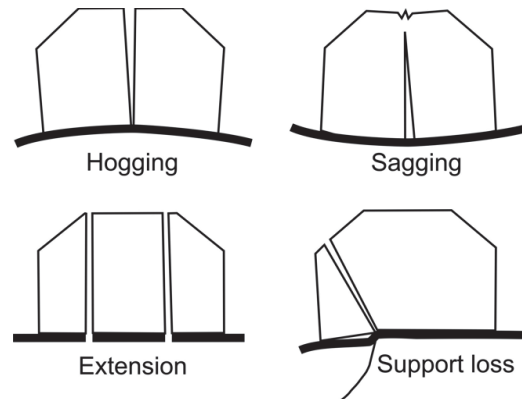


Figure 3.2 Schematic illustration of building damage associated with various types of subsidence movement, some of which may occur together (from Cooper, 2008).

In the scientific literature there are many frameworks and classifications for the building damage caused by ground movements. Many of those have common features, but vary slightly in parameters and categories. According to Cooper (2008), it is possible to individuate four damage schemes, namely:

1. quantitative structural deformation schemes that measure in detail the amount of distortion of structures and accompanying damage (NCB, 1975; Bhattacharya and Singh, 1985; Chiochio et al., 1997);
2. detailed recording schemes that utilise measurements of damage patterns in buildings and relate them to a pattern of stress that affected the structure (Audell, 1996; Building Research Establishment, 1990; Johnson, 2005);
3. established earthquake recording schemes used to assess both earthquake damage and earthquake intensity (Wood and Neumann, 1931; Medvedev et al., 1965; Grünthal, 1998);
4. visual building damage schemes used to record building damage in various geological situations including mining, landslide, shrink-swell clays and general building damage generated by other causes (Burland et al., 1977; Alexander, 1986; Van Rooy, 1989; Geomorphological Services Ltd. 1991; Humphreys and Partners, 1993; Freeman et al., 1994; Palmisano et al., 2016).

The choice of the damage scheme and the ranking to be used to classify the damage level currently or potentially suffered by buildings is closely related to the scale of work (and, therefore, to the analysis purposes) as well as to the available amount of time and money.

From this point of view, the visual building damage schemes are particularly helpful at large (municipal) scale since, in such a case, the methods to be adopted should be fast/easy to apply and preferably limited to the visual inspection of the façades (BRE, 1995). However, it is worth to observe that the gathered information on the current building damage may be biased by: local experiences; caution of professional engineer; occupancy type, market value and saleability of the property (Burland, 2008).

Among the visual building damage schemes provided by the scientific literature, one of the most adopted in geotechnical practice was proposed by Burland et al. (1977). The authors summarize several approaches to quantify the building damage, starting from those used in Britain and arranged by the UK National Coal Board (NCB), as detailed in the Subsidence Engineers Handbook (National Coal Board, 1975). The proposed system of damage categories is based on the ease of repair (Table 3.1) and involves three main criteria:

1. visual appearance;
2. serviceability or function;
3. stability.

In particular, six levels of damage, numbered from 0 to 5 in increasing severity, are established. Normally, the categories from 0 to 2 relate to the attainment of aesthetic damages; 3 and 4 to loss of functionality; and 5 to loss of stability. The authors further underline that:

- *the classification relates only to the visible damage at a given time and not to its cause or possible progression, which are separate issues;*
- *the strong temptation to classify damage solely on crack width must be resisted. It is the ease of repair that is the key factor in determining the category of damage;*
- *the classification, developed for brickwork or blockwork and stone masonry, could be adapted for other forms of cladding. It is not intended to apply to reinforced concrete structural elements. More stringent criteria may be necessary when damage may lead to corrosion, penetration or leakage of harmful liquids and gases or structural failure.*

**Table 3.1 Classification of visible damage to walls with particular reference to ease of repair of plaster and brickwork masonry (from Burland et al., 1977).**

Category of damage	Normal degree of severity	Description of typical damage
0	Negligible	Hairline cracks less than about 0.1 mm.
1	Very Slight	Fine cracks which are easily treated during normal decoration. Damage generally restricted to internal wall finishes. Close inspection may reveal some cracks in external brickworks or masonry. Typical crack widths up to 1 mm.
2	Slight	Cracks easily filled. Re-decoration probably required. Recurrent cracks can be masked by suitable lining. Cracks may be visible externally and some repainting may be required to ensure weathertightness. Door and windows may stick slightly. Typical crack width up to 5 mm.
3	Moderate	The cracks require some opening up and can be patched by mason. Repainting of external brickwork and possibly a small amount of brickwork to be replace. Door and windows sticking. Service pipes may fracture. Weathertightness often impaired. Typical crack widths are 5 to 15 mm or several up to 3 mm.
4	Severe	Extensive repair work involving breaking-out and replacing sections of walls, especially over doors and windows. Windows and door frames distorted, floor sloping noticeably <sup>1</sup> . Walls leaning <sup>1</sup> or building noticeably, some loss of bearing in beams. Service pipes disrupted. Typical crack widths are 15 to 25 mm but also depends of the number of cracks.
5	Very severe	This requires a major repair job involving partial or complete rebuilding. Beams lose bearing, walls lean badly and require shoring. Windows broken with distortion. Danger of instability. Typical crack widths are greater than 25 mm but deepens of the number of cracks.

<sup>1</sup> Note: Local deviation of slope, from the horizontal and vertical, of more than 1/100 will normally be clearly visible. Overall deviations in excess of 1/150 are undesirable.

### 3.3 DAMAGEABILITY CRITERIA

Regarding the methods to predict building damages due to foundation movements, the close examination of the scientific literature reveals that a lot of criteria exists but a wide variety of parameters are adopted to describe the foundation movements and there is seldom uniformity in the terminology. In order to provide definitions and terminology for use internationally, Burland (1995) arranged the reference schemes shown in Figure 3.3.

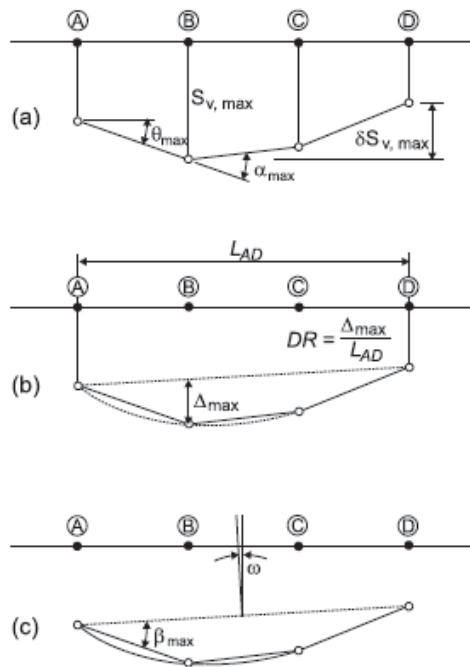


Figure 3.3 Definition of building deformation: a) settlement, differential settlement; b) relative deflection, deflection ratio, c) tilt, relative rotation (after Burland, 1995).

According to these reference schemes, the following deformation parameters are defined:

1. *Settlement*  $S_n$ , defines the vertical movement of a point (positive values indicate downwards movement);
2. *Differential or relative settlement*  $\Delta S_n$ , is the difference between two settlement values;
3. *Rotation or slope*  $\theta$ , describes the change in gradient of the straight line defined by two reference points embedded in the structure;
4. *Angular strain*, produces sagging or upward concavity when positive, while hogging or downward concavity is described by a negative value;
5. *Relative deflection*  $\Delta$ , describes the maximum displacement relative to the straight line connecting two reference points with a distance  $L$ ;
6. *Deflection ratio*  $DR$ , is defined as the quotient of relative deflection and the corresponding length:  $DR = \Delta/L$ ;
7. *Tilt*  $\omega$ , describes the rigid body rotation of the whole superstructure or a well defined part of it. It is difficult to determine as the structure normally flexes itself;
8. *Relative rotation or angular distortion*  $\beta$ , is defined as the rotation of the straight line joining two reference points relative to the tilt.
9. *Average horizontal strain*  $\epsilon_h$ , develops as a change in length  $\delta L$  over the corresponding length  $L$ :  $\epsilon_h = \delta L / L$ .

As far as the damageability criteria are concerned, Negulescu and Foerster (2010) distinguish among three main categories of methods, namely:

- empirical (e.g. Skempton and MacDonald, 1956; Polshin and Tokar, 1957; Sowers, 1962; Bjerrum, 1963; Rüsck and Mayer, 1964; Beeby and Miles, 1969);
- analytical (Burland and Wroth, 1974; Boscardin and Cording, 1989; Boone, 1996; Finno et al., 2005; Bird et al., 2005a,b);
- numerical (Potts e Addenbrooke, 1997; Burd et al., 2000; Son e Cording, 2007).

Skempton and MacDonald (1956) are the authors who first suggested limit values of shallow foundation absolute settlements (and related parameters) on an empirical basis. In particular, they collected

information on 98 buildings, mainly reinforced concrete framed-buildings, deforming under the own-weight. On the basis of this information, they proposed some interesting relationships between the maximum settlement (either absolute or differential) and the maximum angular distortion (Table 3.2) for isolated and rafts foundations, in relation of the soil type (clay and sand); moreover, they suggested a range of limiting values of  $\beta$  (Table 3.3) that moves from damages affecting the aesthetic (architectonic) to those causing loss of stability (structural).

**Table 3.2 Relationships between maximum absolute/differential settlement and angular distortion (after Skempton and MacDonald, 1956).**

Isolated foundations		Rafts	
Clay	Sand	Clay	Sand
$S_{v,\max} = 1000 \cdot \beta_{\max}$	$S_{v,\max} = 600 \beta_{\max}$	$S_{v,\max} = 1250 \beta_{\max}$	$S_{v,\max} = 750 \beta_{\max}$
$\Delta S_{v,\max} = 550 \cdot \beta_{\max}$	$\Delta S_{v,\max} = 350 \beta_{\max}$	$\Delta S_{v,\max} = 550 \beta_{\max}$	$\Delta S_{v,\max} = 350 \beta_{\max}$

**Table 3.3 Limiting values of the angular distortion causing architectonic and structural damage (after Skempton and MacDonald, 1956).**

Damage	$\beta_{\max}$
Architectonic	1/300
Structural	1/150

Polshin and Tokar (1957) recognise different modes of deformation for different types of buildings; therefore, they treated separately unreinforced load bearing walls and framed structures. They define some limit criteria which depend on the “slope” (i.e., the ratio of the difference of settlement of two adjacent supports to the distance between them), the “relative deflection” (ratio of deflection to the deflected part length) and the “average settlement” experienced by building foundations. They identify a common critical tensile strain “ $\epsilon_{\text{crit}}$ ” corresponding to the onset of visible cracks.

As for methods based on structural engineering principles, the most emblematic is the one proposed by Burland and Wroth (1974). The authors analyzed the building damage due to foundation movements by neglecting the interaction between the structure and the underlying ground. Using the elastic deep beam theory (Timoshenko, 1955), they



developed a semi-empirical method that allows relating the settlements of a given foundation system to the onset of visible cracking in the superstructure. The latter was idealised as a linear-elastic, weightless beam of length  $L$ , height  $H$ , and unit thickness (Figure 3.4).

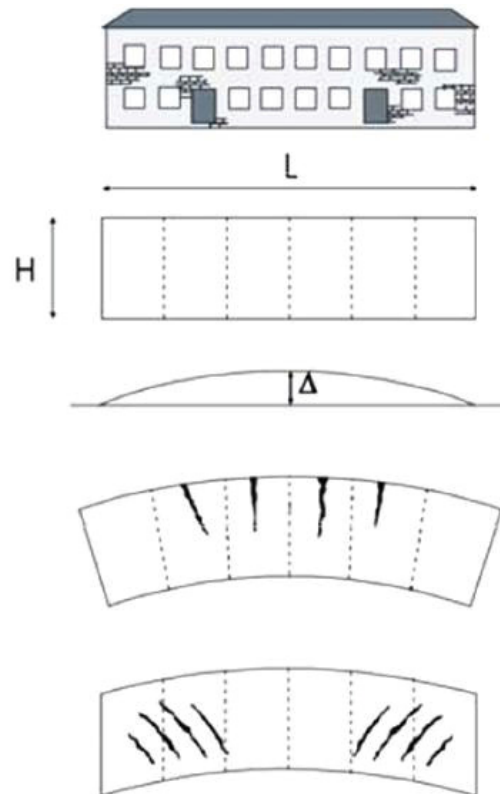


**Figure 3.4** Weightless, elastic beam of unit thickness adopted by Burland and Wroth (1974) to model the behavior of superstructures undergoing settlements in the foundation system.

Assuming that the equivalent elastic deep beam can deform according to the ground surface settlement trough in “greenfield” conditions (i.e., without the building) and setting the horizontal strains equal to zero, Burland and Wroth (1974) derived the relationships between the deflection ratio ( $\Delta/L$ ) and the maximum tensile strain for the equivalent elastic deep beam subject to either pure bending or pure shear deformation. In pure bending, ( $\epsilon_{b,max}$ ) is horizontal; whereas, in pure

shear, the maximum tensile strain ( $\varepsilon_{d,max}$ ) is oriented at  $45^\circ$  (Figure 3.4). The relationships between the maximum tensile strain and  $\Delta/L$  for specified deformation modes is obtained using the following equations, where  $y$  is the distance of the neutral axis from the lower edge of the beam:

$$\frac{\Delta}{L} = \varepsilon_{b,max} \frac{L}{12y} \left[ 1 + \frac{18EI}{L^2HG} \right] \quad (1)$$

$$\frac{\Delta}{L} = \varepsilon_{d,max} \left[ 1 + \frac{L^2HG}{18EI} \right] \quad (2)$$

wherein  $E$  the Young's modulus,  $G$  the shear modulus and  $I$  the second moment of the transversal area of the beam.

In Eqs. (1) and (2), putting the  $\varepsilon_{max} = \varepsilon_{crit}$ , either in bending or in shear, it is possible to plot the relationships in terms of  $(\Delta/L)/\varepsilon_{crit}$  against  $L/H$ , for a given value of  $E/G$  and assuming the position of the neutral axis (e.g. at the base or at mid-height of the beam). An examples is reported in the Figures 3.5a and 3.5b assuming isotropic behaviour,  $E/G = 2.6$  and  $\nu = 0.3$ . From the obtained graphics, the Authors highlight as the deformation mechanism governing the onset of visible cracks for a given  $L/H$  is that yielding the lowest value of  $(\Delta/L)/\varepsilon_{crit}$ .

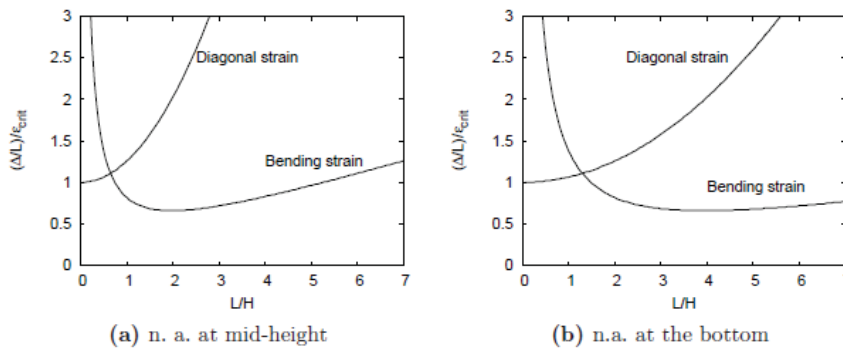


Figure 3.5 a) Relationship between  $\Delta/L\varepsilon_{crit}$  and  $L/H$  for rectangular beams deflecting due to combined bending and shear (neutral axis in the middle). b) Relationship  $\Delta/L\varepsilon_{crit}$  between and  $L/H$  for rectangular beams deflecting due to combined bending and shear (neutral axis at the bottom) (after Burland and Wroth, 1974).

Although the damageability criterion proposed by Burland and Wroth (1974) relies on a theoretical background, difficulties arise in selecting the equivalent beam characteristics (e.g. stiffness parameter values), especially when dealing with a multistory structure. From this point of view, recently studies carried out on this topic by Pickhaver (2006) and Losacco (2011) led to the definition of an “equivalent solid” whose bending and shear stiffness can be estimated taking into account the existence of openings (windows, doors) on buildings.

Boscardin and Cording (1989) complemented the criterion proposed by Burland and Wroth (1974) by including the effects of horizontal strains ( $\epsilon_h$ ) which, in turn, depends on the lateral stiffness of the structure. For instance, a framed structure would be more affected by horizontal strains than a structure with reinforced concrete walls supported by continuous footings or with stiff floor systems. Based on the results of their studies, they categorized the damage to buildings by developing relationships between the horizontal strain and the angular distortion (Figure 3.6).

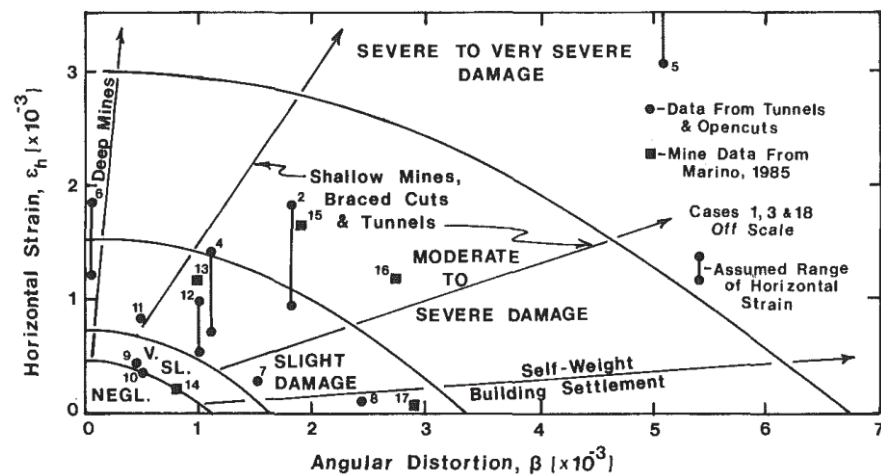


Figure 3.6 Interaction diagram relating angular distortion and horizontal strain for different categories of damage (from Boscardin and Cording, 1989).

Moreover, they superimposed  $\epsilon_h$  to either  $\epsilon_{b,max}$  or  $\epsilon_{d,max}$  (i.e., separating bending and shear deformation modes) and evaluated the resultant strains:

$$\varepsilon_{b,r} = \varepsilon_{b,max} + \varepsilon_h \quad (3)$$

$$\varepsilon_{d,r} = \varepsilon_h \frac{1-\nu}{2} + \sqrt{\varepsilon_h^2 \left(\frac{1-\nu}{2}\right)^2 + \varepsilon_{d,max}^2} \quad (4)$$

It is worth to observe that Eqs. (3) and (4) can be combined with Eqs. (1) and (2); moreover, the concept of  $\varepsilon_{crit}$  can be generalized by introducing limiting tensile strain values ( $\varepsilon_{lim}$ ) properly associated to the damage categories provided by Burland et al. (1977) (Table 3.4).

**Table 3.4 Relations between category of damage and limiting tensile strain (after Boscardin & Cording, 1989).**

Category of damage	Normal degree of severity	Limiting tensile strain [%]
0	Negligible	0 ÷ 0.05
1	Very Slight	0.05 ÷ 0.075
2	Slight	0.075 ÷ 0.15
3	Moderate	0.15 ÷ 0.3
4 & 5	Severe to Very severe	> 0.3

The resulting expressions were plotted by Burland (1995) in terms of  $(\Delta/L)/\varepsilon_{lim}$  versus  $\varepsilon_h/\varepsilon_{lim}$  for different L/H ratios, as shown in Figure 3.7.

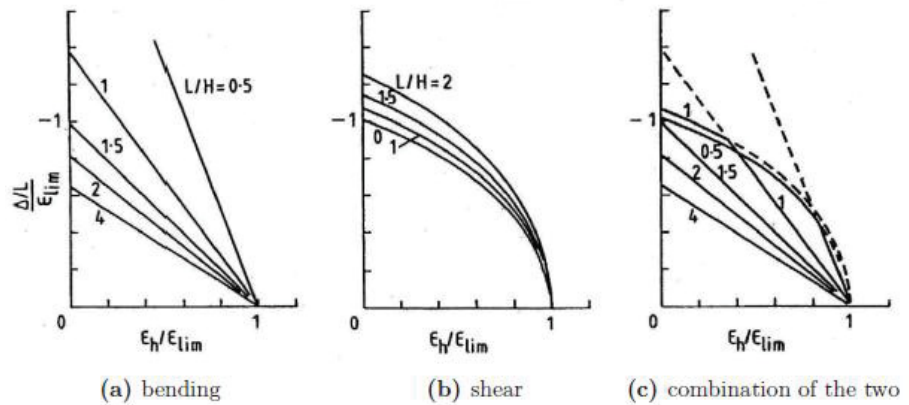


Figure 3.7 Effect of  $\epsilon_h$  on  $\Delta/L$  (after Burland, 1995).

Taking account of the maximum values of limiting tensile strains for each category of damage (Table 3.4), the Figure 3.7c can be easily converted in damage charter where limiting relationships between  $\Delta/L$  and  $\epsilon_h$  are plotted. An example of damage chart is shown in Figure 3.8 for a point loaded beam with  $L/H = 1$ ,  $E/G = 2.6$  and the neutral axis in the bottom of the beam (hogging mode of deformation). Damage charts like this can be used in the damage assessment process.

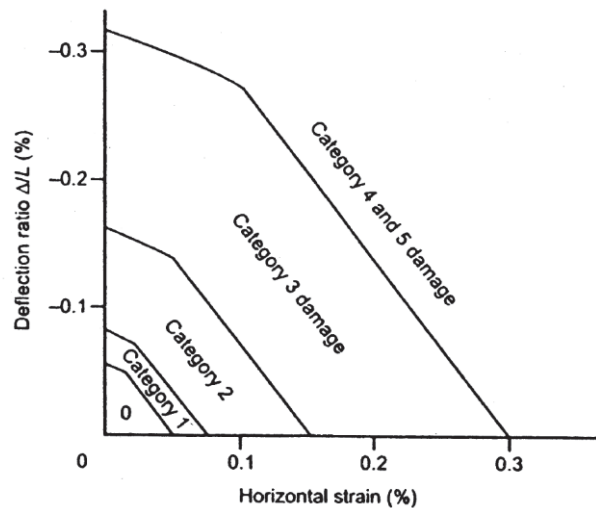


Figure 3.8 Damage chart for a point loaded beam with  $L/H = 1$ ,  $E/G = 2.6$  and the neutral axis in the bottom of the beam (hogging mode of deformation) (after Burland, 1995).

Boone (1996) proposed a Strain Superposition Method (SSM) that uses both equations of fundamental geometry and engineering principles, in order to assess damage to the constructions. The SSM allows assessing the building damage by taking account of ground deformation patterns, damage category criteria and strain concept. The results obtained using the data from over 100 case histories of damaged building treated with Boone's approach are in reasonable agreement with those obtained via the Boscardin and Cording's approach.

Another important approach is the one proposed by Bird et al. (2005a,b) who suggested the use of analytical solutions to assess the expected damage to existing buildings (RC frame) due to liquefaction-induced differential ground movements. In particular, the authors derived the equations representing the deformational capacity of critical columns by applying principles of the displacement-based design; the column deformational demand related to ground motions was obtained on the basis of geometrical considerations. The structure deformation was idealized in four representative cases, hypothesizing differential vertical settlements and lateral movements associated with horizontal and vertical components. Three limit states were considered. A first limit state relates to concrete and steel yield strains and geometrical properties of the section; the second and third limit states relate to the admissible strain values for both materials separately. The study provides interesting conclusions regarding the damage mechanisms due to ground failure and the displacement demand of the floor columns for the RC framed structures, for which the displacement demand is concentrated to the ground floor columns while the upper stories generally rotate as a rigid body. Furthermore, the authors show that, for a single-bay case, deformations take place in the column rather than in the beam. Evolutions of the deep beam model were proposed by Finno et al. (2005) who proposed the use of the ratio  $EI/GA$  (instead of the ratio  $E/G$  first suggested by Burland and Wroth, 1974) to model the deformational behavior of the building. The Authors argued that the main contribution to the bending stiffness of a framed structure building is provided by concrete floor slabs. Walls and diaphragms, instead, offer the main contribution to the shear stiffness. Thus, they proposed the use of a composite, multi-layered deep beam made of  $n$  layers representing floor slabs, separated by  $n - 1$  fillings of different material, representing walls. On that model, once the equivalent bending and shear stiffness of the laminate beam are estimated using a rational approach, the maximum

bending strain at the intrados and at the extrados of the building as well as the angular strain in the  $i$ -th floor can be calculated using the virtual work principle. Finally, the introduction of the  $\varepsilon_{\text{crit}}$  value in obtained equations allows calculating the minimum value of  $\Delta/L$  that cause the onset of cracking in the building.

The limiting values of some parameters that describe the foundation movement and correspond to the attainment of a given level of damage severity on the superstructure according to the synthesized studies, were incorporated in the technical standards and represent today a good starting point for technicians and specialists in charge of either designing new buildings or predicting the response of existing buildings to changes in boundary conditions (e.g. due to anthropic activities). For instance, the Eurocode (EC7) establishes limiting values for foundation movements of new ordinary constructions (CEN, 2007b).

In particular, for open or infilled frames and load bearing or continuous brick walls, the maximum allowed angular distortion ranges from 1/2000 to 1/300, while a limit value of 1/500 is acceptable for many structures in order to prevent the occurrence of a serviceability limit state. Furthermore, considering that the resistance offered by foundations makes the sagging mode of deformation less sensitive than the hogging one, these values must be halved for the hogging mode of deformation (thus 1/4000, 1/600 and 1/1000, respectively). A limitation of the Eurocode is that it refers to new constructions while no advices are provided for existing buildings.

As for numerical approaches, the proper use of advanced methods – such as finite elements (FE) – allow estimating the values of parameters associated to ground and foundation movements via the adoption of appropriate constitutive models. Analyses can be uncoupled (the soil and the structure are studied separately, and the settlement trough is then imposed to the FE building model) or coupled (soil-structure interaction is modeled).

Interesting are the results obtained by Burd et al. (2000) via FE coupled analyses. The Authors highlight that: the building weight tends to increase the general magnitude of settlements that develop underneath; the building stiffness may reduce the differential settlements; depending on the building deformation mode (e.g. sagging or hogging), the soil-structure interactions effects may be more or less pronounced; the lateral restraint offered by the ground may reduce the extent of tensile stresses in the building; differential settlement values obtained as output of

coupled analyses are lower than those of uncoupled analyses, which lead to inaccurate predictions. However, coupled analyses might be too complex and time consuming for practical vulnerability analyses over large areas (e.g., at medium and large scales).

A summary of the explained damageability criteria is shown in Table 3.5.

**Table 3.5 Damageability criteria (modified from Finno et al., 2005).**

Type of method	Limiting parameter	Limiting value	Applicability	Reference
Empirical	$\beta$	1/150	Structural damage	Skempton and MacDonald (1956)
	$\beta$	1/300	Cracking in walls and partitions	
Empirical	$\Delta/L$	1/500	Steel and reinforced concrete frames	Polshin and Tokar (1957)
Deep beam model of building	$\Delta/(L \cdot \varepsilon_{crit})$	$f(L/H, E/G, \text{neutral axis location})$	Load bearing wall ( $E/G=2.6$ ), frame structures ( $E/G=12.5$ ), and masonry building ( $E/G=0.5$ ) assuming no lateral strain	Burland and Wroth (1974)
Extended deep beam model	$\beta, \varepsilon_b$	Chart	$L/H=1$ and assumption horizontal ground and building strains are equal	Boscardin and Cording (1989)
Detailed analysis of structure	Chart width	$\varepsilon_p, \varepsilon_t$	Procedure that considers bending and shear stiffness of building sections, distribution of ground movement, slip between foundation and grade and building configuration	Boone (1996)



---

Laminate beam model	$\Delta/L$	$f(EI/GA, \text{deformation mode})$	The response of a building to imposed deformations is modeled using a laminate beam. It is assumed that the floors offer restraint to bending deformations, and the walls, whether load bearing or infill between columns, offer restraint to shear deformations.	Finno et al. (2005)
---------------------	------------	-------------------------------------	---	---------------------

---

### 3.4 FRAGILITY AND VULNERABILITY CURVES

In the last few years, the attention of technicians and scientists involved in analyses aimed at estimating the vulnerability of buildings to natural dangers (earthquakes, landslides, tsunamis, etc.) has been progressively oriented toward the use of fragility and vulnerability curves. The former provide the conditional probability for every element at risk to be in, or exceed, a certain damage state induced by a phenomenon (or danger) of given intensity; the latter provide, for a given type of building and a given value of the danger intensity, the degree of damage averagely expected. These predictive tools represent a good compromise between the accuracy of the results and the amount of time and money required for the studies; accordingly, they allow providing in a short time the due solutions to the issues related to the occurrence of abovementioned natural dangers whose detrimental effects are worldwide dramatically increasing.

Depending on the scale of the analysis and on the basis of the quality and quantity of available input data, both vulnerability and fragility curves can be generated via the statistical treatment of data collected via heuristic, empirical, analytical or hybrid approach (Saeidi et al. 2009; Negulescu and Foerster 2010; SafeLand Deliverable 2.5, 2011; Mavrouli

et al. 2014). In particular, heuristically-based curves come from the expert judgment of people carrying out the related activities; empirical curves are based on data collected during post-event in-situ surveys; analytical relationships are obtained on the basis of results of numerical analyses performed on structural models; hybrid relationships combine observed data and analytical estimations in order to compensate the scarcity of observational data, the subjectivity of judgmental data and the modeling deficiencies of analytical procedures by combining observed data and analytical estimations.

The generation of fragility and vulnerability curves usually requires a previous classification of the buildings in order to identify similar expected damage mechanisms on the basis of the parameters governing the building response (e.g., the building typology and geometry, the foundation type, the mechanical parameters of constituting materials, the type of resistant system and the efficiency of the connections). Moreover, generating analytical fragility/vulnerability curves on the basis of numerical modeling can result extremely computationally intensive and time consuming; accordingly, this kind of curves can not be easily developed for different areas or countries where, however, different construction techniques might be adopted.

It is worth observing that fragility curves take into account that not all buildings of the same type will suffer the same level of damage for a given intensity of the dangerous phenomenon, while vulnerability curves are representative of the expected average damage for a given type of building for a given value of the danger intensity.

Independently of the method selected to generate fragility and vulnerability curves, the knowledge of three main types of input data is required, namely: *i*) the classification of the building damage severity; *ii*) the building typology; *iii*) the identification of an intensity parameter. In particular, the building damage severity can be classified using limiting values associated to global and local mechanical parameters of the structure; the building typology can be defined according to the parameters governing the resistance of the buildings against the considered danger (e.g. the building materials, age and the quality of construction, foundation type, etc.); the intensity parameter can be selected in relation to the analyzed danger, (e.g., for the earthquakes might be the PGA; for the slow-moving landslides might be the absolute or differential displacement at the building foundation level).

An example of fragility and vulnerability curves is shown in Figure 3.9 (Saeidi et al., 2009) for a massive stone masonry building (Lagomarsino and Giovinazzi, 2006); the curves are derived using a fitting mathematical functions starting from the damage distribution suffered by buildings during an earthquake of given intensity.

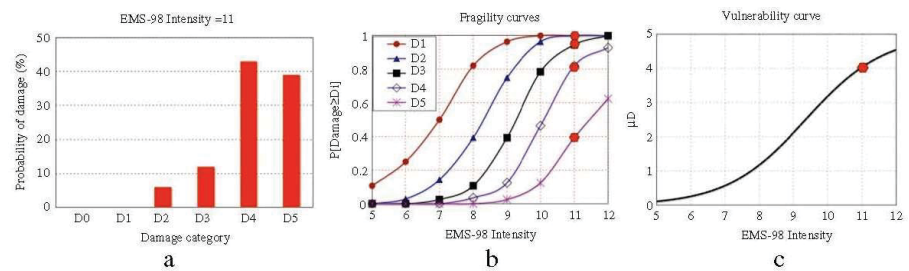


**Figure 3.9 (a) Damage distribution, (b) fragility curves and (c) vulnerability curves for M4 building type, according to EMS-98 (from Saeidi et al., 2009).**

In the scientific literature there are many example and methods in the field of the earthquake engineering for the building vulnerability analysis via the generation of fragility and/or vulnerability curves (Sabetta et al., 1998; Rosetto et al., 2003; Lagomarsino et al., 2006, 2013; Cattari et al., 2004; Rota et al., 2006; Bilgin and Korini, 2012; Penna et al., 2013; Karapetrou et al., 2015, 2016; Zuccaro et al., 2015); whereas few examples can be recovered with reference to fragility and/or vulnerability curves generated for buildings in subsidence- and slow-moving landslide-affected areas.

As for subsidence phenomena, the contributions of Saeidi et al. (2009, 2012) can be mentioned. The Authors generated fragility and vulnerability curves on the basis of the use of empirical and analytical methods, tested and validated with a set of case-histories occurred in Lorraine in the period 1990-1996 and concerning masonry buildings and reinforced masonry buildings with lengths ranging from 10 to 20 m and heights from 7 to 10 m.

As for slow-moving landslides, the contributions of different authors (Negulescu and Foerster 2010; Fotopoulou and Pitilakis 2013a,b; Mavrouli et al., 2014, Pitilakis et al., 2015) are based on the adoption of numerical approaches. For instance, Negulescu and Foerster (2010) generated fragility curves, by assuming the differential displacement as the intensity parameter, with a methodology that consist in using a 2-D

parametric non-linear static time history uncoupled analysis for a simple one bay - one storey cast in-place RC frame. Fotopoulou and Pitilakis (2013a,b) generated fragility curves for low-rise reinforced concrete buildings affected by slow-moving landslides triggered by earthquakes using an extensive numerical parametric study (with different idealized slope configurations, foundation typologies and soil settings as well as different distances of the structure to the slope's crest). Mavrouli et al. (2014) provide a general methodology for calculating the vulnerabilities of reinforced concrete frame structures via numerical fragility curves; in particular, they considered three types of slope instability, namely: slow-moving landslides, rapid flow-type slides and rockfalls.

Scientific contributions on the generation of empirical fragility and vulnerability curves for buildings in slow-moving landslide-affected areas are lacking.

The proposed innovative procedures for the generation of fragility and vulnerability curves at different scales via empirical methods is addressed in Chapter 5 with reference to both subsidence phenomena and slow-moving landslides. It is worth stressing that the obtained empirical fragility and vulnerability curves can be used as predictive tools to assess the conditional probability of reaching or exceed a particular damage level for every element at risk (building) for each building type considered within a given territory, or may be used to assess the damage distribution of all these buildings when applied to a set of buildings.

## 4 THE DInSAR TECHNIQUES

Remote sensing is the science of acquiring information about the Earth's surface without actually being in contact with it. This is achieved by sensing and recording reflected or emitted energy and processing, analyzing, and applying that information (Lillesand and Kiefer, 1987). It is a valuable tool to observe the earth surface or the atmosphere from out of space using satellites (space borne) or from the air using aircrafts (airborne). The energy is in the form of electromagnetic radiation, whose main characteristics are wavelength or equivalently frequency. The wavelength is the length of one wave cycle, which can be measured as the distance between successive wave crests. Frequency refers to the number of cycles of a wave passing a fixed point per unit of time. Therefore, the two are inversely related to each other. The shorter the wavelength, the higher the frequency. Synthetic Aperture Radar (SAR) interferometry is an important branch of remote sensing. It is a powerful and well-established remote sensing technique that enables the highly accurate measurement of important geophysical parameters such as surface topography, ground deformation and subsidence as well as glacier movements, slow-moving landslide, monitoring and control of structures and infrastructures. One of the major applications of the SAR technology is represented by the SAR Interferometry (InSAR) technique which exploits, in its basic form, the phase difference of (at least) two complex valued SAR images. This contribution is further enhanced via the development of innovative algorithms such as those adopted for multipass Differential Interferometric Synthetic Aperture Radar (DInSAR) image processing which today allows, even over large areas, the retrieval of more than 20-year displacements of the topographic surface at fairly affordable costs. The potential of the use of DInSAR data is testified by their increasing diffusion, as recently recorded worldwide with several different applications (e.g. European Space Agency's (ESA) projects MASMOV, ALPS, SLAM, TERRAFIRMA, etc.). Indeed in the last decade, images acquired by Synthetic Aperture Radar (SAR) sensors and processed via Differential Interferometry algorithms (DInSAR) have been increasingly applied by the scientific community to study the measurable effects of natural or anthropogenic

phenomena (or dangers) in different fields of Geosciences – including Geology, Geophysics and Glaciology (Crosetto et al., 2015) – as well as in the Civil and Environmental Engineering. As a result the scientific community analyzed a number of case studies which successfully investigated potential and limits of the DInSAR techniques in order their use in the field of land management.

#### **4.1 SYNTHETIC APERTURE RADAR (SAR)**

Synthetic Aperture Radar (SAR) has been widely used for earth remote sensing for more than 30 years. It provides high-resolution, day-and-night and weather-independent images (Henderson and Lewis, 1998; Franceschetti and Fornaro, 1999) for a multitude of applications ranging from geosciences and climate change research, environmental and earth system monitoring, 2-D and 3-D mapping, change detection, 4-D mapping (space and time), security-related applications up to planetary exploration. The basic concept of Synthetic Aperture Radar is based on the observation that a given target is imaged in a certain number of echoes during the passage of the sensor. The radar system transmits electromagnetic pulses with high power and receives the echoes of the backscattered signal in a sequential way from the lighted target. The typical SAR geometry is illustrated in Figure 4.1, where the platform moves in the azimuth or along-track direction, whereas the slant range is the direction perpendicular to the radar's flight path. The swath width gives the ground-range extent of the radar scene, while its length depends on the data take duration, i.e., how long the radar is turned on. The received echo signal data form a two-dimensional data matrix of complex samples, where each complex sample is given by its real and imaginary part, thus representing an amplitude and phase value. The amplitude and phase of the backscattered signal depends on the physical (i.e., geometry, roughness) and electrical properties (i.e., permittivity) of the imaged object.

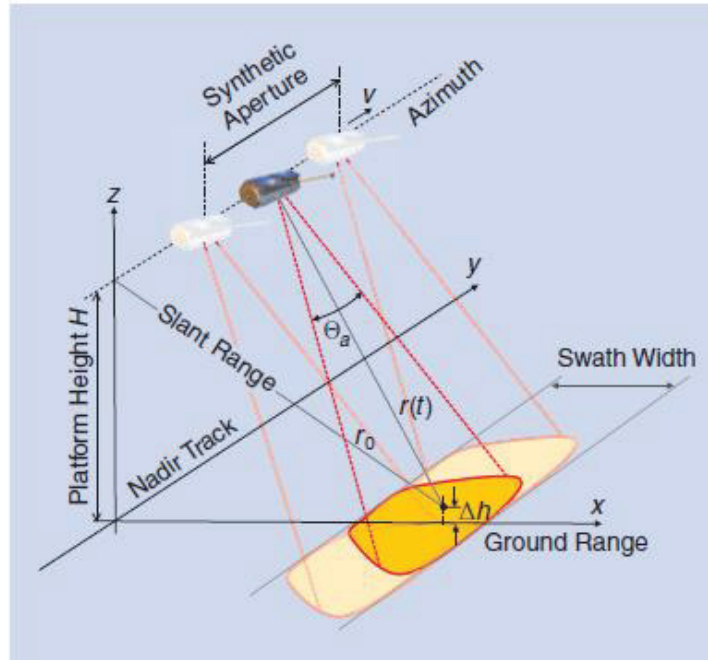


Figure 4.1 Illustration of the SAR acquisition geometry (from Moreria et al., 2013).

All satellites equipped with SAR sensors orbit the earth on a near-polar orbit at an altitude ranging from 500 to 800 km above the earth's surface, depending on the satellite platform hosting the SAR sensor, and follow polar orbits in order to provide a global coverage. Accordingly, scenes may be observed by SAR sensors over ascending or descending orbits typically with opposite ground looking directions. The past and currently available SAR sensors from different Space Agencies, the archives and the achievable resolution are summarized in the Figure 4.2.

The sensor working frequency are generally allocated in the L, C and X bands, corresponding to wavelengths of about 18 cm, 5.6 cm and 3.1 cm, respectively. The time taken for a satellite to re-pass over the same area is called the 'revisiting time'. This latter, spanning from 35 days for old SAR sensors as ERS/ENVISAT to 4 days (on average) in the case for instance of CSK constellation, providing an exceptional capability of collecting stacks of data useful for interferometric analysis (about 30 SAR images) in a shorter time interval, i.e. a few months instead of a few years. Earlier SAR sensors were characterized by fixed swaths (i.e. fixed

illumination beam width), conversely current SAR systems are capable of operating in different imaging modes by controlling the antenna radiation pattern, which allow a trade off between spatial coverage and spatial resolution.

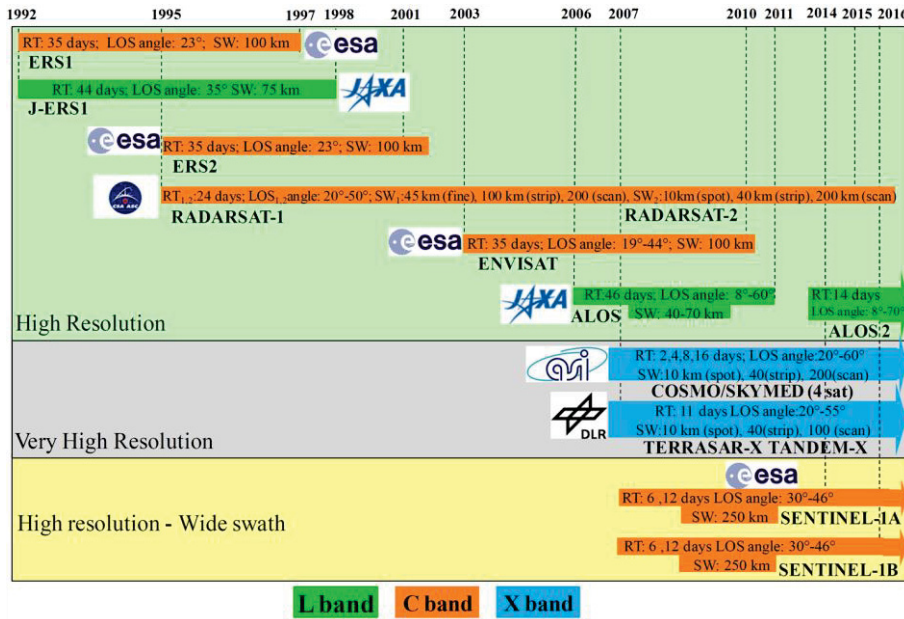


Figure 4.2 The available SAR sensors, the archives and the achievable resolution (modified after Peduto et al., 2015).

In other words, it is possible to have higher resolutions (e.g. up to 1 m for civil applications) with limited coverage (e.g. 10 km) and coarser resolutions (e.g. 10 m) with wider coverage (e.g. a hundred of kilometers or even more). The most fundamental mode is the Stripmap operation, where the pattern is fixed to one swath, thus imaging a single continuous strip. If a wider swath is required, the system can be operated in the ScanSAR mode. In this case, the antenna elevation pattern is successively steered to different elevation angles corresponding to multiple sub-swaths providing a wide-swath SAR image, but with a degraded azimuth resolution compared to the Stripmap mode. When a better azimuth resolution is required, the Spotlight mode can be utilized.

The illumination direction sensor-target is commonly called Line Of Sight (LOS) or slant-range direction. The past generation SAR sensors



were characterized by a fixed illumination direction, whereas modern sensors allow the LOS to be conveniently set. For instance, the LOS angle with respect to the vertical direction was  $23^\circ$  for ERS-1/2, whereas for most of the currently operational sensors it can range from  $20^\circ$  up to  $60^\circ$ . This ability to vary the illumination angle is important when imaging mountainous areas. Moreover, the possibility to change the LOS is also important for monitoring purposes because displacements measured by DInSAR techniques are components of the 3D ground displacement. Taking into account that SAR satellite orbits are polar and radars image the scene typically in the broadside direction – which is orthogonal to the orbit direction – the LOS is almost belonging to the east–west/vertical plane. In particular, LOS direction is downward and being SAR sensors generally right looking, the LOS direction is eastward in ascending passes and westward in descending passes. Ground displacements occurring along North and South directions are, therefore, almost undetectable unless Multiple Aperture Techniques (MAI) – exhibiting significantly coarser resolutions – are used (Jung et al., 2011). For instance, the so-called sensitivity unit vector (Massonet and Feigl, 1998; Colesanti et al., 2003) has components that for ERS/ENVISAT sensors (in absolute values) are: 0.38 for the east component, 0.08 for the north component and 0.92 for the vertical component. Depending on the subswath, for recent satellites the east and the vertical component can be traded off whereas typical orbital inclinations do not allow changing significantly the north component sensitivity.

Another key issue is that SAR sensors are coherent systems but the implementation of interferometric techniques, which are intrinsically characterized by a diversity factor of angular or temporal origin, requires that the scattering on the scene is coherent as well, and similarly that the scattering properties must not change ‘significantly’ over time. In the SAR jargon it is required that the measured echoes from the scene scattering centers are coherent (Fornaro and Pascazio, 2014). The coherence, which is routinely estimated on the available interferometric SAR dataset, can be quantified in terms of statistical characterization of the radar echoes: it is a number between 0 and 1; lower coherence means a higher interferometric phase noise contribution and vice versa. Vegetated areas are prone to temporal coherence losses whereas arid and built up areas are typically associated with higher coherence values, i.e. a better quality of the interferometric signal. The wavelength impacts the coherence; generally the larger the wavelength the higher the coherence.

Therefore lower frequencies are more suitable for the observation of vegetated areas (Fornaro and Pascazio, 2014).

Furthermore, exploiting differences of phases (Interferometric SAR, acronym InSAR) between two or more SAR observations from different orbits (spatial baseline) it is possible to derive digital elevation models (DEMs) (Madsen et al., 1993, Mora et al., 2003), while using also observation acquired at different times (temporal baseline) is possible to estimate surface displacements.

## 4.2 PRINCIPLES OF SAR INTERFEROMETRY

The key idea of SAR interferometry is to compare for a given scene the phase of two or more complex radar images that have been acquired from slightly different positions or at different times. Since the phase of each SAR image pixel contains range information that is accurate to a small fraction of the radar wavelength, it is possible to detect and measure tiny path length differences that can be turned as measure of the sensor-target distance with sub-centimetric accuracy. Therefore, distance variations can be determined by computing, on a pixel by pixel basis, the phase difference (interferometric phase) relative to two (standard two-pass interferometry) or more SAR images. Each SAR image pixel represents the coherent sum of all scattering elements within a resolution cell and contributes both with its own complex reflectivity (amplitude and phase) and with its individual distance from the sensor. The coherent image formation mechanism coupled with the high phase sensitivity prevents the phase value relative to an individual pixel of a single SAR image from being directly exploitable. On the other hand, as long as the complex reflectivity of the pixel as a whole (i.e. the reflectivity of the elementary scatterers and their differential sensor-target path) does not change in the time span between successive radar acquisitions, it is cancelled out from the interferometric phase, thus allowing the measurement of the variation of the range path to the scatterers within the resolution cell. This is the basic assumption for carrying out interferometric measurements and is referred to as absence of decorrelation (or full coherence). The interferometric phase is the combination of several terms that can be grouped in two main categories related to the geometric (deterministic) terms associated to the target-to-

radar path difference and stochastic phase shift (noise) terms. Geometric terms are induced by the target topography in association with the presence of an angular view difference due to the spatial baseline, whereas the Stochastic contributions are due to changes of the scattering properties due to temporal modification (temporal decorrelation) and/or to the different interaction mechanisms between the electromagnetic wave and the ground surface associated to the angular view difference (spatial decorrelation) and propagation delay variation due to the presence of the atmosphere (Atmospheric Phase Screen, or briefly APS). Processing artifacts can be limited by using accurate algorithms for focusing and, particularly for the alignment (registration) of the two images before compare the phase difference. Orbital information inaccuracies can be controlled because they appear as low order spatial contributions on images covering 80x80 km, such as those associated to a frame of ERS and Envisat-ASAR (ERS-like mode) data. The first studies based on the InSAR technique were based on single interferograms (i.e. using an image pair) or a few interferograms, and provided only qualitative information on deformations (Fruneau et al., 1996, 2003, Rott et al., 1999, Kimura, 2000). However, InSAR is limited by the presence of at least two error sources: variations in the Atmospheric Phase Delay (APD) and the inaccuracies of the external Digital Elevation Model (DEM) involved in the cancellation of the topography component from the signal interferences (Massonnet et al., 1993, 1995, Zebker, 1997). These limits were overcome with the development of Multipass Differential SAR Interferometry (MPDInSAR), consisting of the processing of at least 30 images.

### **4.3 DInSAR MULTIPASS ALGORITHMS**

Since early 2000s several multi-pass DInSAR algorithms have been developed and widely used to retrieve information on displacements of the topographic surface, among them: the Persistent Scatterers (PSInSAR) technique (Ferretti et al., 2000, 2001), the Small Baseline Subset (SBAS) technique (Berardino et al., 2002), the Coherent Point Target Analysis (CPTA) (Mora et al., 2003), the Stable Point Network (SPN) (Arnaud et al., 2003), the Interferometric Point Target Analysis

(IPTA) (Wegmüller et al., 2005), the Spatio-Temporal Unwrapping Network (STUN) (Kampes and Adam, 2005), the Stanford Method for Persistent Scatterers (StaMPS) (Hooper et al., 2004) and the Enhanced Spatial Differences (ESD) (Fornaro et al., 2007). The available techniques for the analysis of phase signals in interferometric stacks can be grouped in two classes: Persistent Scatterers Interferometry (PSI) (Ferretti et al., 2000, 2001; Costantini et al., 2008; Crosetto et al., 2008) and Small-Baseline techniques (Berardino et al., 2002; Fornaro et al., 2009). PSI techniques operate at full spatial resolution and identify reliable scatterers by measuring their multitemporal coherence related to the phase stability; monitored scatterers correspond to man-made structures (buildings, roads, bridges) or bare rocks whose size is smaller compared to the system resolution. Conversely, the SBAS techniques are tailored to decorrelating scatterers (i.e. scatterers that may be distributed in the resolution cell or characterized by slow temporal change of the scattering) and to measure ground deformations over large areas (Berardino et al., 2002). These techniques take benefit of a spatial averaging (multilook) to improve the quality of the phase signal thus performing a change of the scale of analysis. Moreover, the interferograms are generated according to small temporal and spatial separation constraints in order to further reduce decorrelation effects associated with possible coherence losses typically present in the analysis of rural areas. The SQueeSAR algorithm (Fumagalli et al., 2011) has been developed to perform a mixed scale of analysis that includes in PSInSAR processing the multilook operation and a data dependent weighting of interferograms in order to improve the capabilities of the original algorithm in the monitoring of decorrelating scatterers. SBAS techniques are suitable for investigating ground deformations at medium scale but can be useful also to calibrate data for full-resolution analysis. At the medium scale, the technique exploits averaged (multi-look) interferograms and allows the generation of mean velocity maps and associated time series for areas extending for some thousands of square kilometres (up to 100 km 100 km), with a ground resolution typically of the order of 80 x 80 m (ERS-1/2 and ENVISAT). SBAS can be used also at large scale by exploiting single-look interferograms, i.e. generated at full spatial resolution (typically of the order of 10 x 10 m for ERS-1/2 and ENVISAT; 3 x 3 m for very high resolution sensors) (Lanari et al., 2004b); however the limitations on the baseline can lead to detection and localization accuracy loss with respect to PSI when dealing with

persistent scatterers (PS) typically associated with man-made targets. With reference to full resolution multitemporal DInSAR analysis, particularly suited for investigating single structures with high resolution sensors (Schack and Soergel, 2014), an advancement is represented by the introduction of tomography approaches (Fornaro et al., 2005) and, more specifically, the Multi-Dimensional Imaging technique (MDI) (Lombardini, 2005; Fornaro et al., 2009) which allows the identification, localization and monitoring of scatterers at full resolution with improved performances with respect to classical PSI approaches. MDI techniques fostered single building monitoring by retrieving better detection and estimation accuracy with respect to PSI also allowing the layover effects on vertical structures (e.g. buildings) – particularly evident in VHR systems – to be solved. MDI is currently used at an operational level by the German Aerospace Center (DLR) for the analysis of urban areas (Wang et al., 2012) with TerraSAR-X data. Furthermore, the resolution improvement allows the capture of more details of single facilities under observation and, hence, their precise monitoring, as testified by the available literature mainly focused on the use of TerraSAR-X data (Gernhardt et al., 2010; Zhu and Bamler, 2010; Reale et al., 2011a,b; Fornaro et al., 2012, 2013). A last important aspect is related to the achievable accuracy of the DInSAR data which depends on a number of factors such as the wavelength, the coherence, the number of images, the overall temporal span and, last but not least, the confidence level of the processing algorithm and implementation issues which may depend also on the processed dataset. Quantitative assessments carried out by comparisons with independent measurements, such as in Colesanti (2003), Casu et al. (2006) and Herrera et al. (2009a), indicate that, as a rule of thumb, the accuracy is of 1–2 mm/year for the average displacement velocity and of 5–10 mm for the single time series displacement. It is worth highlighting that this accuracy was tested, in the available scientific literature, using high resolution data provided by ERS and ENVISAT radar sensors. The use of new radar systems with very high resolution, as TerraSAR-X and Cosmo-SkyMed, jointly with the processing algorithms, which are increasingly sophisticated, can lead to have results that are even more accurate. An experimental evidence of the possibility to achieve an accuracy up to the order of 1 mm on a single displacement measurement was provided in Fornaro et al. (2013), although the results refer to the monitoring of a specific structure (a reinforced concrete bridge). For the buildings, an accuracy up to the

order of 1 mm/year for the average displacement velocity is tested in this work (see Appendix A) with reference to the very-high resolution DInSAR data provided by TerraSAR-X radar sensor.

#### **4.4 DInSAR APPLICATIONS TO SUBSIDENCE PHENOMENA AND SLOW-MOVING LANDSLIDES**

The first experimental demonstration of interferometric techniques were presented by Zebker and Goldstein (1986) for topographic mapping purposes and by Gabriel et al. (1989) for the detection and mapping of small elevation changes by using SEASAT SAR sensor operating in the period June–October 1978. However, the beginning of the development that brought interferometry to operational applications is associated with the launch of ERS-1 satellite in 1991, followed by the twin sensor ERS-2 launched in 1995. Starting from these sensors and several other launched over the years as well as the development of the processing algorithms, many applications have been developed in various natural phenomena and different fields of geosciences (Crosetto et al., 2003).

Indeed, the capability of DInSAR technology was demonstrated in the seismic field (Massonnet et al., 1993; Peltzer and Rosen, 1995; Peltzer et al., 1999; Reilinger et al., 2000; Pedersen et al., 2001, Prati et al., 2010, Eberhard et al., 2010, Reale et al., 2011b); in post seismic deformation studies (Peltzer et al., 1996; Massonnet et al., 1996; Jónsson et al., 2003; Reale et al., 2011b), the monitoring of a seismic (Rosen et al., 1998) and interseismic tectonic events (Chorowicz et al., 1995; Wright et al., 2001; Colesanti et al., 2003); in vulcanology, with several studies of volcanic deflation and uplift, e.g. see (Massonnet et al., 1995; Amelung et al., 1999; Lu et al., 2000; Salvi et al., 2004; Lee et al., 2013; Catalano et al., 2014, De Michele et al., 2016) and in glaciology field with researches mainly carried out on the ice sheets of Greenland and Antarctica including InSAR ice topography measurements (Kwok and Fahnestock, 1996; Joughin et al., 1996); ice velocity measurements (Goldstein et al., 1993; Joughin et al., 1995; Joughin et al., 1998; Mohr et al., 1998); and other glaciological applications, like the determination of the discharge of glaciers (Rignot et al., 1997; Joughin et al., 1999). Other applications are related to subsidence and slow-moving landslides, including the

monitoring and control of structures and infrastructures at different scales of analysis.

As for natural or anthropogenic subsidence the available studies – carried out by using data acquired via European Space Agency (ESA) and Canadian Space Agency (CSA) high resolution (Brefort, 2011) ERS-1/2, ENVISAT SAR and RADARSAT-1/2 sensors – demonstrated the capability of DInSAR technology to monitor ground surface displacements induced by either mining (Carnec et al., 1995; Haynes, 2000; Kircher et al., 2003; Raucoles et al., 2003; Crosetto et al., 2005; Wang et al., 2009; Herrera et al., 2010b) or water extraction (Haynes, 2000; Galloway et al., 2000; Cascini et al., 2006, 2007b; Herrera et al., 2009b; Calderhead et al., 2011; Cigna et al., 2012b; Sanabria et al., 2014; Tomás et al., 2014, Peduto et al., 2015) or underground construction works (Giannico et al., 2012, Bandini et al., 2015). Recently, a breakthrough for the monitoring of subsiding urban areas at detailed scale ( $>1:5000$ ) was provided by the last generation X-Band very high resolution (Brefort, 2011) SAR sensors TerraSAR-X/TanDEM-X (TSX/TDX) mission of the German Aerospace Center (DLR) and the COSMO-SkyMed (CSK) constellation of the Italian Space Agency (ASI) (Herrera et al., 2010b; Cascini et al., 2013a; Fornaro et al., 2014). Such sensors are characterized by a higher revisiting time than that pertaining to the ESA sensors (35 days); in particular, in the case of CSK the use of a constellation of satellites allows bringing the revisiting time down to 4 days (on average) thus providing exceptional capability of collecting stacks of data useful for interferometric analysis (about 30 SAR images) in a shorter time interval, i.e. few months instead of few years. Furthermore, the resolution improvement allows more details of single facilities to be observed and hence their precise monitoring, as testified by the available literature reporting on the use of TerraSAR-X data (Gernhardt et al., 2010; Zhu and Bamler, 2010; Reale et al., 2011a; Fornaro et al., 2012, 2013). Moreover, the recently launch of Sentinel mission of the European Space Agency provides continuity of ERS-1/2 and ENVISAT data archives with reduced revisiting times and larger coverage swath. In Table 4.1 a summary of DInSAR applications to detect and monitor subsiding areas, whose number has increased substantially during the last decade, is reported highlighting the high potential of the technique for the analysis at different scales.

**Table 4.1 Applications of DInSAR technique to subsidence in analysis at different scale (modified after Arena, 2014).**

Case study	Causes	Scale of analysis	Author
Piemonte Region, Italy	Consolidation of recent sediments and construction of buildings	Small scale	Meisina et al. (2008)
Campania Region, Italy	Tectonic structures	Small scale	Milone et al. (2011)
	Water withdrawals	Small scale	Vilardo et al. (2009), Milone et al. (2011)
Su-Xi-Chang area and Shanghai City, China	Water withdrawals	Small scale	Shi et al. (2008)
Campanian Region, Italy	Water withdrawals	Medium scale	Peduto et al. (2015)
Arno River Basin	Water withdrawals and compactation of soft soils	Medium scale	Canuti et al. (2006)
Barcellona province, Spain	Salt mine	Medium scale	Crosetto et al. (2005)
Toluca Valley basin, Mexico	Water withdrawals	Medium scale	Calderhead et al. (2011)
Campanian Plain, Italy	Water withdrawals	Medium scale	Cascini et al. (2007a)
Campanian Plain, Italy	Water withdrawals	Medium scale	Peduto et al. (2015)
Rome	Consolidation process	Large scale	Stramondo et al. (2008)
Murcia metropolitan area, Spain	Water withdrawals	Large scale	Herrera et al. (2009a, 2010b); Tomas et al. (2010)



Bologna, Italy	Water withdrawals and active tectonics.	Large scale	Stramondo et al. (2007)
Sarno, Italy	Water withdrawals	Large scale	Cascini et al. (2006: 2007); Peduto (2008)
Manfredonia Gulf, Italy		Large scale	Triggiani et al. (2011)
Shanghai, Tianjin, Badong, and Three Gorges Dam (China)	Water withdrawals	Large scale	Perissin et al.(2011)
Mexico City, Mexico	Water withdrawals	Large scale	Lopez-Quiroz et al. (2009); Osmanoglu et al. (2011)
Mokpo City, Korea	Soil Compaction	Large scale	Kim et al. (2008)
Calcutta City, India	Water withdrawals	Large scale	Chatterjee et al. (2006)
Vauvert salt mine (France).	Mining	Large scale	Raucoles et al. (2003)
Bangkok, Thailand	Water withdrawals	Large scale	Worawattanamateekul et al. (2003)
Venice, Italy	Natural and anthropic	Large scale	Strozzi et al. (2001)
Campi Flegrei Caldera, Italy	Bradism	Large scale	Lundgren et al. (2001) Berardino et al. (2003)
Los Angeles USA	Active faults, petroleum and water pumping	Large scale	Berardino et al. (2003)
Paris, St.Lazare, France	Water pumping for underground construction.	Large scale	Fruneau et al. (2003)

			Berardino et al. (2002)
Vomero quarter, Naples (Italy)	Underground construction	Large scale	Lanari et al. (2004a)
			Cascini et al. (2007b)
Sarno, Italy	Water withdrawals	Large scale	Cascini et al. (2007a, 2011a); Peduto (2008)
La Union, Spain	Collapse of an abandoned underground mine gallery	Large scale	Herrera et al. (2012)
Different urban areas, Spain	Water withdrawals, soil compaction, mining	Large scale	Tomas et al. (2014)
Orihuela, Spain	Water withdrawals	Large scale	Sanabria et al. (2014)
Baronissi, Italy	Water withdrawals	Large scale	Peduto et al. (2015)
Rovigo, Italy	Underground construction	Detailed	Jurina et al. (2004)
Sarno, Italy	Water withdrawals	Detailed	Cascini et al. (2007b, 2011a)
Rome	Consolidation process	Detailed	Arangio et al. (2013)
Orihuela, Spain	Water withdrawals	Detailed	Sanabria et al. (2014)
Baronissi, Italy	Water withdrawals	Detailed	Peduto et al. (2015)
Florentine area, Italy	Water withdrawals	Detailed	Pratesi et al. (2015)
The Netherlands	Soft soil compaction	Detailed	Peduto et al. (2016a); Nicodemo et al. (2016); Peduto et al. (2017)

As for the application of remote sensing techniques to slow-moving landslides, the usefulness of DInSAR data for landslide characterization and mapping has been investigated in several studies. In these studies, the DInSAR data were mainly used for slow-moving landslide characterization and mapping carried out at different scale of analysis (Fell et al., 2008): small ( $<1 : 100\ 000$ ) (Meisina et al., 2008); medium ( $1 : 100\ 000$  to  $1 : 25\ 000$ ) (Catani et al., 2005; Cascini et al., 2009a,b, 2010a, Lu et al., 2012); large ( $1 : 25\ 000$  to  $1 : 5000$ ) (Notti et al., 2010) and detailed ( $>1:5000$ ) (Colesanti et al., 2003; Herrera et al., 2011). Moreover, the types of slow-moving landslides (Varnes, 1978) investigated by DInSAR data analyses in the aforementioned studies are mainly: slides and earth flows, deep-seated gravitational movements and creep phenomena (Tofani et al., 2014). Some of these studies at small and medium scales resulted in original procedures to update the landslide inventory map by combining conventional thematic data (e.g., topographic, geological, land use maps, and optical images) and on-site investigations with DInSAR data. The scientific literature has widely discussed also the limits and potentiality of the application of the DInSAR techniques to slow-moving landslides. The main limitations for application to landslide field, are related:

- 1) displacement data represent the one dimensional projection in the Line Of Sight (1D LOS projection) of a deformation that can actually occur in all three dimensions (Rocca, 2003; Manzo et al., 2006).
- 2) The ambiguity of phase measurements implies the impossibility to track correctly (i.e., unambiguously) the relative LOS displacement between two scatterers exceeding  $\lambda/4$  ( $=1.4$  cm for ERS) within one revisiting time interval (35 days for ERS), i.e. approximately 14.5 cm/yr. In practice, it is extremely difficult to detect LOS displacement rates exceeding 8–10 cm/yr in the presence of low density of stable scatterers, such as in the case of landslides where topography and vegetation introduce a limitation in the number of detected scatterers. This limits cause the use of DInSAR data only to landslides ranging from extremely to very slow phenomena according to the velocity classification of Cruden and Varnes (1996).

Despite of the above limits, as above mentioned in the scientific literature several papers deal with the application of PSI – and more generally DInSAR – techniques to the study of slow-moving landslides (Colesanti et al., 2003, Casu et al., 2006, Calò et al., 2012; 2014; Bianchini et al., 2013; Cascini et al., 2013a; Garcia-Davalillo et al., 2013, Herrera et

al., 2013; Tofani et al., 2014; Wasowski and Bovenga 2014; Notti et al., 2014, Gullà et al., 2017a) and in the last years, in analysis of the consequences, monitoring and control of structure and infrastructure with them interacting (Perissin et al., 2009; Cascini et al., 2013a; Arangio et al., 2013; Tomás et al., 2013; Di Martire et al., 2014; Costantini et al., 2014, Binachini et al., 2015, Di Martire et al, 2015, Gullà et al, 2017a, Peduto et al, 2016). In Table 4.2 is reported a summary of DInSAR applications to slow-moving landslide for the analysis at different scales.

**Table 4.2 Application of DInSAR technique to landslide in analysis at different scale (modified after Arena, 2014).**

Case of study	Scale of analysis	Author
Umbria Region, Italy	Small scale	Guzzetti et al. (2009)
Piemonte Region, Italy	Small scale	Meisina et al. (2008)
Liri-Garigliano e Volturno River Basin, Italy	Medium scale	Cascini et al. (2009b, 2010a, 2013a)  Catani et al. (2005)
Arno River Basin, Italy	Medium scale	Farina et al. (2006)  Lu et al. (2012, 2013)
Sicily, Italy	Medium scale	Di Martire et al. (2015)
Ancona, Italy	Large scale	Colesanti et al. (2003)
Torrice and Frosinone, Italy	Large scale	Cascini et al. (2010a)
Naro, Italy	Large scale	Cigna et al. (2011)
Verbicaro, Italy	Large scale	Cigna et al. (2012a)
Shuping landslide, China	Large scale	Fu et al. (2010)

La Clapiere, France	Large scale	Fruneau et al. (1996)
La Vallette, France	Large scale	Squarzoni et al. (2003)
Corvara landslide	Large scale	Strozzi et al. (2005)
Costa della Gaveta, Italy	Large scale	Di Martire et al. (2013)
Lungro, Italy	Large scale	Gullà et al. (2017a,b)
Volterra, Italy	Detailed scale	Bianchini et al. (2015)
Lungro, Italy	Detailed scale	Peduto et al. (2016)

Owing to the complexity of DInSAR data, as described in Crosetto et al. (2005), the most advanced applications and the best results are usually achieved through a close cooperation between DInSAR specialists and people able to use DInSAR data in order to analyse the danger at hand. In this context DInSAR specialists can play a fundamental role in helping the end-users to be fully aware of limits and potentials of the techniques, on the other hand, the expert of the analyzed phenomenon, can properly use the DInSAR data in relation to goals and scale of analysis. This allows the full integration of DInSAR data in current practices in order to help the Authorities in charge of land use planning and management as well as technicians and engineers engaged in design activities and adequately support standardized procedures both for updating of inventory map and analysis of consequence of structures and infrastructure interacting with the under study phenomenon.

## 5 THE PROPOSED PROCEDURES

In this Chapter original empirically- and numerically -based procedures for the multi-scale analysis and prediction of the damage to buildings in subsiding or slow-moving landslide-affected areas are summarised. The applicability of the proposed empirical procedures is demonstrated with reference to well-documented case studies in Chapters 6 (for subsidence-affected areas) and 7 (for slow-moving landslide-affected areas); whereas for numerical procedures, results of analyses carried out on a structural model representative of a single building are discussed in Chapter 8. The latter highlight the role played by some factors (i.e. the mechanical properties, the soil type, the distribution of the intensity parameter) in the achievement of a given level of the damage severity, so overcoming the inherent uncertainties of the empirical models.

### 5.1 EMPIRICAL PROCEDURE FOR THE ANALYSIS AND PREDICTION OF THE DAMAGE TO BUILDINGS IN SUBSIDING AREAS

The proposed multi-scale procedure – specifically oriented to the analysis and prediction of subsidence-induced damage to buildings built on shallow/piled foundations on soft soils – includes three different Phases (Figure 5.1).

The first Phase (0) involves carrying out activities at medium scale over large areas and it is aimed at quantifying the role played by the thickness of soft soil deposits in predisposing the subsidence occurrence and its development. To this aim, PSI data on cumulative settlements are preliminarily distinguished, based on their elevation, in PS at ground level and PS on (top of) the buildings.

---

The contents of Section 5.1 are published in:

Peduto D., Nicodemo G., Maccabiani J., Ferlisi S. (2017). Multi-scale analysis of settlement-induced building damage using damage surveys and DInSAR data: A case study in The Netherlands. *Engineering Geology*, 218:117-133.

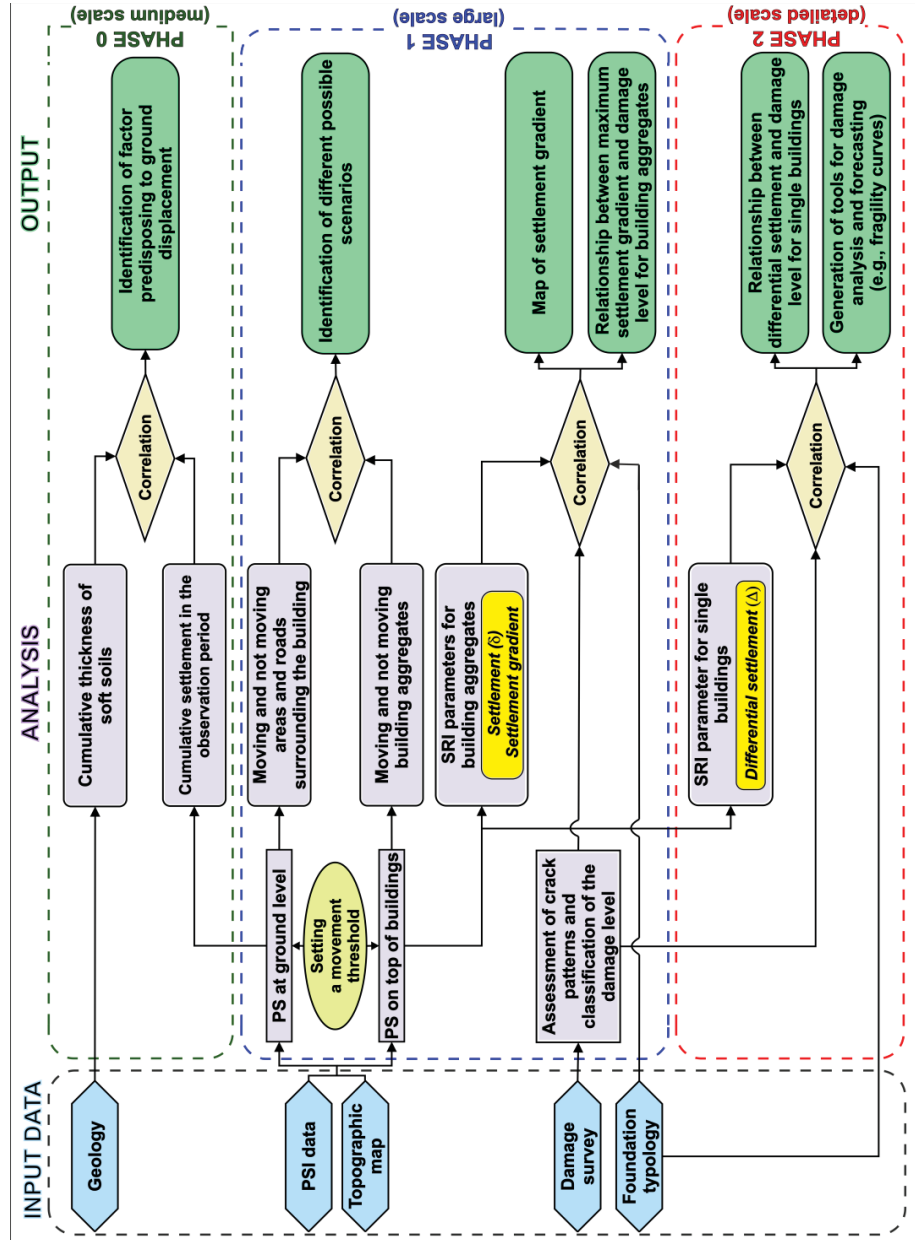


Figure 5.1 Flowchart of the proposed empirical procedure for the analysis and prediction of the damage to buildings in subsidence-affected areas.

Then, “free-field” cumulative settlements (i.e. derived from PS at ground level) are computed by multiplying the PS average velocities along the vertical direction at ground level for the acquisition period of SAR images. The separation in height is necessary because, more often than not, buildings are founded on piles reaching less compressible soils and PSI data from those buildings are not representative of the factors predisposing to ground displacements.

Once the predisposing factors are identified, it is possible to move to the second Phase (1). This Phase, to be carried out at large scale, includes different steps in order to detect the elements at subsidence risk – in terms of building aggregates (Ferlisi et al., 2007; Cascini et al., 2013a; Peduto et al., 2016b) – and, subsequently, analyze their settlements.

In particular, after fixing a movement threshold on PSI velocity, different possible scenarios for building aggregates and areas surrounding the buildings can be identified by comparing the velocities exhibited by PS at ground level and on (top of) the buildings. This allows distinguishing possible ground displacements and related effects on either buildings or infrastructures and utilities (e.g. roads, sidewalks, sewers, pipelines, etc.) or both of them. Then, PSI data on top of the buildings allow the computation of the magnitude of the considered subsidence-related intensity (SRI) parameter describing the movement experienced by the foundation system (i.e., settlement gradients) (Cascini et al., 2006, 2007, 2013b; Peduto et al., 2015) in order to first produce settlement gradient maps; then, referring to settlement profiles along longitudinal cross-sections of the exposed building aggregates, relationships between the maximum values of settlement gradients and the “equivalent damage” level (Sect. 6.1.3) resulting from in-situ damage surveys are derived. For each surveyed building, the recorded damage severity is categorized in six levels: D0 = negligible; D1 = very slight; D2 = slight; D3 = moderate; D4 = severe; D5 = very severe. These levels are adapted from the classification proposed by Burland et al. (1977). In particular, the damage levels D1-D2 refer to aesthetic damage characterized by hairline/fine cracks which can be easily treated during normal decoration or require easy repair work. Starting from level D3, when moderate damages can occur, maintenance works are necessary. Once damage levels D4 and D5 are reached, there is a risk for building safety since the damage can affect its structural stability. According to the scale of analysis, the damage severity (in terms of the equivalent damage level) attributed to a certain building aggregate is estimated as



the average level of damage severity (weighted according to the number of buildings per damage level) recorded on the group of structurally dependent single buildings composing the ‘row house’ aggregate (Peduto et al., 2016b).

As for the last Phase (2), the analysis – to be carried out at detailed scale – focuses on structurally independent single buildings in order to associate the SRI parameter for single buildings, i.e. the differential settlement defined as the maximum difference of PSI-derived vertical settlement between two points of the foundation system (see also Sanabria et al., 2014; Peduto et al., 2016a, 2016b), with the damage severity recorded on each building and grouped according to the building foundation typology. Finally, empirical fragility curves for single buildings resting on either shallow or deep foundations are generated.

## **5.2 EMPIRICAL PROCEDURE FOR THE ANALYSIS AND PREDICTION OF THE DAMAGE TO BUILDINGS IN SLOW-MOVING LANDSLIDE-AFFECTED AREAS**

As highlighted in Section 3.3, the damageability criteria proposed in the scientific literature to analyze and predict the level of damage severity suffered or likely to be suffered by superstructures in relation to the magnitude of the intensity parameters experienced by the corresponding foundation systems are mainly based on heuristic, empirical, analytical (numerical) or hybrid procedures; among these, few contributions are only provided on the analytical generation of fragility and vulnerability curves for single buildings interacting with slow-moving landslides.

In this Section an innovative procedure is proposed. In particular, by adopting an empirical approach which combines DInSAR and damage survey data, fragility and vulnerability curves for single buildings affected by slow-moving landslides are generated at large (municipal) scale. The proposed procedure (Figure 5.2) includes: a first Phase (I), in which the

---

The contents of Section 5.2 are published in:

Nicodemo G., Peduto D., Ferlisi S., Gullà G., Borrelli L., Fornaro G., Reale D. (2017). Analysis of building vulnerability to slow-moving landslides via A-DInSAR and damage survey data. Proceedings of the 4th World Landslide Forum, WLF4 – Ljubljana, Slovenia May 29 – June 2, 2017. (Accepted).

elements at risk are identified; a second Phase (II) requiring the damage classification along with the selection of an intensity parameter; a final Phase (III) leading to the generation of fragility and vulnerability curves.

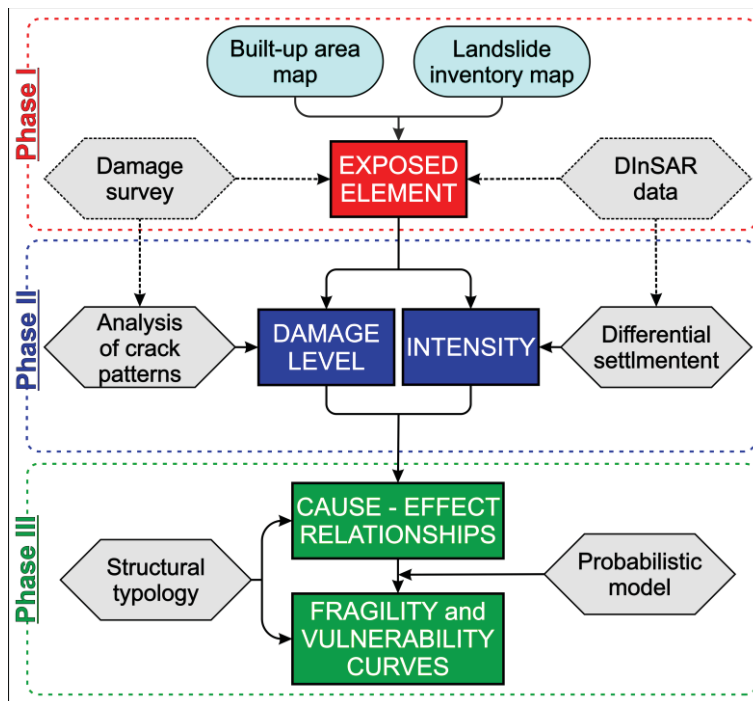


Figure 5.2 Flowchart of the proposed empirical procedure for the analysis and prediction of damages to buildings affected by slow-moving landslides.

As far as Phase I is concerned, the exposed elements (i.e. single buildings with structural typology in reinforced concrete or masonry) are identified, according to the scale of analysis, by overlapping in a GIS environment the topographic maps with the landslide inventory maps. Then, in Phase II, the damage level as well as the intensity parameter are estimated for each identified exposed element. In particular, the level of damage severity pertaining to single building is classified on the basis of data collected – during in-situ surveys – via ad-hoc predisposed fact-sheets and according to six classes (D0 = no damage; D1 = very slight; D2 = slight; D3 = moderate; D4 = severe; D5 = very severe) adapted from the ones given by Burland et al. (1977). The considered slow-moving landslide intensity parameter corresponds to the maximum

differential settlement experienced by a given building; it is defined as the maximum value of the difference of vertical settlements between two points of the foundation system, in turn derived from the analysis of high and very high-resolution DInSAR data. Finally, in Phase III, the information gathered on both damage severity and magnitude of the intensity parameter, homogenized according to the structural typology (reinforced concrete or masonry), are first managed in order to determine the relationships between cause (differential settlement) and effect (damage); then, they are used for the generation of fragility (by adopting a probabilistic model) and vulnerability (by adopting a regression model) curves (Sect. 3.4).

### **5.3 PROCEDURE FOR THE ANALYSIS AND PREDICTION OF THE DAMAGE TO BUILDINGS VIA NUMERICAL APPROACH**

The analysis and prediction at detailed scale ( $> 1:5,000$ ) of the damage to buildings currently or potentially affected by a certain phenomenon (or danger) via advanced methods (Fell et al., 2008a) is not an easy task since it requires gathering a number of relevant information on the characteristics of both the phenomenon (e.g. magnitude of intensity parameters) and all buildings (material, stiffness/strength, number of floors, state of maintenance, etc.) at risk. Accordingly, the use of structural computational codes (mainly implementing numerical methods) brings along difficulties in generating simple and, at the same time, reliable models able to simulate the real behaviour of buildings. In this regard, the proposal of procedures should require the proper identification of few representative parameters whose values might be calibrated on the basis of easily retrievable data, in order to limit expensive and time-consuming field survey operations. On the other hand, it is worth observing that numerical analyses carried out via structural computational codes on representative single buildings can allow investigating issues concerning limits and potentialities of the empirical procedures described in the Sections 5.1 and 5.2 (their adoption mainly relate to the scale of analysis and related goals to be pursued, along with time and costs required to carry out the activities) as well as to enucleate (via sensitivity analyses) the role played by the

different factors contributing to the occurrence and development of building damages.

To these aims, in this Thesis a numerical analysis at detailed scale (single building) was carried by adopting a procedure (Figure 5.3) leading to the generation of fragility curves.

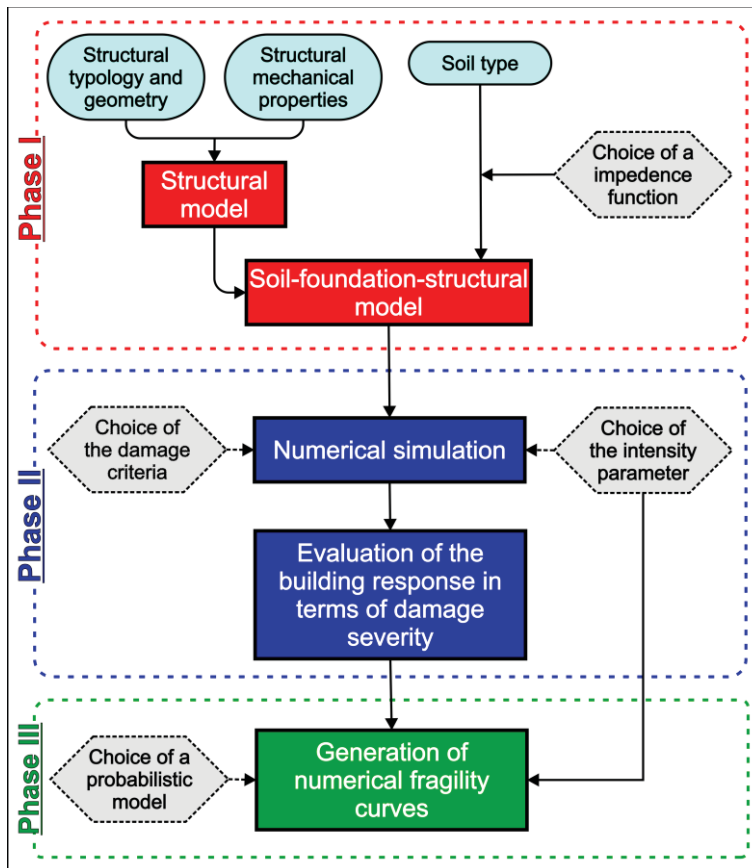


Figure 5.3 Flowchart of the proposed procedure for the analysis and prediction of the damage to building via numerical approach.

The proposed procedure is based on three cascading steps that can be adapted and specialized with reference to a certain building resting on a given soil. Indeed, the first Phase (I) involves generating the structural model and the soil-structure interaction model, through the definition of the geometry and the mechanical properties of the building as well as the

identification of the soil type. The outcomes of this activity allow (Phase II) analysing – via numerical methods – the (super)structural response in terms of damage severity levels, provided that a damageability criterion and an intensity parameter (e.g. differential settlement) are established. The latter, in turn, can be imposed at the building foundation level as displacement patterns simulating credible modes of deformation.

As far as the damageability criterion is concerned, similarly to the approach adopted in the seismic field, threshold values of the damage limits states can correspond to the maximum drift values pertaining to buildings affected by differential settlements and categorised in five classes: LS1 = slight; LS2 = moderate; LS3 = extensive; LS4 = very heavy; LS5 = collapse.

The results obtained in Phase II are, then, used in Phase III that finally leads to the generation of numerical fragility curves by adopting a probabilistic model.

## 6 ANALYSIS AND PREDICTION OF THE DAMAGE TO BUILDINGS IN SUBSIDING AREAS: CASE STUDIES IN THE NETHERLANDS

This Chapter focuses on the application of the proposed innovative multi-scale procedure (see Chapter 5 – Section 5.1) oriented to analyze and predict the damage to subsidence-affected buildings on shallow and piled foundations via an empirical approach that combines information concerning the characteristics of the subsoil, the DInSAR-derived displacement rates of the buildings and the damage recorded on those via field surveys.

### 6.1 STUDY AREA AND AVAILABLE DATASET

The proposed multi-scale procedure (Figure 5.1, Chapter 5) was applied to densely urbanized areas with different building typologies resting on different foundation systems (i.e. shallow and piled foundations) located in the south-western part of The Netherlands (Figures. 6.1a, 6.1b, 6.1c) where the subsoil includes highly compressible clayey and peaty soil layers extending to depths of about 20 m.

The selected area for the analysis at medium scale includes the cities of Rotterdam and Schiedam (Figure 6.1a) over an area of about 15 km<sup>2</sup>; the

---

The contents of Chapter 6 are published in:

Peduto D., Nicodemo G., Maccabiani J., Ferlisi S. (2017). Multi-scale analysis of settlement-induced building damage using damage surveys and DInSAR data: A case study in The Netherlands. *Engineering Geology*, 218:117-133.

Peduto D., Nicodemo G., Maccabiani J., Ferlisi S., D'Angelo R., Marchese A. (2016). Investigating the behaviour of buildings with different foundation types on soft soils: two case studies in The Netherlands. *Proceedings of the VI Italian Conference of Researchers in Geotechnical Engineering – Geotechnical Engineering in Multidisciplinary Research: from Microscale to Regional Scale*, CNRIG – Bologna, Italy 20-23 September, 2016. *Procedia Engineering*, pp. 529-534.

analysis at large scale focused on a smaller area of about 2 km<sup>2</sup> represented by a neighborhood of Schiedam (Figure 6.1b); whereas for the analysis at detailed scale, a portion of the neighborhood of Schiedam (Figure 6.1c) including 310 structurally independent buildings was considered.

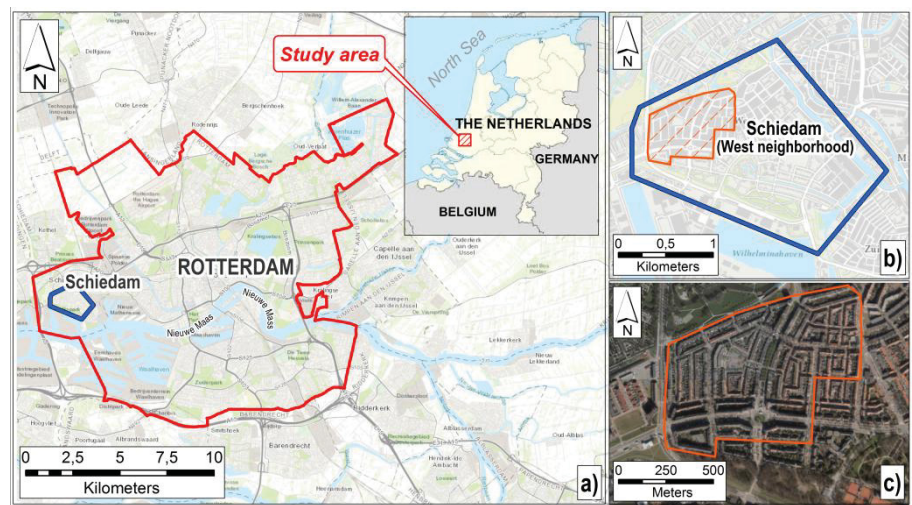


Figure 6.1 The study area: a) area analyzed for investigating factors predisposing to ground settlements at medium scale; b) the study area at large scale and c) the study area at detailed scale.

### 6.1.1 Geological setting

The Netherlands is predominantly a flat country; about 60% of shallow soil deposits are of Holocene age and of fluvial and coastal origin (Figure 6.2). The sediments of coastal origin have their current ground surface elevations at or below the mean sea level. The eastern part of the country consists almost entirely of Pleistocene deposits, mainly constituted by sandy soils sloping upwards to the south and east with an average elevation between 10 and 20 m above of the mean sea level and exceeding 100 m only in the extreme southeast (van der Meulen et al., 2013). Since the 1960s onward, the Geological Survey of The Netherlands (GSN) started a detailed geological mapping program focused on the south-western part of The Netherlands. This activity resulted in a database of maps at 1:50,000 scale along with vertical cross-

sections (Hageman, 1964; van Rummelen, 1965, 1972; Vos and Van Heeringen, 1997). More recently, GSN has built the 3D geological ‘GeoTOP’ model (DINOloket, 2016) that represents a sound basis on properties and features of the national subsoil.

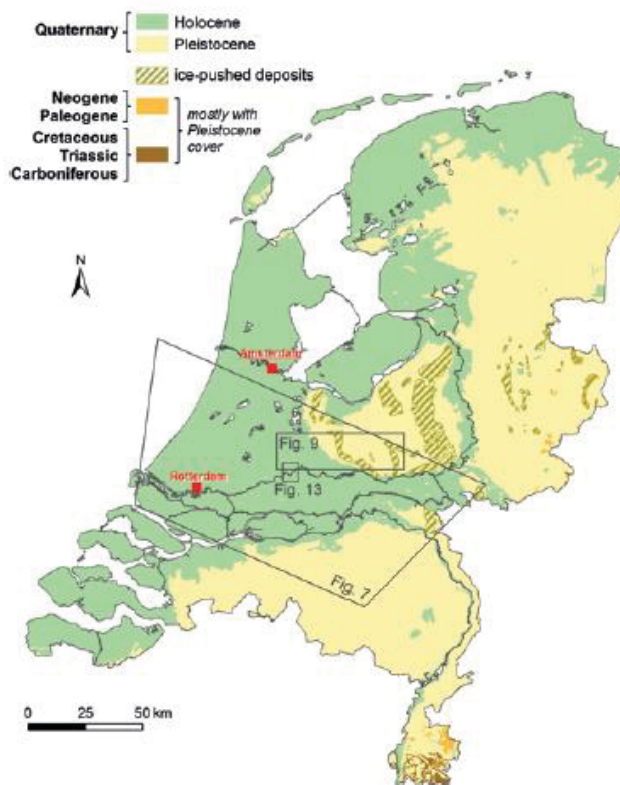


Figure 6.2 Geological map of The Netherlands (from van der Meulen et al., 2013)

The model was developed based on a systematic collection and analysis of hundreds of thousands borehole data and cone penetration tests through a layer modelling (Figure 6.3) which has led to define lithostratigraphically subvolumes in the model space that were then voxelised (Stafleu et al., 2011). The model extends down to a depth of 50 m below the ground surface (Figure 6.4a) with almost a nationwide coverage, schematizing the national territory in millions of voxels, each measuring  $100 \times 100 \times 0.5$  m (height  $\times$  width  $\times$  depth). Each voxel contains



information on the litho-stratigraphy (Figure 6.4b) including the probability of occurrence of each lithological class (Figure 6.5c).

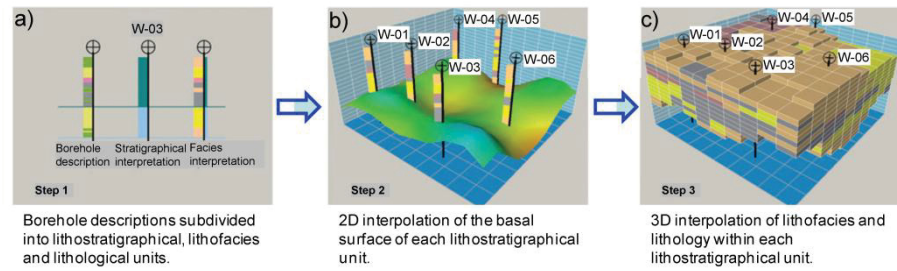


Figure 6.3 GeoTop modelling workflow: a) borehole descriptions subdivided into lithostratigraphical, lithofacies and lithological units; b) 2D interpolation of the basal surface of each lithostratigraphical unit; c) 3D interpolation of lithofacies and lithology within each lithostratigraphical unit (modified from van der Meulen et al., 2013).

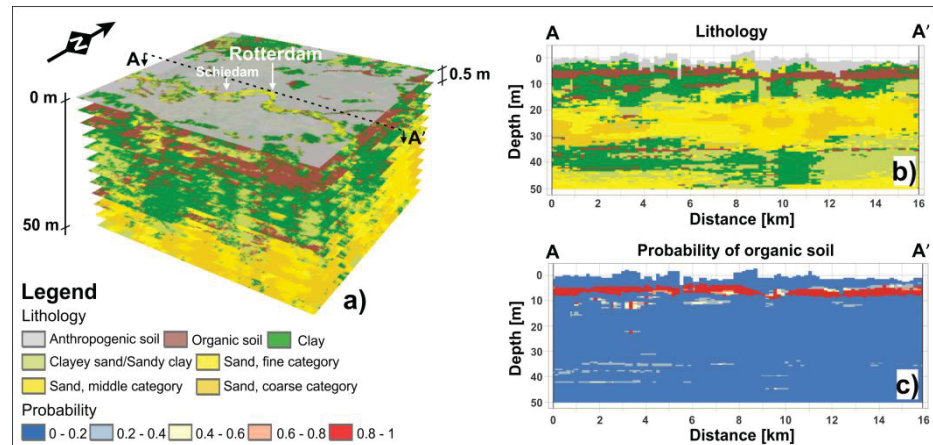


Figure 6.4 a) GeoTop model; b) example of geological cross-section and c) probability of occurrence of organic soil along the A–A' profile sketched in a) (extracted from the portal of the Geological Survey of the Netherlands – DINOloket).

With reference to the study area (Figure 6.1a), GeoTOP-derived information was used to generate the land cover map (Figure 6.5a), the cumulative thickness maps for soft (Figure 6.5b) and sandy soils (Figure 6.5c). Figure 6.5d shows a typical section in the study area with soft soil

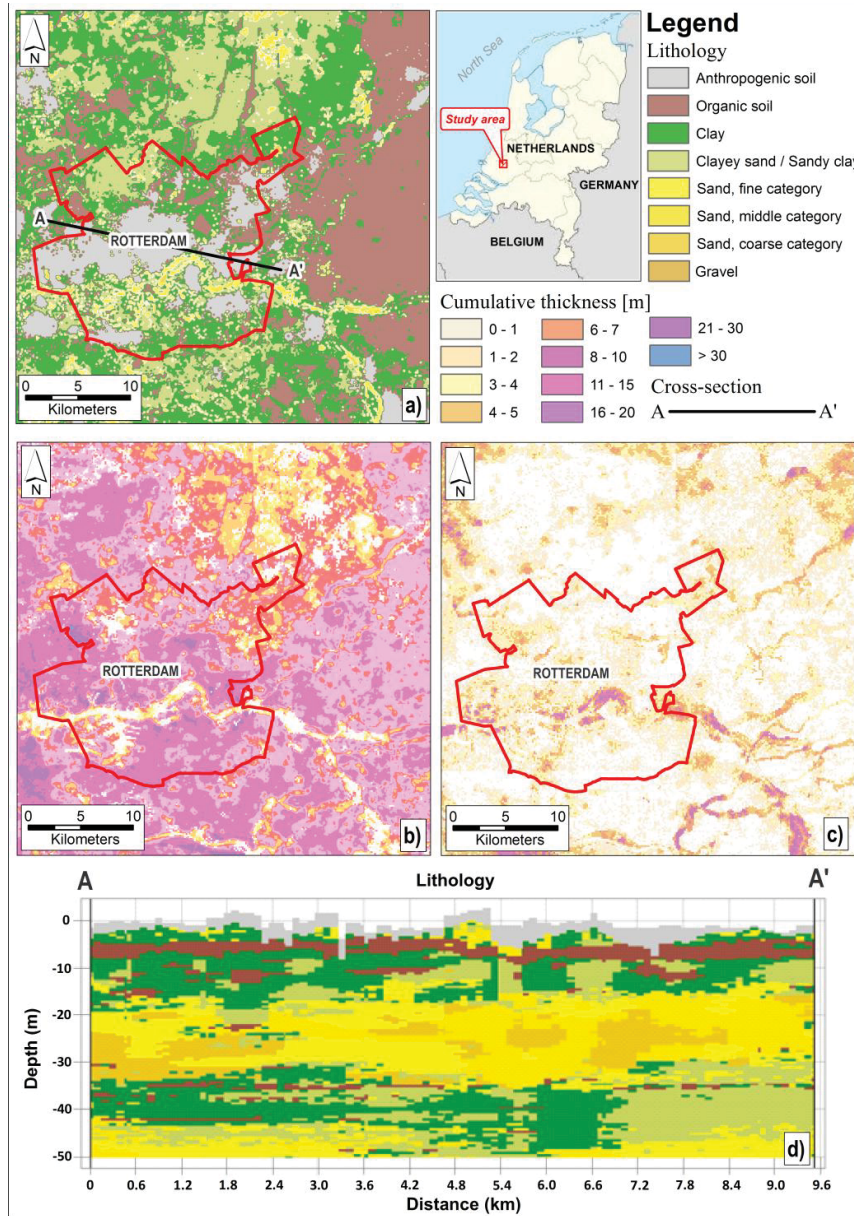


Figure 6.5 Geological setting of the study area: a) land cover; b) cumulative thickness of soft soils (organic and clayey); c) cumulative thickness of sandy soils, and d) geological cross-section along the A–A' profile sketched in a) (extracted from the portal of the Geological Survey of the Netherlands – DINOloket).

layers of Holocene age – with total thicknesses not exceeding 20 m – superimposed on a sandy layer of similar thickness. Below, soft soils including narrow lenses of sandy soils rests on a sandy deposit of Pleistocene age.

### 6.1.2 DInSAR dataset

The available SAR dataset over the study area consists of 285 images (133 from the ascending orbit and 162 from the descending orbit) acquired by the TerraSAR-X (TSX) constellation of satellites in the period spanning 2009–2014 (Table 6.1). These data were processed by SkyGeo Netherlands B.V. using their commercial processing chain ‘Antares’, which implements the PSI method described in Ferretti et al. (2001) and a great number of state-of-art improvements and complementary techniques. As an input DEM, the SRTM90 (e.g. USGS, 2016) was used. Considering the flatness of Dutch topography, this resolution is sufficient to reach the desired precision. The resulting PSI velocity measurements passed a quality assurance protocol from which the measurement precision shown in Table 6.2 was derived for both datasets using the ascending and the descending orbit images. For purposes of the present analysis, the PSI data were projected from the Line of Sight (LOS) to the vertical direction (Cascini et al., 2007b) since subsidence-related displacements were assumed as mainly vertical. In theory, data from the ascending and descending directions can be combined to derive the vertical deformation component (Manzo et al., 2006; Peduto et al., 2015) with greater precision.

**Table 6.1 Main features of the TerraSAR-X datasets (processed by PSI technique) used for the analysis.**

Sensor	Orbit direction	Period of acquisition	No. of images	Ground resolution (m × m)	Incidence angle (°)
TerraSAR-X	Ascending	06/04/2009	133	3 × 3	39.3
		29/09/2014			
TerraSAR-X	Descending	08/04/2009	162	3 × 3	24.1
		20/09/2014			

**Table 6.2 Main PSI measurement precision.**

Measurement	Precision achieved
Single displacement measurement	< 4 mm
Linear displacement velocity	< 1 mm/year
Geolocation precision (x,y,z)	1.5 m
Geocoding precision (x,y)	< 1 cm

In this case the method was not used because a comparison of the same PSI dataset with leveling benchmarks (see Appendix A) demonstrated that the assumption of verticality does not introduce significant errors and the total error is well below 1 mm/year. Furthermore, the data originating from the tops of buildings were separated from those referring to the ground level via the use of AHN2 (2016), a detailed and publicly available LiDAR-derived DEM of The Netherlands with a vertical precision of 5 cm at 50 cm resolution cells.

Based on the analysis of the histograms of the heights, all PS heights < 2 m above the DEM terrain height were assigned to the “ground level” class. Another source of error is that PS can originate from the top of buildings or from the facade at different heights. However, considering the geolocation precision of the PS, no attempt to correct for this were carried out because the errors introduced in this manner are so small that the total error is still < 1 mm/year.

The spatial distribution of PSInSAR-derived velocities is shown in Figures 6.6 and 6.7. It can be noticed that Figures 6.6a and 6.6b (respectively showing PS on top of the buildings and at ground level), which were derived from the ascending dataset, and Figures 6.7a and 6.7b (respectively showing PS on top of the buildings and at ground level), which were derived from the descending dataset, exhibit almost similar velocity patterns independently of the acquisition geometry. Moreover, the high density coverage in the study area can be appreciated (7136 PS/km<sup>2</sup> on ascending orbit and 8793 PS/km<sup>2</sup> on descending orbit) thus confirming the improved capability of last generation X-band sensors in built-up area monitoring.

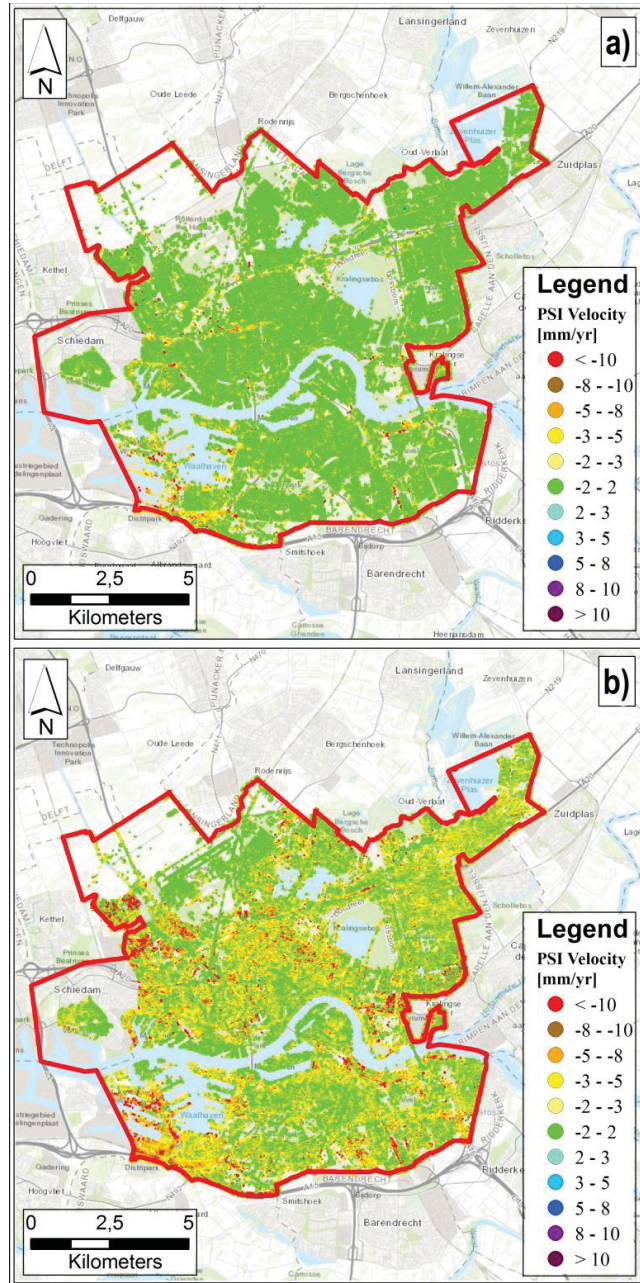


Figure 6.6 Distribution of PSI data provided by the TerraSAR-X radar sensor projected along the vertical direction: PSI data on ascending orbit a) on top of the buildings and b) at ground level.

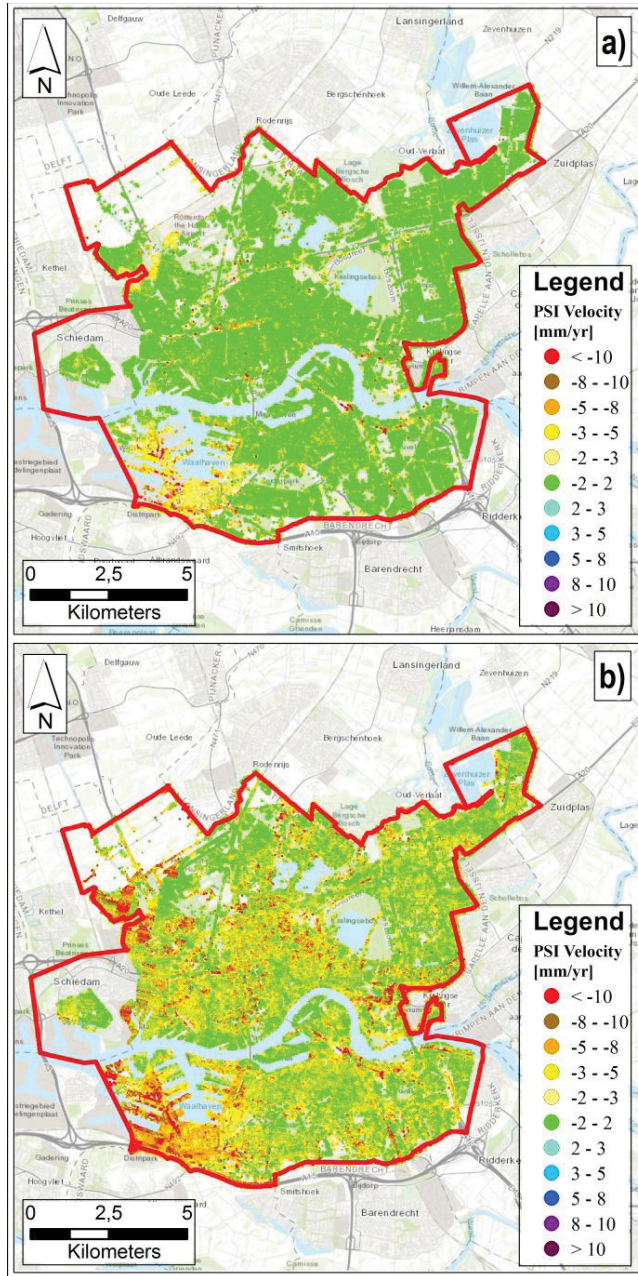


Figure 6.7 Distribution of PSI data provided by the TerraSAR-X radar sensor projected along the vertical direction: PSI data on descending orbit a) on top of the buildings and b) at ground level.

### 6.1.3 Buildings damage survey

As already highlighted in the Chapter 2, (infra)structures resting directly on subsoil including alternating layers of soft soils can suffer from differential settlements that cause damages of different severity. With reference to the buildings, this occurs especially in masonry structures since they have a low capacity of adapting to differential settlements or angular distortions. This is the reason why many buildings in the Northern European countries, as The Netherlands, were founded on piles. Unfortunately, many of these piled foundations are aging badly and do not work properly anymore, causing similar damages as with shallow foundations. The resulting damages are commonly visible as widespread cracks on the walls (Ortiz et al., 2015) which, in the most dangerous cases, can compromise their stability. Therefore, the analysis of crack patterns exhibited by building façades provides useful information in order to establish correlations between cause (differential settlements) and effects (damage) suffered by superstructures (Bianchini et al., 2015; Ferlisi et al., 2015; Palmisano et al., 2016) which can be used to derive helpful tools for the analysis of the expected damage on element at risk and forecasting purposes. To this end, in-situ damage surveys were carried out in April and May of 2015. These surveys were focused on the portion the Municipality of Schiedam where damages to buildings had been recorded (Figure 6.1c). In particular, in order to investigate both the severity and the distribution of damage to buildings, ad-hoc predisposed fact-sheets were filled in for surveyed buildings. The used fact-sheets consist of different sections that allow systematical recording of the archive information regarding the geological features and available settlement measurements as well as the information gathered from the in-situ surveys. An example of a filled fact-sheet is shown in Figure 6.8. In particular, section 1 gathers information concerning the building location and its description in terms of structural type, foundation typology, number of floors, age of construction and occupancy type. The available datasets concerning the geological features and the PSI data are included in Section 2. Section 3 reports the photo collection of damage recorded on building façades such as the presence of cracks and/or disjunction in the outer walls and their position, as well as their distortion or tilt, and finally the assignment of the observed damage severity.

**BUILDING FACT-SHEETS**

DATE: 2015/05/12

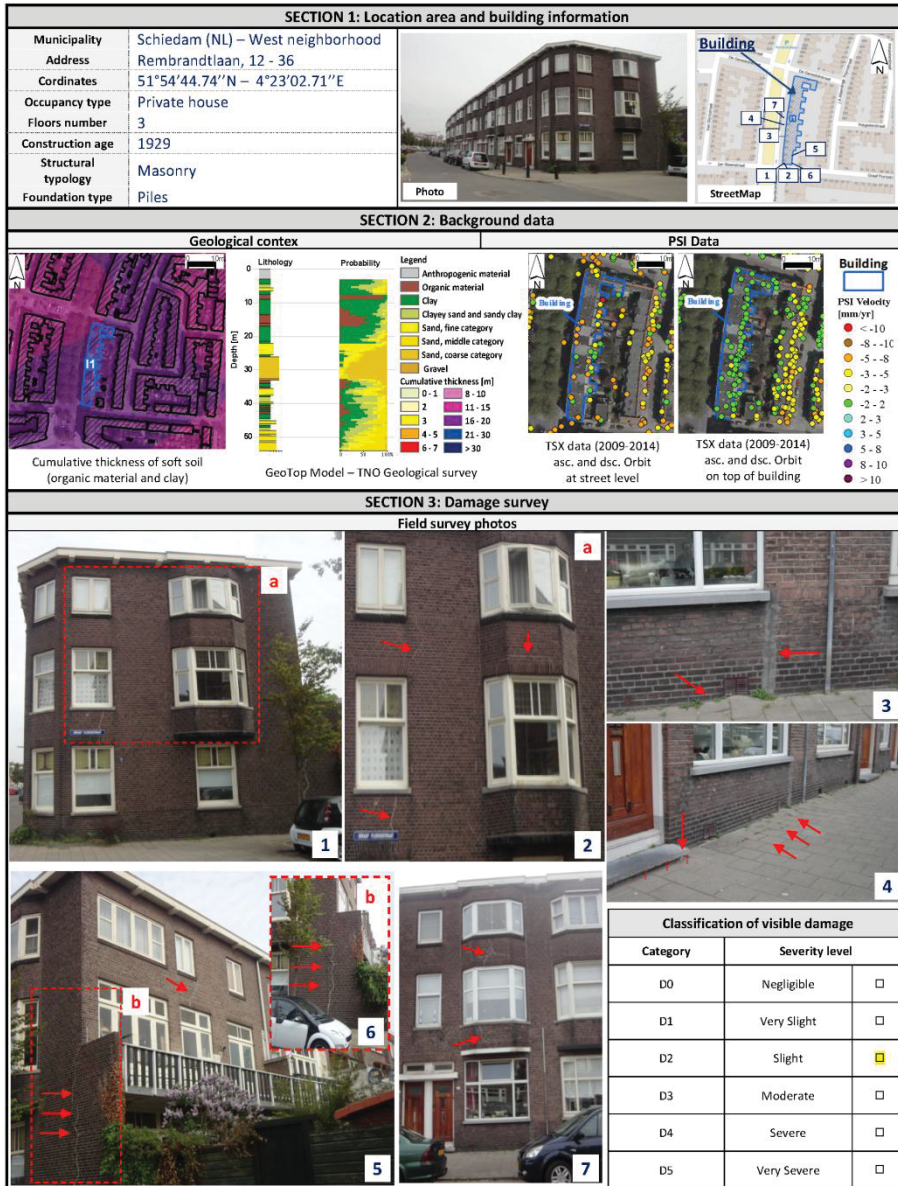


Figure 6.8 Building fact-sheet: (Section 1) location area and building information; (Section 2) background data related to the geological context and PSI velocities; (Section 3) some photos of the field survey and damage severity levels.



This latter, as described in Section 5.1, was differentiated in six levels: D0 = negligible; D1 = very slight; D2 = slight; D3 = moderate; D4 = severe; D5 = very severe, adapted from the ones proposed by Burland et al. (1977); moreover, according to the scale of analysis, it was attributed to the single building for analyses at detailed scale or to a certain building aggregate for analyses at large scale. In the latter case, the “equivalent damage” level was evaluated as average level of damage severity – weighted according to the number of buildings per  $D_i$  and approximated to the closer level – recorded on the group of structurally dependent single buildings composing the considered “row house” aggregate. The results of the survey campaign are shown in Figure 6.9a and 6.9b on building aggregates characterized by masonry structures built on different foundation types (43% shallow foundations, 49% piled foundations and 8% unknown) and in Figure 6.10a and 6.10b for the single buildings.

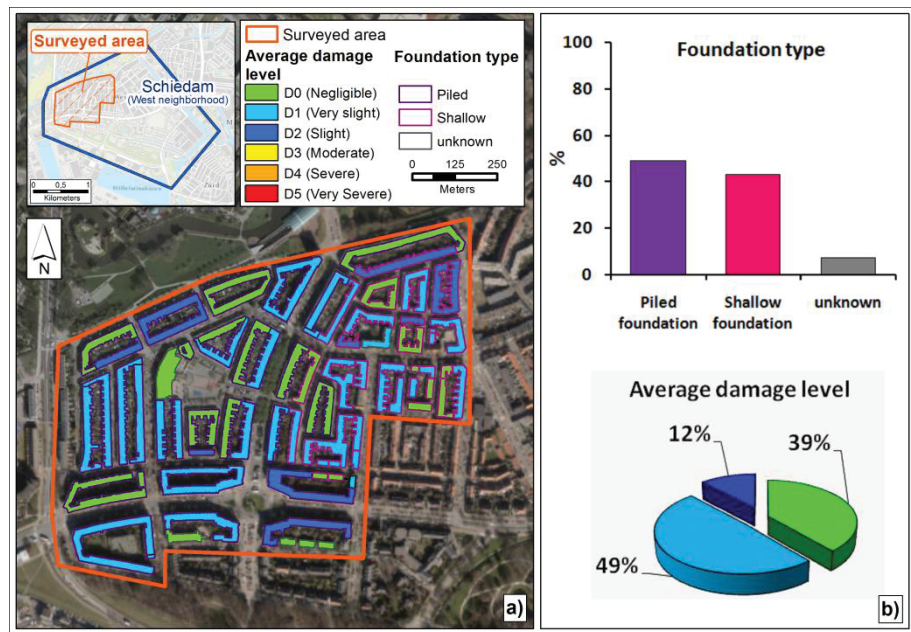


Figure 6.9 a) Map of surveyed building aggregates distinguished according to the recorded equivalent damage level and foundation type; b) distribution (in percentage) of foundation types and equivalent damage levels in the surveyed area.

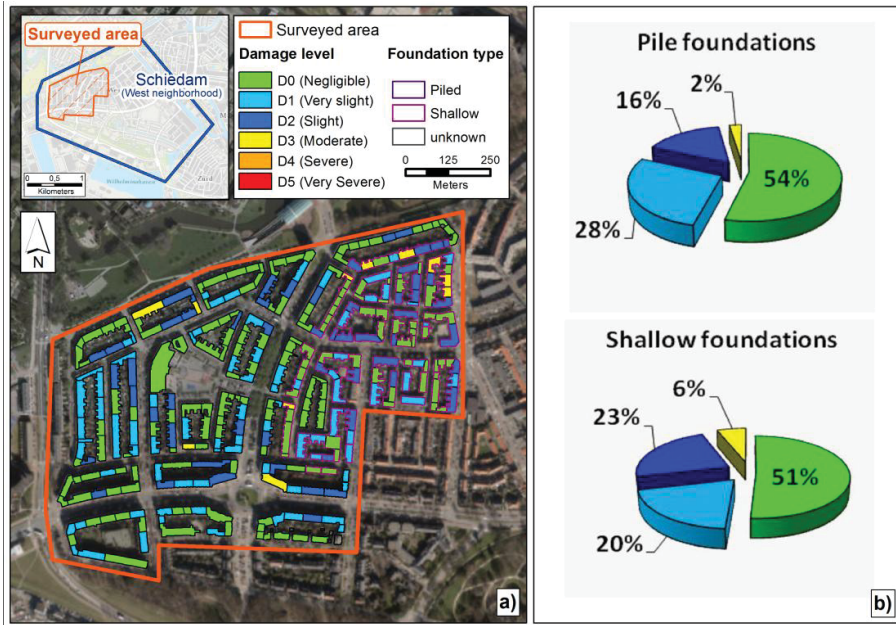


Figure 6.10 a) Map of surveyed single building distinguished according to the recorded equivalent damage level and foundation type; b) distribution (in percentage) of damage levels according to building foundation type.

The analysis of the collected data highlighted that 39% building aggregates out of the total do not exhibit damage; whereas 61% of all estimated equivalent damages do not exceed the D2 level (D1 = 49%; D2 = 12%). As for single buildings, the survey revealed the presence of 146 buildings exhibiting damages on the total of 310, whose distribution is different for buildings built on piled or shallow foundations; however, in both cases, their severity does not exceed the D3 level.

## 6.2 RESULTS

### 6.2.1 Analysis at medium scale

Ground displacements associated with the creeping behavior of soft soil layers are generally highly variable in time and space according to both

the spatial distribution of their cumulative thickness and their compressibility, in turn mainly related to the organic matter content and acting effective stresses (van Asselen et al., 2010). Therefore, in the study area, the role played by the factors predisposing to ground displacements was first investigated at medium scale (Figure 6.1a) by recovering the relationship between the soft soil cumulative thickness and the PSI-derived settlement magnitude in free-field conditions. To this aim, only PSI data at ground level were considered. Then, according to both the scale of analysis (Fell et al., 2008; Peduto et al., 2015) and the accuracy of the available geological model, a grid was imposed on the area under investigation with a cell size of  $100 \times 100$  m on which the vertical PSI velocities were interpolated using the Inverse Distance Weighting (IDW) method. The velocity values computed for each cell were then multiplied for the acquisition period of the radar sensor images, thereby generating the cumulative settlement maps shown in Figures 6.11a and b.

It can be observed that cumulative settlements in the period 2009–2014 range up to 3–5 cm. In a few areas, coloured in red in Figure 6.11a and b, they even exceed 5 cm. It is worth noting that the available piezometric measurements in the study area do not show significant changes over time so that the groundwater level can be assumed as a constant. This confirms that the recorded settlements in the study area can be merely ascribed to the intrinsic characteristics of the soft soil layers. Therefore, the PSI-derived settlement maps (Figures 6.12a and 6.12c) were compared with the map of cumulative soft soil thickness (organic and clayey material) (Figure 6.12e).

After drawing a generic cross-section (e.g. section A–A' in Figures 6.12a, c and e) it can be observed that the maximum settlements (Figures 6.12b and 6.12d) are recorded where the maximum cumulative thicknesses of soft soils (Figure 6.12f) are present. In particular, this mainly occurs where the organic matter content increases in the soft soil layers (with probability of occurrence close to one, see Figure 6.12g). For instance, this can be easily noticed in the first part of the geological cross section of Figure 6.11h moving from A to A'. Conversely, where soft soil thicknesses are lower and the organic matter content decreases, lower PSI-derived settlements are recorded.

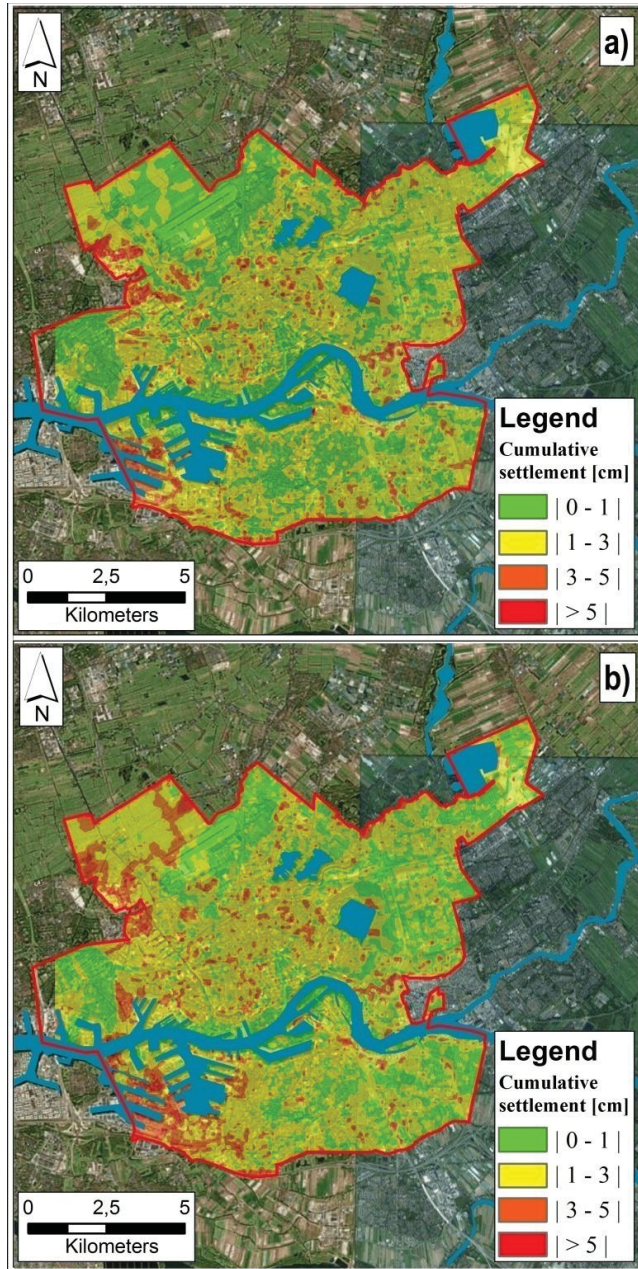


Figure 6.11 Map of cumulative settlements in the period 2009–2014 using TerraSAR-X data at ground level along the vertical direction on a) ascending and b) descending orbit.

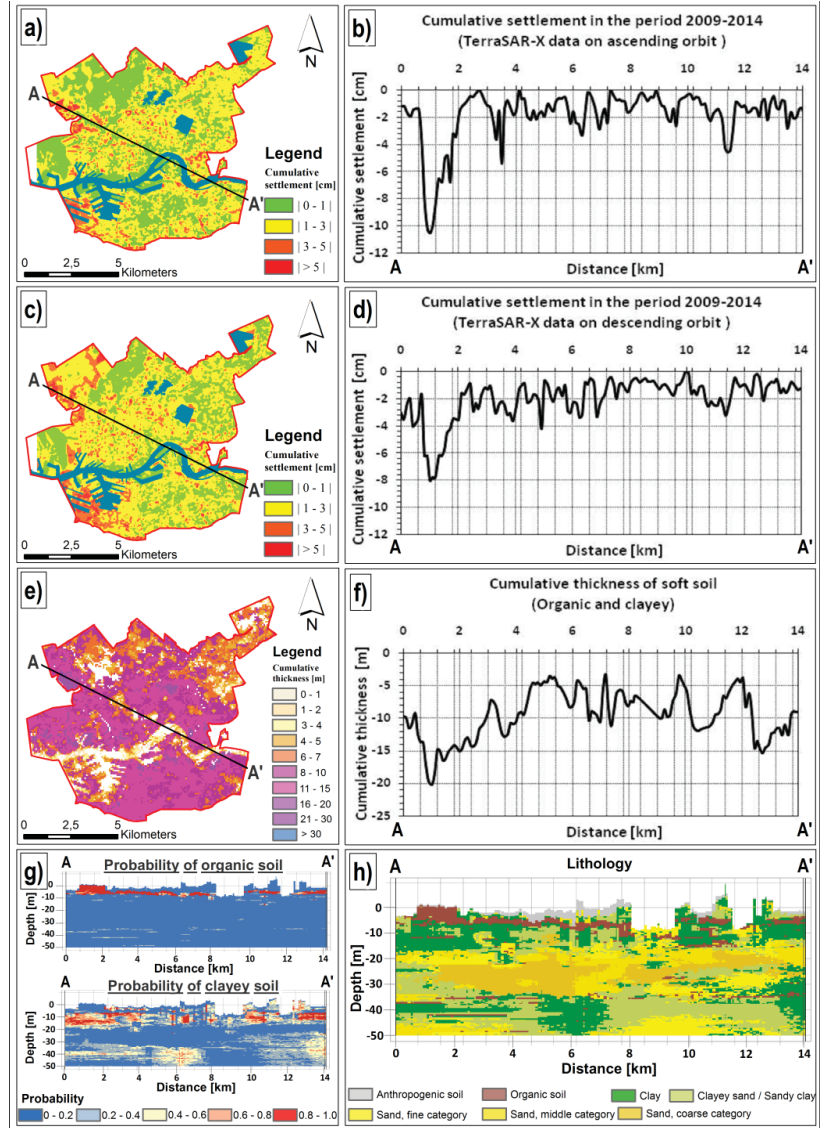


Figure 6.12 Correlation between cumulative settlements derived by high-resolution TerraSAR-X data at ground level and geological information: maps of spatial distribution of cumulative settlements on a) ascending and c) descending orbit; cross-section along the A–A' profile of the cumulative settlements on b) ascending and d) descending orbit in the period 2009–2014; e) map of spatial distribution and f) cross-section along the A–A' profile of soft soils (organic and clayey); h) geological cross-section along the A–A' profile and g) probability of occurrence of soft soil (organic and clayey) extracted from the portal of the Geological Survey of the Netherlands – DINOloket.

As a result, the areas with the thickest cumulative soft soil layers and the highest settlements (red and orange areas in Figure 6.11a and b) were confirmed to be the most affected by settlements. In these areas, the most severe consequences to structures and infrastructures are to be expected.

### 6.2.2 Analysis at large scale

The analysis at large scale was carried out on a neighborhood of the city of Schiedam (Figure 6.1b) where mainly masonry buildings resting on different types of foundation, i.e. shallow and piled foundations (as mentioned in Section 6.1), can be recovered. The available PSI data show different values of the average velocities at ground level and on top of buildings, as highlighted in the 3D view of Figure 6.13. For instance, during the image acquisition period the vertical velocity values at ground level mostly range from  $-3$  to  $-5$  mm/year. Lower velocities are recorded on top of the buildings, mainly in those supported by foundations piled into Pleistocene sand layers.

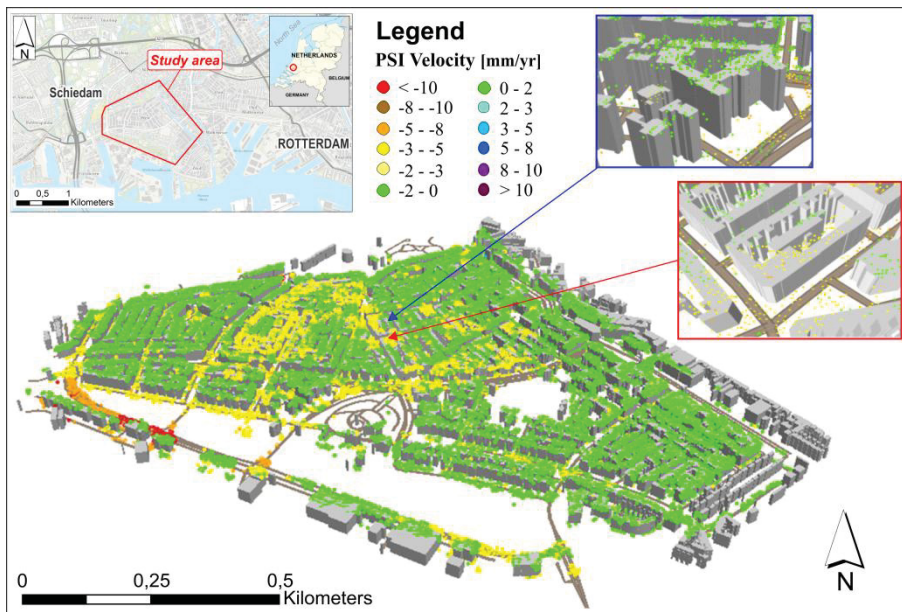


Figure 6.13 3D view of the study area at large scale with spatial distribution of PSI vertical velocities at ground level and on top of the buildings.

In order to identify the buildings affected by settlements and analyze their behavior, PSI data at ground level and on top of buildings were preliminarily used to differentiate the building aggregates and the areas/roads surrounding the buildings that are “moving” from those that are “not moving”. To this aim, based on the available digital topographic map, building aggregates were identified with the 'row houses' typical of the local architecture. For each building aggregate, all PS at roof level were selected considering a 2-meter buffer-distance around each building aggregate. The 2-meter buffer-distance is a practical consideration. Since the geolocation precision of the PS is  $< 1.5$  m, a large number of PS are projected outside of the building outlines, which themselves have a geolocation precision of circa 10 cm. In Dutch practice, there are only a few potential sources of irrelevant data within 2 m from a building façade, i.e. lighting poles. By using a 2-meter buffer-distance, many valid PS are included in the analysis, while only few invalid PS are introduced. A “moving/not moving” conservative threshold of 2 mm/year was fixed taking into account the validation test carried out with the same PSI-dataset over 180 leveling points in the Schiedam area (Appendix A), which revealed an average difference of about 0.67 mm/year with a standard deviation of 0.48 mm/year between the yearly average velocity derived from leveling and PSI data. The carried out analysis showed that 33% of 648 building aggregates in the study area are covered by at least one “moving” PS (Figure 6.14a). Similarly, the analysis of PS at ground level highlighted that 79% of the total area covered by roads and areas surrounding the buildings is moving (Figure 6.14b).

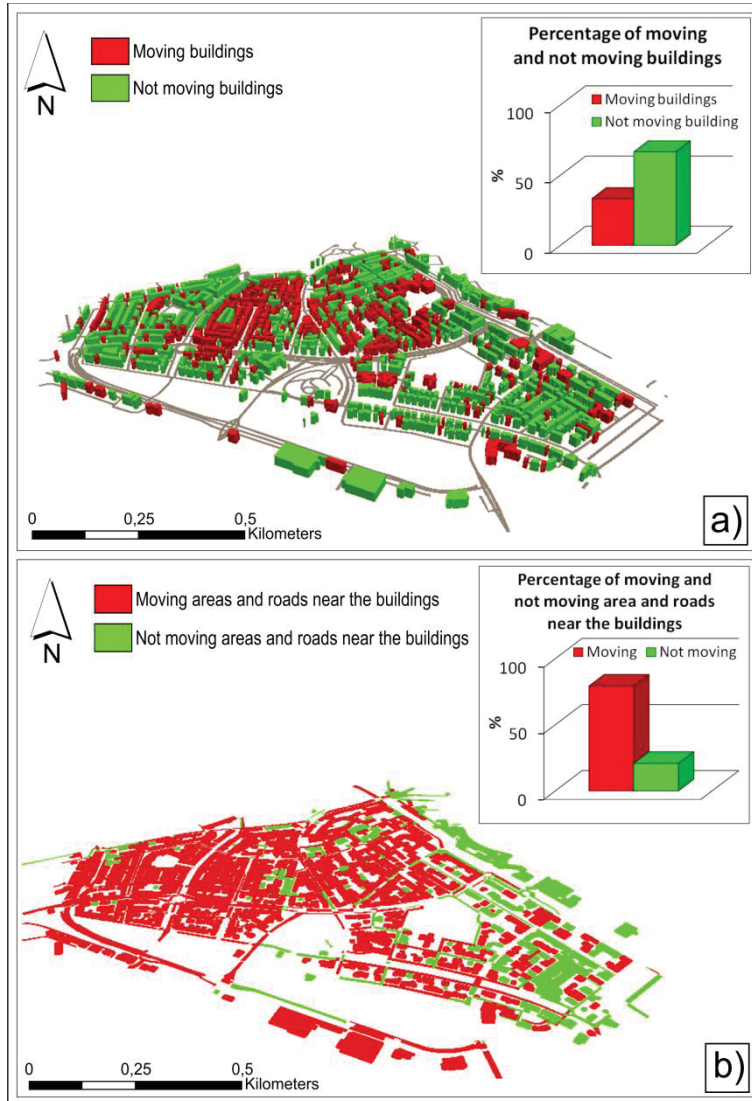


Figure 6.14 Analysis of high-resolution PSI data at large scale: a) moving and not moving building aggregates and b) moving and not moving areas/roads surrounding the buildings

Following the distinction of “moving/not moving” building aggregates and surrounding areas and roads, four possible scenarios were identified as cases C1–C4. Their spatial distribution and description are summarized, respectively, in Figure 6.15a and Figure 6.15b.



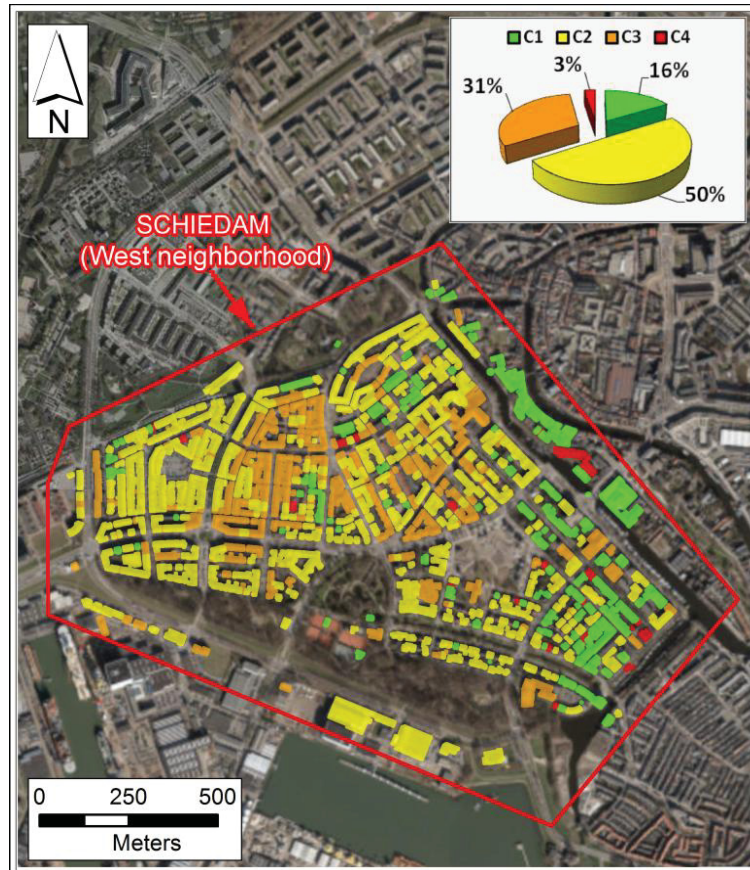


Figure 6.15a Spatial distribution of different possible scenarios resulting from the correlation analysis between moving and not moving PSI data located on top of the building aggregates and on area/roads surrounding the buildings.

The above zoning of the study area allows the identification of portions of the territory where different problems may exist. For instance, if possible damages to roads and services are to be investigated, the analysis should focus on the parts of the territory belonging to classes C2, C3 and C4; conversely, if the analysis of building behavior is addressed, only classes C3 and C4 are relevant. Overall, the analysis shows that 84% of the study area is affected by settlements, but only within 34% of it there might be buildings involved.

Once the areas where buildings likely to be affected by settlement-related problems (C3 and C4) were identified, the information on the damage level detected during in-situ damage surveys and attributed to buildings





<b>Cases</b>	<b>PSI data</b> · green point: no moving PS · yellow point: moving PS	<b>Description of typical problem</b>
<b>C1</b>		<p>PSI data show velocity values under the set movement threshold (i.e. 2.0 mm/year). The area is stable, no problems for buildings and services.</p>
<b>C2</b>		<p>PSI data show velocity values that are under the set movement threshold (i.e. 2.0 mm/year) on top of the buildings and over 2.0 mm/year at street level. The area at ground level is not stable with possible problems and damages to the roads and services (e.g., sidewalks, sewers, pipeline, etc.).</p>
<b>C3</b>		<p>PSI data show velocity values that are over the set movement threshold (2.0 mm/year) both on top of the buildings and at street level. Possible problems and damages can be recorded to both roads and services (e.g., sidewalks, sewers, pipeline, etc.), and on the buildings (e.g., crack or tilt of the walls) depending on the intensity of the settlements.</p>
<b>C4</b>		<p>PSI data show velocity values that are over the set movement threshold (i.e. 2.0 mm/year) on top of the buildings and under 2.0 mm/year at street level. Structural problems and damages can be recorded on the buildings (e.g., foundation failure with crack or tilt of the walls). Interruptions of building services are possible as well (e.g. break in sewers, sidewalks).</p>

Figure 6.15b Description of different possible scenarios resulting from the correlation analysis between moving and not moving PSI data located on top of the building aggregates and on area/roads surrounding the buildings.

aggregates considering the scale of analysis, were put in correlation with the magnitude of the subsidence-related intensity (SRI) parameters experienced by the foundation system evaluated using the PSI data on top of the buildings.

For this reasons, focusing on the surveyed building aggregates, the settlements and related gradients suffered by each of them were evaluated following the steps shown in Figure 6.16 for a sample aggregate.

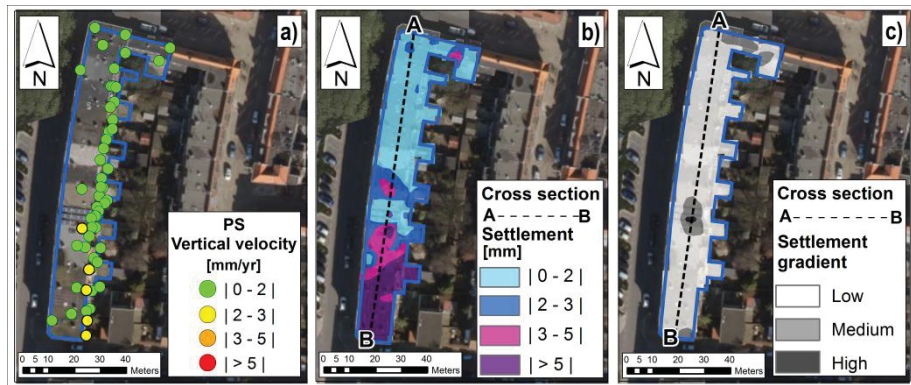


Figure 6.16 Analysis of high-resolution PSI data at large scale: a) distribution of TerraSAR-X data on top of building aggregates; b) map of cumulative settlements and c) map of settlement gradients derived from TerraSAR-X data (period 2009–2014).

In particular, vertical PSI velocities on top of the buildings (Figure 6.16a) were interpolated on a superimposed grid with cell sizes of  $2 \times 2$  m using an IDW interpolation. Then, the velocity for each cell was multiplied for the acquisition period of the radar images in order to generate the cumulative settlement map for each building aggregate (Figure 6.16b). Subsequently, starting from the measured cumulative settlements (Figures 6.64b) the settlement gradient map (Figure 6.16c) was generated and gradient moduli were grouped into the three classes (Low, Medium and High). In particular, these classes refer to the gradient values (expressed in degrees) which range respectively from 0 to  $5.7 \times 10^{-2}$  (corresponding to a differential settlement of 0 to 2 mm within the grid cell), from  $5.7 \times 10^{-2}$  to  $1.4 \times 10^{-1}$  (corresponding to a differential settlement of 2 to 5 mm within the grid cell) and  $> 1.4 \times 10^{-1}$  (corresponding to a differential settlement  $> 5$  mm within the grid cell).

Then, since damage occurrence and severity for a given building is related to the magnitude of settlements, or their derived parameters describing foundation movements, the trend of settlements and the settlement gradient profile along the cross-section of the building aggregate was evaluated. In Figure 6.17 an example of the trends settlement and settlement gradient is reported, with reference to the sample building aggregate of Figure 6.16, along the A-B profile in Figure 6.16 a and b.

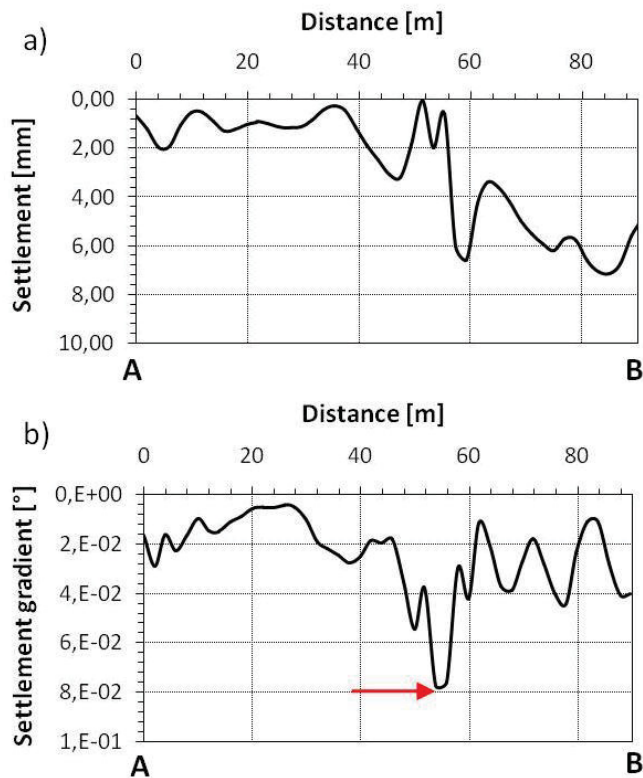


Figure 6.17 Analysis of high-resolution PSI data at large scale: a) cumulative settlements and b) settlement gradients along the A-B profile sketched in Figure 6.16a) and b).

In particular, the settlement gradient profile (Figure 6.17b) highlights rather low values with a maximum in the section indicated by the red arrow. This result was corroborated by the damage survey carried out in

the area that revealed the presence of some cracks on the façades of the building with deformations of the sidewalk and detachments from the laying surface exactly at the location where the gradient peak is recorded (Figure 6.8 – Section 6.1.3 – pictures 3, 4 and 7).

Extending the same procedure to all 67 building aggregates, the maximum values of the settlement gradients were computed from the longitudinal profiles drawn along the settlement gradient maps. These values were then associated with the estimated equivalent damage, differentiating between building aggregates with shallow and deep foundations (Figure 6.18a and b). The obtained results show a general increasing trend of the equivalent damage when the value of the maximum gradient increases for both foundation types (i.e. shallow and deep ones). This aspect was further investigated in the analysis at detailed scale carried out on single buildings.

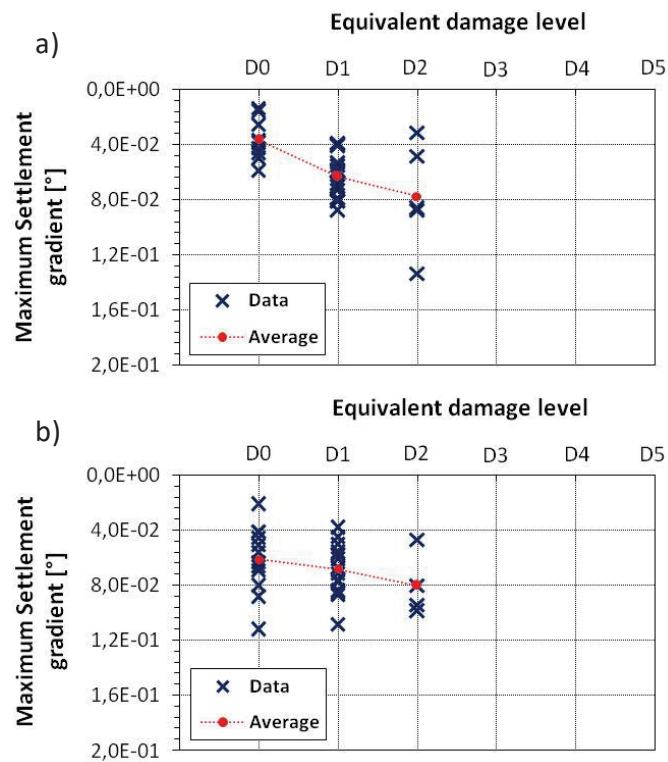


Figure 6.18 Maximum settlement gradients and related equivalent damage levels for building aggregates with a) shallow and b) piled foundations.

### 6.2.3 Analysis at detailed scale

The analysis at detailed scale focused on 310 single (or independent) buildings (see Figure 6.10) which correspond to the 67 (see Figure 6.9) “row house” aggregates analyzed at large scale. For each single building, the minimum ( $\delta v_{\min}$ ) and the maximum ( $\delta v_{\max}$ ) vertical settlement along the longitudinal cross-section (Figure 6.19a and b) were computed on the cumulative settlement map.

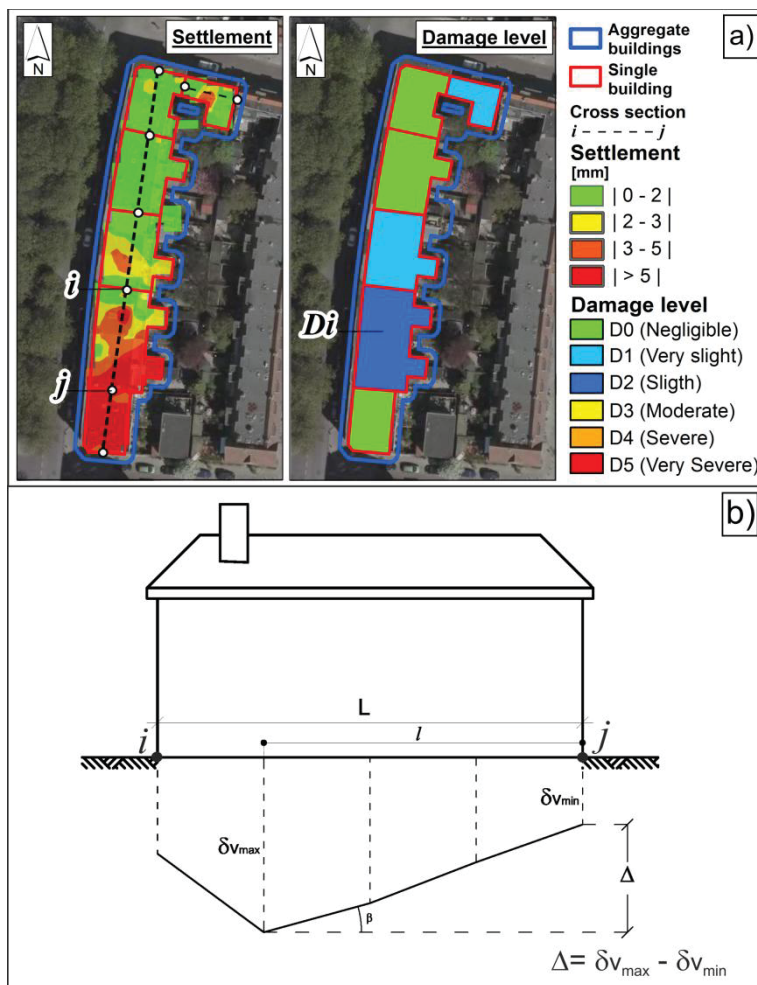


Figure 6.19 Analysis of high-resolution PSI data at detailed scale: a) map of cumulative settlements and damage severity recorded in 2015 damage surveys; b) scheme of differential settlement assessment on the single building.

The differential settlement ( $\Delta$ , Figure 6.19b) was defined as the maximum difference of vertical settlement between any two points on the single building's foundation ( $\delta_{v_{max}} - \delta_{v_{min}}$ ).

The obtained values were in turn correlated with the damage severity recorded for each building (Figure 6.19a) in order to determine the relationship between cause (differential settlements) and effect (recorded damage level). Derived separately for shallow and piled foundations, a similar increasing trend of damage severity with the differential settlement was found for both foundation types (Figures 6.20a and b).

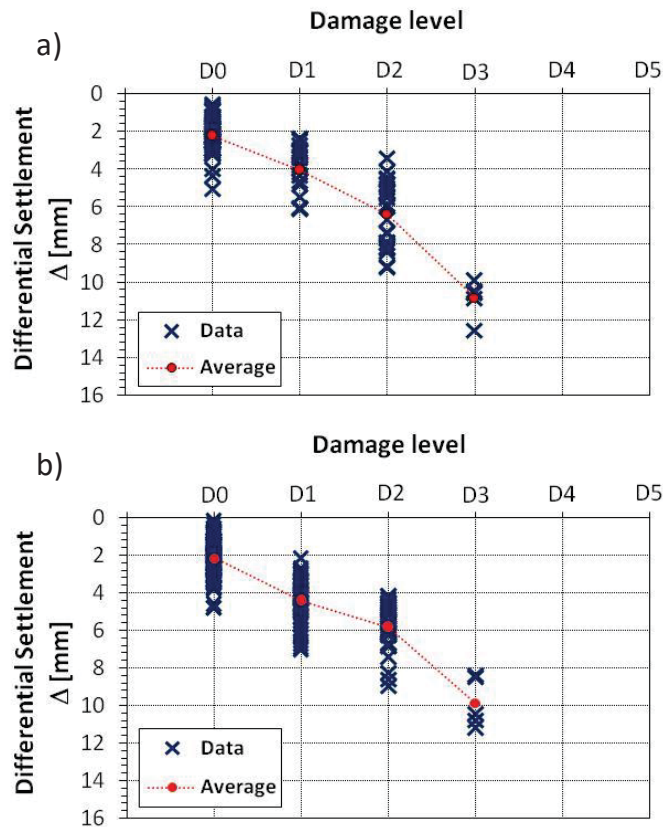


Figure 6.20 Damage level vs. differential settlements for buildings with c) shallow and d) piled foundations.

Note that in Figures 6.20a and b the damage severity ranges from D0 up to D3 levels (see also Figure 6.10a), whereas the equivalent damage estimation on building aggregates (shown in Figures 6.18a and 6.18b) limited damage severity within the D0–D2 range.

Subsequently, under the assumption that the differential settlement is the representative intensity parameter of the natural event causing damage of different severity to the single buildings, empirical fragility curves were derived for a given foundation type and fixed differential settlement values. For this purpose, the frequency of occurrence of each level of damage severity was calculated for different classes of PSI-derived differential settlements (Figures 6.21a and b).

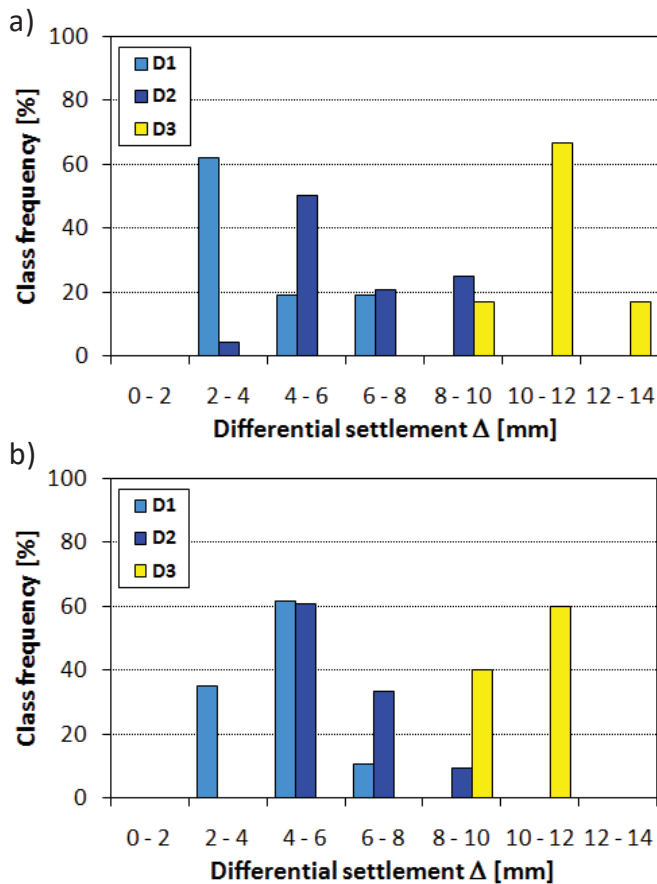


Figure 6.21 Class frequency of the different levels of damage severity recorded to single buildings with a) shallow and c) piled foundations.



Then, using methods common in different engineering fields (Fotopoulou et al., 2013a,b; Mavrouli et al., 2014; Negulescu and Foerster, 2010; Negulescu et al., 2014; Pitilakis and Fotopoulou, 2015; Peduto et al., 2016a,b, 2017; Saeidi et al., 2009, 2012; Zhang and Ng, 2005), the probabilities were calculated using a cumulative log-normal distribution function (Eq.6.1):

$$P(\text{Damage} \geq D_i | \Delta) = \Phi \left[ \frac{1}{\beta} \ln \left( \frac{\Delta}{\bar{\Delta}} \right) \right] \quad (i = 0, \dots, 5) \quad (6.1)$$

where  $P(\cdot)$  is the probability of reaching or exceeding a particular damage level  $D_i$  for a fixed intensity of differential settlement  $\Delta$ ;  $\Phi[\cdot]$  is the standard normal cumulative distribution function;  $\bar{\Delta}$  is the median value of  $\Delta$  where the building reaches each  $D_i$ ; and  $\beta$  is the standard deviation of the natural logarithm of  $\Delta$  for each  $D_i$ . The median values of  $\Delta$ , corresponding to each  $D_i$ , are those that give 50% probability of exceeding each damage level; whereas the standard deviation  $\beta$  describes the variability associated with each fragility curve.

The parameters of all computed fragility functions are synthesized in Table 6.3, whereas the empirical fragility curves obtained for the surveyed masonry buildings with shallow and piled foundations are respectively shown in the Figures 6.22a and b.

**Table 6.3 Median and standard deviation parameters of the lognormal distribution function used for each damage levels and distinguished according to the foundation type.**

Damage level	Shallow foundations		Piled foundations	
	Median [mm]	Stand. dev. [mm]	Median [mm]	Stand. dev. [mm]
D1 (Very slight)	3.86	0.32	4.35	0.26
D2 (Slight)	5.94	0.28	5.64	0.19
D3 (Moderate)	10.58	0.08	10.47	0.14

The Figures 6.22b and d highlight that, independently of the foundation type, for differential settlements lower than 9 mm the probability of

reaching or exceeding the D3 (moderate) level of damage severity – often associated to losses of functionality – is negligible. Indeed, only damages whose severity (of D1 or D2 level) might affect the aesthetics – with different  $P(\cdot)$  values according to the considered  $\Delta \leq 9$  mm – are expected. Moreover, as the differential settlement increases (for  $\Delta$  values larger than 9 mm), the probability of reaching or exceeding the D3 level increases more rapidly for buildings on shallow foundations (Figure 6.22a) than those on piled foundations (Figure 6.22b).

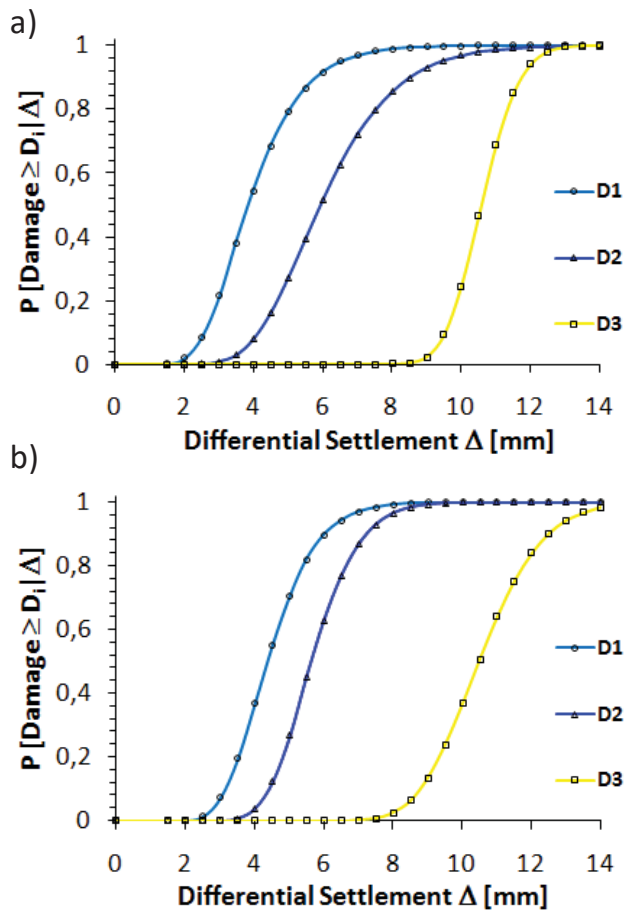


Figure 6.22 Results of PSI-derived differential settlements and damage survey relationship for single buildings at detailed scale: empirical fragility curves generated by using the log-normal distribution for single buildings with a) shallow and b) piled foundations.

The reliability of the cumulative log-normal distribution function used to describe the probability of reaching or exceeding a given damage level was checked using the Kolmogorov–Smirnov (K-S) goodness-of-fit test. The result of the K-S test, which confirms the assumption that the cumulative log-normal distribution function can be accepted to describe the probability of exceeding a given level of damage severity for different significance levels taken as references, is shown in the Appendix B. The obtained fragility curves can represent a powerful empirical model to predict the damage level that can affect the buildings over time. Taking into account that the investigated structural and foundation typologies well represent the Dutch urban fabric, the obtained empirical fragility curves could be used for analysis and forecasting purposes (dealing with the buildings located in the study area as well as the ones, having the same structural typology, which fall in similar subsiding geological contexts), provided that a validation phase is carried out as shown in the next Section.

### **6.3 VALIDATION OF THE EMPIRICAL FRAGILITY CURVES**

The analysis at detailed scale that led to the generation of empirical fragility curves shown in Figure 6.22 was extended to two other urban areas of The Netherlands for validation purposes.

The above urban areas include two densely urbanized municipalities located in the northern (Zaanstad) and southern (Dordrecht) part of The Netherlands (Figure 6.23a and 6.23b) where masonry buildings, on either shallow or deep (wooden pile) foundations, suffered from settlement-induced damages of different severity. This prompted both Zaanstad and Dordrecht Municipalities to commission extensive campaigns of the building foundation inspections aimed at investigating their type and conservation state.

Basing on the use of the nationwide 3D-‘GeoTop’ model ([www.dinoloket.nl/en](http://www.dinoloket.nl/en)), Figures 6.23a and 6.23b highlight that the study areas exhibit the typical Dutch geological setting, very similar to the Schiedam area previously analyzed, consisting of Holocene clayey and peaty layers with alternating lenses of sandy soils and superimposed to sandy deposits of Pleistocene age. In particular, a generic cross-section along the A-A’ profile (Figure 6.23a) shows that in Zaanstad area the

upper part of the subsoil consists of soft soils (i.e. mainly clay and peat with thickness not exceeding 10 m) resting on a sandy layer that includes some narrow lenses of clayey soils or sandy clay. As for Dordrecht area, an alternation of soft soil and sandy layers with similar thickness can be observed along the B-B' cross section (Figure 6.23b).

This slightly different geological setting influenced in the past the technical decisions about the most suitable building foundation system. Indeed, in Zaanstad historic centre masonry buildings were built mainly on wooden piles (Figure 6.23, a1 and a2) in order to prevent from loading the superficial highly compressible layer; on the other hand, in Dordrecht city masonry buildings with wooden pile foundations coexist with other resting on shallow foundations (Figure 6.23 b1).

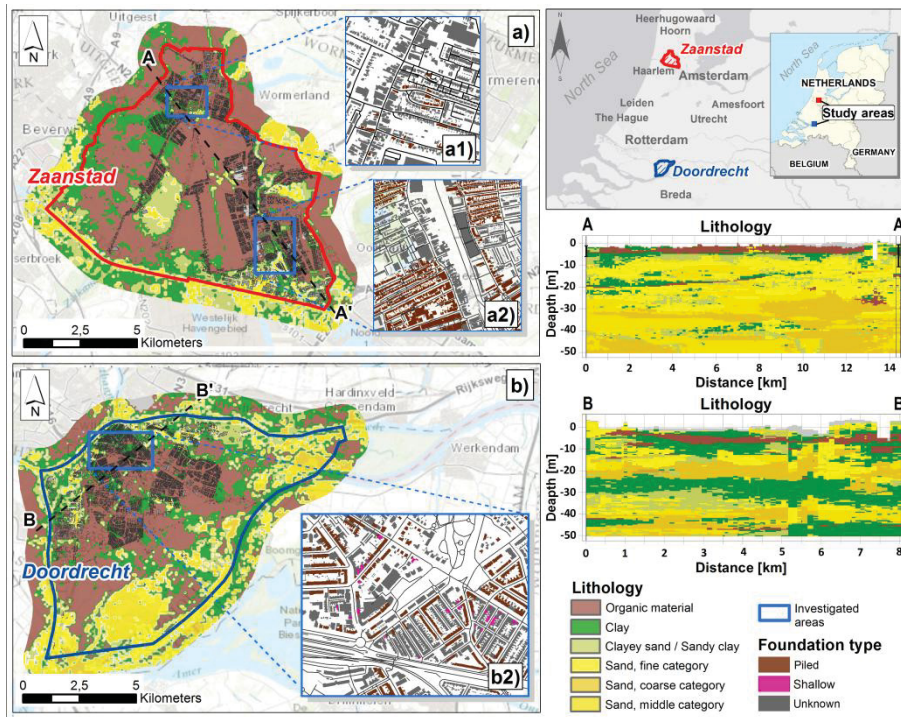


Figure 6.23 a) Zaanstad and b) Dordrecht study areas: geological setting and cross-sections along the A-A' profile sketched in a) and B-B' profile sketched in b) (extracted from the portal of the Geological Survey of the Netherlands – DINOloket). Spatial distribution of the available foundation type on the investigated areas: north a\_1) and south a\_2) neighborhood of the Municipality of Zaanstad; central portion b\_1) of the Municipality of Dordrecht.

The SAR dataset available for both study areas consists of the same stock of images at very high-resolution achieved by TerraSAR-X (TSX) radar sensor in the period spanning from 2009 to 2015 and used for the analysis of the previous case; these images were processed via a PSI-like approach (Ferretti et al., 2001) by SkyGeo Netherlands B.V. company using their commercial processing chain ‘Antares’. As described in Section 6.1.2, the data originating from the tops of buildings were again separated from the data originating from ground level and only the PS-InSAR data on top of the buildings, whose velocities are projected along the vertical direction (Cascini et al., 2007) were considered for analysis purposes. The spatial distribution of PS-InSAR-derived velocities on top of the buildings is shown in Figure 6.24 (a\_1 and a\_2) and Figure 6.24 (b\_1) respectively for the neighborhood of Zaanstad Municipality and the central portion of Dordrecht Municipality.



Figure 6.24 Spatial distribution (on ascending and descending orbit) of high-resolution TerraSAR-X data on top of the buildings projected along the vertical direction (period 2009-2015) for the investigated north (a\_1) and south (a\_2) neighborhood of Zaanstad Municipality and central portion (b\_1) of Dordrecht Municipality.

As for the damage to buildings, similarly to the neighborhood of Schiedam, an extensive damage survey was carried out in February-March 2016 for both study areas, using the fact-sheets described in Section 6.1.3. The distribution of different levels of the recorded damage on both study areas is shown in Figure 6.25, whereas some photos of the field survey and damage recorded via the visual inspection of the building façades are reported in Figure 6.26.

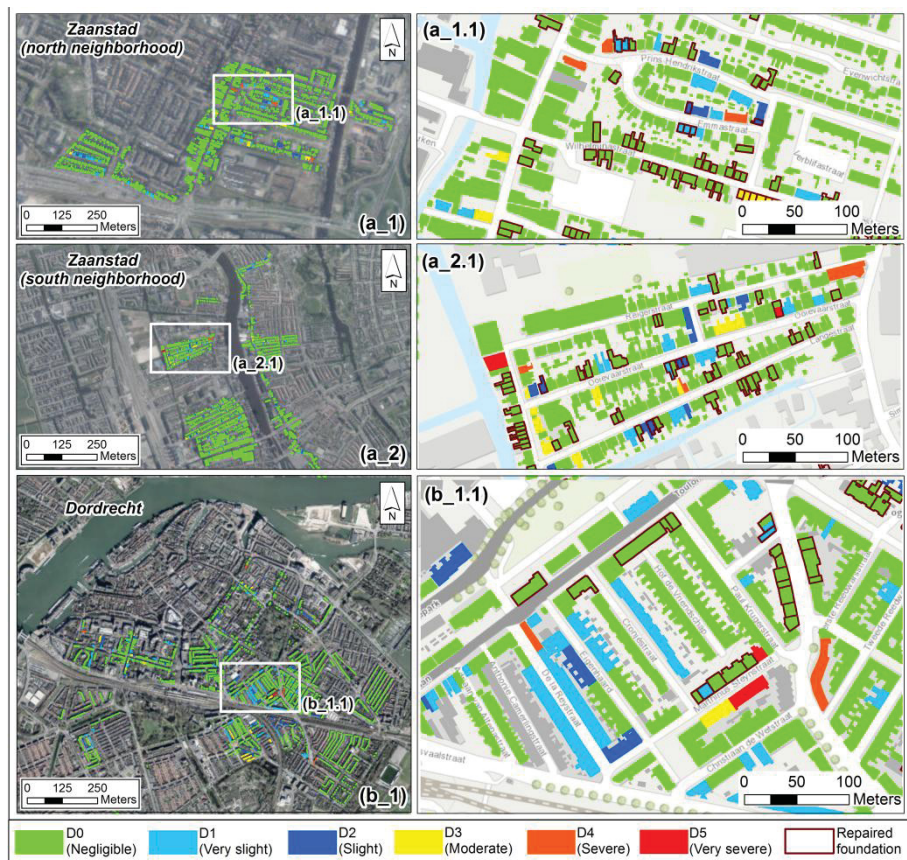


Figure 6.25 Map of surveyed buildings distinguished according to the recorded damage severity for the investigated north (a\_1) and south (a\_2) neighborhood of Zaanstad Municipality and central portion (b\_1) of Dordrecht Municipality.



Figure 6.26 Some photos of damage recorded on the building facades during the field survey in Zaanstad and Dordrecht Municipality.

The sample of surveyed buildings, distinguished according to the recorded damage severity, consists of 132 masonry structures in the Dordrecht area built on different foundation typologies – 76 shallow (number of buildings per damage level: D0 = 56; D1 = 9; D2 = 5; D3 = 6; D4 = 0; D5 = 0) and 56 wooden pile foundations (number of buildings per damage level: D0 = 23; D1 = 16; D2 = 9; D3 = 4; D4 = 2; D5 = 2) – and 81 masonry structures resting on wooden pile foundations in the Zaanstad area (number of buildings per damage level: D0 = 8; D1 = 31; D2 = 20; D3 = 16; D4 = 6; D5 = 0).

For each building, the results of the in-situ damage survey were combined with the differential settlements ( $\Delta$ ) computed, along a longitudinal cross-section of the building, as the maximum difference of



PSInSAR-vertical settlement between any two points on the single building's foundation ( $\delta v_{\max} - \delta v_{\min}$ ). Merging the above information for both case studies allowed retrieving the relationship between differential settlements and damage severity for masonry buildings with either shallow (Figure 6.27a) or wooden pile foundations (Figure 6.27b). The obtained relationships show a general increase of the damage level with the magnitude of differential settlements, with a higher gradient for buildings resting on shallow foundations.

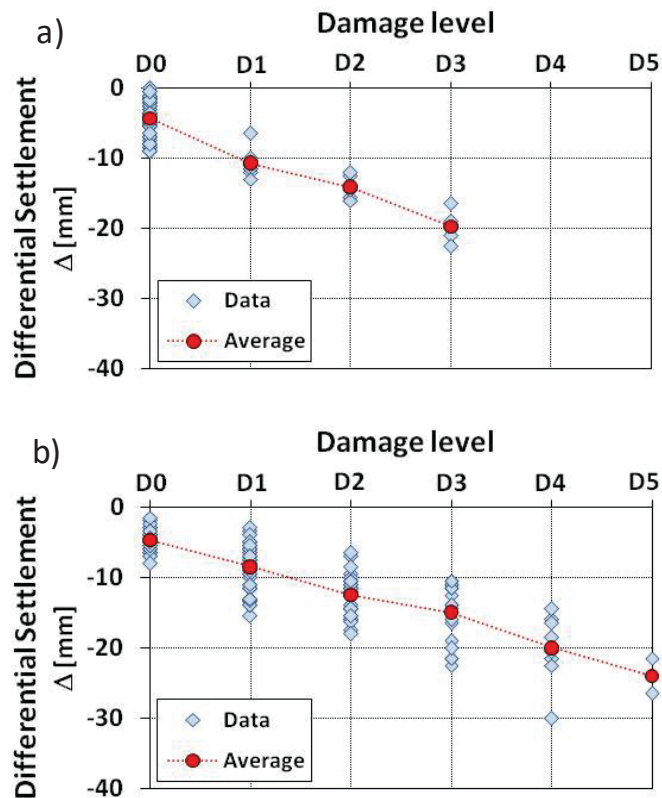


Figure 6.27 Damage level vs. differential settlements for buildings with a) shallow and b) piled foundations in Zaanstad and Dordrecht Municipality.

Then, by using the cumulative log-normal distribution function (Eq. 6.1), empirical fragility curves (Figures 6.28a and 6.28b) were derived and the parameters of corresponding functions are synthesized in Table 6.4.

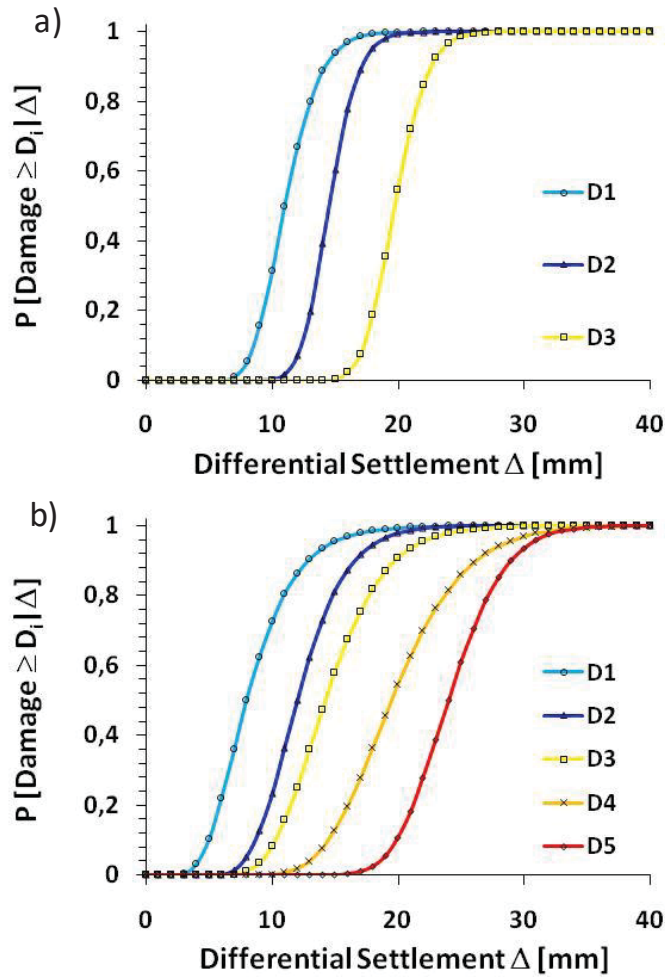


Figure 6.28 Empirical fragility curves generated by using the log-normal distribution for single buildings with a) shallow and b) piled foundations in Zaanstad and Dordrecht Municipality.

**Table 6.4 Median and standard deviation parameters of the lognormal distribution function used for each damage levels and distinguished according to the foundation type for the union of the Zaaastad and Dordrecth case studies.**

Damage level	Shallow foundations		Piled foundations	
	Median [mm]	Stand. dev. [mm]	Median [mm]	Stand. dev. [mm]
D1 (Very slight)	11.00	0.20	8.00	0.37
D2 (Slight)	14.50	0.13	12.00	0.25
D3 (Moderate)	19.75	0.10	14.25	0.26
D4 (Severe)	-	-	19.50	0.23
D5 (Very severe)	-	-	24.00	0.15

Of course, the obtained fragility curves show that the probability of reaching or exceeding a certain damage level increases as the differential settlements increase independently of the building foundation type. However, it is possible to observe that, for a fixed value of the differential settlement (e.g., lower than 10 mm), the probability of reaching or exceeding a damage level from D1 to D3 increases more rapidly for buildings on piled foundations than for those on shallow foundations; the latter, in turn, do not exhibit (at least with reference to the sample of the investigated buildings) damage levels from D4 to D5. This result is probably related to the capability of masonry buildings to sustain differential settlements affecting “continuous” shallow foundations (this is especially true when the sagging mode of deformation prevails) rather than “discrete” pile systems (often associated to a global erratic behaviour).

In order to validate the empirical fragility curves shown in Figure 6.22, the latter were compared with the ones jointly generated for Zaanstad and Dordrecht case studies. To this aim, the probability functions corresponding to each considered damage level for both cases were first recalculated considering a unique value of the standard deviation (Figure

6.29). In particular, since the values of the standard deviation of each curve is always lower to 0.5 (see Table 6.1 and Table 6.2), a  $\beta$  equal to 0.5 was fixed. Indeed, the choice of a fixed value of  $\beta = 0.5$  allows easily comparing two fragility curves by estimating the quantitative differences among the probabilities of reaching or exceeding a certain damage level for a given value of the differential settlement.

The comparison concerned the curves of Figures 6.29.a and 6.29.c (masonry buildings on shallow foundations) and those of Figures 6.29d and 6.29b (masonry buildings on piled foundations) for the D1, D2 and D3 damage levels; six values of the differential settlement (from 5 mm to 40 mm) were considered. The obtained results are summarized in Table 6.5.

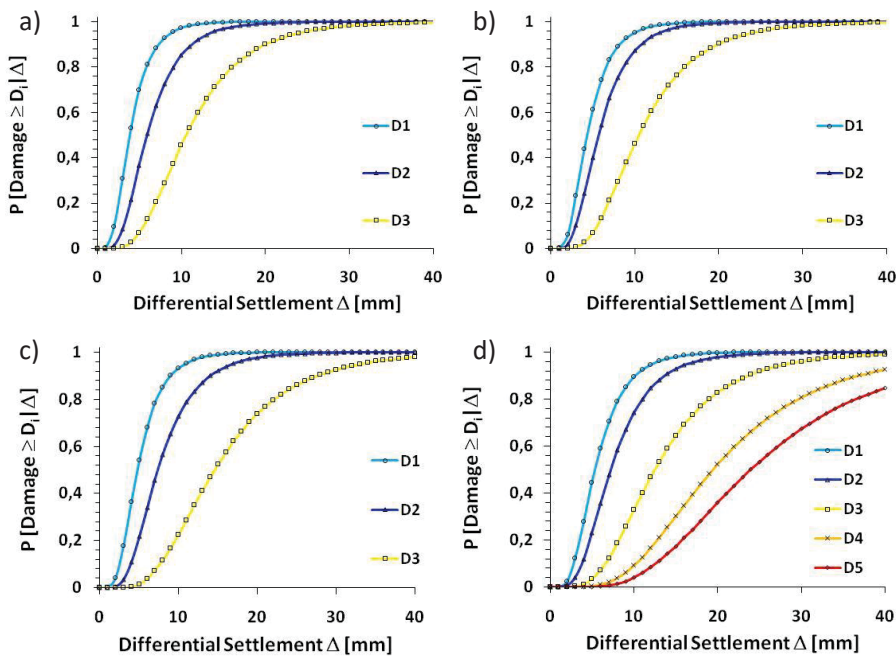


Figure 6.29 Empirical fragility curves generated by using the log-normal distribution with a fixed value of standard deviation for single buildings in Schiedam Municipality with a) shallow and b) piled foundations and single buildings in Zaanstad and Dordrecht Municipality with c) shallow and d) piled foundations.

**Table 6.5 Differences between the probabilities of reaching or exceeding a particular damage level  $D_i$  for different intensity values of the differential settlements derived from the empirical fragility curves showed in figure 6.29.**

Damage level	Intensity $\Delta$ [mm]	Shallow foundations			Piled foundations		
		P[Di(S*)]	P[Di(Z'+D*)]	Diff.**	P[Di(S)]	P[Di(Z'+D*)]	Diff.**
<b>D1</b>	5	0.70	0.06	<b>0.64</b>	0.70	0.10	<b>0.60</b>
	10	0.97	0.42	<b>0.55</b>	1.00	0.73	<b>0.27</b>
	15	1.00	0.74	<b>0.26</b>	1.00	0.95	<b>0.05</b>
	20	1.00	0.88	<b>0.12</b>	1.00	0.99	<b>0.01</b>
	30	1.00	0.98	<b>0.02</b>	1.00	1.00	<b>0.00</b>
	40	1.00	1.00	<b>0.00</b>	1.00	1.00	<b>0.00</b>
<b>D2</b>	5	0.36	0.02	<b>0.34</b>	0.27	0.00	<b>0.27</b>
	10	0.85	0.23	<b>0.62</b>	1.00	0.23	<b>0.76</b>
	15	0.97	0.53	<b>0.44</b>	1.00	0.81	<b>0.19</b>
	20	0.99	0.74	<b>0.25</b>	1.00	0.98	<b>0.02</b>
	30	1.00	0.93	<b>0.07</b>	1.00	1.00	<b>0.00</b>
	40	1.00	0.98	<b>0.02</b>	1.00	1.00	<b>0.00</b>
<b>D3</b>	5	0.07	0.00	<b>0.07</b>	0.00	0.00	<b>0.00</b>
	10	0.46	0.09	<b>0.37</b>	0.37	0.08	<b>0.28</b>
	15	0.76	0.29	<b>0.47</b>	1.00	0.58	<b>0.42</b>
	20	0.90	0.51	<b>0.39</b>	1.00	0.91	<b>0.09</b>
	30	0.98	0.80	<b>0.18</b>	1.00	1.00	<b>0.00</b>
	40	1.00	0.92	<b>0.08</b>	1.00	1.00	<b>0.00</b>

\* Note: S= Schiedam Municipality; Z+D= Union of Zaanstad and Dordrecht Municipality.

\*\* Note: Diff. = Difference between the probabilities.

The differences of the obtained probability turn out to be low, except for the curve related to the damage level D1 which, exhibited the largest differences between the two models. Indeed, it should be noted that D1 is relative to anaesthetic damage level (i.e. very slight) which is more difficult to quantify being characterized by only hairline/fine cracks that not affect the stability of the structures. This confirm that the two obtained series of empirical fragility curves (in the calibration and

validation phases) well represent the behavior of the investigated Dutch urban fabric in terms of structural response and expected damage level when buildings are subjected to differential settlements.

On the basis of this result, in order to generate fragility curves to be used for prediction purposes, the datasets were combined for masonry buildings on shallow (Figure 6.30a) or piled (Figure 6.30b) foundations.

The obtained fragility curves, once even further validated, can facilitate local authorities in charge of the land-use planning in selecting areas suitable for urbanization as well as - provided that they are properly used - in addressing restoration and adaptation policies. This result could be achieved at more affordable costs than the use of conventional monitoring techniques over wide number of exposed buildings.

For the masonry buildings on piled foundations, since they compose a well statistically representative sample (344 buildings) with damage levels that cover the whole considered classification system (from D0 to D5), an empirical vulnerability curve, representative of the average expected damage level for a given intensity, was derived. In particular, the vulnerability curve was generated by fitting the empirical data according to the Eq. (6.2) proposed by Lagomarsino and Giovinazzi (2006):

$$\mu_D = a [b + \tanh(c \cdot \Delta + d)] \quad (6.2)$$

where ( $\mu_D$ ) is the weighted average of the damage level severity for a given value of the intensity parameter ( $\Delta$ ), that can be computed according to the formula:

$$\mu_D(\Delta) = \sum_{i=0}^5 P_i \cdot d_i \quad (6.3)$$

where  $P_i$  is the discrete probability associated with a damage severity level ( $D_i$ ) whose numerical index equals  $d_i$  (taken for this application as 1, 2, 3, 4 and 5 for D1, D2, D3, D4 and D5, respectively). Finally,  $a$ ,  $b$ ,  $c$  and  $d$  are four fitting coefficients that, in turn, have to be determined for the analyzed building typology.

The obtained vulnerability curve is shown in Figure 6.31 and the corresponding fitting coefficients of Eq. (6.2) are:  $a = 2.8673$ ;  $b = 0.7438$ ;  $c = 0.0821$ ;  $d = -0.9589$ .

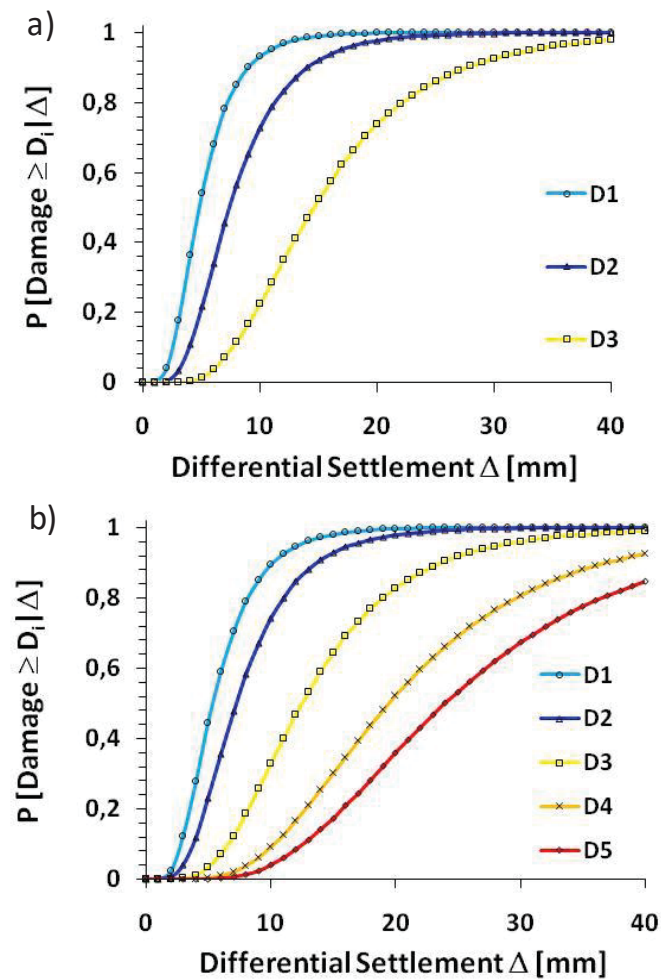


Figure 6.30 Empirical fragility curves derived from the combination of the Schiedam, Zaanstad and Dordrecht case studies for single buildings with a) shallow and b) piled foundations.

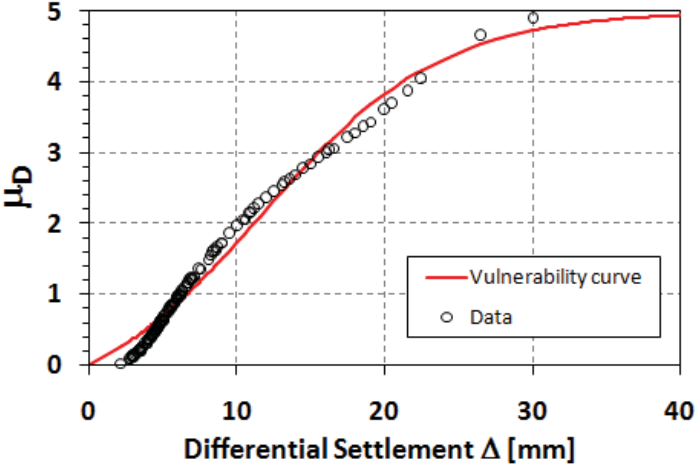


Figure 6.31 Empirical vulnerability curves for single masonry building with piled foundations.



## **7 ANALYSIS AND PREDICTION OF THE DAMAGE TO BUILDINGS IN SLOW-MOVING LANDSLIDE-AFFECTED AREAS**

This Chapter focuses on the application of the proposed innovative procedure (see Chapter 5 - Section 5.2) that, based on a joint use of DInSAR and damage survey data, aims to analyze and predict the damage to buildings affected by slow-moving landslides through the generation - at municipal scale - of empirical fragility/vulnerability curves. The proposed procedure is tested on two urban areas - preliminarily selected within the territory of the Calabria region (southern Italy) by means of an analysis at small scale - affected by slow-moving landslides, which over the time caused relevant effects on the buildings with consequent high socio-economic impacts.

### **7.1 THE SELECTED STUDY AREAS**

The considered test sites for the analysis and prediction of the damage to buildings affected by slow-moving landslides through the generation of empirical fragility/vulnerability curves are two urban areas located in the northern sector of Calabria Region (southern Italy). This region has been suffering from slow-moving landslides that - over the time - have strongly conditioned the land-use planning as well as the urban management (Greco et al., 2010). The study areas, represented by the municipalities of Lungro and Verbicaro (Cosenza Province), were selected through a preliminary analysis performed at small scale (1:100,000) on the whole territory of the Cosenza Province (Gullà et al., 2017b). For this area, the landslide inventory map drawn-up within the Hydrogeological Setting Plans of Calabria Region (2001) at 1:10,000 scale, the map of urban areas at 1:10,000 scale (Greco et al., 2010) as well as ERS1-2 PSInSAR (Ferretti et al., 2001) data (period 1992-2000) on both ascending and descending orbits provided by the Italian Ministry of Environment within the nationwide “Piano Straordinario di

‘Telerilevamento Ambientale – PST Project’ (MATTM, 2010) are available.

The analysis at small scale was based on the adoption of a municipal vulnerability index ( $V_i$ ) useful to rank the municipalities where vulnerable areas concentrate and studies at more detailed scale are required for planning and designing risk mitigation measures. Vulnerable areas were defined as the urban areas interacting with slow-moving landslides that are or can be potentially moving. In particular, the municipal vulnerability index ( $V_i$ ) was computed according to the formula (7.1):

$$V_i = \frac{VA_i/VA_{tot}}{UA_i/UA_{tot}} \quad (7.1)$$

where  $VA_i$  is the vulnerable area of the  $i_{th}$  municipality falling within the administrative boundary (in this case, the territory of the Cosenza Province) taken into account;  $VA_{tot}$  is the total vulnerable area of all municipalities within the administrative boundary; while  $UA_i$  and  $UA_{tot}$  are, respectively, the urban area of the  $i_{th}$  municipality and the total urban area of all considered municipalities.

The vulnerable areas were identified using the following procedure. Starting from the landslide inventory map, only the slow-moving landslides were selected (accordingly, the first-failure phenomena- such as rock falls and debris flows- were excluded). The obtained slow-moving landslide inventory map was overlapped to PSInSAR data in order to derive: a) the slow-moving landslide inventory map covered by PSInSAR data and b) the slow-moving landslide inventory map not covered by PSInSAR data.

Then, following the procedure shown in Figure 7.1 the vulnerable areas for each of the  $i_{th}$  considered municipality were retrieved. Finally, the vulnerability index ( $V_i$ ) was computed using the formula (7.1).

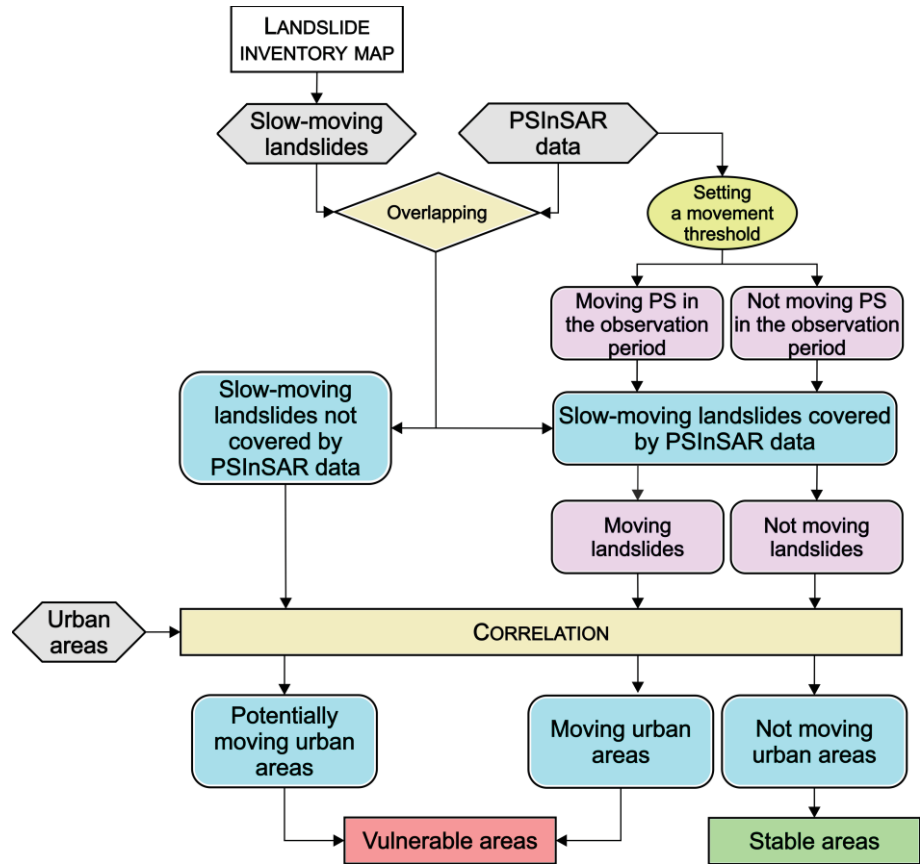


Figure 7.1 Flowchart for the identification of the vulnerable areas at small scale.

The results of the analysis carried out at small scale for the municipalities within the CosenzaProvinceare shown in Figure 7.2.

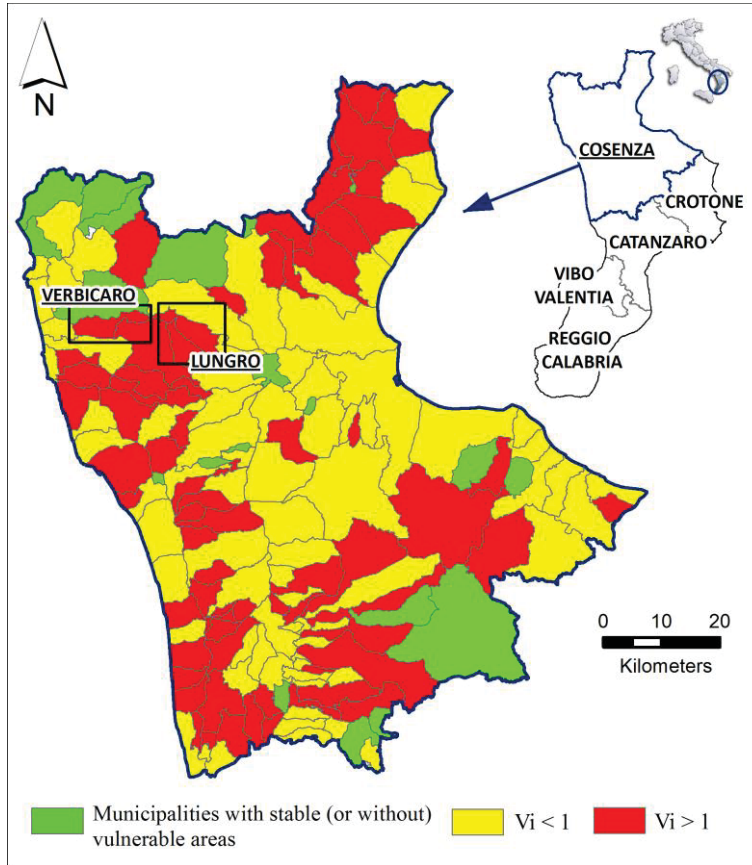


Figure 7.2 Map of municipalities of the Cosenza Province in which fall: vulnerable areas, not vulnerable areas or stable urban centres.

In particular, the red coloured municipalities ( $V_i > 1$ ) represent the urban areas that primarily need more detailed studies in order to identify, by means of an integrated multi-scale approach, the most appropriate strategies for urban planning and structural and/or non-structural risk mitigation measures. It is worth underlining that the followed procedure could be refined by extending the analysis to the whole territory of Calabria region also referring to homogeneous geological contexts.

Figure 7.2 highlights that several municipalities, falling within the territory of the Cosenza Province, exhibit vulnerability index  $V_i > 1$ . Among them, the urban areas of Lungro and Verbicaro were selected to test the proposed procedure for the analysis and prediction of damage to buildings affected by slow-moving landslides.

## 7.2 THE LUNGRO CASE STUDY

Lungro (Figure 7.3), located in the southern Apennines between 400 and 650 m a.s.l. in the northwest sector of Calabria region (Cosenza Province, Italy), is a small town composed of a historical centre (HC) mainly characterized by masonry buildings and new developed urban areas where masonry buildings are mixed with reinforced concrete structures built since the middle of the last century. The new urbanized areas can be differentiated in three zones according to geomorphological features and urban fabric (Gullà et al., 2017a): Carmine (CA); Lafcantino (LA); San Leonardo (SL).

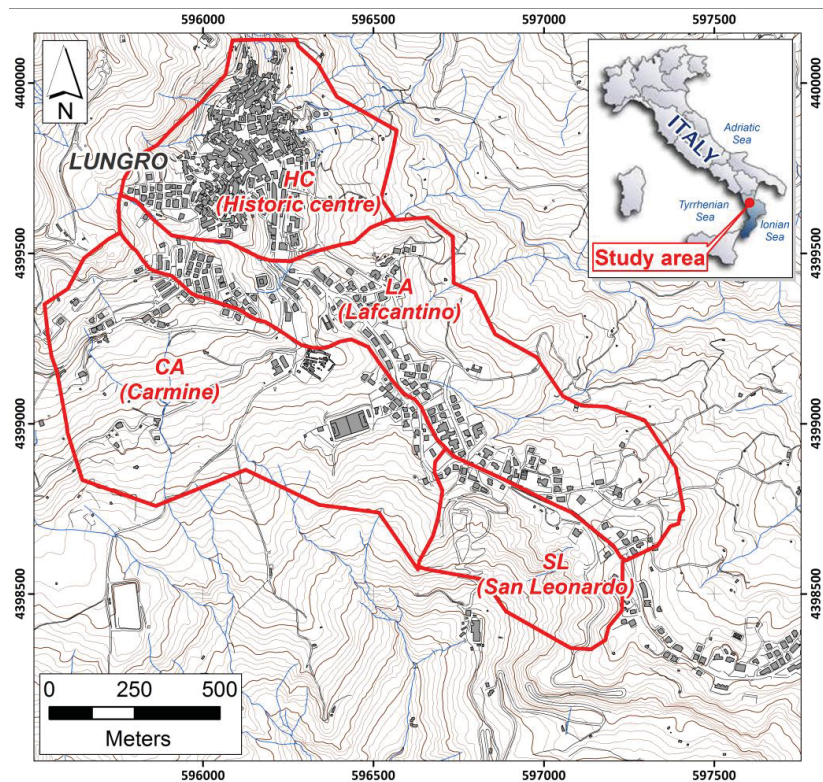


Figure 7.3 The Lungro study area

The contents of Section 7.2 are published in:

Peduto D., Ferlisi S., Nicodemo, G., Reale D., Pisciotta G., Gullà, G. (2017). Empirical fragility and vulnerability curves for buildings exposed to slow-moving landslides at medium and large scales. *Landslides* (in press), DOI: 10.1007/s10346-017-0826-7.

The analysis of historic data collected over the study area (Gullà et al. 2006) highlighted that the old centre of Lungro and the newly built-up areas have been recurrently affected by landslide phenomena, usually slow-moving. Anyway, the instability of the area was well-known and documented for a long time (Almagià 1910) so that it was included in the list of the centers that had to be relocated to more stable areas (Law 9 July 1908, No. 445).

Despite the awareness about slope instabilities, several private houses, public buildings, and facilities, as well as road networks, were built-up in this area. As a consequence, the instability problems, which initially affected only the buildings located in the historical centre, progressively involved the newly developed constructions with damage that in some cases compromised the stability of the superstructures.

### **7.2.1 Geological and geomorphological setting**

Lungro urban area is located in a geological context (Figure 7.4) where the Lungro-Verbicaro Unit, dating back to the Middle Trias and made up of metapelites and metacarbonates, prevails (Gullà et al. 2017a). The Lungro-Verbicaro Unit, next to the dwelled area of Lungro, moves towards the Ophiolitic Unit of Diamante-Terranova (Lower Jurassic-Cretaceous), with a clear extensional tectonic contact. The cover of the Diamante-Terranova Unit, made up of phyllites and slates, crops out in the study area that form a "melange structure" made up of blocks and fragments of different nature (e.g. phyllites, slates and metacarbonates) in a prevalently clayey matrix, derived from the degradation of phyllites (Antronico et al. 2014; 2013).

The metasediments of the Diamante-Terranova Unit are overlaid by an Upper Tortonian-Messinian sequence composed of coarse sandstone and shale interbedded with gypsiferous sandstone and gypsum. The Early Miocene succession ends with deposits dating back to the Middle Pliocene-Pleistocene, represented by sandy and conglomeratic beds. Moreover, colluvium and landslide debris, with a maximum thickness of about 10 m, are prevalently present on the Unit of Diamante-Terranova phyllite (Antronico et al. 2013).

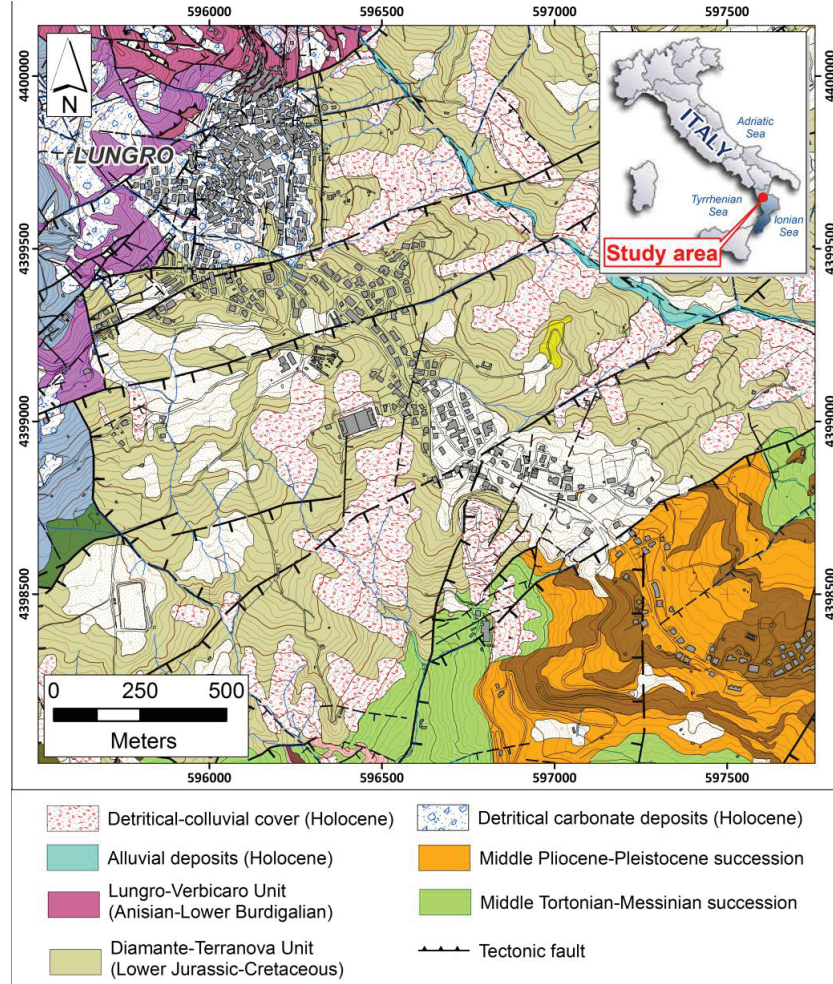


Figure 7.4 Geological map of Lungro study area (modified from Antronico et al., 2014).

The official landslide inventory map of the study area (drafted at 1:10,000 scale within the Hydrogeological Setting Plans of the Calabria Region in 2001) was updated by Antronico et al. (2014) using aerial photographs acquired in 1955 (scale 1:33,000), 1980 (scale 1:25,000), 1991 (scale 1:33,000), 2001 (scale 1:15,000) and field surveys (Figure 7.5).

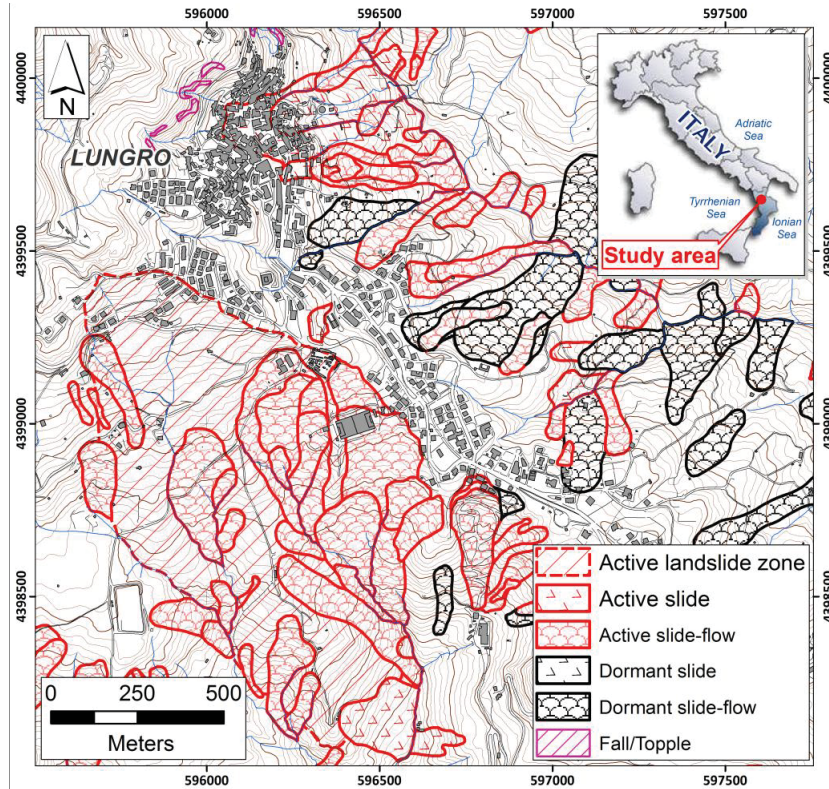


Figure 7.5 Landslide inventory map of Lungro area (modified from Antronico et al., 2014)

The landslide inventory map highlights that the study area is affected by a large number of landslides classified as slides, complex slide/flow (Varnes, 1978) and landslide zones. The landslide zone represents an area where clustering of phenomena is so tight that it is impossible to distinguish the different bodies, but sometimes mass movements can be mapped inside it (Greco et al. 2007). This type of mass movement is present on the left slope of the urban center, characterized by the presence of a large amphitheater-shaped landslide zone inside which some active mass movements were mapped (Antronico et al., 2014).

The landslides mapped in the study area were then typified by Gullà et al. (2017a) according to the proposed "a posteriori (aPosIn)" procedure based on the joint use of geomorphological studies, field surveys and ground displacement monitoring data achieved by both geotechnical and advanced differential interferometric synthetic aperture radar (A-



DInSAR) data. The typified landslides inventory map is shown in Figure 7.6.

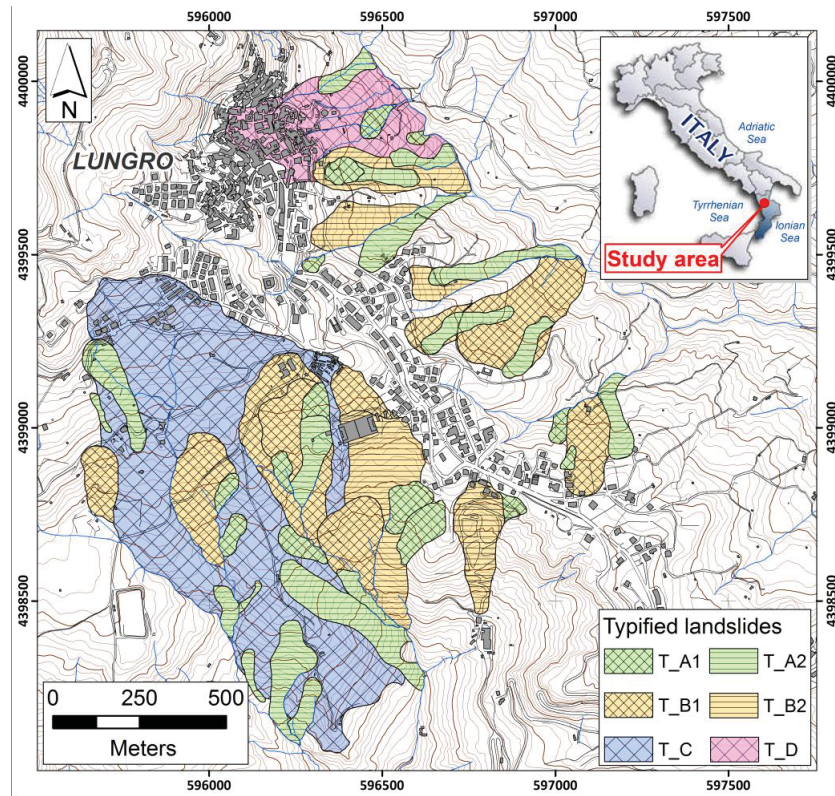


Figure 7.6 Map of typified landslide in Lungro urban area (modified from Gullà et al., 2017a)

In particular, the landslide phenomena were distinguished in six typified categories (Table 7.1) that from a kinematic point of view present the following characteristics: *i*) T\_A1 landslides (slide-flow complex type) with ordinary velocity from 2 to 4 cm/year and critical velocity (i.e. in the paroxysmal phases) higher than 200 cm/year; *ii*) T\_A2 landslides (slide-flow complex type) with ordinary velocity from 5 to 7 cm/year and critical velocity higher than 20 cm/year; *iii*) T\_B1 landslides (slide-flow complex type) with ordinary velocity from 0.5 to 5 cm/year and critical velocity higher than 80 cm/year; *iv*) T\_B2 landslides (slide-flow complex type) with ordinary velocity from 4 to 20 cm/year and critical velocity

higher than 100 cm/year; *v*) T\_C landslides (defined as landslide zone according to the definition provided in Antronico et al., 2014) with ordinary velocity from 0.5 to 5 cm/year and critical velocity higher than 40 cm/year; *w*) T\_D landslides (slide type) with ordinary velocity from 0.2 to 0.5 cm/year and critical velocity from 2 to 5 cm/year.

**Table 7.1 Main features of the typified landslides in Lungro urban area (modified from Gullà et al., 2017a)**

Typified landslide	Width (W) [m]	Length (L) [m]	L/W	Depth [m]	Velocity [cm/year]		Involved soil	Kinematic type
					ordinary	critical		
T_A1	25-100	≤ 180	≤ 2.5	about 6	2-4	> 200	detritic-colluvial covers	Complex landslide
T_A2	15-100	≥ 80	> 2.5	about 10	5-7	> 20	deeply weathered and chaotic phyllites	Complex landslide
T_B1	90-260	130-550	< 2.5	10-20	0.5-5	> 80	deeply weathered and chaotic phyllites	Complex landslide
T_B2	80-220	> 300	≥ 2.5	10-16	4-20	> 100	deeply weathered and chaotic phyllites	Complex landslide
T_C	830	1500	1.8	20-30	0.5-5	> 40	deeply weathered and chaotic phyllites	Landslide zone
T_D	100-250	350-550	2.2-3.2	20-30 / 10-15	0.2-0.5	2-5	weathered and chaotic phyllites	Slide

The typified landslide map was used in this Thesis, jointly with the topographic map at 1:5,000 scale, in order to identify the exposed elements (i.e. single buildings) according to the first step of the proposed procedure (see Chapter 5 - Section 5.2).

### 7.2.2 DInSAR dataset

The SAR image dataset used in this study was processed in collaboration with the Institute for Electromagnetic Sensing of the Environment (IREA-CNR) of Naples, according to the SAR tomographic analysis (Fornaro et al. 2009, 2014), which is a recent extension of the DInSAR processing framework particularly effective for single building monitoring with very high-resolution data (Cascini et al. 2013b; Peduto

et al. 2015). The dataset (Table 7.2) consists of 35 ENVISAT images acquired on ascending orbit (August 2003 to January 2010) as well as 39 COSMO-SkyMed images acquired on ascending orbit from October 2012 to April 2014.

**Table 7.2 Main features of the Envisat and Cosmo-Skymed datasets used for the analysis in Lungro area.**

Sensor	Orbit direction	Period of acquisition	No. of images	Incidence angle (°)
Envisat	Ascending	August 2003	35	23
		to January 2010		
Cosmo-Skymed	Ascending	October 2012	39	34
		to April 2014		

It is worth noting that the COSMO-SkyMed mission, composed by a constellation of four satellites, is currently one of the most advanced operational SAR system particularly effective for monitoring purposes of the built environment thanks to the very high spatial resolution of the acquired images as well as to the very fast acquisition scheduling of the multi-sensor mission. Figures 7.7a and b show the distribution of DInSAR benchmarks derived from ENVISAT (7,299 DInSAR benchmarks) and COSMOSky-Med data (15,252 DInSAR benchmarks).

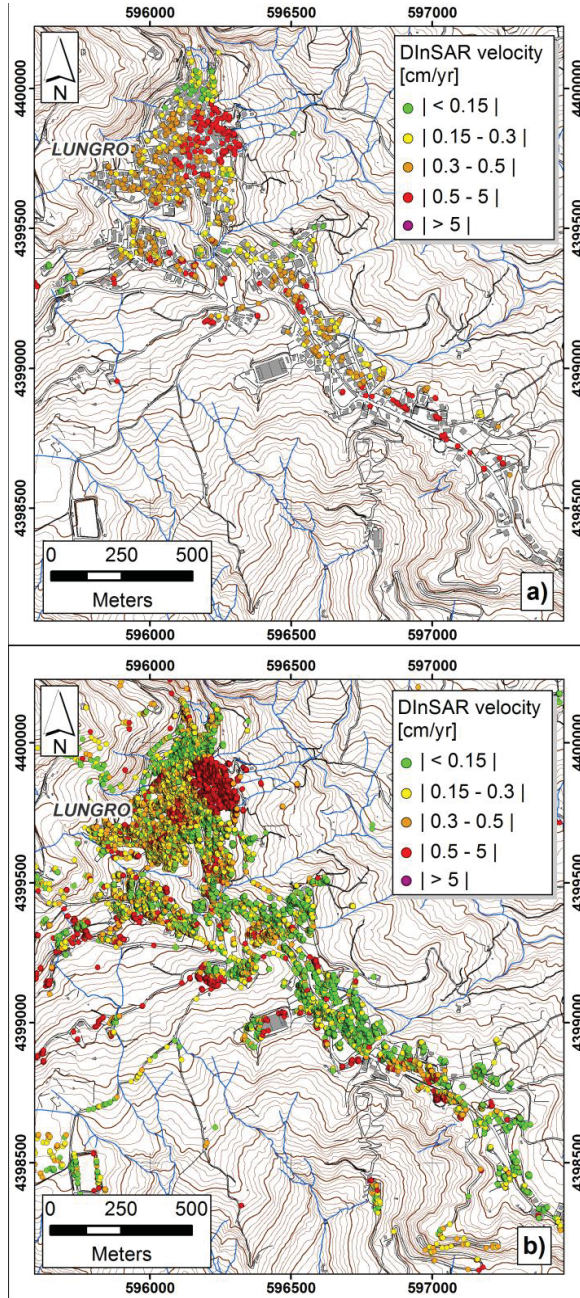


Figure 7.7 DInSAR data distribution over the study area: a) ENVISAT DInSAR benchmarks on ascending orbit for the period 2003-2010 and b) COSMO-SkyMed DInSAR benchmarks on ascending orbit for the period 2012-2014.

In the Figures 7.7a-b it is possible to appreciate the significant coverage increase achieved by COSMOSky-Med data (Figure 7.7b) and the highest velocity values recorded in both datasets in the central eastern portion of the historic centre, mainly affected by T\_D landslides (Figure 7.6). The coverage increasing achieved by COSMO-SkyMed data was also evaluated as percentage of covered buildings (Figure 7.8a) and average number of coherent PS per building in the study area (Figure 7.8b).

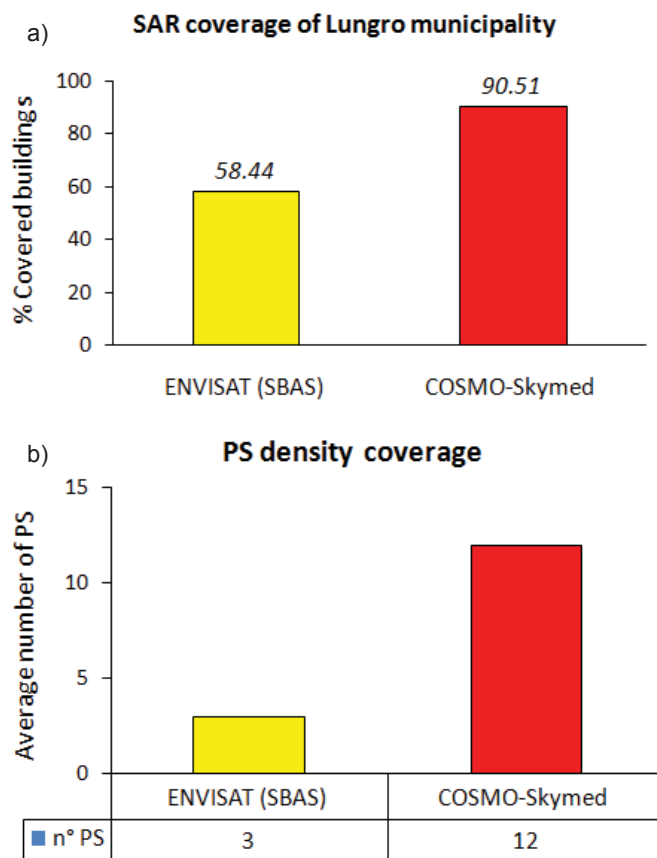


Figure 7.8 Comparison between ENVISAT and COSMO-SkyMed data in terms of a) percentage of covered buildings and b) number of coherent PS per building.

As it will be shown in Section 7.2.4, the DInSAR dataset was used to derive the intensity parameter, identified as the differential settlement suffered by each exposed element (i.e. the single building).

### **7.2.3 Building damage survey**

As already described in the previous chapter, it is well-known that the analysis of crack patterns exhibited by building façades provides useful information in order to establish relationships between settlements and damage suffered by a given structure (Cascini et al. 2013a; Bianchini et al. 2015; Ferlisi et al. 2015; Palmisano et al. 2016). For this purpose, an extensive analysis of damage severity levels suffered by buildings was carried out in Lungro urban area. First of all, multi-temporal damage dataset, derived from detailed field surveys conducted by the Research Institute for Geo-Hydrological Protection of Cosenza (IRPI-CNR) were analyzed to evaluate the distribution, degree and evolution of the damage to buildings located within or close to active landslides.

The information collected in the period from 2005 to 2011 highlighted damages affecting the buildings located both in the historic center and in the new developed urban areas with different levels and their severity evolution in the time (Antronico et al., 2014). In particular, several masonry structures of the historical centre (where also the Town Hall and a school are located) are characterized by severe cracks and deformations, as a consequence of the slow-moving phenomena affecting the built up area since earlier times. In the observation period, an increase of the degradation state on the buildings was registered and some of them were subject to repair works in order to increase their safety level and reduce the risk of collapse. In the new developed areas, buildings (mainly reinforced concrete structures) built since the second half of last century on active landslides show several structural damage which compromised their stability.

In order to have an updated view of the damage severity with the built-up area, an in-situ damage survey was carried out in October 2015 over the entire urban area. In such a case, ad-hoc predisposed fact-sheets (modified from Ferlisi et al., 2015) were filled in for surveyed buildings. These latter allowed to collect - through direct surveys on structures and a photographic documents - information about crack widths in order to distinguish clearly the structural pathologies pertaining to each of the exposed buildings, thus providing an overview of both state of

maintenance and damage severity. An example of a filled fact-sheet is shown in Figure 7.9 for a masonry building located in the historical center and in Figure 7.10 for a reinforced concrete building located in the new developed area.

The fact-sheet includes different sections regarding the building location and its description in terms of structural type and geometrical characteristics; age of construction and occupancy type; the damage recorded by visual observation of the external façades of the buildings (the presence of cracks and/or disjunction in the outer walls, distortion of structures and walls that lost their verticality, as well as partial collapse of buildings).

The sheets were completed in a second phase with information regarding the position of the structure in the landslide body (e.g., head, body, toe) and with available monitoring information (e.g., GPS velocity, DInSAR displacement-time series, etc.).

The results of the survey campaign are shown in Figure 7.11, where the damage severity recorded on the buildings was classified adapting the six classes (D0 = negligible; D1 = very slight; D2 = slight; D3 = moderate; D4 = severe; D5 = very severe) proposed by Burland et al. (1977). The collected data revealed that in October 2015, 111 buildings of the Lungro urban area are located in slow-moving landslide-affected areas (Figure 7.11), with a damage severity level spanning from D0 to D5.

In Figure 7.12 and 7.13, the distribution of different levels of recorded damage severity is shown referring, respectively, to building typology and typified landslides.

The analysis of the collected data highlighted that 34% out of the total number of reinforced concrete buildings do not exhibit damage (Figure 7.12), whereas 66% exhibit damage of different severity (D1 = 33%; D2 = 17%; D3 = 8%; D4 = 8%). A higher percentage of damage is recorded for masonry buildings 91% (D1 = 16%; D2 = 32%; D3 = 23%; D4 = 13%; D5 = 7%) mainly located in the historic centre, where D5 level is recorded by buildings interacting with T\_D landslides (Figure 7.13).

# Chapter 7

**SCHEDE MONOGRAFICHE DELL'EDIFICIO**  
SCHEDE N° 1001000010 - DATA DI COMPLETAMENTO: 05-10-2015

**SEZIONE 1 - INQUADRAMENTO TERRITORIALE**

**SEZIONE 2 - IDENTIFICAZIONE EDIFICIO**

REGIONE: CALABRIA  
PROVINCIA: COSENZA  
COMUNE: LUNGRO  
Indirizzo: VIA ALBANIA  
N° edificio identificato in mappa: 442  
Coordinate Geografiche: ...

**SEZIONE 3 - DESCRIZIONE EDIFICIO**

USO: ...  
TECNOLOGIA STRUTTURALE: ...  
MATERIALE: ...

**SEZIONE 4 - LIVELLO DI DANNO (Classifica del danno)**

Grado: ...  
Descrizione: ...

**DOCUMENTAZIONE FOTOGRAFICA**

05-10-2015

Figure 7.9 Building fact-sheet filled in for a masonry building located in the historic center of the Lungro municipality.

**SCHEDE MONOGRAFICHE DELL'EDIFICIO**  
SCHEDE N° 1001000011 - DATA DI COMPLETAMENTO: 05-10-2015

**SEZIONE 1 - INQUADRAMENTO TERRITORIALE**

**SEZIONE 2 - IDENTIFICAZIONE EDIFICIO**

REGIONE: CALABRIA  
PROVINCIA: COSENZA  
COMUNE: LUNGRO  
Indirizzo: VIA S. LEONARDO  
N° edificio identificato in mappa: 91  
Coordinate Geografiche: ...

**SEZIONE 3 - DESCRIZIONE EDIFICIO**

USO: ...  
TECNOLOGIA STRUTTURALE: ...  
MATERIALE: ...

**SEZIONE 4 - LIVELLO DI DANNO (Classifica del danno)**

Grado: ...  
Descrizione: ...

**DOCUMENTAZIONE FOTOGRAFICA**

05-10-2015

Figure 7.10 Building fact-sheet filled in for a reinforced concrete building located in the new developed area of the Lungro municipality.



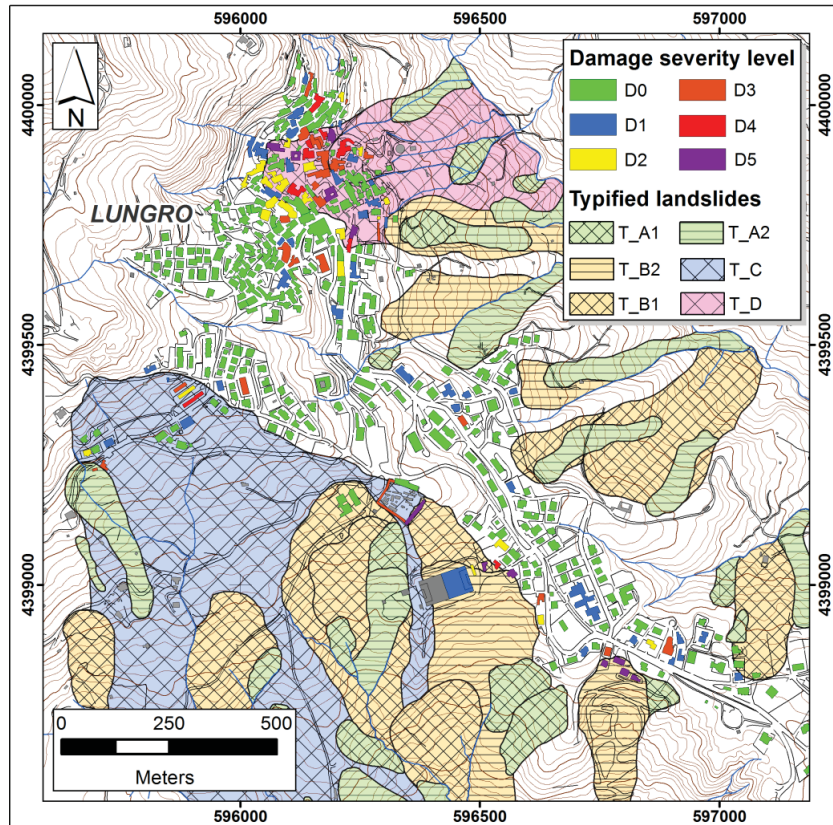


Figure 7.11 Map of surveyed buildings distinguished according to the recorded level of damage severity (for the legend of typified landslides, refer to Table 7.1).

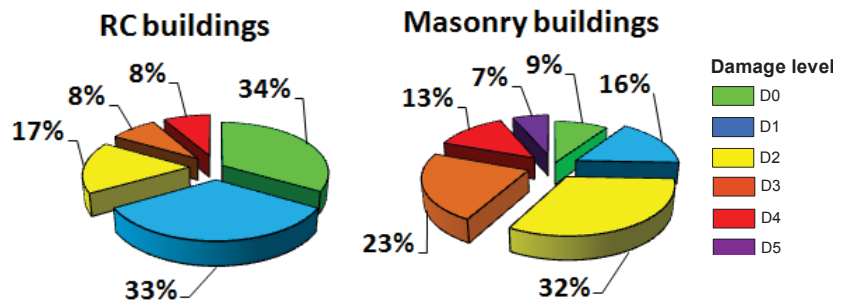


Figure 7.12 Distribution of the building damage severity on basis the building typology.

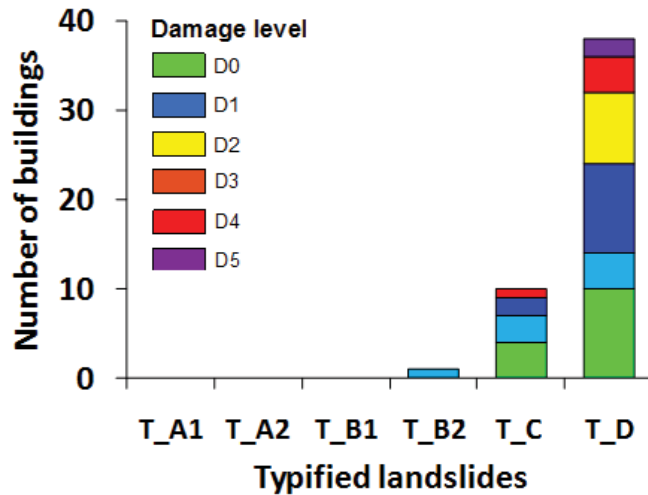


Figure 7.13 Distribution of the building damage severity on basis the typified landslides (for the legend of typified landslides, refer to Table 7.1).

#### 7.2.4 Results

Starting from the first step (phase I) of the proposed procedure (Section 5.2 - Chapter 5), the exposed elements (i.e. single reinforced concrete or masonry buildings) were identified by intersecting the information gathered from the topographic map (at 1:5,000 scale) with the typified landslide inventory map. For the purpose of this study, considering that the chosen representative intensity parameter is the differential settlement suffered by the structure due to a given slow-moving landslide, the analysis focused on 49 exposed buildings (12 of reinforced concrete and 37 of masonry structure) which were covered by at least two DInSAR benchmarks for both ENVISAT and COSMO-SkyMed available datasets. Figure 7.14 shows an example of the analysis carried out for a reinforced concrete building located on the boundary of an active roto-traslational slide, for which a DInSAR dataset covering about 10 years (ENVISAT and COSMO-SkyMed datasets) was available. In particular, it is possible to follow the increase of the cumulative displacement that can be compared with the gradual increase of damage severity recorded during in-situ damage surveys.

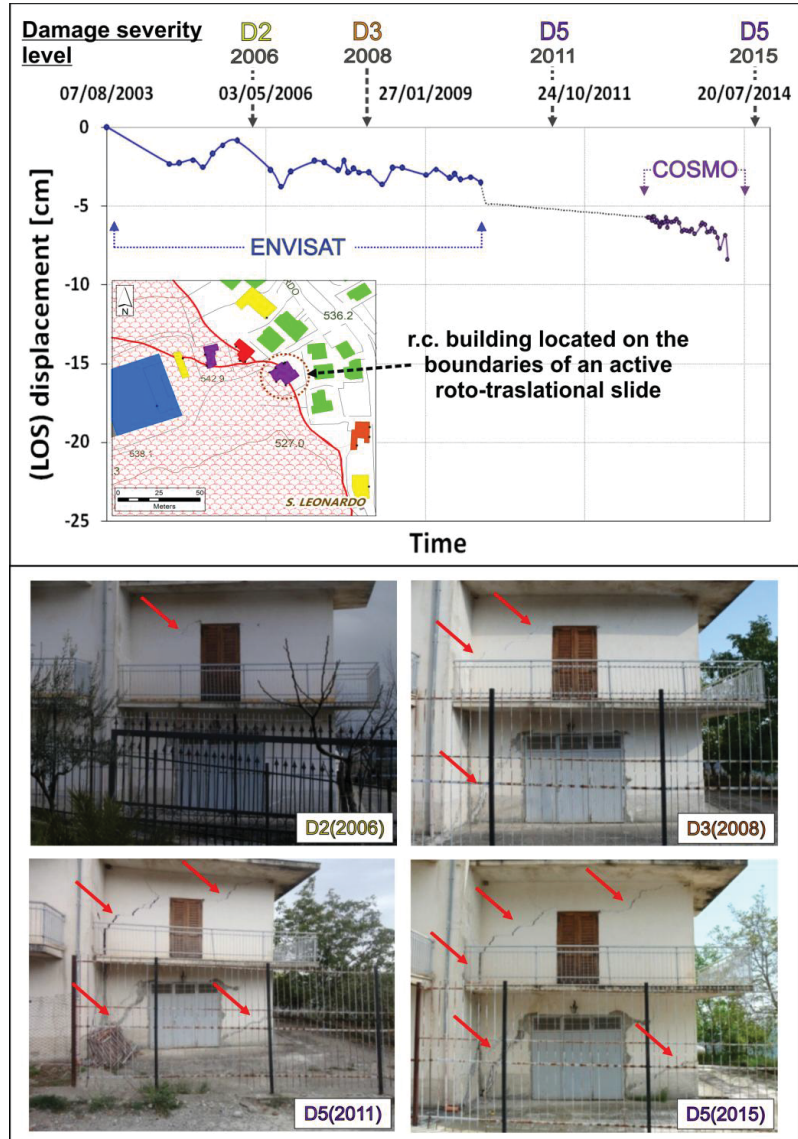
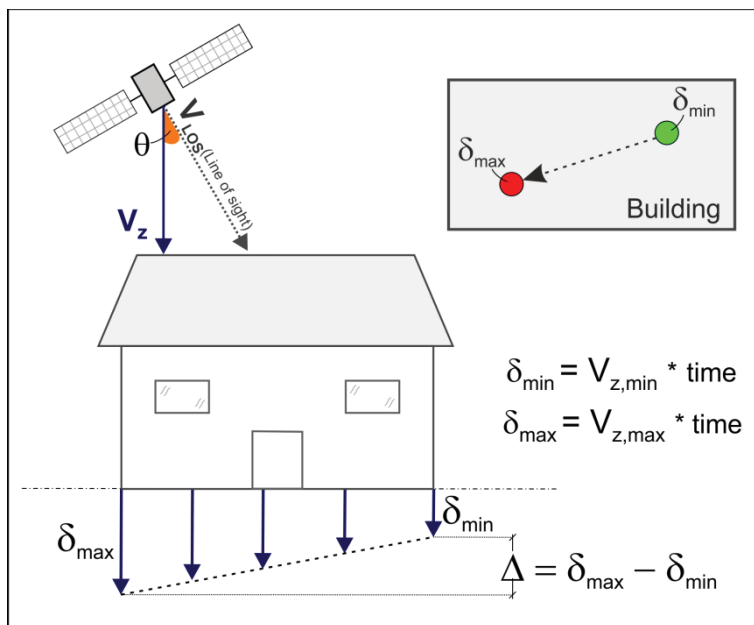


Figure 7.14 Monitoring of building damage evolution over the time via DInSAR data. The example refers to a reinforced concrete building located on the boundary of an active roto-traslational slide.

Then in Phase II, for each identified exposed element, the differential settlements ( $\Delta$ ) were computed (Figure 7.15) as the maximum difference ( $\delta v_{\max} - \delta v_{\min}$ ) of the cumulative settlements recorded by the DInSAR

benchmarks within its perimeter (Bianchini et al., 2015; Sanabria et al., 2014) which, in turn, were derived by multiplying the average velocity along the vertical direction (i.e. derived from the Line of Sight sensor-target direction) of each DInSAR benchmark covering a single building for the period of observation of the available datasets. Moreover, for the period February 2010 - October 2012, when DInSAR data were lacking, a constant velocity value equal to the one associated to the longest available dataset (i.e. ENVISAT) was assumed.



**Figure 7.15** Sketch of computation of DInSAR-derived differential settlement ( $\Delta$ ) for each building.

Once evaluated the differential settlements suffered by the examined buildings and classified their damage severity levels by means of the in-situ damage survey results (Figure 7.11), the two datasets were merged in order to retrieve the relationship between differential settlements and the level of damage for both reinforced concrete (Figure 7.16a) and masonry (Figure 7.16b) buildings located on different typified landslides within Lungro area.

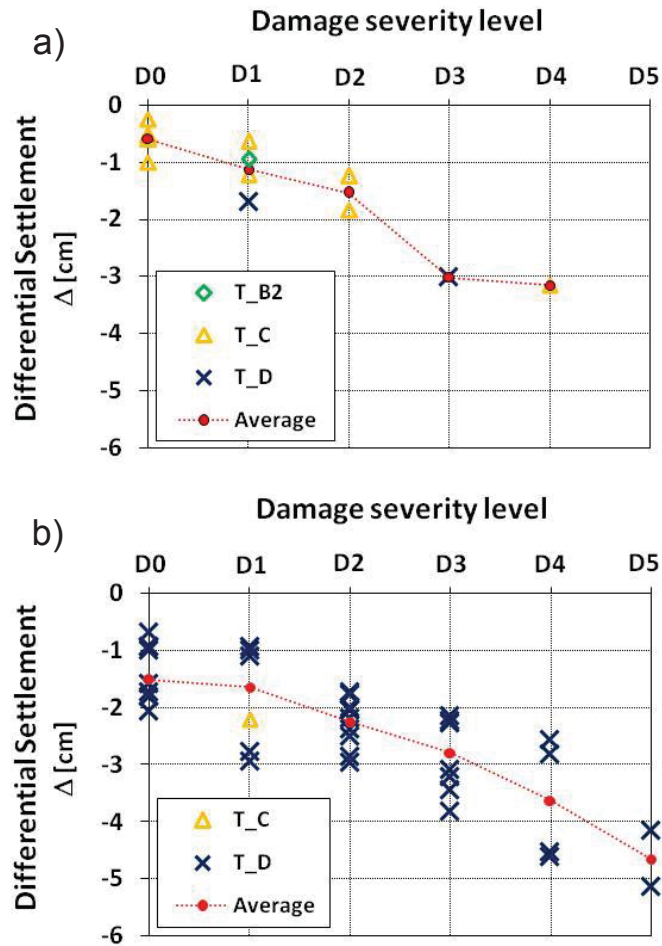


Figure 7.16 Damage severity level vs. differential settlements for a) reinforced concrete and b) masonry buildings located on different typified landslides within Lungro area (for the legend of typified landslides, refer to Table 7.1).

Starting from the obtained relationships, referring to masonry buildings (Figure 7.16b), whose sample included structures suffering from damage severity levels spanning from D1 to D5, empirical fragility curves were derived assuming the value of DInSAR-derived differential settlement ( $\Delta$ ) as representative intensity parameter.

For this purpose, first of all the frequency of occurrence of each level of damage severity was calculated for different classes of DInSAR-derived differential settlements (Figure 7.17).

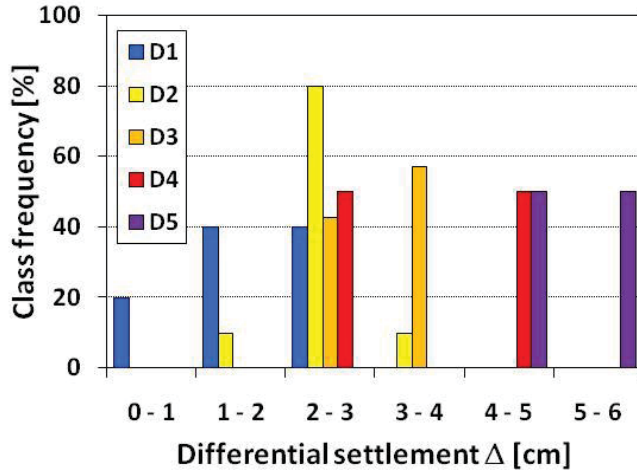


Figure 7.17 Class frequency of occurrence for each damage level suffered by masonry buildings for a given range of differential settlement.

Then, empirical fragility curves were derived following the procedure proposed by several authors (Fotopoulou and Ptilakis. 2013a,b; Mavrouli et al. 2014; Negulescu et al. 2010, 2014; Peduto et al., 2016a,b, 2017; Saeidi et al. 2009, 2012). In particular, the probability of reaching or exceeding a particular damage ( $D_i$ ) severity level for a fixed ( $\Delta$ ) intensity parameter was calculated using a cumulative log-normal distribution function (Eq.7.2):

$$P(\text{Damage} \geq D_i | \Delta) = \Phi \left[ \frac{1}{\beta} \ln \left( \frac{\Delta}{\bar{\Delta}} \right) \right] \quad (i = 0, \dots, 5) \quad (7.2)$$

where  $\Phi[\cdot]$  is the standard normal cumulative distribution function;  $\bar{\Delta}$  is the median value of the intensity parameter  $\Delta$  at which the building reaches the damage ( $D_i$ ) severity level; and  $\beta$  is the standard deviation of the natural logarithm of the intensity parameter.

The derived empirical fragility curves are shown in Figure 7.18, while the values of median and standard deviation parameters used to derive the fragility functions are synthesized in Table 7.3.

**Table 7.3 Median and standard deviation parameters used to derive the fragility functions for each damage levels for masonry buildings within the Lungro urban area.**

Damage severity level	Median [cm]	Stand. dev. [cm]
D1 (very slight)	1,10	0.50
D2 (slight)	2,11	0.18
D3 (moderate)	3,08	0.24
D4 (severe)	3,67	0.31
D5 (very severe)	4,65	0.15

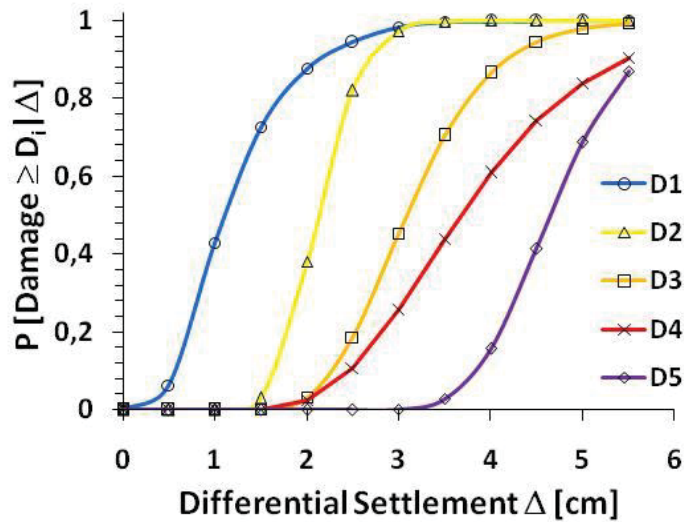


**Figure 7.18 Empirical fragility curves obtained via the adoption of the log-normal distribution function for masonry buildings within the Lungro urban area.**

Also in this case, the reliability of the used cumulative log-normal distribution function was checked using the K-S test (see Appendix B),

which confirms the assumption that the cumulative log-normal distribution function is acceptable to describe the probability of exceeding a given level of damage severity for different significance levels taken as references.

Finally, the vulnerability curve was derived for masonry buildings of the study area by fitting the (Eq. 7.3) proposed by Lagomarsino and Giovinazzi (2006):

$$\mu_D = a [b + \tanh(c \cdot \Delta + d)] \quad (7.3)$$

In particular, for a given  $\Delta$  value,  $\mu_D(\Delta)$  can be computed according to the formula (7.4) adapted from Pitilakis and Fotopoulou (2015):

$$\mu_D(\Delta) = \sum_{i=0}^5 P_i \cdot d_i \quad (7.4)$$

where  $P_i$  is the discrete probability associated with a damage severity level ( $D_i$ ) whose numerical index equals  $d_i$  (taken for this application as 1, 2, 3, 4 and 5 for  $D_1$ ,  $D_2$ ,  $D_3$ ,  $D_4$  and  $D_5$ , respectively). The generated vulnerability curve is shown in Figure 7.19 with corresponding fitting coefficients equal to:  $a = 2.6745$ ;  $b = 0.8695$ ;  $c = 0.4810$ ;  $d = -1.3310$ .

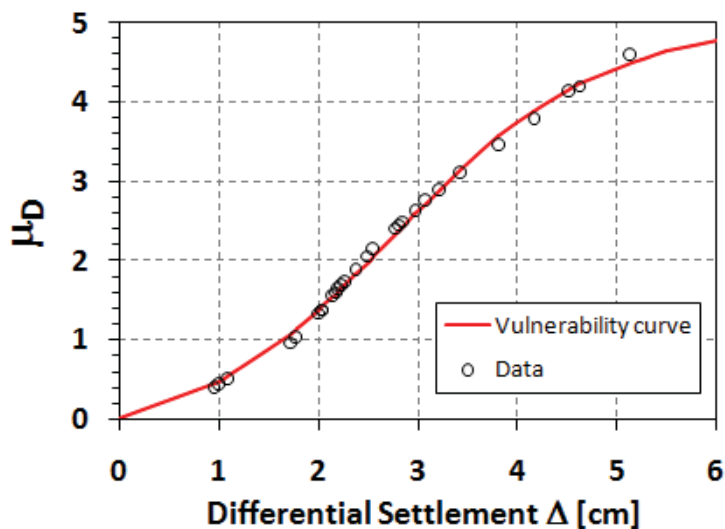


Figure 7.19 Empirical vulnerability curve for masonry buildings within the Lungro urban area.



The obtained results either in terms of fragility or vulnerability curves, show that both the probability of reaching/exceeding a certain damage level (fragility curves) and the degree of damage averagely expected (vulnerability curve) for a masonry buildings increases when the intensity parameter (i.e., differential settlement) increases, thus reflecting the general increasing trend of the severity levels with the slow-moving landslide intensity highlighted by the cause-effect relationships (Figure 7.16). However, it is worth remembering that, in order to achieve statistically reliable results, the available dataset (i.e., buildings interacting with slow-moving landslides for which the damage levels and relative intensity parameters are known) must to be necessarily representative. Accordingly, within this Thesis work, as it will be shown in the next Section, the analysis was extended to another urban area of Calabria Region (Municipality of Verbicaro, Cosenza Province), characterized by similar geological-geomorphological contexts and urban fabric of Lungro area and affected by several slow-moving landslides that induced damages of different severity levels to structures and infrastructures.

### 7.3 THE VERBICARO CASE STUDY

The urban area of Verbicaro (Figure 7.20), is located in the southern Apennines on the opposite side of the same relief where the municipality of Lungro is located. Similarly to the municipality of Lungro, the urban area of Verbicaro (about 2 km<sup>2</sup>) is composed by a historic centre (HC), characterized by mainly masonry buildings and newly developed areas (localized in the northwest and east sectors of the old centre), with reinforced concrete structures built since the early 1960s.

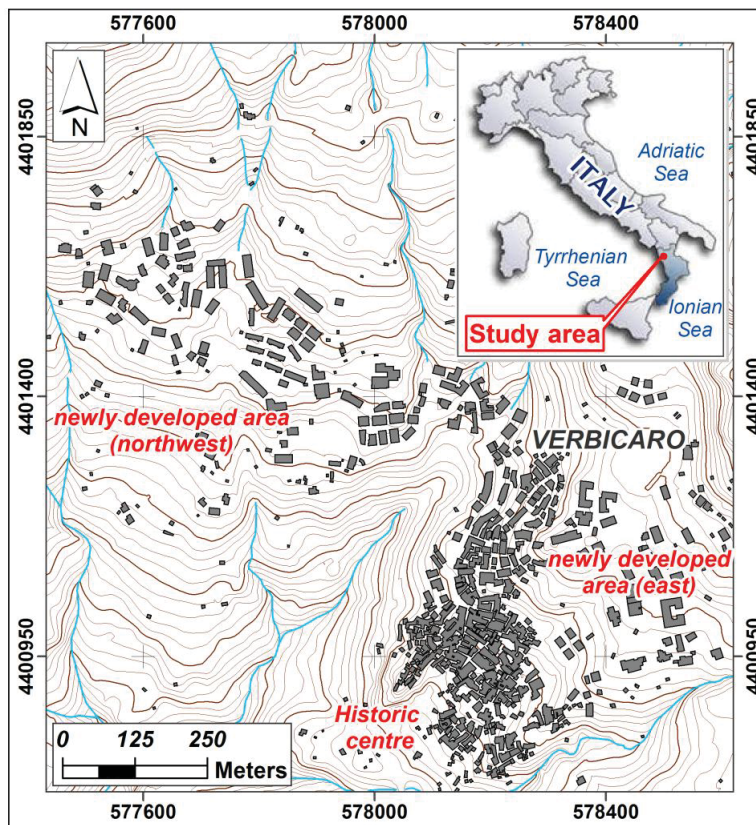


Figure 7.20 The Verbicaro study area.

The contents of Section 7.3 are published in:

Nicodemo G., Peduto D., Ferlisi S., Gullà G., Borrelli L., Fornaro G., Reale D. (2017). Analysis of building vulnerability to slow-moving landslides via A-DInSAR and damage survey data. Proceedings of the 4th World Landslide Forum, WLF4 – Ljubljana, Slovenia May 29 – June 2, 2017. (Accepted).

The whole urban area has been suffering from slope instability for a long time. Consequently, the Authorities included Verbicaro in the list - never implemented - of the centers that had to be relocated in more stable areas (Law 9 July 1908, No. 445). During past decades, many structures were damaged and the municipal council delivered several evacuation/repair/demolition ordinances. However, the seriousness of the problem highly increased since the early 1960s, due to the urban sprawl towards the unstable slopes located in the area located north-west of the old centre, where some reinforced concrete buildings have experienced damages compromising even their stability.

### 7.3.1 Geological and geomorphological setting

From a geological point of view, the Verbicaro urban area rests on the Frido Unit, constituted by low-grade metamorphic rocks usually marked by extensional brittle–ductile shear zones, including metapelites, phyllites, shales and metalime-stones, tectonically overlaid to the Lungro–Verbicaro Unit (Amodio Morelli et al. 1976). At the top of the Unit, locally covered by colluvial deposits, blocks and fragments of metamorphic rocks in a prevalently clayey matrix can be found.

For the purpose of this study, an update of the official landslide inventory map – drawn-up at 1:10,000 scale within the Hydrogeological Setting Plans of the Calabria Region (2001) - of the study area was prepared (Ferlisi et al. 2015).

The new landslide inventory map (Figure 7.21), developed in collaboration with the Research Institute for Geo-Hydrological Protection, Cosenza (IRPI-CNR) at 1:5,000 scale, was drawn using multi-temporal aerial photographs, available monitoring data (i.e., geological boreholes, inclinometers, piezometers) and field surveys. In particular, the mapped phenomena consist of: roto-translational slides, complex landslides (Varnes, 1978) and landsliding areas (Gullà et al. 2017a), which mainly involve detrital covers constituted by colluvial deposits and completely degraded phyllites, with grain size distributions varying from slightly sandy clay with silt to silt with clay.

The updated landslide inventory map was used to identify the exposed elements (i.e. single buildings located in the landslide-affected area). In particular, the slow-moving landslides mapped as active (roto-translational and complex) affect both the southeastern portion of the old centre- where mainly masonry buildings (up to 3 floors) showing

damages of different severity levels are present -and the new developed urban area located north-west of the old centre, where reinforced concrete buildings - mainly built in early 60s (up to 7–8 floors) - have suffered damages that led in some cases to their demolition.

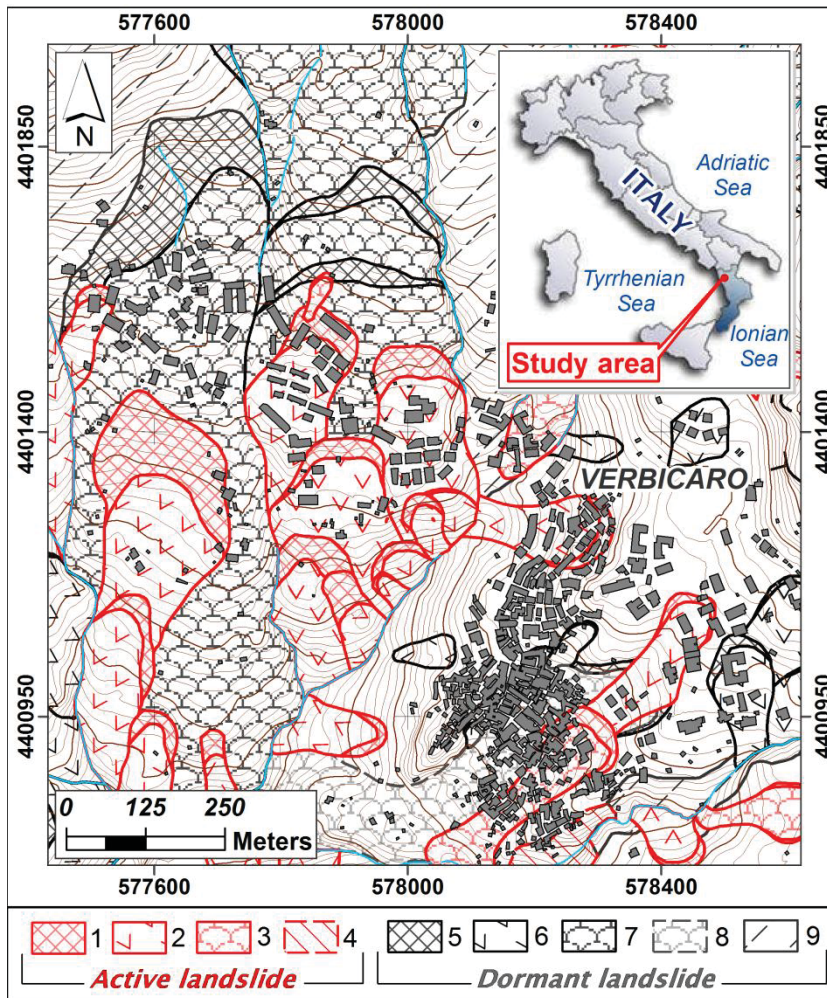


Figure 7.21 Landslide inventory map of Verbicaro area. Legend: 1) scarp of active landslide; 2) active roto-translational slide; 3) active complex landslide; 4) active landsliding area; 5) scarp of dormant landslide; 6) dormant roto-translational slide; 7) dormant complex landslide; 8) stabilized dormant complex landslide; 9) active landsliding area.

### 7.3.2 DInSAR dataset

The used SAR dataset (Table 7.4) consists of 69 ENVISAT images, acquired on both ascending (no. 29, August 2003 to January 2010) and descending (no. 40, May 2003 to July 2010) orbits, and 53 COSMO-SkyMed images, acquired on ascending (no. 39, October 2012 to April 2014) and descending (no. 14, April 2013 to December 2013) orbits.

The images were processed according to the SAR tomographic analysis (Fornaro et al. 2009, 2014) that, as mentioned in the Section 7.2.2, provides a high quality information on reflective targets in particular for COSMO-SkyMed datasets.

The spatial distributions of DInSAR velocities derived from both radar sensors are shown in Figure 7.22a and b for ENVISAT and in Figure 7.23a and b for COSMO-SkyMed, on both ascending and descending orbits, highlighting also in this case the significant coverage increase of COSMO-SkyMed dataset.

**Table 7.4 Main features of the Envisat and Cosmo-Skymed datasets used for the analysis in Verbicaro area.**

Sensor	Orbit direction	Period of acquisition	No. of images	Incidence angle (°)
Envisat	Ascending	August 2003	29	23
		to January 2010		
Envisat	Descending	May 2003	40	23
		to July 2010		
Cosmo-Skymed	Ascending	October 2012	39	34
		to April 2014		
Cosmo-Skymed	Descending	April 2013	14	32
		to December 2013		

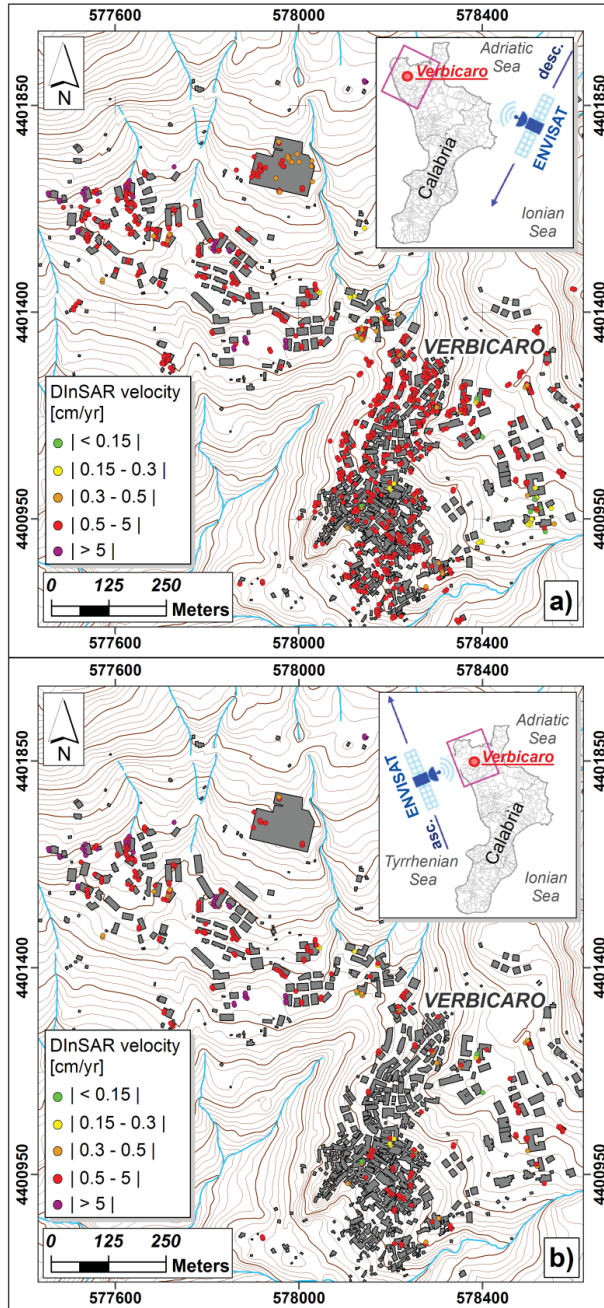


Figure 7.22 Spatial distribution of DInSAR data provided by ENVISAT radar sensor in the period 2003-2010 on a) descending and b) ascending orbit for Verbicaro urban area.

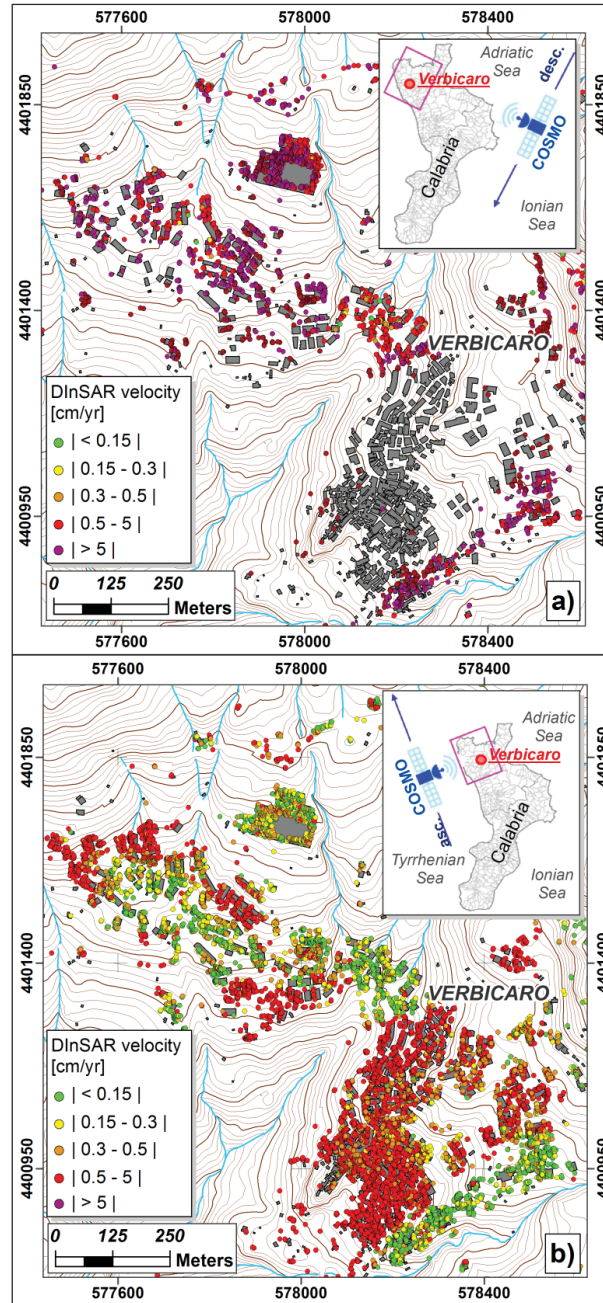


Figure 7.23 Spatial distribution of DInSAR data provided by COSMOSky-med radar sensor in the period 2012-2014 on a) descending and b) ascending orbit for Verbicaro urban area.

### 7.3.3 Building damage survey

As for the damage to buildings, as mentioned above, the entire urban area of Verbicaro has been suffering from slope instability for a long time. Consequently, in the last decades the municipal council delivered several evacuation/repair/demolition ordinances of many buildings both in the old centre and for new reinforced concrete buildings built in the northwestern urban area.

The information contained in the ordinances delivered by the municipal council within the period 1989–2009 were collected and analyzed according to *i*) the year of issue, *ii*) the type of order (i.e. evacuation/repair/demolition), *iii*) the reference location of the building in a GIS map, *iv*) some descriptive notes on the state of damage experienced by the structure.

A total of 95 ordinances were analyzed (42% evacuation, 33% repair, 25% demolition), mainly concentrating in the period 1998–2000. As a result, it was clear that in the last years masonry structures - mainly located in the historical centre - recorded severe cracks and deformations as a consequence of a combined effect of slope movements and degradation effects. Furthermore, slope instabilities led to compromise the stability of some reinforced concrete buildings located in the new developed northwestern area.

For the purpose of the present study, a damage survey was carried out in April-May 2014 over the entire study area.

Both severity and distribution of damage within the urban area of Verbicaro were investigated (Figure 7.24a) via the analysis of crack patterns exhibited by the building façades. Once again these data were collected filling-in the fact-sheets described in the Section 7.2.2 for 253 reinforced concrete (Figure 7.24b) and 239 masonry (Figure 7.24c) buildings.

The severity of the recorded damages were distinguished using six classes (from D0 = negligible to D5 = very severe) adapted from those provided by Burland et al. (1977), and the collected data show that 34% out of the total surveyed reinforced concrete structures and 50% of the masonry buildings exhibit damages whose severity level is higher than D0.



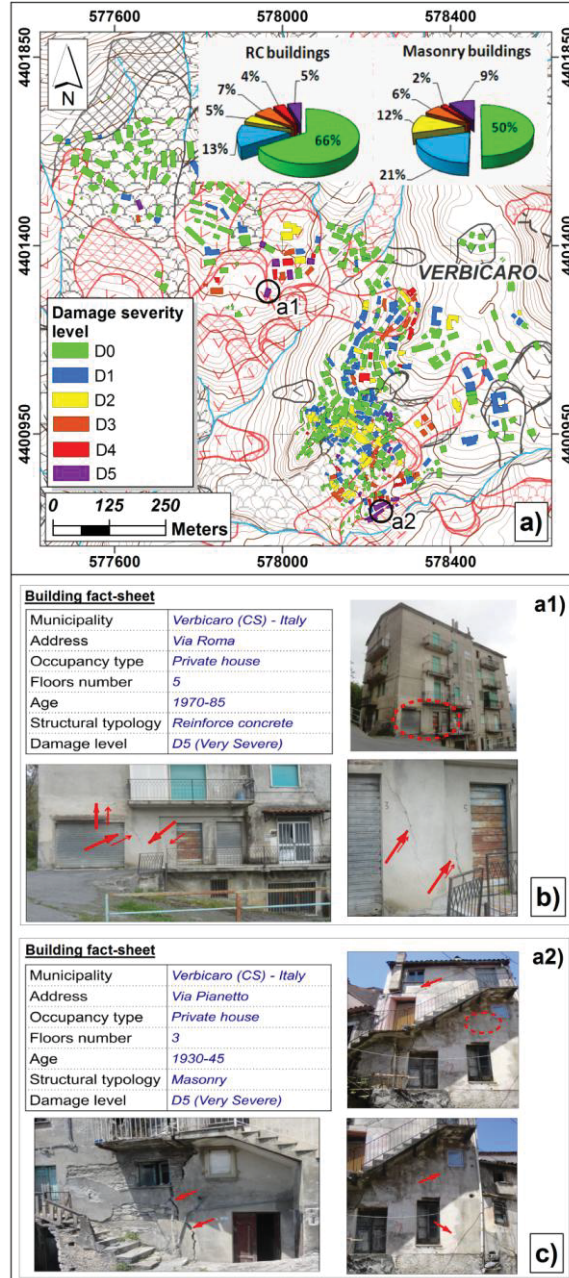


Figure 7.24 Map of surveyed buildings distinguished according to the recorded damage severity based on data collected in 2014 via fact-sheets for both b) reinforced concrete and c) masonry buildings. (for the legend of landslides inventory, refer to Figure 7.19).

### 7.3.4 Results

Following the procedure shown in Figure 5.2 (Section 5.2 - Chapter 5), the exposed buildings were preliminarily identified by overlaying the topographic map to the landslide inventory map. Out of a total of 492 surveyed buildings, 347 (197 reinforced concrete and 150 masonry buildings) resulted to be located on landslide-affected areas. Then, focusing on a sub-sample of 141 buildings (66 of reinforced concrete and 75 of masonry structure), a check of the distribution of damage severity - ranging from D1 to D5 - was carried out according to both the landslide typology and structural characteristics of the buildings (Figure 7.25a and b). Moreover, also the position of the buildings (i.e. at the head, body or toe) with respect to the landslide-affected areas was considered (Figure 7.26a and 7.26b).

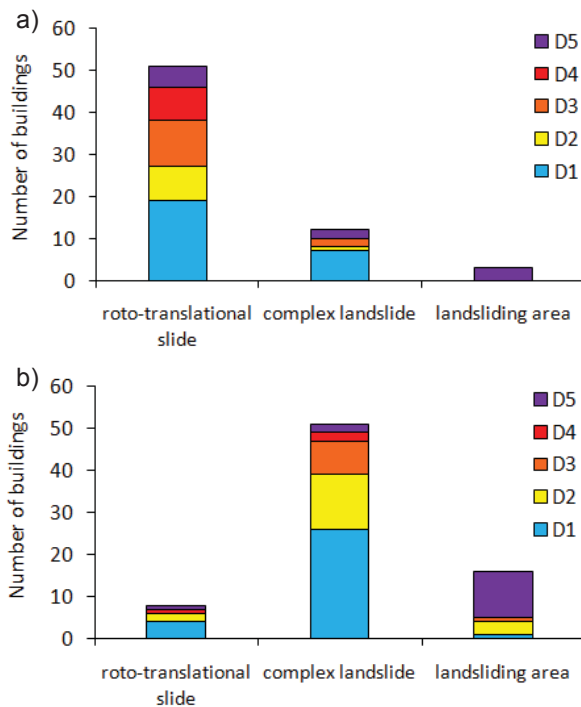
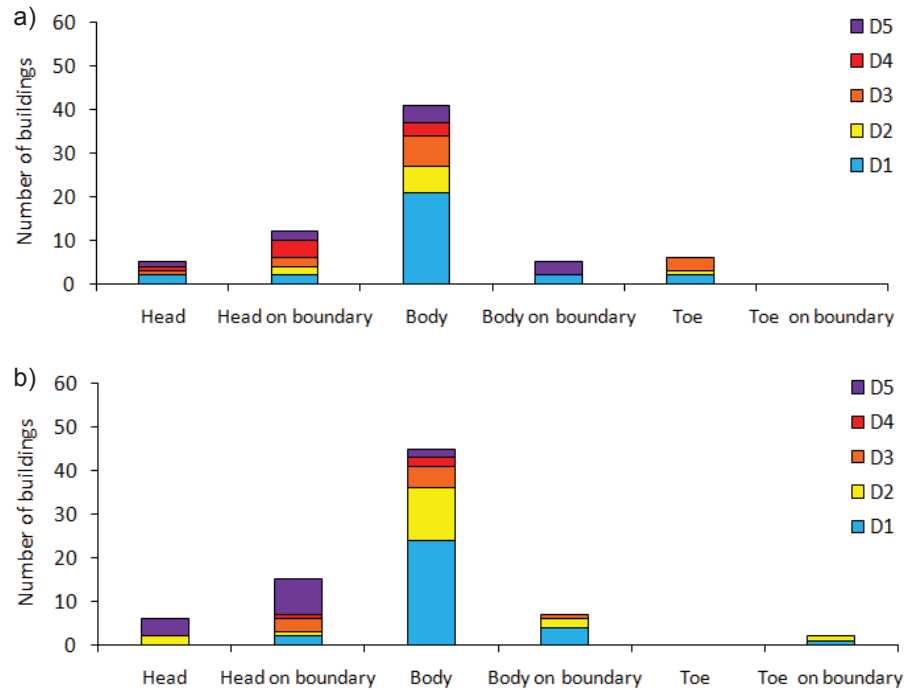


Figure 7.25 Distribution of damage severity according to landslide typology for a) reinforced concrete and b) masonry buildings.



**Figure 7.26** Distribution of damage severity for a) reinforced concrete and b) masonry buildings according to their position with respect to the landslide-affected areas.

Figures 25a and b show that the distribution of the damage severity suffered by buildings for both structural typologies seems independent of the landslide typology with which the structure interacts. More severe damages are recorded when the building is located at the head or in the body of the landslide-affected area (Figures 26a and b).

With reference to 40 reinforced concrete and 51 masonry damaged buildings, located on landslide affected areas and covered by at least one coherent pixel in both ENVISAT and COSMO-SkyMed datasets, the DInSAR-derived maximum settlements values were evaluated.

In particular, as for the Lungro case study, the cumulative settlements ( $\delta v$ ) were derived for each building by multiplying the average velocity along the vertical direction (i.e. derived from the Line of Sight sensor-target direction considering the different acquisition LOS angles of different used radar sensors:  $23^\circ$  for ENVISAT and  $32^\circ$  for COSMO-SkyMed) for the period of observation of each available dataset,

considering for the period (February 2010 - October 2012) where the DInSAR data are lacking, a constant velocity value equal to the one associated to the longest available dataset (i.e. ENVISAT). The above information was merged with the results of the damage survey providing a preliminary analysis of the relationship between the maximum cumulative settlements exhibited by each building and the recorded damage severity for both reinforced concrete (Figure 7.27a) and masonry (Figure 7.27b) buildings according to their position with respect to the landslide-affected areas.

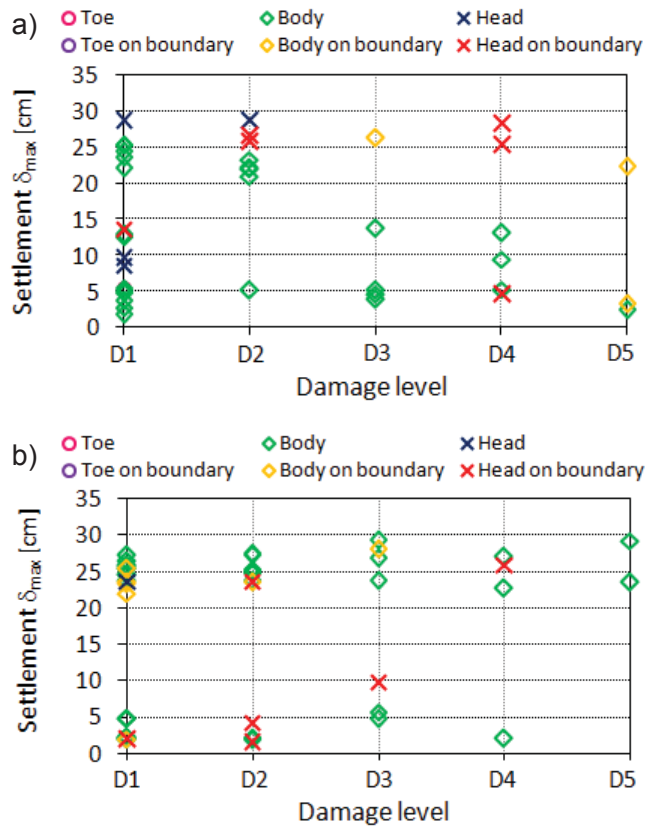


Figure 7.27 Damage level vs. maximum cumulative settlement ( $\delta_{max}$ ) distinguished for a) reinforced concrete and b) masonry buildings according to their position with respect to the landslide-affected areas.

Then, the differential settlements ( $\Delta$ ) were computed as the maximum difference ( $\delta v_{\max} - \delta v_{\min}$ ) of the cumulative settlements recorded within the perimeter of 40 damaged buildings (21 reinforced concrete and 19 masonry) located within the landslide-affected areas and covered by at least two coherent pixels in both ENVISAT and COSMO-SkyMed datasets. Merging the obtained differential settlements with the corresponding damage severity allowed investigating the relationship between cause (differential settlements) and effect (damage) for both reinforced concrete (Figure 7.28a) and masonry (Figure 7.28b) buildings affected by slow-moving landslides within Verbicaro area.

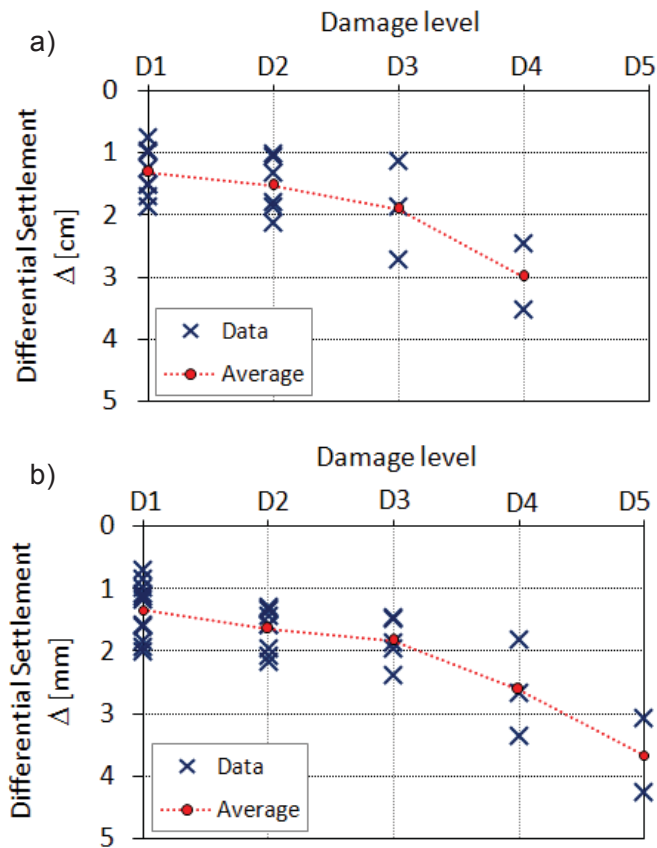


Figure 7.28 Damage level vs. differential settlement for a) reinforced concrete and b) masonry buildings.

The obtained diagrams show that the damage severity increases as the differential settlement, on average, increases. Then, similarly to the previous case study (Lungro), assuming the differential settlement as the representative intensity parameter of the natural event causing damage to buildings, for each structural typology empirical fragility curves (Figure 7.29a and b) were derived by adopting a log-normal distribution function (Eq. 7.2). The values of the median and standard deviation used to derive the fragility functions are reported in Table 7.5.

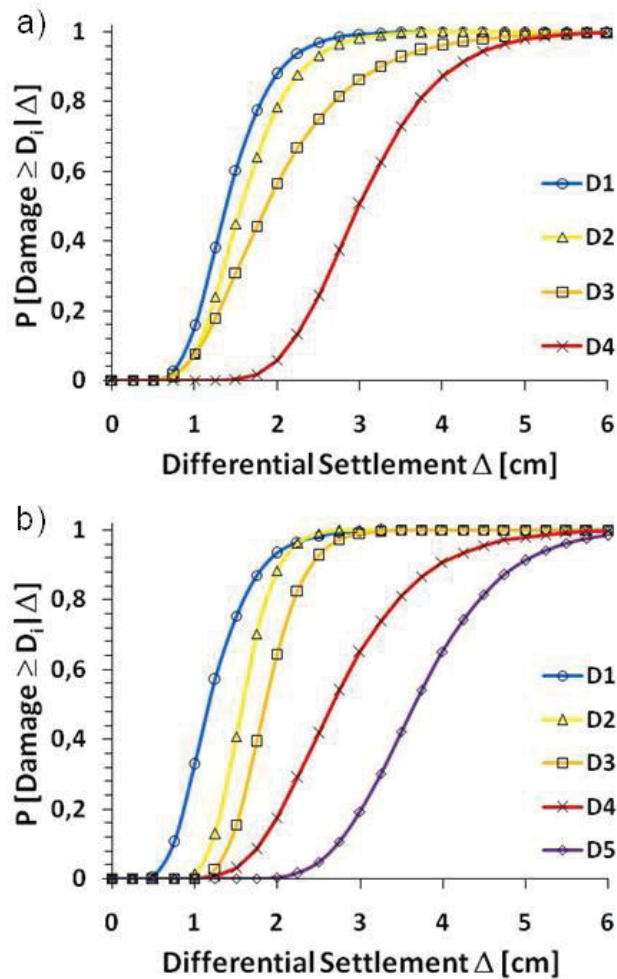


Figure 7.29 Empirical fragility curves obtained via the adoption of the log-normal distribution function for a) reinforced concrete and b) masonry buildings within the Verbicaro urban area.

**Table 7.5 Median and standard deviation parameters used to derive the fragility functions for each damage levels for reinforced concrete and masonry buildings within the Verbicaro urban area.**

Damage level	R.C. building		Masonry building	
	Median [cm]	Stand. dev. [cm]	Median [cm]	Stand. dev. [cm]
D1 (Very slight)	1.38	0.03	1.17	0.04
D2 (Slight)	1.56	0.03	1.57	0.02
D3 (Moderate)	1.86	0.04	1.85	0.02
D4 (Severe)	3.00	0.03	2.67	0.03
D5 (Very severe)	-	-	3.66	0.02

The obtained fragility curves highlight also for the Verbicaro case study, the increase of the probability of reaching/exceeding a certain damage level with the increase of the differential settlement suffered by the building, also confirming that the masonry buildings are generally more damageable than reinforced concrete ones, for a given value of the landslide intensity parameter (Burland et al. 1977).

With reference to sample of masonry buildings, with damage severity distribution ranging from D1 to D5, a vulnerability curve (Figure 7.30) was derived using the (Eq. 7.3) with corresponding fitting coefficients equal to:  $a = 2.5679$ ;  $b = 0.9471$ ;  $c = 0.9069$ ;  $d = -1.8032$ .

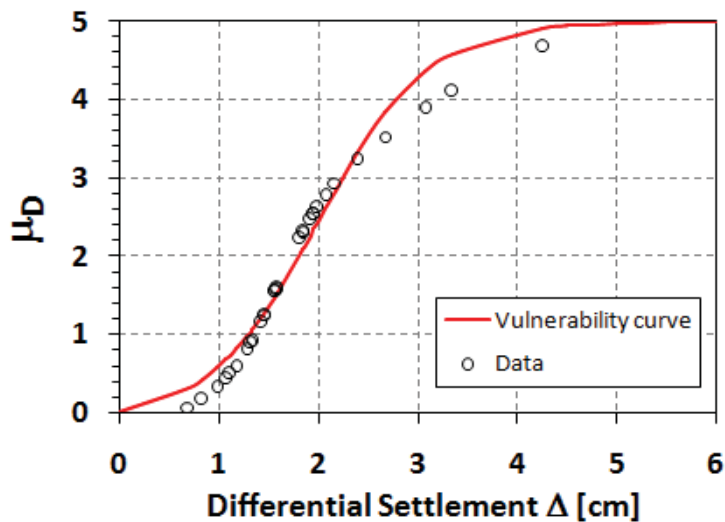


Figure 7.30 Empirical vulnerability curve for masonry buildings within the Verbicaro urban area.

The obtained results show, as evidenced from the application of the proposed procedure to two urban slow-moving affected-areas (Lungro and Verbicaro case studies), the potential of a combined use of DInSAR and damage survey data for the analysis and prediction of damage to buildings affected by slow-moving landslides. The obtained empirical fragility and vulnerability curves, once further validated, could represent powerful tools for the authorities in charge of urban management, for the engineers as well as for the householders in decisional processes that yearly require large amount of money.

It is worth underlining that the empirical fragility/vulnerability curves for buildings affected by slow-moving landslides (but the same is true for the curves presented for subsidence-affected buildings), derived following the proposed procedures based on an empirical approach, are representative of a sample of buildings homogenized (where the information was available) according to their structural typology or foundation type (in the Netherlands case studies). In practical terms, their use requires a deep knowledge on the nature of the available dataset and the awareness of uncertainties typical of empirical approaches.

Nevertheless, once the empirical relationships are obtained, numerical analyses developed using representative single buildings, can provide useful information in order to go in-depth in the uncertainty assessment



of the proposed empirical models and to better investigate the limits and the potential of these approaches for building vulnerability assessment. For this purpose, the next chapter shows the results of a numerical analysis carried out through the application of the procedure illustrated in Chapter 5 (Section 5.3) with reference to a masonry building.

## 8 NUMERICAL ANALYSIS OF BUILDING DAMAGE

This Chapter presents the results of a numerical analysis carried out on a masonry building model subjected to differential settlements according to the procedure explained in Chapter 5 (Section 5.3). These results are represented in terms of fragility curves in order to highlight the role played by some relevant factors (i.e. mechanical properties of both media simulating the behaviour of the masonry walls and the soil and the deformation mode of the shallow foundation system) in the attainment of given limit states.

### 8.1 MODEL DESCRIPTION

The old city centers of many country of the world are characterized by the presence of masonry buildings often subjected to ground instabilities induced by different causes. This is the case of the well-documented case studies, presented in the previous Chapters, where most of buildings in subsidence- or slow-moving landslide-affected areas just consist of masonry superstructures that, over the time, suffered from damages of different severity levels.

For this reason, the structural model considered for the numerical analyses presented in this Chapter is a masonry building reinforced by tie-rods located at every floor level (Figure 8.1a). This work hypothesis is based on the evidence that many buildings located in the historic centers of the above mentioned case studies, in particular those classified at high seismic risk, have been subjected to maintenance works with the application of reinforcing elements (mainly of steel) aimed at increasing their strength and reducing their vulnerability.

From a geometric point of view (Figure 8.1a), the building model is composed of three storeys with a total height of 9 m (3 m per each level) above ground level with a rectangular footprint whose dimensions are 10 m  $\times$  14 m ( $L_1 \times L_2$ ). Different thicknesses were used for the internal and external masonry walls. In particular, interior walls are thinner with a thickness of 36 cm for the two first storeys and 24 cm for the third one,

while the external walls present a thickness of 60 cm for the two first storeys and 40 cm for the third one. The same thicknesses of the walls located at first floor were used to model the foundation system (Figure 8.1b) resting on a bed of independent springs aimed at simulating the soil behaviour. Floors are modelled by 5 cm thick elastic membrane element with reinforcements composed by steel tie-rods located at every floor level.

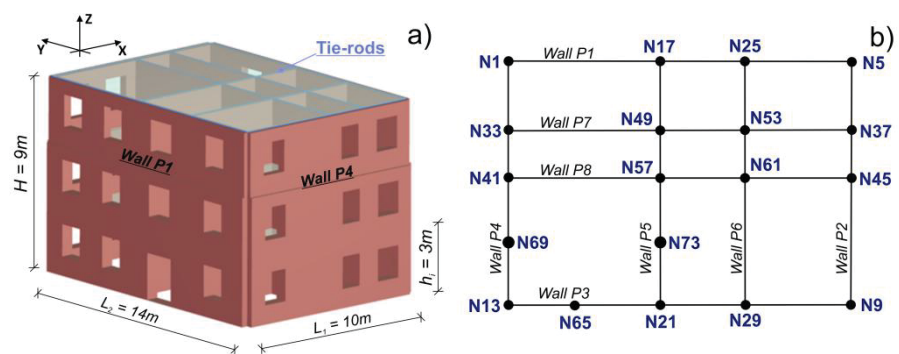


Figure 8.1 a) 3D view and b) foundation level of the modelled masonry building.

For the purpose of this study and considering the complex non-linear behaviour of the masonry structures characterised by high heterogeneity as well as degradation effects of mechanical properties in the time, the use of a code based on macroelements was preferred in comparison to more refined models based on the discrete element method. In particular, the examined building was modelled by adapting a TREmuri software, developed by Lagomarsino et al. (2012) for the analysis of the seismic response of masonry structures.

The software is based on FME (Frame by macro elements) method (Figure 8.2a) which simulates the non-linear global behaviour of masonry structures by using an equivalent frame model. The latter implements three main in-plane failure modes of the masonry walls, including bending-rocking, shear sliding and diagonal cracking (Figure 8.2b). The bending-rocking failure is evaluated by considering the average resistance in compression of the masonry (based on confidence factor "FC" according to the structural knowledge level) and no-traction material where a non linear reallocation of the stress is performed. The shear failure is evaluated according to the Mohr-Coulomb criterion for both new and existing buildings. In the case of existing buildings, according to

the Italian code, the shear failure can be also computed using Turnšek and Cačovic criterion. In the software, the walls are schematically modelled with piers and spandrels connected by rigid nodes (Lagomarsino et al. 2013).

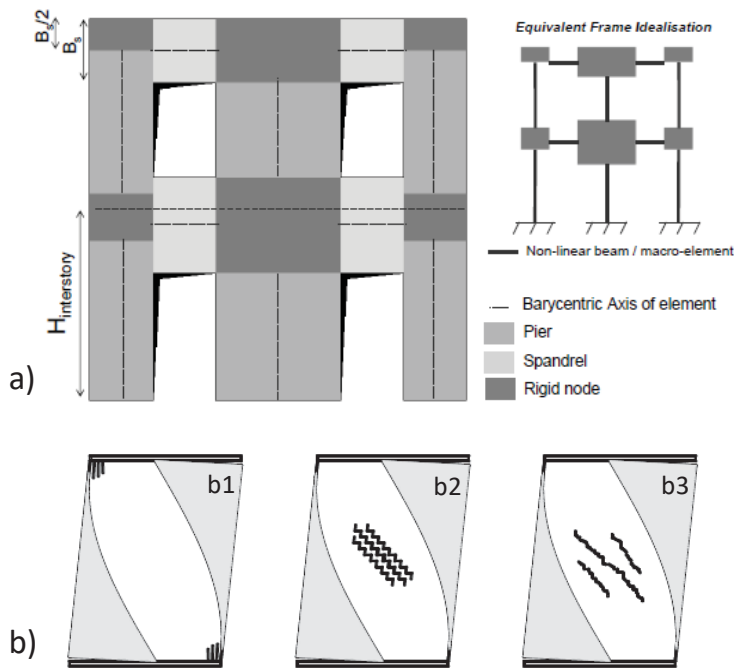


Figure 8.2 a) Idealization of the equivalent frame of the masonry wall in the case of a regular arrangement of the openings; b) schematization of the failure mechanisms of the masonry panel: banding-rocking b1, shear sliding b2 and diagonal cracking b3 (modified from Lagomarsino et al., 2012).

A 2D view of the four exterior walls of the modelled structure is shown in Figure 8.3 where: *i*) the red rectangles are masonry elements with pier behaviour, *ii*) the green ones are masonry elements with spandrel behaviour and *iii*) the blue ones are rigid links between the masonry macro-elements.

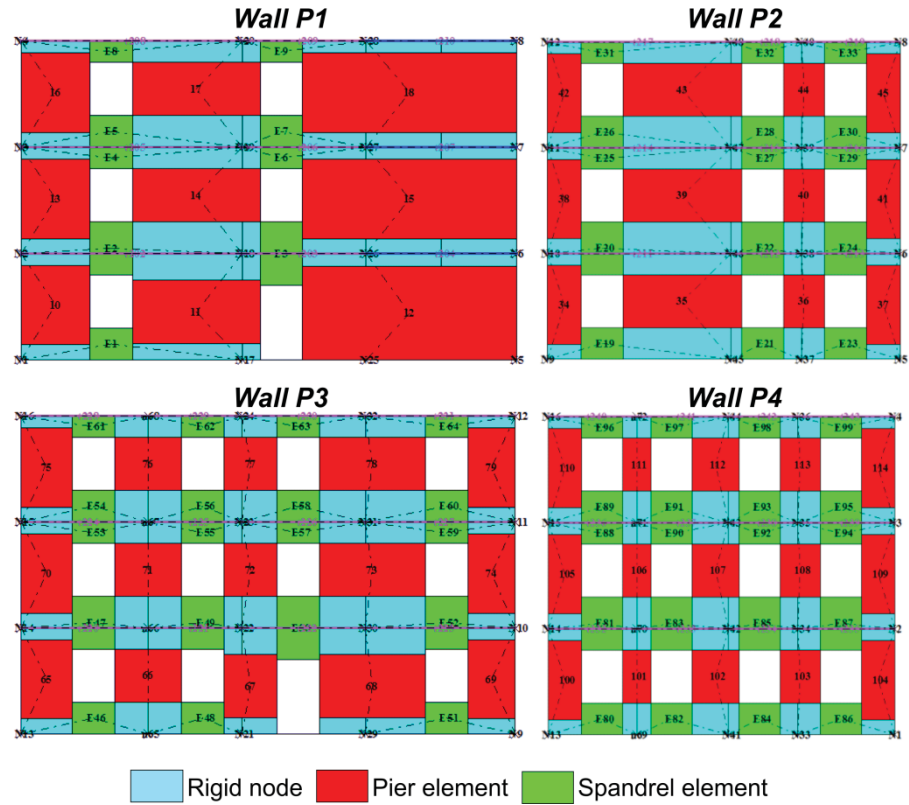


Figure 8.3 2D view of the four exterior walls of the modelled structure by TREmuri software.

As for the mechanical properties of the masonry walls as well as the soil characteristics used for the analysis, they were changed in order to evaluate their role on the response of the structure in terms of expected damage severity as described in the following Section.

## 8.2 PARAMETRIC ANALYSIS

Starting from the building model with the geometrical features described in the previous Section, the response of the structure in terms of damage severity levels and the derived fragility curves, were evaluated via a parametric analysis (Figure 8.4). In particular, each step of the general methodology proposed in Figure 5.3 (Chapter 5 – Section 5.3) was

specialized to the case study at hand and some characteristics of the model were parameterised in order to evaluate the role by them played in the reaching of a certain limit state by the superstructure and understand their relapse on the generation of fragility curves. In particular, once the geometrical features of the structure are fixed, the parameters that were changed are: *i)* the mechanical properties of the medium simulating the masonry wall behaviour; *ii)* the mechanical properties of the medium simulating the soil behaviour; *iii)* the deformation mode of the shallow foundation system. In particular, the mechanical properties of the superstructure as well as of the soil type were modified in the the phase I (Figure 8.4) in order to define different soil-foundation-structural model to be used in the analyses.

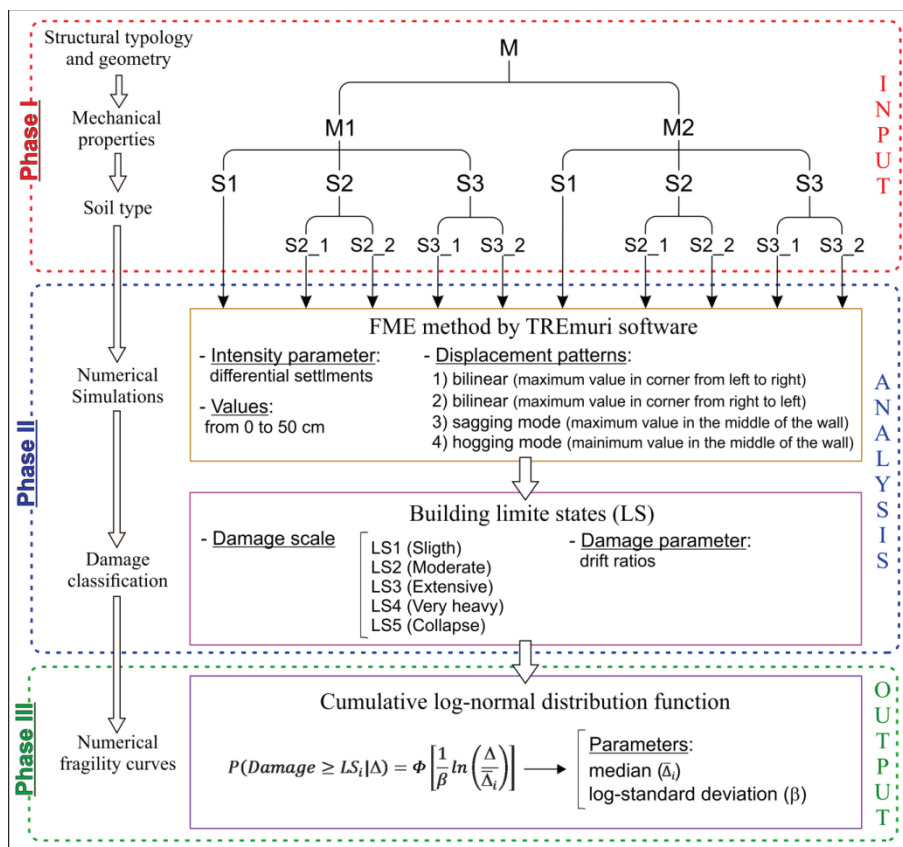


Figure 8.4 Flowchart of the carried out analysis using the parametric approach

Two different types of masonry were considered (i.e. M1 and M2), each of them resting on different soils (Si) with different strength characteristics. In detail, the building classified as M1 is representative of a masonry typology in disorganized stones (pebbles, or erratic/irregular stones) with a lower mechanical strength of the building classified as M2, representative of a masonry typology in brick and lime mortar. The masonry mechanical parameters used for the analysis, summarized in Table 8.1, refer to the average values suggested by the Italian technical code “NTC-14/02/2008” and reported in table C8A.2.1 of the Ministerial Circular n. 617 of 2<sup>th</sup> February 2009 for existing buildings. As for the soil, three main types are considered: S1= soft soil; S2 = clay and S3 = sand. These latter, in turn, were distinguished in soft (S2\_1) and medium/ hard (S2\_2) clay as well as in loose (S3\_1) and dense (S3\_2) sand. The values of elastic parameters used for the analysis are reported in Table 8.2.

**Table 8.1. Masonry mechanical parameters (from M.C. n. 617 – NTC/2008)**

Masonry types		Mechanical Properties			
		Mechanical parameter	Value		
			Min	Max	Average
M1	Masonry in disorganized stones (pebbles, or erratic/irregular stones)	E (Young modulus) [MPa]	690	1050	<b>870</b>
		G (Shear modulus) [MPa]	230	350	<b>290</b>
		$\rho$ (Density) [kg/m <sup>3</sup> ]	1900		<b>1900</b>
		F <sub>c</sub> (Compressive strength) [MPa]	1.0	1.8	<b>1.4</b>
		F <sub>sh</sub> (Shear strength) [MPa]	0.02	0.032	<b>0.026</b>
M2	Masonry in brick and lime mortar	E (Young modulus) [MPa]	1200	1800	<b>1500</b>
		G (Shear modulus) [MPa]	400	600	<b>500</b>
		$\rho$ (Density) [kg/m <sup>3</sup> ]	1800		<b>1800</b>
		F <sub>c</sub> (Compressive strength) [MPa]	2.4	4.0	<b>3.2</b>
		F <sub>sh</sub> (Shear strength) [MPa]	0.06	0.092	<b>0.076</b>

Table 8.2. Soil elastic properties

Soil types			Elastic Properties					
			E [MPa]			ν [MPa]		
			Lower limit	Upper limit	Average	Lower limit*	Upper limit	Average
S1	Soft-soil	Organic peat and clay	0.5	6	<b>3.5</b>	0.15	0.5	<b>0.3</b>
S2	Clay	S2_1 Soft	2	10	<b>6</b>	0.4	0.5	<b>0.45</b>
		S2_2 Medium / Hard	12	60	<b>36</b>			
S3	Sand	S3_1 Loose	10	25	<b>17.5</b>	0.2	0.35	<b>0.3</b>
		S3_2 Dense	30	80	<b>55</b>	0,3	0,4	<b>0.35</b>

As mentioned above, the soil behaviour was taken into account by putting a bed of springs at the base of the building model, whose stiffness in both vertical and horizontal direction was evaluated using the conventional impedance function proposed by Gazetas (1991). This model enables to take into consideration the frequency-dependent stiffness and damping of the soil through the elastic parameters ( $E$ ,  $G$ ,  $\nu$ ) characterizing the soil type on which the building is founded and the contact area of the foundation. An example of calculation is shown in Figure 8.5 with reference to a generic node of the foundation.

In particular, the stiffnesses in vertical ( $K_z$ ) and horizontal ( $K_y$ ;  $K_x$ ) direction were evaluated using the formulas (Gazetas, 1991):

$$K_z = \left[ \frac{2GL}{1-\nu} \right] * (0.73 + 1.54 \chi^{0.75})$$

$$K_y = \left[ \frac{2GL}{2-\nu} \right] * (2 + 2.50 \chi^{0.85})$$

$$K_x = K_y - \left[ \frac{0.2}{0.75-\nu} \right] * GL \left( 1 - \frac{B}{L} \right)$$

where  $\chi$  is computed as:



$$\chi = \frac{A_b}{4L^2}$$

G is the shear modulus;  $\nu$  the poisson's ratio; B and L are, respectively, the half-width and half-length of the circumscribed rectangle "influence area" (Figure 8.5 – see also Gazetas, 1991).

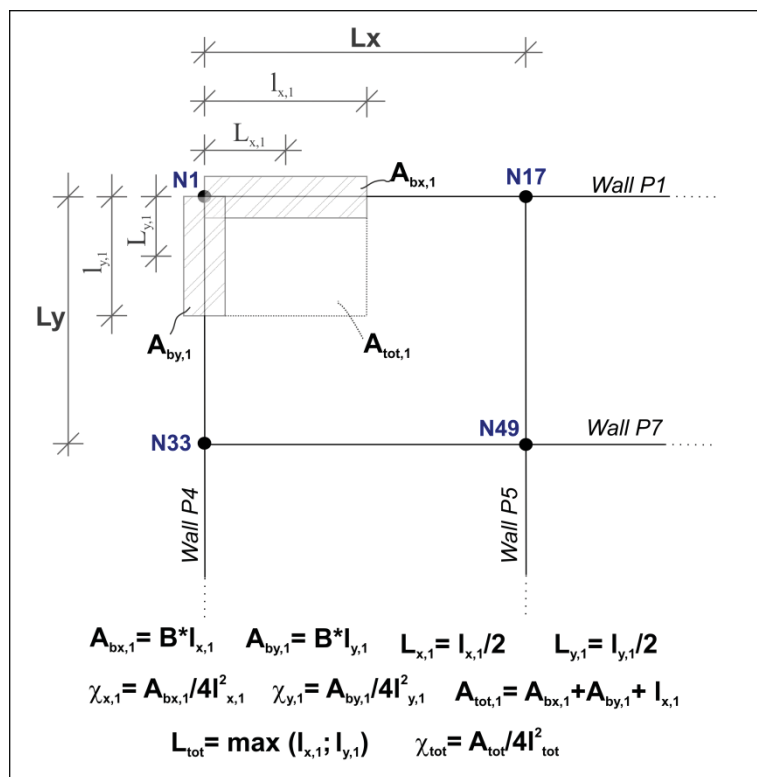


Figure 8.5 Example of calculation of the soil-foundation stiffness using the model proposed by Gazetas, 1991.

The choice of different mechanical properties of the masonry walls and different soil types on which the building resting on led to define ten different soil-foundation-structural models. In Phase II, each of them was subjected to differential settlements (Figure 8.4) and their response, in terms of damage severity, was classified on the basis of the reaching of a certain damage limit state (LSi). The numerical simulation, as above

mentioned, was performed via the FME method by adapting the TREmuri software, in which the differential settlement was applied at the base of the foundation system (with a magnitude progressively increasing from 0 to 50 cm) subjected to a given deformation mode. In particular, four displacement patterns were considered for analysis purposes (Figure 8.6).

The first two cases (Figure 8.6a and b) allow investigating the building behaviour when the differential settlement affects the terminal part of the walls. Since the 3D behaviour of the building has to be investigated, the displacement was applied with a bi-linear trend and a maximum value in the left (Figure 8.6a) and right (Figure 8.6b) corner since the building model at hand does not presents symmetrical openings at left and right respect to an central axis in the y-transversal direction. The third and fourth deformation modes (Figure 8.6c and d) were taken into account in order to examine the building response when the differential settlement affects the middle part of the walls according to a sagging (Figure 8.6c) or hogging (Figure 8.6d) deformation mode.

An example of the simulation results, in terms of damage evolution exhibited by the masonry macro-elements (piers and spandrels) with references to the wall P1 of the building M1 resting on medium/hard clay (S1\_2), is represented in Figure 8.7 for the four considered deformation modes and maximum settlement magnitudes equal to 0, 12.5, 25 and 50 cm. This analysis was performed for all the walls of the building model, for the ten considered soil-foundation-structural models, each of them subjected to four deformation modes for a total of forty simulations. The results of all simulations are reported in Appendix C.

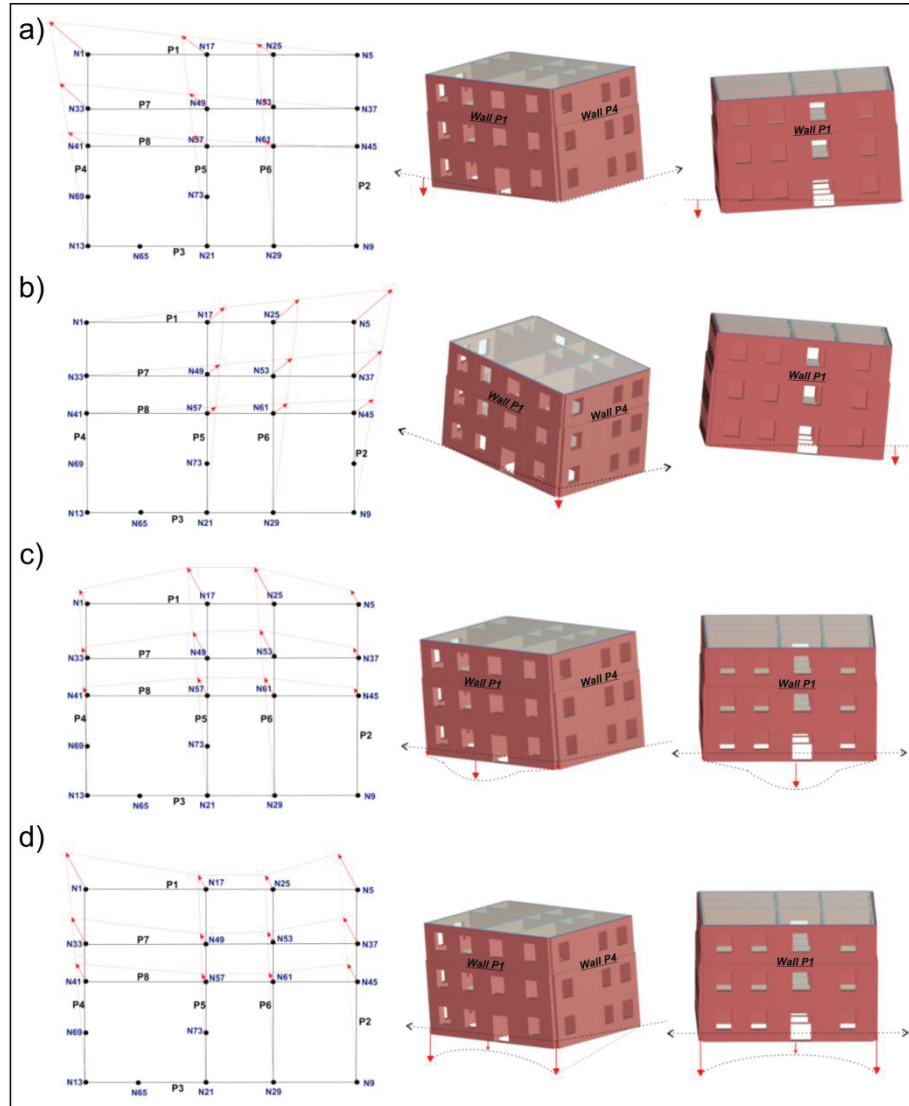


Figure 8.6 3D view of the structure and layout of the imposed differential settlements at the foundation level for the four considered deformation modes: a) bilinear left; b) bilinear right; c) sagging; d) hogging.

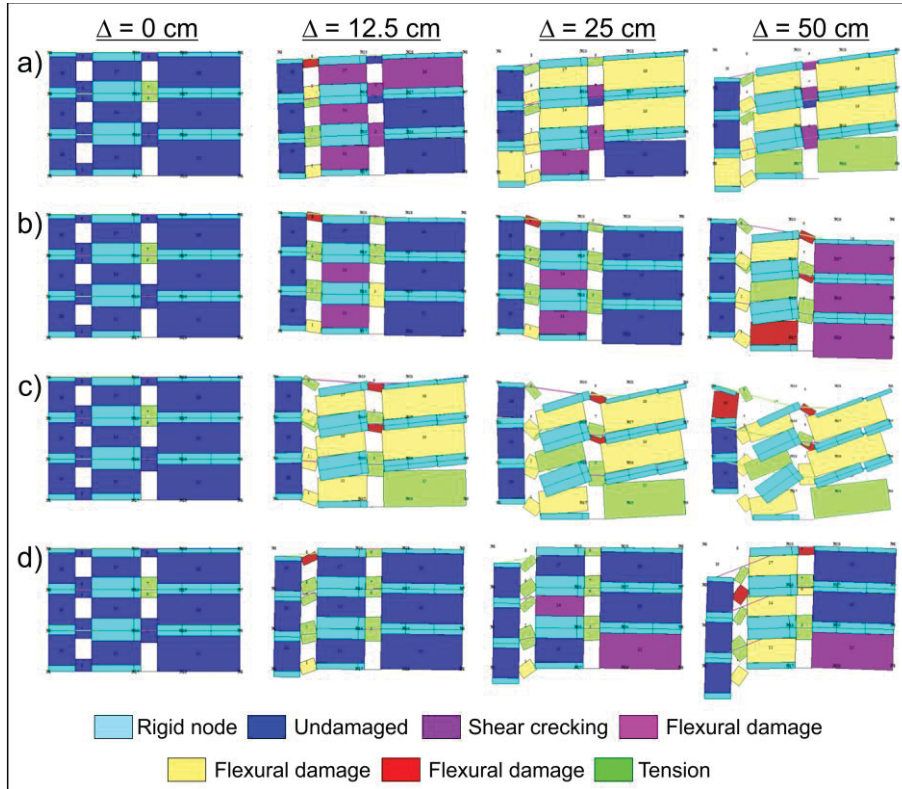


Figure 8.7. Damage evolution of the wall P1 to the building M1 resting on medium/ hard clay (S1\_2), during the progressive increase of the differential settlements from 0 to 50 cm for different deformation modes: a) bilinear left; b) bilinear right; c) sagging; d) hogging.

Whit reference to the example showed in Figure 8.7, the magnitude related to 0 cm is representative of the starting condition (gravity loads only) when the building is not subject to any displacement; then, the differential settlement is linearly increased at each step. As it possible to see, for an equal imposed differential settlement ( $\Delta$ ) magnitude (or intensity), a different structural response is exhibited by the wall according to the different deformation modes. In all cases, when only the gravity load is applied, most of the structural elements are undamaged. Nevertheless, two of the middle panels (spandrels) are unexpectedly in tension (green color), probably due to some limitations of the software. For a  $\Delta = 12.5$  cm, many pier elements present shear cracking (purple color) for the deformation mode bilinear left (Figure

8.6a) in comparison to the bilinear right (Figure 8.6b); moreover, they reached a shear failure (yellow color) for the sagging deformation mode (Figure 8.6c), while are still all undamaged (blue color) for the hogging configuration (Figure 8.6d). In all deformation modes, many of the spandrel elements presents shear cracking and shear failure or are only in tension; the bending failure is first reached at the third storey (red color) for the bi-linear (left and right) and hogging configurations while, in the sagging deformation mode, this happen contextually at second and third storeys. When  $\Delta$  increases, as expected, the damage layout of the wall also increases but not in a similar manner for the different considered deformation modes, as it is possible to see in Figure 8.6 for values of  $\Delta$  equal to 25 and 50 cm.

As shown in Figure 8.7, the outputs of the numerical simulation allow, evaluating the structural response in terms of damage severity (failure modes) suffered by each of the macro-elements that compose the building walls. Focusing on single-wall behaviours, this result could be used to define a “wall damage index” based on the number of damaged macro-elements over the total number of macro-elements composing the modelled wall.

For the purposes of this PhD Thesis, in order to investigate the response of buildings subjected to differential settlements through the generation of analytical fragility curves, the results of numerical simulations were used to analyze the global behavior of the structure on the basis of the reaching of a damage limit state (LS<sub>i</sub>). To this end, five limit states (LS1 = slight; LS2 = moderate; LS3 = extensive; LS4 = very heavy; LS5 = collapse) were considered.

The thresholds of each of them were determined by adapting a well-tested approach proposed in the seismic field, based on the the definition of the maximum drift ratios values. Indeed, in earthquake engineering, the thresholds of the damage limit states – reached by a masonry building subjected to an earthquake – can be determined according to the equations proposed by the RISK-UE project (Milutinovic and Trendafiloski, 2003) on the basis of the pushover curve. These relations provide a correlation between the yield ( $d_y$ ) and ultimate ( $d_u$ ) displacement in the pushover curve and the EMS-98 (Grunthal, 1998) damage scale.

A similar approach was adopted in this case, considering the scheme shown in the Figure 8.8a.

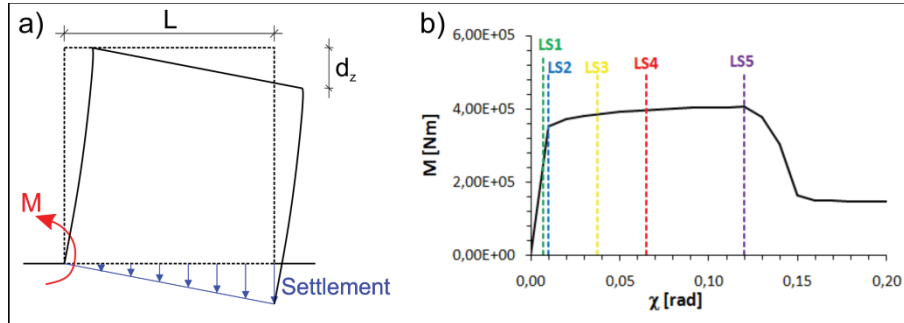


Figure 8.8. a) scheme of the drift ratio b) Moment-Curvature relationship.

Since, the masonry walls are subject to a displacement pattern that occur in the vertical direction, the drift was defined as the ratio between the displacement  $d_z$  that occurs at the head of the wall due to the settlement imposed at the foundation level and the length  $L$  of the wall. The values of the drift ratios, which corresponds to the reaching of a certain limit state (LS<sub>i</sub>), were obtained by drawing the relationship between the moment ( $M$ ) and the curvature ( $\chi$ ) for each value of the imposed settlement (Figure 8.8b), using the same equations proposed in the seismic field (Milutinovic and Trendafiloski, 2003).

In particular, as reported in Table 8.3, the thresholds of drift ratios (in percentage) for each considered limit state were established using the  $d_z$  values corresponding to  $M$  and  $\chi$  values associated to the settlement applied at foundation level.

Table 8.3. Thresholds of the damage limits states

LS	M [Nm]	$\chi$ [rad]	$d_z$ [cm]	Drift[%]
LS1	245899	0.007	0.008	0.0013
LS2	351284	0.010	0.011	0.0019
LS3	364880	0.038	0.044	0.0073
LS4	378476	0.065	0.076	0.0127
LS5	405667	0.120	0.141	0.0235

With reference to each of the examined models and for a given value of the differential settlement, the computed drift values were compared to the thresholds reported in Table 8.3 in order to individuate the limit state (LS<sub>i</sub>) reached by the building.

In the Phase III, this information was used to derive the fragility curves. In particular, similarly to the empirical approach, the curves were generated using a cumulative log-normal distribution function (Fotopoulou and Pitilakis. 2013a,b; Mavrouli et al. 2014; Negulescu et al. 2010, 2014; Peduto et al., 2016a,b, 2017; Saeidi et al. 2009, 2012):

$$P(\text{Damage} \geq \text{LS}_i | \Delta) = \Phi \left[ \frac{1}{\beta} \ln \left( \frac{\Delta}{\bar{\Delta}} \right) \right]$$

where the probability  $P(\bullet)$  of reaching or exceeding a particular damage limit state (LS<sub>i</sub>) is related to the magnitude of the selected intensity parameter (i.e. the differential settlement  $\Delta$ ).

### 8.3 RESULTS

The fragility curves were derived for the studied masonry building according to the procedure shown in Figure 8.4. Each curve, providing the conditional probability of reaching or exceeding a specific damage limit state (LS1 = slight; LS2 = moderate; LS3 = extensive; LS4 = very heavy; LS5 = collapse) for a given differential settlement (ranging from 0 to 50 cm in this application), was obtained by counting – for different values of imposed  $\Delta$  – the number of situations, out of the total, which led to the reaching of the  $i$ -th limit damage state (LS<sub>i</sub>); the assumed probabilistic model was the cumulative log-normal distribution function. A total of forty cases were considered, according to the range of values fixed for the mechanical properties of the masonry walls (M1 and M2), and the soil type on which the building is founded (S1, S1\_1, S1\_2, S2\_1, S2\_2) along with the deformation mode of the shallow foundation system (bilinear left and right, sagging and hogging mode of deformation). The parameters (median and standard deviation) of all computed fragility functions are summarized in Table 8.4.

It is worth highlighting that – differently from the empirical approach where the damage severity levels is related to crack patterns exhibited by the building façades at the time of their inspection during field surveys, neglecting information (if any) on the damage severity evolution over the

time – the numerical approach allows following the damage severity evolution starting from an initial condition in which the superstructure is undamaged. Accordingly, it is possible to estimate the value of the intensity parameter causing the transition from a certain damage limit state to the next one, with a consequent reduction of the uncertainties inherent to fragility curves.

In order to highlight the role played by the deformed shape of the shallow foundation system on the reaching of damage limit states, Figure 8.9 shows the fragility curves generated for both type of buildings M1 (Figure 8.9a and b) and M2 (Figure 8.9c and d) resting on S2\_1 soil with reference to given deformation modes. In particular, since the buildings do not present a symmetrical opening geometry, they exhibit a different response if the differential settlement is applied with a bi-linear deformation mode and the maximum settlement value is in the left or in the right corner. In both cases (Figure 8.9a for building M1) and (Figure 8.9c for building M2), for a given differential settlement, the probabilities of reaching or exceeding a damage limit state (from LS1 to LS5) are higher when the buildings are subjected to a “bilinear left” deformation mode. This different behaviour can be linked to the presence of more openings at the left side of the building (Figure 8.6a) which produce a weakening of the walls and, consequently, a less capacity to resist at bending and shear strains induced by settlements.

A different behaviour can also be appreciated when the differential settlement affects the middle part of the walls according to a sagging or a hogging mode of deformation. Both buildings M1 (Figure 8.9b) and M2 (Figure 8.9d) show a less resistance and, consequently, a higher probability of reaching or exceeding – for a given value of the imposed differential settlement – a certain limit state  $LS_i$ , when they are subjected to a hogging mode of deformation. This result is in agreement with the observations of Burland et al. (1977) (Section 3.2). Indeed the authors experimentally observed that, for a given magnitude of the relative deflection, a brick wall exhibits crack patterns that in hogging are much wider than in sagging.

Similar responses (trends of the fragility curves) are observed when the masonry buildings (both M1 and M2) are founded on the other soil types considered in the analyses.

This Figure 8.10 and 8.11 show the fragility curves (for each considered damage limit state  $LS_i$ ) generated for the masonry buildings M1 and M2 for given mechanical properties of the soil type and deformation modes.



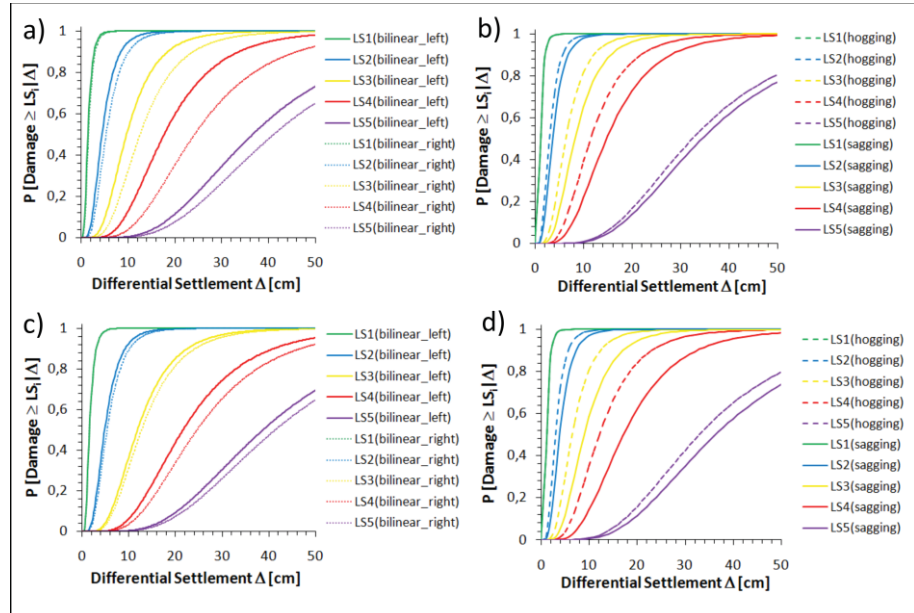


Figure 8.9. Fragility curves for masonry building resting on S2\_1 (medium/hard clay): M1 affected by differential settlement with a) bilinear left/right and b) sagging/hogging deformation modes; M2 affected by differential settlement with c) bilinear left/right and d) sagging/hogging deformation modes.

It is worth to observe that, in the case of a bi-linear deformation mode with maximum settlement in the left corner, the building M2 shows, for a given value of the differential settlement, probabilities of reaching or exceeding a certain damage limit state lower than those of building M1 (Figure 8.10b,c,d,e). Conversely, these differences are not observed in the case where the buildings are subjected to a deformation mode with a maximum settlement in the right corner (Figure 8.10a,b,c,d and e). Similar considerations can be done when the deformation mode is in sagging or hogging (Figure 8.11). In fact, also in such cases, the higher mechanical resistance offered by the building M2 plays an important role on the building response – for all considered soil types – when the sagging mode of deformation is taken into account; while only small differences can be appreciated for the curves related to LS4 and LS5 damage limit states when the hogging mode of deformation is imposed and the building model rests on soils classified as S2\_2, S3\_1 and S3\_2 (Figure 8.11c,d and e). The peculiarities of observed behaviours are reflected in the median values pertaining to the fragility curve functions (Table 8.4).

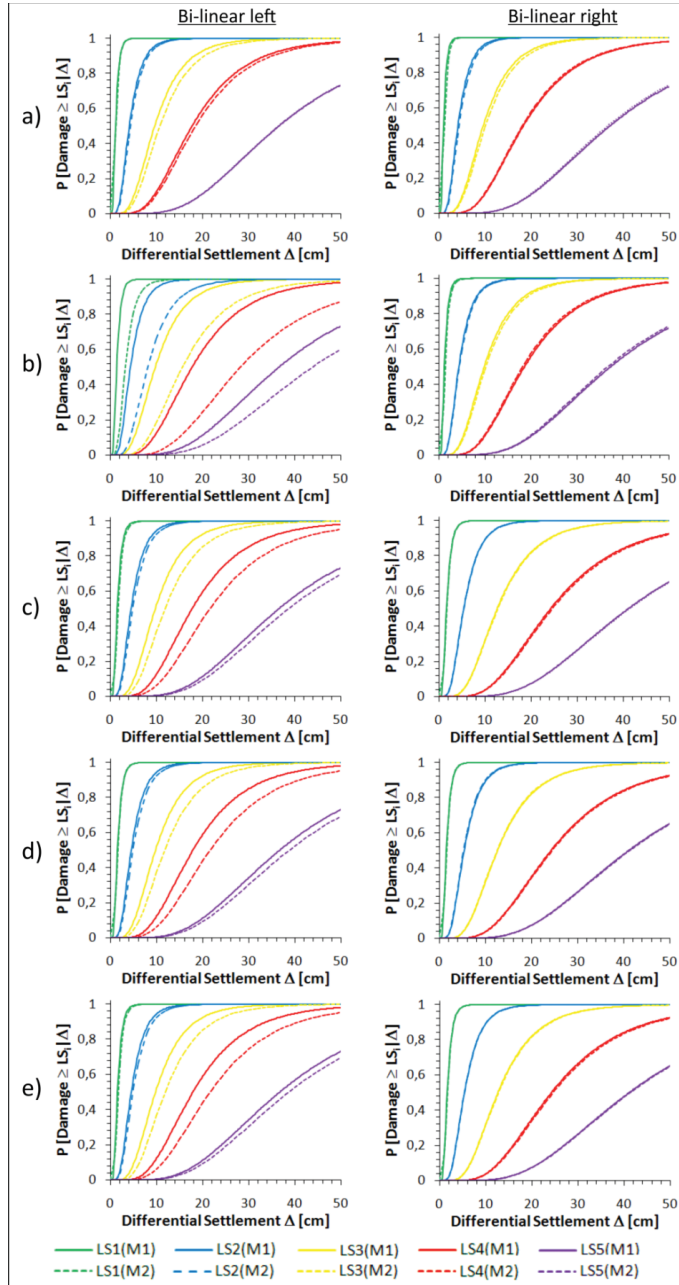


Figure 8.10. M1 vs M2 fragility curves for bi-linear displacement patterns (left and right) on different soil types: a) S1= soft soil; b) S2\_1= soft clay; c) S2\_2= medium/hard clay; d) S3\_1= loose sand; e) S3\_2= dense sand.

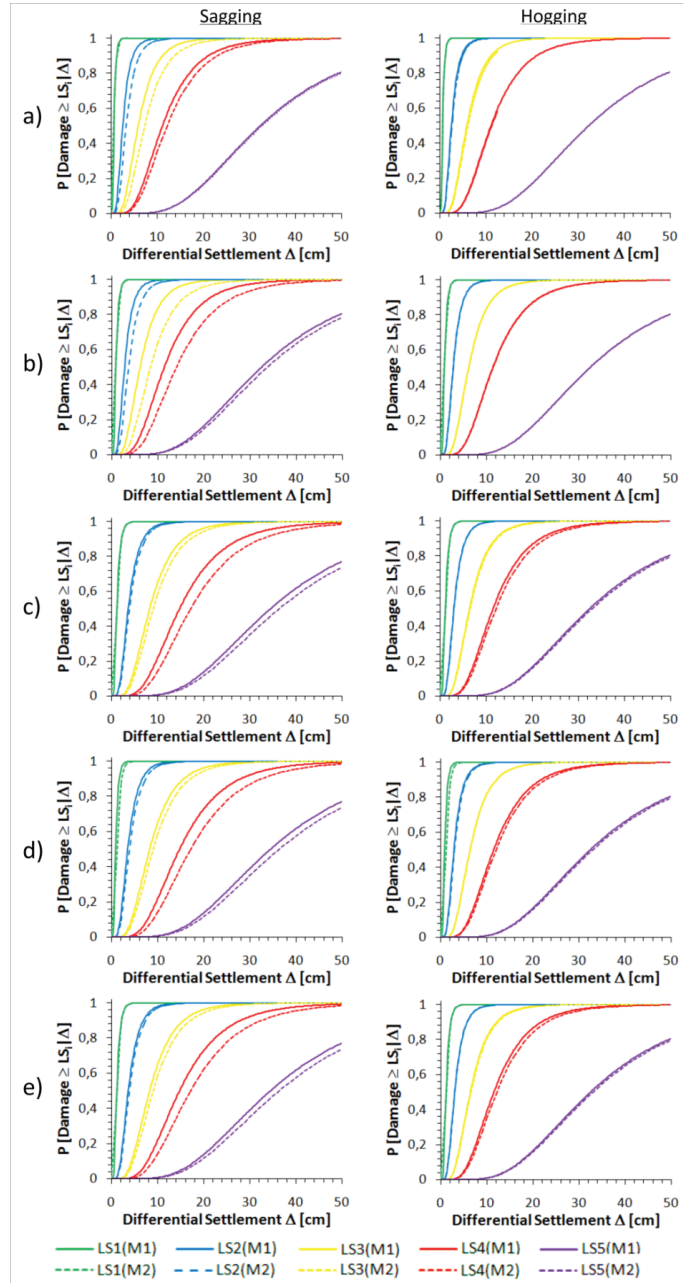


Figure 8.11. M1 vs M2 fragility curves for sagging and hogging displacement patterns on different soil types: a) S1= soft soil; b) S2\_1= soft clay; c) S2\_2= medium/hard clay; d) S3\_1= loose sand; e) S3\_2= dense sand.

**Table 8.4. Median  $\mu$  and standard deviation  $\beta$  parameters of the lognormal distribution function used for each damage limits states and distinguished according to the deformation mode and soil type.**

Damage state	Soil type	$\beta$	$\mu$ [cm]							
			bi-linear		bi-linear		sagging		hogging	
			M1	M2	M1	M2	M1	M2	M1	M2
LS1	S1	0.5	1.13	1.13	1.00	1.13	0.63	0.63	0.63	0.63
	S2_1	0.5	1.38	3.25	1.25	1.38	0.88	0.88	0.88	0.88
	S2_2	0.5	1.50	1.63	1.63	1.63	1.13	1.13	1.13	1.13
	S3_1	0.5	1.50	1.50	1.50	1.50	0.88	1.13	0.88	1.13
	S3_2	0.5	1.50	1.63	1.63	1.63	1.13	1.13	1.13	1.13
LS2	S1	0.5	4.13	4.38	4.13	4.38	2.50	3.25	2.50	2.63
	S2_1	0.5	4.38	8.13	4.38	4.50	2.75	3.63	2.75	2.75
	S2_2	0.5	4.50	4.88	5.38	5.38	3.63	3.88	3.00	3.00
	S3_1	0.5	4.50	4.88	5.38	5.25	3.50	3.88	2.88	3.00
	S3_2	0.5	4.50	4.88	5.38	5.38	3.63	3.88	3.00	3.00
LS3	S1	0.5	9.63	10.7	9.63	10.1	5.88	7.25	5.88	6.13
	S2_1	0.5	9.75	15.6	9.88	10.2	6.13	8.38	6.13	6.13
	S2_2	0.5	9.75	11.8	12.6	12.7	8.25	9.00	6.38	6.50
	S3_1	0.5	9.75	11.7	12.6	12.5	8.25	9.00	6.38	6.38
	S3_2	0.5	9.75	11.8	12.6	12.7	8.25	9.00	6.38	6.50
LS4	S1	0.5	17.7	18.5	18.3	18.1	11.1	12.1	11.1	11.2
	S2_1	0.5	17.7	28.2	18.6	18.2	11.3	14.0	11.3	11.3
	S2_2	0.5	17.7	21.6	24.2	24.6	14.7	17.1	11.5	12.1
	S3_1	0.5	17.8	21.6	24.2	24.5	14.7	17.1	11.5	12.0
	S3_2	0.5	17.8	21.6	24.2	24.6	14.7	17.1	11.5	12.1
LS5	S1	0.5	36.6	36.5	37.2	36.7	32.3	32.7	32.3	32.3
	S2_1	0.5	36.6	43.8	37.3	36.7	32.5	33.7	32.5	32.5
	S2_2	0.5	36.6	38.7	41.1	41.3	34.5	36.3	32.5	33.0
	S3_1	0.5	36.7	38.8	41.1	41.3	34.5	36.3	32.5	33.0
	S3_2	0.5	36.7	38.7	41.1	41.3	34.5	36.3	32.5	33.0

The results of the numerical analysis also allowed investigating the role played on the structural response by the soil type. In this regard, Figures 8.12 and 8.13 show, respectively, the fragility curves generated for M1 and M2 buildings under given deformation modes of the shallow foundation system for different soils types.

For a given building type, small differences between the fragility curves can be noticed passing from a soil type to another one; this observation could be objectivised considering that the numerical analysis was carried out by imposing the magnitude of  $\Delta$  values that, independently of the soil type, were progressively increased from 0 to 50 cm. Anyway, the fragility curves are still dependent on the deformation mode. Indeed, especially for the cases where the deformation mode is bi-linear with a maximum settlement value in the right corner and in sagging configuration, passing from soft soil (S1) to soft clay (S2\_1) or medium/hard clay (S2\_2), the probability of reaching or exceeding a certain damage limit state for a given differential settlement progressively decreases; whereas the influence of sandy soils (either loose or dense) seems less relevant.

Generally, the observed differences could relate to the soil-foundation interaction that influences the stress distribution in the different elements composing the superstructure and, consequently, the strain patterns whose changes are responsible of the reaching of a certain damage limit state. Moreover, the higher is the stiffness of soil the lower is the building damageability; or, similarly, a higher value of the differential settlement – for a given deformation mode – must be imposed at the foundation level of a building type in order to reach a certain damage limit state.

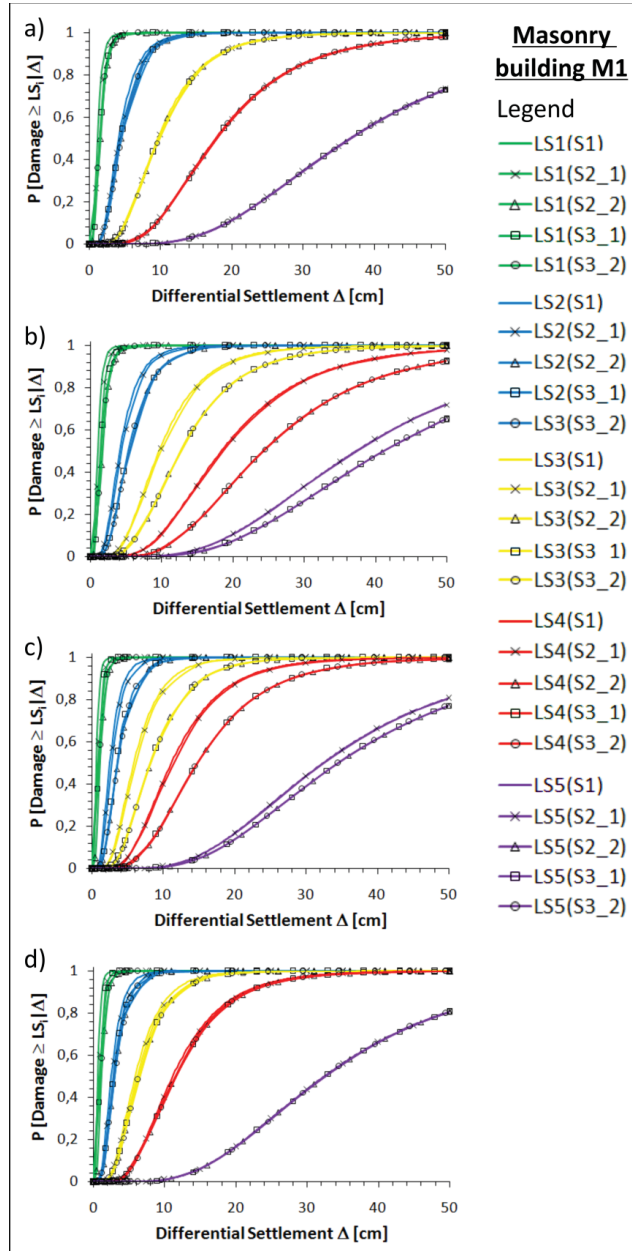


Figure 8.12. Comparison between the fragility curves obtained for M1 building resting on different soils types subjected to different deformation modes: a) bilinear left; b) bilinear right; c) sagging and d) hogging. Legend:  $LS_i$  =  $i$ th damage limit state; S1= soft soil; S2\_1= soft clay; S2\_2= medium/hard clay; S3\_1= loose sand; S3\_2= dense sand.

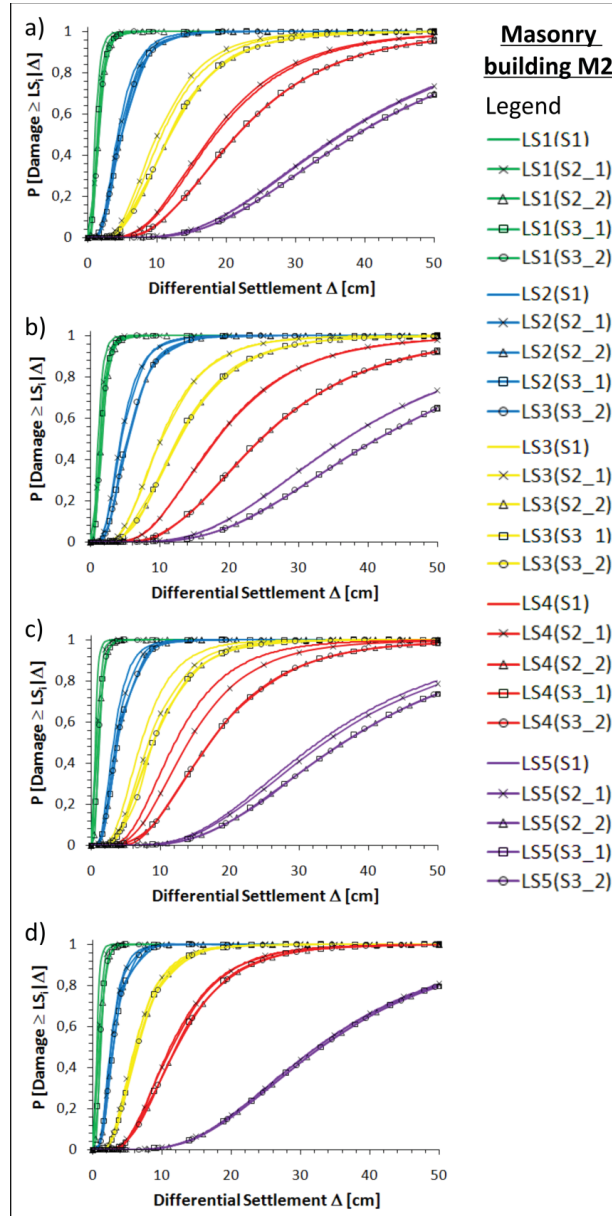


Figure 8.13. Comparison between the fragility curves obtained for M2 building resting on different soils types subjected to different deformation modes: a) bilinear left; b) bilinear right; c) sagging and d) hogging. Legend: LSi = *i*th damage limit state; S1= soft soil; S2\_1= soft clay; S2\_2= medium/hard clay; S3\_1= loose sand; S3\_2= dense sand.

## 9 DISCUSSION AND CONCLUSIONS

This PhD Thesis was focused on the development of procedures aimed at generating fragility and vulnerability curves of buildings in areas affected by slow-moving landslides and subsidence phenomena.

The work first addressed: *i*) a literature review on the main features of the analyzed phenomena and their consequences in urban areas (Chapter 2); *ii*) the relevance of the consequence analysis for the quantification of the risk to the exposed buildings with the main damageability criteria adopted in engineering practice along with the newly proposed probabilistic approaches for the analysis and prediction of the damage to buildings (Chapter 3); *iii*) the principles and characteristics of the DInSAR techniques used to obtain the magnitude of the intensity parameter related to slow-moving landslides and subsidence phenomena, highlighting their potential and limitations (Chapter 4).

Then, based on this background and bearing in mind the main goal to be pursued, innovative procedures for the generation, via empirical and numerical approaches, of fragility and vulnerability curves were proposed (Chapter 5). In particular, the empirical procedures based on the joint use of data coming from SAR images processed via DInSAR techniques and damage surveys on buildings, were tested on well-documented case studies dealing with subsidence phenomena (Chapter 6) in The Netherlands and slow-moving landslides (Chapter 7) in Calabria region (southern Italy). Finally, the numerical analysis (Chapter 8) was carried out on a masonry building model subjected to differential settlements and, in this regard, the role played by some factors on the achievement and distribution of a given damage severity level (limit state) for a given value of intensity parameter was investigated.

As far as the analysis of subsidence phenomena is concerned, the results of the proposed methodology highlight the potential of an integrated multi-scale approach for the analysis of the building response to ground settlements by combining information on the subsoil setting, PSI data and the results of damage surveys to buildings. In particular, the preliminary analysis carried out at *medium scale* (Section 6.2.1) allows confirming the role played by soft soils in predisposing the ground settlement occurrence in the selected urban area in The Netherlands.



Although in the analyzed region monitoring data are properly archived in well-organized databases freely accessible to end-users, the availability of such a distributed displacement dataset as PSI data provides an unprecedented overview of the problems that the Dutch built-up environment usually has to face. The good match between the soft soil thickness map and the cumulative settlement map enables to zone the areas that are most prone to ground surface lowering and, thus, where damages to the built-up environment are most likely to be found or expected.

At *large scale* (Section 6.2.2), the preliminary identification of different scenarios can be helpful for authorities in charge of land management to focus the attention on either structures or infrastructures (including utilities) for what concerns settlement-related consequences. Then, the relationship retrieved between cause (settlements) and effect (damage level) with reference to building aggregates provides an overview on their behavior depending on the foundation typology. In this regard, the results obtained in the study area underline that the equivalent damage recorded to building aggregates does not exceed the slight level (D2) for both shallow and deep foundations. These latter, while usually being able to reduce absolute settlements, suffer from higher settlement gradient values just in correspondence of the sections where the highest levels of building damage severity are recorded. This circumstance can be related to the peculiar foundation type of the examined buildings that are located in the study area. These buildings, built up from the beginning of the 19th century to the 1980s, present foundations consisting of both wooden and reinforced concrete piles. For the wooden piles, decay effects of the wood induced by both fungi and bacteria, which inhibit capability of piles to reduce settlements, may cause loss of functionality of some piles with the onset of localized settlement gradients and consequent damage on the superstructure. The same problems may occur on buildings founded on reinforced concrete piles in highly compressible soils which are not designed to respond to effects such as the negative skin friction.

As for the analysis at *detailed scale* on 310 single buildings in the neighborhood of Schiedam municipality (Section 6.2.3), although the damage severity recorded during the survey campaign proved not to be as high as to cause concern for structure stability – this seems to be confirmed also from the low values of settlements and settlement gradients most likely related to secondary (creep) consolidation processes

developing over very long times in the underlying soft soils – the performed analysis allowed to derive the empirical relationships between differential settlements suffered by the superstructures and relative damage levels. This information was, then used to derive the fragility curves for single buildings in the study area for both shallow and deep foundations. It is worth underlining that the damage recorded on many surveyed structures – although of low severity at present – highlighted a structural suffering due to ground movements. This requires continuous settlement monitoring in order to implement appropriate mitigation strategies before the damages increase. In this regard, the obtained fragility curves can represent a powerful empirical tool to predict the damage level that is likely to be expected for both categories of buildings (i.e. with shallow and deep foundations) located in the study area. Considering that the investigated structural and foundation typologies well represent the Dutch urban fabric, the obtained empirical fragility curves can also be exported to buildings in other similar subsidence-affected areas.

Anyway, as mentioned in the Section 6.2.3, the correct and reliable use of an empirical tool needs carrying out proper calibration and validation phases. In this regard, the comparison between the empirical fragility curves derived for the Schiedam municipality with the ones generated for two other densely urbanized municipalities located in the northern (Zaanstad) and southern (Dordrecht) part of The Netherlands (Section 6.3), show a good agreement for buildings having the same structural typology and foundation type. This evidence allowed merging the information in single datasets, distinguished for foundation type (shallow or piled), useful to generate fragility curves that are statistically more representative of the response – in terms of expected damage probability – of analyzed masonry buildings to a given differential settlement. Then, for the sample including 344 single masonry buildings founded on wooden piles with damage levels spanning from D0 to D5, an empirical vulnerability curve – which is representative of the damage severity level that can be averagely expected on the considered buildings for a given value of the differential settlement – was obtained.

With reference to the vulnerability analysis of buildings affected by slow-moving landslides, the application of the proposed procedure at *large scale* on two study areas (Lungro and Verbicaro municipalities) of Calabria region (southern Italy) showed the potential of an empirical approach based on the joint use of damage surveys and remote sensing data for

the generation of tools aimed at analyzing and predicting the damages suffered by structures interacting with the above phenomena. Indeed, although the potential of DInSAR data use in building damage assessment has been already demonstrated in the scientific literature, the proposed procedure for the analysis of building vulnerability to slow-moving landslides allowed – for the first time – the retrieval of empirical relationships between the damage severity levels and the selected DInSAR-derived intensity parameter (i.e., differential settlement) and their use for the generation of empirical fragility and vulnerability curves. The results obtained for the case study of Lungro municipality (Section 7.2.4) show that the probability of reaching or exceeding a certain damage level (fragility curves) or the damage degree averagely expected (vulnerability curve) by masonry buildings, increases as the intensity parameter (i.e., differential settlement) increases. Similar results were obtained for the case study of Verbicaro municipality (Section 7.3.4) where the cause-effect relationships as well as the empirical fragility curves were retrieved also for reinforced concrete buildings. The joint use of these empirical tools with a continuous monitoring of the intensity parameter, which can be achieved using conventional (e.g., inclinometers, GPS, topographic leveling) or innovative (DInSAR techniques) monitoring systems, can allow the analysis of the damage suffered by buildings interacting with slow-moving landslides along with its prediction, helpful for authorities in charge of slow-moving landslide risk mitigation.

However, it must be observed that whereas the differential settlement is a parameter that well represents the intensity of subsidence phenomena (the related ground surface displacements mainly occur in the vertical direction), in the case of slow-moving landslides – where buildings might be located in different position with respect to the affected areas – the use of the above parameter is not straightforward. In this regard, also other parameters – such as angular distortion (Skempton and MacDonald 1956), deflection ratio (Burland 1995) and horizontal strain (Boscardin and Cording 1989) – should be considered, without neglecting the role of tilt (i.e. rigid body rotation), which a building might experience, in concurring to the attainment of serviceability/ultimate limit states. In particular, the availability of DInSAR data acquired on both ascending and descending orbits (condition that for landslide applications is not common due to SAR acquisition geometry constraints), allows – via a combination, where possible, of the datasets –

the retrieval of the horizontal displacements that could play a relevant role in building damaging (Boscardin and Cording 1989; Burland et al. 2004). Furthermore, enlarging the dataset would allow further deepening concerning different factor presiding over the damage occurrence such as, among others, the location of the building within the landslide-affected area (Corominas et al. 2014), issue that was partially analyzed in the case study of Verbicaro (Section 7.3.4), as well as the foundation typology, so as to derive a more complete dataset of fragility/vulnerability curves.

The applicability/exportability of the obtained results, although site-specific, could be significant if one considers that most of the small villages in Italian southern Apennines exhibit similar urban fabric and structural typology as the ones considered in this study. In particular, widening the sample of analyzed buildings in similar geological contexts would allow a proper calibration and validation of the fragility/vulnerability curves.

As for the numerical analysis, the application carried out on a masonry building model subjected to differential settlements allowed investigating – at the single building scale – the role played by some factors (such as: the mechanical proprieties of both the media simulating the behavior of the material composing the superstructure and the soil type, the deformation mode of the shallow foundation system) on the achievement and distribution of a given damage severity level (or limit state) for a given value of the intensity parameter. The obtained information, along with the one gathered from the empirical analysis, allows going in-depth with issues concerning the proper use of empirical and/or numerical approaches and the quantification of the model uncertainties that can support a better understanding of the different aspects concurring to the generation of building damages.

First of all, the results of the numerical analysis (Section 8.3) show that, independently of the mechanical proprieties characterizing the masonry walls of the superstructure and the soil type, the building response in terms of damage severity levels (limit states) and distribution (trends of the fragility curves) changes according to the deformation mode of the foundation system. In particular, as expected, the probabilities of reaching or exceeding a limit state (from LS1 to LS5) are higher when the building is subjected to a “bilinear left” deformation mode instead of a “bilinear right”. Indeed, the presence of more openings on the left side of the building, with respect to a central axis in the y-transversal

direction, brings about a weakening of the walls and, consequently, less capacity of resisting to bending and shear strains induced by settlements; moreover, the damageability increases passing from the “sagging” to the “hogging” mode of deformation.

Considering that the numerical analysis was carried out by controlling the magnitude of differential settlements – which, independently of the soil type, were progressively increased from 0 to 50 cm – the properties of the soil model interacting with the foundation system influenced the development of the strain patterns and the consequent cracking suffered by the bearing walls. This effect, which in turn determined a different response of the building in terms of distribution (trends) of the fragility curves, is still dependent of the imposed deformation mode.

In conclusion, the results achieved in this PhD Thesis demonstrated the huge potential of fragility and vulnerability curves generated via empirical approaches as tools for the analysis – at *medium* and *large scale* – of the damage to buildings located in areas affected by slow-moving landslides and subsidence phenomena. Powerful tools that, once even further validated, might be valuably used for forecasting purposes, thus facilitating the authorities in charge of land-use planning/urban management in either selecting areas suitable for urbanization or addressing restoration and adaptation policies. This goal can be achieved at more affordable costs than those associated to the use of conventional monitoring techniques over a wide number of exposed buildings.

Moreover, the results of both empirical and numerical analyses at *detailed* (single building) *scale* – although not always directly comparable due to the macroscopic differences between the “empirical limit states” (normally established on the basis of a damage classification system only requiring a visual inspection of crack patterns exhibited by building’s façades) and the “numerical limit states” (usually associated to the maximum values of drift ratios in the case of masonry structures or strain limits of steel and concrete materials in the case of reinforced concrete buildings) – allow addressing relevant issues on the generation of building damages, with remarkable relapses on planning the most suitable risk mitigation strategies as well as on the design of countermeasures based on a performance-based approach.

## REFERENCES

- Agostini A., Tofani V., Nolesini T., Gigli G., Tanteri L., Rosi A., Cardellini S., Casagli N. (2013). A new appraisal of the Ancona landslide based on geotechnical investigations and stability modelling. *Quarterly Journal of Engineering Geology and Hydrogeology*, 1-10, ISSN:1470-9236.
- AHN2 (2016). Actueel Hoogtebestand Nederland 2. <https://www.pdok.nl/nl/atomfeed/ahn2-05-meter-maaiveld-raster-opgevuld>, in Dutch (accessed 28.10.2016).
- Alexander D., (1986). Landslide damage to buildings. *Environmental Geology and Water Science*, 8: 147-151.
- Allen D.R. and Mayuga M.N. (1969). The mechanics of compaction and rebound, Wilmington oil field, Long Beach, California, USA. *Land Subsidence*, Vol. 2, Internat. Assoc. Sci. Hydrology Pub, 89, Tison L. J. (Eds), pp. 410-422.
- Almagia` R. (1910). Studi geografici sulle frane in Italia. *Memorie Società Geografica Italiana*, 14(2):431, (in Italian).
- Amatruda G., Bonnard Ch., Castelli M., Forlati F., Giacomelli L., Morelli M., Paro L., Piana F., Pirulli M., Polino R., Prat P., Ramasco M., Scavia C., Bellardone G., Campus S., Durville J.-L., Poisel R., Preh A., Roth W., Tentschert E.H., (2004). A key approach: the IMIRILAND project method. *In: Identification and mitigation of large landslide risks in Europe*. Advances in Risk Assessment. Imiriland Project, Balkema – Leiden, pp. 13-43.
- Amelung F., Galloway D.L., Bell J.W., Zebker H.A., Laczniak, R.J. (1999). Sensing the ups and downs of Las Vegas: InSAR reveals structural control of land subsidence and aquifer system deformation. *Geology*, 27(6):483-486.
- Amodio Morelli L., Bonardi G., Colonna V., Dietrich D., Giunta G., Ippolito F., Liguori V., Lorenzoni S., Paglionico A., Perrone V., Piccarreta G., Russo M., Scandone P., Zanetti-Lorenzoni E., Zuppetta A. (1976.) L'Arco Calabro-Peloritano nell'orogene appenninico-maghrebide. *Memorie della Società Geologica Italiana*, 17:1-60, (in Italian).

- Angeli M.G., Gasparetto P., Pasuto A. and Silvano S. (1989). Examples of landslides instrumentation (Italy). *Proceedings of the 12th International Conference on Soil Mechanics and Foundation Engineering*, Rio de Janeiro, Vol. 3, pp. 1531-1534.
- Antronico L., Borrelli L., Coscarelli R., Gullà G. (2014). Time evolution of landslide damages to buildings: the case study of Lungro (Calabria, southern Italy). *Bulletin of Engineering Geology and the Environment*, 74:47-59.
- Antronico L., Borrelli L., Peduto D., Fornaro G., Gullà G., Paglia L., Zeni G. (2013). Conventional and innovative techniques for the monitoring of displacements in landslide affected area. In: Margottini C., Canuti P, Sassa K (Eds.) *Landslide science and practice – Early warning, instrumentation and monitoring*. Springer-Verlag, – Vol. 2, pp. 125-131.
- Arnaud A., Adam N., Hanssen R., Inglada J., Duro J., Closa J., Eineder M. (2003). ASAR ERS Interferometric Phase Continuity. In: *Proceedings International Geoscience and Remote Sensing Symposium*, Toulouse, 21–25 July, pp. 1133–1135.
- Arangio S., Calò F., Di Mauro M., Bonano M., Marsella M., Manunta M. (2013). An application of the SBAS-DInSAR technique for the assessment of structural damage in the city of Rome, in *Structure and Infrastructure Engineering: Maintenance, Management, Life-Cycle Design and Performance*, Vol. 10, pp. 1469-1483, <http://dx.doi.org/10.1080/15732479.2013.833949>.
- Audell H.S., (1996). Geotechnical nomenclature and classification system for crack patterns in buildings. *Environmental and Engineering Geoscience*, 2:225-248.
- Bandini A., Berry P., Boldini D. (2015). Tunnelling-induced landslides: The Val di Sambro tunnel case study. *Engineering Geology*, Vol. 196:71-87.
- Barends F.B.J., Brouwer F.J.J., Schröder F.H. (1995). Land subsidence. In: *Proceedings of the Fifth International Symposium on Land Subsidence, Vol. 1, The Hague, Netherlands*. IAHS Publ. 234, Wallingford, UK.
- Beeby A. W. and Miles J. R. (1969). Proposals for the control of deflection in the new unified Code. *Concrete*, 3(3):101–110.
- Bell F.G. (1994). *Fundamentals of Engineering Geology*, Blackie Academic and Professional.
- Berardino P., Fornaro G., Lanari R., Sansosti E. (2002). A new algorithm for surface deformation monitoring based on small baseline

- differential SAR interferograms. *IEEE Transactions Geoscience Remote Sensing*, 40 (11):2375–2383.
- Berardino P., Costantini M, Franceschetti G., Iodice A, Pietranera, L, Rizzo V. (2003). Use of differential SAR interferometry in monitoring and modelling large slope instability at Maratea (Basilicata,Italy). *Engineering Geology*, 68:31-51.
- Bertini T., Cugusu F., D'Elia B., Rossi-Doria M. (1986). Lenti movimenti di versante nell'Abruzzo adriatico: caratteri e criteri di stabilizzazione. *XVI Convegno Nazionale di Geotecnica*, (in Italian).
- Bianchini S., Herrera G., Mateos R.M., Notti D., Garcia I., Mora O., Moretti S. (2013). Landslide activity maps generation by means of persistent scatterer interferometry. *Remote Sensing*, 5(12):6198–6222.
- Bianchini S., Pratesi F., Nolesini T., Casagli N., (2015). Building Deformation Assessment by Means of Persistent Scatterer Interferometry Analysis on a Landslide-Affected Area: The Volterra (Italy) Case Study. *Remote Sensing*, 7:4678-4701.
- Bilgin H. and Korini O., (2012). Seismic capacity evaluation of unreinforced masonry residential buildings in Albania. *Natural Hazards Earth Systems Sciences*, 12:3753-3764.
- Bird J. F., Crowley H., Pinho R., Brommer, J. J., (2005a). Assessment of building response to liquefaction-induced differential ground deformations. *Bulletin of New Zealand Society for Earthquake Engineering*, 38(4), 20 pp.
- Bird J. F., Brommer J. J., Crowley H., Pinho R., (2005b). Modelling liquefaction-induced building damage in earthquake loss estimation. *Soil Dynamic Earthquake Engineering*, 26:15–30.
- Bhattacharya S. and Singh M.M., (1985). Development of subsidence damage criteria, final report. *Engineers International Inc. Westmont for U.S. Department of the Interior, Office of Surface Mining Reclamation and Enforcement*, pp. 229.
- Bjerrum L., (1963). Allowable Settlement of Structures. *Proceedings of the 3rd European Conference on Soil Mechanics and Foundation Engineering*, Wiesbaden, 2, Brighton, England, 135–137.
- Blahut J., Glade T., Sterlacchini S., (2014). Debris Flows Risk Analysis and Direct Loss Estimation: the Case Study of Valtellina di Tirano, Italy. *Journal of Mountain Science*, 11(2): 288-307.
- Bloch B. and Braun B. (2005). Economic assessment of landslide risks in the Schwabian Alb, Germany - research framework and first



- results of homeowners and experts surveys. *Natural Hazards Earth Systems Sciences*, 5:389–396.
- Blong R.J. (1973). A numerical classification of selected landslides of the debris slideavalanche-flow type. *Engineering Geology*, 7, pp. 99-144.
- Bonachea J., Remondo J., Díaz de Terán J.R., González-Díez A., Cendrero A., (2009). Landslide risk models for decision making. *Risk Analysis*, 29(11):1629–1643.
- Bonnard C.H., Tacher L., Beniston M. (2008). Prediction of landslide movements caused by climate change: modelling the behaviour of a mean elevation large slide in the Alps and assessing its uncertainties. In: *Chen et al (eds), Proceedings, 10th International Symposium on Landslides and Engineered Slopes*, Xi'an, China, 1:217–227.
- Booker J.R., Small J.C., Carter J.P. (1985). Prediction of subsidence caused by pumping of groundwater. In: *21<sup>th</sup> Congress of the International Association of Hydraulic Engineering and Research*, Melbourne, pp. 130-134.
- Boone S. J., (1996). Ground-Movement-Related Building Damage, *Journal of Geotechnical Engineering-ASCE*, 122(11): 886–896.
- Boscardin M. D. and Cording E. G., (1989). Building Response to Excavation Induced Settlement. *Journal of Geotechnical Engineering-ASCE*, 115:1–21.
- Brefort, T. (2011). GMES Data Access Specifications of the Earth Observation Needs Over the period 2011–2013, Commission européenne, B-1049 Bruxelles/ Europese Commissie, B-1049 Brussel – Belgium. U:nSpacedocnPolicynData policynEO data Specifications Under the Delegation AgreementnV1.8 (CR Awifs)nData Warehouse SpecificationV1 8 clean.doc.
- Buckle P., Mars G., Smale S., (2000). New approaches to assessing vulnerability and resilience. *Australian Journal of Emergency Management*. Winter, pp. 8–14.
- Bucx T.H.M., van Ruiten G., Erkens G., de Lange G. (2015). An integrated assessment framework for land subsidence in delta cities. In *Proc. LAHS, 372, Prevention and mitigation of natural and anthropogenic hazards due to land subsidence*, 485-491. Copernicus Publications.
- Building Research Establishment, (1981). Assessment of damage in low-rise buildings with particular reference of progressive foundation movement. *UK Building Research Establishment Digest*, 251, pp 8.

- Burd H. J., Houlby G. T., Augarde C. E., Liu G., (2000). Modelling tunnelling-induced settlement of masonry buildings. *Proc. Institution of Civil Engineers, Geotechnical Engineering*, 11831, 143:17–29.
- Burland J.B., Broms B.B., De Mello V.F.B. (1977). Behaviour of foundations and structures. *Proceedings of 9th International Conference SMFE – Vol 2*. Tokyo. pp. 495-546.
- Burland J. B. and Wroth C. P., (1954). Settlement of Buildings and Associated Damage. *Proceedings of the Conference on Settlement of Structures – Session V*, Cambridge, England, 611–654.
- Burland J. B., (1995). Assessment of risk of damage to buildings due to tunnelling and excavation. *Invited Special Lecture, 1st International Conference on Earthquake Geotechnical Engineering*, IS.Tokyo '95.
- Burland J. B., (2008). A case history of the failure of some silos during discharge. *International Conference on Structures and Granular Solids - From Scientific Principles to Engineering Applications*, CRC Press-Taylor & Francis Group, pp. 135-143.
- Calderhead A.I., Therrien R., Rivera A., Martel R., Garfias J. (2011). Simulating pumping-induced regional land subsidence with the use of InSAR and field data in the Toluca Valley, Mexico. *Advances in Water Resources*, 34:83–97.
- Calò F., Ardizzone F., Castaldo R., Lollino P., Tizzani P., Guzzetti F., Lanari R., Angeli M.C., Pontoni F., Manunta M. (2014). Enhanced landslide investigations through advanced DInSAR techniques: the Ivancich case study, Assisi, Italy. *Remote Sensing of Environment*, 142:69–82.
- Calò F., Calcaterra D., Iodice A., Parise M., Ramondini M. (2012). Assessing the activity of a large landslide in southern Italy by ground-monitoring and SAR interferometric techniques. *International Journal of Remote Sensing*, 33(11):3512–3530.
- Canuti P., Casagli N., Farina P., Ferretti A., Marks F., Menduni G.(2006). Analisi dei fenomeni di subsidenza nel bacino del fiume Arno mediante interferometria radar. *Giornale di Geologia Applicata*, 4:131-136, doi: 10.1474/GGA.2006-04.0-17.0145.
- Cascini L., Calvello M., Grimaldi G.M. (2010b). Groundwater Modeling for the Analysis of Active Slow-Moving Landslides. *Journal of Geotechnical and Geoenvironmental Engineering*, Vol. 136, pp. 1220-1230 - ISSN:1090-0241.
- Cascini L., Gullà G. (1992a). Analisi di dettaglio delle caratteristiche fisico meccaniche dei terreni prodotti dall'alterazione degli gneiss di

- S. Pietro in Guarano (CS). *Geologia Applicata e Idrogeologia*, Vol. XXVII, pp. 49-76, (in Italian).
- Cascini I., Gullà G. (1992b). Grado di alterazione e meccanismi di rottura nei terreni prodotti dall'alterazione degli gneiss di S. Pietro in Guarano (CS). Risultati preliminari. *CNR-IRPI, Rapporto interno, N.363*; (in Italian).
- Cascini L., Di Maio C. (1994). Emungimento delle acque sotterranee e cedimenti nell'abitato di Sarno: analisi preliminare. *Italian Geotechnical Journal*, 3:217-231, (in Italian).
- Cascini L., Ferlisi S., Fornaro G., Lanari R., Peduto D., Zeni G. (2006). Subsidence monitoring in Sarno urban area via multitemporal DInSAR technique. *International Journal of Remote Sensing*, 27:1709–1716.
- Cascini L., Ferlisi S., Peduto D., Fornaro G. (2011a). The use of DINSAR techniques to analyse ground deformations and related effects to buildings. In: *Fifth International Symposium on Deformation Characteristics of Geomaterials Seoul* (Corea del Sud), 1-3 Settembre 2011 Hanrimwon Co., Ltd. Edition. Vol.2, pp.1239-1246 ISBN:9788957082065.
- Cascini L., Ferlisi S., Peduto D., Di Nocera S., Fornaro G., Serafino F. (2007a). A Land Subsidence Study via DInSAR Technique Over Large Urbanised Areas. In: *Proceedings of the Urban Remote Sensing Joint Event.*, Paris 11–13 April, pp. 1–7. <http://dx.doi.org/10.1109/URS.2007.371877>.
- Cascini L., Ferlisi S., Peduto D., Fornaro G. and Manunta M. (2007b). Analysis of a subsidence phenomenon via DInSAR data and geotechnical criteria. *Italian Geotechnical Journal*, 4:50-67.
- Cascini L., Ferlisi S., Peduto D., Pisciotta G., Di Nocera S. and Fornaro G. (2009a) Multitemporal DInSAR data and damage to facilities as indicators for the state of activity of slow-moving landslides. Landslides and Engineered Slopes – From the past to the future, edited by: Chen, Z., Zhang, J., Li, Z., Wu, F., and Ho, K., *Proceedings of the 10th International Symposium on Landslides and Engineered Slopes*, 30 June-4 July 2008, Xi'an (China), CRC Press, 2:1103–1109, 2008.
- Cascini L., Fornaro G. and Peduto D. (2009b). Analysis at medium scale of low-resolution DInSAR data in slow-moving landslide affected areas. *ISPRS Journal of Photogrammetry and Remote Sensing*, 64:598–611.

- Cascini L., Fornaro G. and Peduto, D.(2010a). Advanced low- and full resolution DInSAR map generation for slow-moving landslide analysis at different scales. *Engineering Geology*, 112:29–42.
- Cascini L., Gullà G., Sorbino G. (2006). Groundwater nodelling of a weathered gneiss cover. *Canadian Geotechnical Journal*, 43(11):1153–1166.
- Cascini L., Peduto D., Pisciotta G., Arena L., Ferlisi S., Fornaro G., (2013a). The combination of DInSAR and facility damage data for the updating of slow-moving landslide inventory maps at medium scale. *Natural Hazards Earth Systems Sciences*, 13:1527–1549.
- Cascini L., Peduto D., Reale D., Arena L., Ferlisi S., Verde S., Fornaro G. (2013b). Detection and monitoring of facilities exposed to subsidence phenomena via past and current generation SAR sensors. *Journal of Geophysics and Engineering*, 10(6), 064001.
- Casu F., Manzo M., Lanari R. (2006). A quantitative assessment of the SBAS algorithm performance for surface deformation retrieval from DInSAR data. *Remote Sensing of Environment*, 102 (3–4):195–210.
- Carnec C., King C., Massonnet D. (1995). Measurement of land subsidence by means of differential S.A.R. Interferometry to sites of small extent. *Geophysical Research Letters*, 23:3579–3582.
- Catalano S., Bonforte A., Guglielmino F., Romagnoli G., Tarsia C., Tortorici G. (2014). The influence of erosional processes on the visibility of Permanent Scatterers Features from SAR remote sensing on Mount Etna (E Sicily). *Geomorphology*, 198:128–137.
- Catani F., Casagli N., Ermini L., Righini G. and Menduni G. (2005). Landslide hazard and risk mapping at catchment scale 2005 Arno River basin. *Landslides*, 2:329–342.
- Cattari S., Curti E., Giovinazzi S., Lagomarsino S., Parodi S., Penna A. (2004). A mechanical model for the vulnerability assessment and damage scenario of masonry buildings at urban scale. *In: Proc. 11<sup>th</sup> Italian conference on earthquake engineering*, Genoa, Italy.
- Cigna F., Del Ventisette C., Liguori V., Casagli N. (2011). Advanced radar-interpretation of InSAR time series for mapping and characterization of geological processes. *Natural Hazards Earth Systems Sciences*, 11: 865—881, doi:10.5194/nhess-11-865-2011.
- Cigna F., Bianchini S., Casagli N. (2012a). How to assess landslide activity and intensity with Persistent Scatterer Interferometry (PSI): the PSI-based matrix approach. *Landslides*, doi: 10.1007/s10346-012-0335-7.

- Cigna F., Osmanoglu B., Dixon T.H., De Mets C., Wdowinski S. (2012b). Monitoring land subsidence and its induced geological hazard with synthetic aperture radar interferometry: a case study in Morelia, Mexico. *Remote Sensing of Environment*, 117:146–161.
- Chatterjee RS, Fruneau B, Rundant JP, Roy PS, Frison P-L, Lakhera RC, Dadhwal VK, Saha R (2006). Subsidence of Kolkata (Calcutta) city, India during the 1990s as observed from space by Differential Synthetic Aperture Radar Interferometry (D-InSAR) technique. *Remote Sensing of Environment*, 102:176–185.
- Chiocchio C., Iovine G., Parise M., (1997). A proposal for surveying and classifying landslide damage to buildings. In: *Marinos, P.G., Koukis, G.C., Tsiambaos, G.C. & Stournaras G.C. (eds) Engineering Geology and the Environment, Proceedings of the LAEG International symposium on engineering geology and the environment*, Athens, June, 1997. Balkema - Rotterdam, pp. 553-558.
- Chorowicz J., Luxey P., Rudant J. P., Lyberis N., Yürür T., Gündoğdu N. (1995). Slip-motion estimation along the Ovacik Fault near Erzincan (Turkey) using ERS-1 radar image: evidence of important deformation inside the Turkish plate. *Remote Sensing of Environment*, 52:66-70.
- Clementino R.V., Proudfoot D.W., Law D.J., Skirrow R. (2008). Embankment slope stabilization using subhorizontal drains at Highway 39 near Drayton Valley. *Alberta Proceedings, 4th Canadian Conference on Geohazards*, Quebec, Canada, pp. 511–517.
- Corominas J., van Westen C., Frattini P., Cascini L., Malet J. P., Fotopoulou S., Catani F., Van Den Eeckhaut M., Mavrouli O., Agliardi F., Pitilakis K., Winter G.M., Pastor M., Ferlisi S., Tofani V., Hervàs J., Smith J. T. (2014). Recommendations for the quantitative analysis of landslide risk (2014). *Bulletin of Engineering Geology and the Environment*, 13:209-263.
- Colesanti C., Ferretti A., Novali F., Prati C., Rocca F. (2003). SAR monitoring of progressive and seasonal round deformation using the permanent scatterers technique. *IEEE Transactions on Geoscience and Remote Sensing*, 41:1685–1701.
- Cooper A.H., (2008). The classification, recording, databasing and use of information about building damage caused by subsidence and landslides. *Quarterly Journal of Engineering Geology and Hydrogeology*, 41(3):409-424. 10.1144/1470-9236/07-223.

- Costantini M., Falco S., Malvarosa F., Minati F. (2008). A new method for identification and analysis of persistent scatterers in series of SAR images. *In: IEEE International Geoscience & Remote Sensing Symposium*, July 6–11, 2008, Boston, Massachusetts, USA, pp. 449–452.
- Costantini M., Falco S., Malvarosa F., Minati F., Trillo F., Vecchioli F. (2014). Persistent scatterer pair interferometry: approach and application to high-resolution COSMOSkyMed SAR data. *IEEE Journal of Selected Topics in Applied Earth Observations and Remote Sensing*, (manuscript ID JSTARS-2014-00117).
- Cotecchia F. (1989). Studio di un movimento franoso nelle Unità Iripine dell'alta valle dell'Ofanto. *Italian Geotechnical Journal*, 2:57-84, (in Italian).
- Cotecchia, V. (2006). The Second Hans Cloos Lecture. Experience drawn from the great Ancona landslide of 1982. *Bulletin of Engineering Geology and the Environment*, 65:1–41.
- Crescenti U., Ciancetti G.F., Coltorti M., Dramis F., Gentili B., Melidoro G., Nanni T., Pambianchi G., Rainone M.L., Semenza E., Sorriso-Valvo M, Tazioli G.S. (1983) - La Grande Frana di Ancona del 1982. *Atti XV Convegno Nazionale di Geotecnica*, Vol. III, Spoleto 4-6 Maggio, 1983. (in Italian).
- Crosetto M., Biescas E., Duro J. (2008). Generation of advanced ERS and Envisat interferometric SAR products using the stable point network technique. *Photogrammetric Engineering & Remote Sensing*, 4:443–450.
- Crosetto M., Castillo M., Arbiol R. (2003). Urban subsidence monitoring using radar interferometry: algorithms and validation. *Photogrammetric Engineering & Remote Sensing*, 69 (7):775–783.
- Crosetto M., Crippa B., Biescas E. (2005). Early detection and in-depth analysis of deformation phenomena by radar interferometry. *Engineering Geology*, 79:81–91.
- Crosetto M., Monserrat O., Cuevas-González M., Devanthéry N., Crippa B. (2015). Persistent Scatterer Interferometry: A review. *ISPRS Journal of Photogrammetry and Remote Sensing*, <http://dx.doi.org/10.1016/j.isprsjprs.2015.10.011>.
- Cruden D.M. (1991). A simple definition of a landslide. *Bulletin of IAEG*, 43: 27-29.
- Cruden D.M., Varnes D.J. (1996). Landslide types and processes. Landslides: investigation and mitigation. *Transportation Research Board*,

- Special Report, No. 247*, National Research Council, National Academy Press, Washington DC, USA 36-75.
- De Michele M., Raucoules D., Arason P. (2016). Volcanic Eruptive-Column (Plume) Elevation Model and its Velocity Derived From Landsat 8. In: IGARSS 2016 - *IEEE International Geoscience and Remote Sensing Symposium*, 6669–6671.
- Den Haan, E.J. and Kruse, G.A.M. (2006). Characterisation and Engineering Properties of Dutch Peats. In: *Tan, T.S., Phoon, K.K., Hight, D.W. and Leroueil, S. (Eds), Characterisation and Engineering Properties of Natural Soils*, Taylor & Francis Group, London, 3, pp. 2101-33.
- DINoloket, 2016. Data and information on the Dutch subsurface. Open data portal of the geological survey of the Netherlands. <https://www.dinoloket.nl/en> (accessed 28.10.2016).
- Di Martire D., Iglesias R., Monells D., Centolanza G., Sica S., Pagano L., Mallorquí J.J., Ramondini M., Calcaterra D. (2014). Comparison between differential SAR interferometry and ground measurements data in the displacement monitoring of the earth-dam of Conza della Campania (Italy). *Remote Sensing of Environment*, 148C:58–69. <http://dx.doi.org/10.1016/j.rse.2014.03>.
- Di Martire D., Ramondini M., Calcaterra D., Nirchio F. (2013). Risultati preliminari del monitoraggio interferometrico di una frana a cinematica lenta mediante differenti sensori sar in banda x. *Incontro Annuale dei Ricercatori di Geotecnica*, Perugia 16-18 settembre 2013, Università degli Studi di Perugia, Pag.1-6, ISBN:9788890642135.
- Di Martire D., Tessitore S., Brancato D., Ciminelli M.G., Costabile S., Costantini M., Graziano G.V., Minati F., Ramondini M., Calcaterra D. (2015). Landslide detection integrated system (LaDIS) based on in-situ and satellite SAR interferometry measurements. *Catena*, 137:406-421.
- Eberhard M.O., Baldrige S., Marshall J., Mooney W., Rix G.J. (2010). The MW 7.0 Haiti earthquake of January 12, 2010. USGS/EERI advance reconnaissance team report. *U.S. geological survey open-file report*, 58:2010–1048.
- EEA (2012). Annual report 2012 and Environmental statement (2013). *European Environment Agency*, pp. 95, ISSN 1561-2120 - ISBN: 978-92-9213-393, doi:10.2800/91164.
- Esser A.J. (2000). Case of a slope failure in lacustrine Deposits. Landslides in research, theory and practice. In *Bromhead et al (eds)*

- Proceedings, 8th International Symposium on Landslides*, Cardiff, UK, 1:531–536.
- Ericson, J.P., Vörösmarty, C.J., Dingman, S.L., Ward, L.G., Meybeck, M. (2006). Effective sealevel rise and deltas: causes of change and human dimension implications. *Global and Planetary Change*, 50:63–82. <http://dx.doi.org/10.1016/j.gloplacha.2005.07.004>.
- Farina P., Colombo D., Fumagalli A., Marks F., Moretti S. (2006). Permanent Scatterers for landslide investigations: outcomes from the ESA-SLAM project. *Engineering Geology*, 88:200–217.
- Fell R., Corominas J., Bonnard C.h., Cascini L., Leroi E., Savage W.Z. (2008). On behalf of the JTC-1 Joint Technical Committee on Landslides and Engineered Slopes. Guidelines for landslide susceptibility, hazard and risk zoning for land-use planning, Commentary. *Engineering Geology*, 102:99–111.
- Fell R., Hartford D., (1997). Landslide risk management. In: Cruden C, Fell R (eds), *Landslide risk assessment. Proceedings of the international workshop on landslide risk assessment*, Honolulu. A. A. Balkema, Rotterdam, pp. 51–109.
- Ferlisi S., and Pisciotta G. (2007). A preliminary study of landslide induced property damages to wards consequence analysis. In: *First North American Landslide Conference Vail (Colorado, USA)*, pp. 180-190.
- Ferlisi S., Peduto D., Gullà G., Nicodemo G., Borrelli L., Fornaro G. (2015). The use of DInSAR data for the analysis of building damage induced by slow-moving landslides. In: Lollino G, Giordan D, Crosta GB, J. Corominas J, Azzam R, Wasowski J, Sciarra N (Eds.), *Engineering Geology for Society and Territory – Landslide Processes*, © Springer International Publishing – Vol. 2, pp. 1835-1839. doi: 10.1007/978-3-319-09057-3\_325.
- Ferretti A., Prati C., Rocca F. (2000). Nonlinear subsidence rate estimation using permanent scatterers in differential SAR interferometry. *IEEE Transactions on Geoscience and Remote Sensing*, 38 (5):2202–2212.
- Ferretti A., Prati C., Rocca F. (2001). Permanent scatterers in SAR interferometry. *IEEE Transactions on Geoscience and Remote Sensing*, 39 (1):8–20.
- Finno R. J., Voss F. T., Rossow E., Blackburn J. T., (2005). Evaluating Damage Potential in Buildings Affected by Excavations. *Journal of Geotechnical and Geoenvironmental Engineering*, 131(10):1199–1210.



- Fornaro G., Serafino F., Lombardini F. (2005). 3D multipass SAR focusing: experiments with long-term spaceborne data. *IEEE Transactions on Geoscience and Remote Sensing*, 43 (4):702–712.
- Fornaro G. and Pascazio V. (2014a). SAR Interferometry and Tomography: Theory and Applications. In: *Chellapa, R., Theodoridis, S. (Eds.), Academic Press Library in Signal Processing, Vol. 2, Communications and Radar Signal Processing* Chennai. New York, USA: Academic, 1034–1117.
- Fornaro G., Lombardini F., Pauciullo A., Reale D., Viviani F. (2014b). Tomographic Processing of Interferometric SAR Data: Developments, applications, and future research perspectives. *IEEE Signal Processing Magazine*, 31(4): 41-50.
- Fornaro G., Pauciullo A., Serafino F. (2007). Multipass SAR Processing for urbanized areas imaging and deformation monitoring at small and large scales. In: *Proceedings of the Urban Remote Sensing Joint Event*, Paris 11–13 April, pp. 1–7. <http://dx.doi.org/10.1109/URS.2007.371879>.
- Fornaro G., Reale D., Serafino F. (2009). Four-dimensional SAR imaging for height estimation and monitoring of single and double scatterers. *IEEE Transactions on Geoscience and Remote Sensing*, 47 (1): 212–237.
- Fornaro G., Reale D., Verde S. (2012). Potential of SAR for monitoring transportation infrastructures: an analysis with the multi-dimensional imaging technique. *Journal of Geophysics and Engineering*, 9:S1.
- Fornaro G., Reale D., Verde S. (2013). Bridge thermal dilation monitoring with millimeter sensitivity via multidimensional SAR imaging. *IEEE Geoscience and Remote Sensing Letters*, 10:677–681.
- Fotopoulou S. D. and Pitilakis K. D. (2013a). Vulnerability assessment of reinforced concrete buildings subjected to seismically triggered slow-moving earth slides. *Landslides*, 10:563-582.
- Fotopoulou S. D. and Pitilakis K. D., (2013b). Fragility curves for reinforced concrete buildings to seismically triggered slow-moving slides. *Soil Dynamics and Earthquake Engineering*, 48:143-161.
- Franceschetti G. and Fornaro G. (1999). Synthetic aperture radar interferometry. In: *G. Franceschetti and R. Lanari (Eds.), Synthetic Aperture Radar Processing*, CRC Press. Boca Raton, FL: 167-223.
- Freeman T.J., Littlejohn G.S., Driscoll R.M.C., (1994). Has your house got cracks: a guide to subsidence and heave of buildings on clay. *Institution of Civil Engineers and Building Research Establishment*, pp. 114.

- Fruneau B., Achache J., Delacourt C. (1996). Observation and Modeling of the Saint-Etienne-de-Tinée Landslide Using SAR Interferometry. *Tectonophysics*, 265:181–190.
- Fruneau B., Achache J., Delacourt C. (1999). Observation and Modeling of the Saint-Etienne-de-Tinée Landslide Using SAR Interferometry. *Tectonophysics*, 256:181-190.
- Fruneau B., Carnec C., Colesanti C., Deffontaines B., Ferretti A., Mouelic S., Le Parmentier A.M., Rudant J.P. (2003). Conventional and PS differential SAR interferometry for monitoring vertical deformation due to water pumping. The Haussmann-St-Lazare case example (Paris, France). *Proc. FRINGE 2003*, 1-5 December, Frascati (Italy).
- Fu W., Guo H., Tian Q. and Guo, X. (2010). Landslide monitoring by corner reflectors differential interferometry SAR. *International Journal of Remote Sensing*, 31(24):6387-6400.
- Fujisawa K., Higuchi K., Koda A., Harada T. (2007). Landslide detection, monitoring, prediction, emergency measures and technical instruction in a busy city, Atami, Japan. *Proceedings, First North American Landslide Conference*, Vail, Colorado, pp. 65–73.
- Fumagalli A., Novali F., Prati C., Rocca F., Rucci A. (2011). A new algorithm for processing interferometric data-stacks: SqueeSAR. *IEEE Transactions on Geoscience and Remote Sensing*, 49 (9):3460–3470.
- Gabriel, K., Goldstein, R.M., Zebker, H.A., 1989. Mapping small elevation changes over large areas: differential interferometry. *Journal of Geophysical Research*, 94:9183–9191.
- Galloway D.L., Burgmann R., Fielding E., Amelung F., Lacziak R.J. (2000). Mapping recoverable aquifer-system deformation and land subsidence in Santa Clara Valley, California, USA, using space-borne synthetic aperture radar. In: *Carbognin, L., Gambolati, G., Johnson, A.I. (Eds.) Proceedings of the 6th International Symposium on Land Subsidence*, (Ravenna, Italy), Vol. 1, pp. 237–248.
- Galloway D.L., Jones D.R., Ingebritsen (1999). Land subsidence in the United States. Circular 1182, *US Geological Survey*.
- García-Davalillo J.C., Herrera G., Notti D., Strozzi T., Álvarez-Fernández I. (2013). DInSAR analysis of ALOS PALSAR images for the assessment of very slow landslides: the TenaValley case study. *Landslides*, 1–22.

- Gazetas G. (1991). Formulas and charts for impedances of surface and embedded foundation. *ASCE Journal of Geotechnical Engineering*, 117:1363-1381.
- Geomorphological Services Ltd., (1991). Coastal Landslip Potential Assessment: Isle of Wight Undercliffe, Ventnor. Technical Report for the department of the Environment. Research Contract RECD 7/1/272.
- Gernhardt, S., Adam, N., Eineder, M., Bamler, R., 2010. Potential of very high resolution SAR for persistent scatterer interferometry in urban areas. *Ann. GIS* 16 (2):103–111.
- Giannico C., Ferretti A., Alberti S., Jurina L., Ricci M., Sciotti A. (2012). Application of satellite radar interferometry for structural damage assessment and monitoring Life-Cycle and Sustainability of Civil Infrastructure Systems: IALCCE'12. In: *Strauss, A., Frangopol, D.M., Bergmeister, K. (Eds.), Proc. of the 3rd Int. Symp. on Life-Cycle Civil Engineering*, (Vienna, Austria, 3–6 Oct.), (Boca Raton, FL: CRC Press), 2094–101.
- Gillon M.D. and Saul G.J. (1996). Stabilisation of Cairnmuir Landslide. Landslides. In: *Senneset (eds) Proceedings, 7th International Symposium on Landslides*, Balkema, Rotterdam, 3:1693–1698.
- Glade T., (2003). Vulnerability assessment in landslide risk analysis. *Erde*, 134:123–146.
- Goldestein M., Engelhardt H., Kamb B., Frolich R.M. (1993). Satellite radar interferometry for monitoring ice sheet motion. *Science*, 262:1525.
- Greco R., Sorriso-Valvo M., Catalano E. (2007). Logistic regression analysis in the evaluation of mass-movements susceptibility - the Aspromonte case study, Calabria. *Engineering Geology*, 89:47–66.
- Greco R., Gullà G., Sorriso-Valvo M. (2010). Metodologia base, approfondita a partire dal PAI, per la valutazione indicizzata di pericolosità, vulnerabilità e rischio – [RF0a]. *POR Calabria 2000-2006*, G. Gullà (Responsabile scientifico), L. Antronico, M. Brunetti, R. Coscarelli, S. Critelli, F. Dramis, G. Iovine, M. Mattei, P. Molin, F. Muto, T. Nanni, O. Petrucci, G. Robustelli, M. Sorriso-Valvo, P. Versace. *Misura 1.4 Sistemi Insediativi*, CNR-IRPI, pp. 60, (in Italian), [http://www.regione.calabria.it/abr/allegati/studi\\_ricerca/POR%202000-2006/lotto\\_1\\_documentiWEB/RF0a.pdf](http://www.regione.calabria.it/abr/allegati/studi_ricerca/POR%202000-2006/lotto_1_documentiWEB/RF0a.pdf).
- Grünthal G., (1998). European Macroseismic Scale 1998, Cahiers du Centre Européen de Géodynamique et de Seismologie. Conseil de l'Europe, Luxembourg.

- Gullà G, Antronico L, Borrelli L, Cilento M, Aceto L, Scionti V (2006) Relazione Finale -Parti I-III e Cartografia. Convenzione di consulenza tecnico-scientifica Esecuzione di un programma di studi ed indagini finalizzati alla individuazione delle cause che hanno determinato la gravissima situazione di dissesto idrogeologico nel territorio del Comune di Lungro (CS). *CNR-IRPI, OPCM n. 3460/2005*. Unpublished report, (in Italian).
- Gullà G., Ferlisi S., Nicodemo G., Peduto D. (2017b). Un approccio metodologico per la gestione del rischio in aree urbane affette da frane a cinematica lenta. *Submitted to XXVI – CNG Convegno Nazionale di Geotecnica – Roma 2017*, (in Italian).
- Gullà G., Fornaro G., Borrelli L., Antronico L., Reale D., Verde S. (2014). Integrazione progressiva di dati geotecnici e da satellite nell'analisi del rischio da frana in area urbana: il quartiere di Ianò-Catanzaro. *Atti del XXV Convegno Nazionale di Geotecnica, Vol. 2 – La Gestione nella difesa del Territorio e delle Infrastrutture dalle Calamità Naturali*. Baveno, Italia, 4-6 giugno 2014, pp. 571-578 (in Italian).
- Gullà G., Nicesano D., Antronico L., Ferrari E., Sorriso-Valvo M., Tansi C., Terranova G., Aceto L. (2003). Linee guida per interventi di stabilizzazione di pendii in aree urbane da riqualificare. *CNR-IRPI Sezione di Cosenza, Regione Calabria - P.O.P. 1994/99 - Misura 4.4 “Ricerca Scientifica e Tecnologica” Tutela dell'ambiente e del territorio – “Metodologie e strumenti per la riqualificazione urbana”*, Rubbettino Industrie Grafiche ed Editoriali, pp.196, (in Italian).
- Gullà G., Peduto D., Borrelli L., Antronico L., Fornaro G. (2017a). Geometric and kinematic characterization of landslides affecting urban areas: the Lungro case study (Calabria, southern Italy). *Landslides*, 14(1):171-188, DOI: 10.1007/s10346-015-0676-0.
- Guzzetti F., Manunta M., Ardizzone F., Pepe A., Cardinali M., Zeni G. and Lanari R. (2009). Analysis of ground deformation detected using the SBAS-DInSAR technique in Umbria, Central Italy. *Pure and applied Geophysics*, 166(8-9):1425-1459.
- Hageman B.P. (1964). BladGoeree en Overflakkee, Toelichtingbij de GeologischeKaart van Nederland, 1:50.000. *Rijks Geologische Dienst Haarlem*, pp. 89 (in Dutch).
- Haynes M. (2000). Wide-area precision surveying of land subsidence from space using radar interferometry. In: Carbognin, L.,

- Gambolati, G., Johnson, A.I. (Eds.) *Procee. of the 6th Int. Symp. on Land Subsidence*, (Ravenna, Italy), vol. 2, pp. 213–8.
- Henderson F. M and Lewis A. J. (1998). Principles and Applications of Imaging Radar. *Manual of Remote Sensing*, Vol. 2, New York: J. Wiley.
- Herrera G., Fernandez-Merodo J., Tomás R., Cooksley G., Mulas J. (2009a). Advanced interpretation of subsidence in Murcia (SE Spain) using A-DInSAR data-modelling and validation. *Natural Hazards and Earth Systems Science*, 9:647–661.
- Herrera G., Gutiérrez F., García-Davalillo J.C., Guerrero J., Notti D., Galve J.P., Fernández- Merodo J.A., Cooksley G. (2013). Multi-sensor advanced DInSAR monitoring of very slow landslides: the TenaValley case study (Central Spanish Pyrenees). *Remote Sensing of Environment*, 128:31–43.
- Herrera G., Notti D., Garcia-Davalillo J.C., Mora O., Cooksley G., Sanchez M., Arnaud A., Crosetto M. (2011). Analysis with C- and X-band satellite SAR data of the Portalet landslide area. *Landslides*, (8):195–206.
- Herrera G., Tomas R., Lopez-Sanchez J.M., Delgado J., Vicente F., Mulas J., Cooksley G., Sanchez M., Duro J., Arnaud A., Blanco P., Duque S., Mallorqui J.J., De la Vega-Panizo R., Monserrat O. (2009b). Validation and comparison of advanced differential interferometry techniques: Murcia metropolitan area case study. *ISPRS Journal of Photogrammetry and Remote Sensing*, 64(5):501–512.
- Herrera G., Tomas R., Vicente F., Lopez-Sanchez J.M., Mallorqui J.J., Mulas J. (2010b). Mapping ground movements in open pit mining areas using differential SAR interferometry. *International Journal of Rock Mechanics and Mining Sciences*, 47(7):1114–1125.
- Herrera G, Álvarez Fernández MI, Tomás R, González-Nicieza C, López-Sánchez JM, Álvarez Vigil AE. (2012). Forensic analysis of buildings affected by mining subsidence based on Differential Interferometry (Part III). *Eng. Fail. Anal.*, 24:67–76. doi:10.1016/j.engfailanal.2012.03.003.
- Holzer T.L. (2009). Living with Unstable Ground. American Geosciences Institute publication, ISBN: 0-922152-82- 9978-0-922152-82-7, pp. 68. Environmental awareness series.
- Hooper A., Zebker H., Segall P., Kampes B. (2004). A new method for measuring deformation on volcanoes and other natural terrains using InSAR persistent scatterers. *Geophysical Research Letters*, 31, L23611.

- Howard Humphreys and Partners, (1993). Subsidence in Norwich. London, HMSO, pp. 99.
- Hungr O., Evans S.G., Bovis M.J., Hutchinson J.N. (2001). A review of the classification of landslides of the flow type. *Environmental & Engineering Geoscience*, VII (3), pp.221 – 238.
- Hungr O., Leroueil S., Picarelli L. (2014). The Varnes classification of landslide types, an update. *Landslides*, 11:167:194.
- Hutchinson J.N. (1988). Morphological and Geotechnical parameters of Landslides in relation to Geology and Hydrogeology. State of the art Report. *Proc. V Intl. Symposium on Landslides*, Lausanne, Vol. 1, pp. 3 – 35.
- Iovine G., Petrucci O., Rizzo V., Tansi C. (2006). The March 7th 2005 Cavallerizzo (Cerzeto) landslide in Calabria – Southern Italy. *Proceedings of the 10th LAEG Congress*, Nottingham, Great Britain, 6–10 September 2006, 785, 1–12.
- Ireland R.L., Poland J.F., Riley F.S. (1984). Land Subsidence in the San Joaquin Valley, California, as of 1980. *U.S. Geological Survey*, 437-1, pp.93.
- ISPRA - Istituto Superiore per la Protezione e la Ricerca Ambientale. (2006). Pericolosità Di Origine Naturale. *Annale Dei Dati Ambientali*, pp. 1023–7, (in Italian).
- Johnson R., (2005). Significance of cracks in low-rise buildings – what you need to know. *Civil Engineering, Paper 13014*, 158:30-35
- Jones C.J.F.P., Bellamy J.B. (1973). Computer prediction of ground movements due to mining subsidence. *Geotechnique*, 23: 515-530.
- Jónsson S., Segall P., Pedersen R., Björnsson G. (2003). Post earthquake ground movements correlated to pore-pressure transients. *Nature*, 424: 179-183.
- Joughin I.R., Gray L., Bindschadler R., Price S., Morse D., Hulbe C., Mattar K., Werner C. (1999). Tributaries of west Antarctic ice streams revealed by radarsat interferometry. *Science*, 286(5438):283–286.
- Joughin I.R., Winebrenner D.P., Fahnestock M.A. (1995). Observations of ice-sheet motion in Greenland using satellite radar interferometry. *Geophysical Research Letters*, 22(5):571–574.
- Joughin I., Winebrenner D., Fahnestock M., Kwok R., Krabill W. (1996). Measurement of ice-sheet topography using satellite radar interferometry. *Journal of Glaciology*, 42(140).

- Joughin I.R., Kwok R., Fahnestock M.A. (1998). Interferometric estimation of three-dimensional ice-flow using ascending and descending passes. *IEEE Transactions on Geoscience and Remote Sensing*, 36(1):25-37.
- Jung H.S., Lu Z., Won J.-S., Poland M.P., Miklius A. (2011). Mapping three-dimensional surface deformation by combining multiple-aperture interferometry and conventional interferometry: application to the June 2007 Eruption of Kilauea Volcano, Hawaii. *IEEE Geoscience and Remote Sensing Letters*, 8 (1): 34– 38. <http://dx.doi.org/10.1109/LGRS.2010.2051793>.
- Jurina L., Ferretti A., (2004). Un caso emblematico di un parcheggio interrato: diagnosi di un dissesto. *Progettare il sottosuolo, per un edificato sicuro Milano*, 6 maggio 2004.
- Jworchan I., O'Brien A., Rizakalla E. (2008). Landslide stabilization for residential development. In: *Chen et al (eds) Proceedings, 10th International Symposium on Landslides and Engineered Slopes*, Xi'an, China, 2:1757–1763.
- Kampes B.M. and Adam N. (2005). The STUN Algorithm for Persistent Scatterer Interferometry. *Fringe 2005 Workshop*. Frascati, Italy.
- Karapetrou S.T., Fotopoulou S.D., Pitolakis K.D., (2015). Seismic vulnerability assessment of high-rise non-ductile RC buildings considering soil–structure interaction effects. *Soil Dynamics and Earthquake Engineering*, 73:42-57.
- Kim S.W.S., Wdowinski T.H., Dixon F., Amelung, Won J.S., and Kim W.J. (2008). InSAR-based mapping of surface subsidence in Mokpo City, Korea, using JERS-1 and ENVISAT SAR data. *Earth Planets Space*, Vol. 60, pp. 453-461.
- Kimura H., and Yamaguchi Y. (2000). Detection of landslide areas using satellite radar interferometry. *Photogrammetric Engineering & Remote Sensing*, 66(3):337–344.
- Kircher M., Roth A., Adam N., Kampes B.M., Neugebauer H.J. (2003). Remote sensing observation of mining induced subsidence by means of differential SAR interferometry. In: *Proceedings of the Geoscience and Remote Sensing Symposium, 2003, IGARSS '03*, Toulouse, France, 21–25 July 2003, Vol. 1, pp. 209–211.
- Kjekstad O. and L. Highland (2009). Economic and Social Impacts of Landslides. *Sassa, K., Canuti, P. (Eds.), Disaster Risk Reduction*. Springer-Verlag, Berlin Heidelberg, pp. 573–588.

- Klaassen R. K.W.M. and Creemers J.G.M. (2012). Wooden foundation piles and its underestimated relevance for cultural heritage. *Journal of Cultural Heritage*, 13:123-128.
- Klaassen R. K.W.M. (2015). Life Expectation of Wooden Foundations – a Non-Destructive Approach. In *Proc. of International Symposium Non-Destructive Testing in Civil Engineering (NDT-CE)*, September 15-17, 2015, Berlin, Germany, pp. 775-779.
- Konogai K., Asakura T., Suyama S., Kyokawa H., Kiyota T., Eto C., Shibuya K. (2012). Soil subsidence map of the Tokyo bay area liquefied in the March 11<sup>th</sup> great east Japan earthquake. In *Proceeding of the International Symposium on Engineering Lessons Learned from the 2011 Great East Japan Earthquake*, March 1-4, 2012, Japan.
- Kwok R., Fahnestock M.A. (1996). Ice sheet motion and topography from radar interferometry. *IEEE Transactions on Geoscience and Remote Sensing*, 34(1):189-200.
- Lanari R., Berardino P., Borgstrom S., Del Gaudio C., De Martino P., Fornaro G., Guarino S., Ricciardi G.P., Sansosti E., Lundgren P. (2004a). The use of IFSAR and classical geodetic techniques for caldera unrest episodes: application to the Campi Flegrei uplift event of 2000. *Journal of Volcanology and Geothermal Research*, 247–260.
- Lanari R., Mora O., Manunta M., Mallorqui J.J., Berardino P., Sansosti E. (2004b). A small baseline approach for investigating deformations on full resolution differential SAR interferograms. *IEEE Transactions on Geoscience and Remote Sensing*, 42 (7): 1377– 1386.
- Lee J.Y. and Jiang G. (2013). Displacement measurement using a wavelength phase-shifting grating interferometer. *Optics Express*, 21:25553-25564.
- Lillesand, T.M. and Kiefer, R.W. (1987). Remote Sensing and Image Interpretation. *Sec. Ed., John Wiley and Sons, Inc.*, Toronto.
- Lagomarsino S. and Giovinazzi S. (2006). Macro seismic and mechanical models for the vulnerability and damage assessment of current buildings. *Journal of Earthquake Engineering*, 4:415\_43.
- Lagomarsino S., Penna A., Galasco A., Cattari S. (2012). TREMURI program: Seismic Analyses of 3D Masonry Buildings, Release 2.0, University of Genoa – Italy.
- Lagomarsino S., Penna A., Galasco A., Cattari S. (2013). TREMURI program: an equivalent frame model for the nonlinear seismic analysis of masonry buildings. *Engineering Structures*, 56:1787–1799.



- Lanzo G., D'Elia B. (1997). Experiences on slope movements in clayey soils. *Rivista Italiana di Geotecnica*. XXI, 2:15-27.
- Léone F., Aste J.P., Leroi E., (1996). Vulnerability assessment of elements exposed to mass-movement: working toward a better risk perception. *In: Senneset K (eds.), Landslides*. Balkema, Rotterdam, pp. 263–270.
- Leroueil S., Locat J., Vaunat J., Picarelli L., Lee H., Faure R.(1996). Geotechnical characterization of slope movements. *Proceedings 7th International Symposium Land-slides*, Trondheim, Norway 1:53-74.
- Leroueil S., Locat J. (1998). Slope movements–Geotechnical characterization, risk assessment and mitigation. *Geotechnical Hazard, Maric, Lisac & Szavits-Nossan (eds)*. Balkema, Rotterdam.
- Lombardini, F., 2005. Differential tomography: a new framework for SAR interferometry. *IEEE Transactions on Geoscience and Remote Sensing*, 43:37–44.
- Lopez-Quiroz P., Doing M.P., Tupin F., Briole P. and Nicolas J.M. (2009). Time series analysis of Mexico City subsidence constrained by radar interferometry. *Journal of Applied Geophysics*, 69(1).
- Losacco N., (2011). Development and testing of a simplified building model for the study of soil-structure interaction due to tunnelling in soft ground. *Phd Thesis*, pp.231.
- Lu P., Casagli N., Catani F., Tofani, V. (2012). Persistent Scatterers Interferometry Hotspot and Cluster Analysis (PSI-HCA) for detection of extremely slow-moving landslides. *International Journal of Remote Sensing*, 33:466–489.
- Lu P., Catani F., Tofani, V. and Casagli, N. (2013). Quantitative hazard and risk assessment for slow-moving landslides from Persistent Scatterer Interferometry. *Landslides*, 1-12.
- Lu Z., Wicks C., Dzurisin D., Thatcher W., Freymuller J.T., McNutt S.R., Mann D. (2000). Aseismic inflation of westdahl volcano, alaska, reveled by satellite radar interferometry. *IEEE Transactions on Geoscience and Remote Sensing*, 43:37–44. *Geophysical Research Letters*, 27 (11):1567-1570.
- Lundgren P., Usai S., Sansosti E., Lanari R., Tesauro M., Fornaro G., Berardino P. (2001). Modeling surface deformation observed with synthetic aperture radar interferometry at Campi Flegrei caldera. *Journal of Geophysical Research*, 106 (B9):19355– 19366.

- Madsen S.N., Zebker H.A., Martin J. (1993). Topographic Mapping Using Radar Interferometry: Processing Techniques. *IEEE Transactions on Geoscience and Remote Sensing*, 31(1):246-256.
- Malone A.W., Hansen A., Hencher S.R., Fletcher C.J.N. (2008). Post-failure movements of a large slow rock slide in Schist near Pos Selim, Malaysia. In: *Chen et al (eds) Proceedings, 10th International Symposium on Landslides and Engineered Slopes*, Xi'an, China, 1:457–461.
- Mansour, M. F., Morgenstern, N. R., Martin, C. D. (2011). Expected damage from displacement of slow-moving slides. *Landslides*, 7:117–131.
- Manzo M., Ricciardi G.P., Casu F., Ventura G., Zeni G., Borgstrom S., Berardino P., Del Gaudio C., Lanari R. (2006). Surface deformation analysis in the Ischia Island (Italy) based on spaceborne radar interferometry. *Journal of Volcanology and Geothermal Research*, 151(4):399–416.
- Maquaire O, Thiery Y, Malet J-P, Weber C, Puissant A, Wania A (2004). Current practices and assessment tools of landslide vulnerability in mountainous basins – identification of exposed elements with a semi-automatic procedure. In: *Lacerda W, Ebrlich M, Fontoura SAB, Sayão ASF (Eds.). Landslides: evaluation and stabilization. Proc of the 9th Int Symp on Landslides*. A.A. Balkema Publishers – Vol. 1, pp. 171-176.
- Massonnet D., Feigl, K.L., (1998). Radar interferometry and its application to changes in the earth's surface. *Reviews of Geophysics*, 36 (4):441–500.
- Massonnet D., Briole P., Arnaud A. (1995). Deflation of Mount Etna monitored by spaceborne radar interferometry. *Nature*, 375:567–570
- Massonnet, D., Rossi M., Carmona C., Adragna F., Peltzer G., Felgl, K., Rabaute T. (1993). The displacement field of the Landersearthquake mapped by radar interferometry. *Nature*, 364:138–142.
- MATTM (2010). Piano Straordinario di Telerilevamento Ambientale (PSTA), Linee guida per l'analisi dei dati interferometrici satellitari in aree soggette a dissesti idrogeologici. *Italian Ministry of the Environment and Protection of Land and Sea (MATTM)*, pp. 108pp, (in Italian).
- Mavrouli O., Fotopoulou S., Pitilakis K., Zuccaro G., Corominas J., Santo A., Cacace F., De Gregorio D., Di Crescenzo G., Foerster E., Ulrich T. (2014). Vulnerability assessment for reinforced concrete

- buildings exposed to landslides. *Bulletin of Engineering Geology and the Environment*, 73:265-289.
- Medvedev S., Sponheuer W., Karnick V., (1965). The MSK Intensity Scale, Veroff Institute für Geodynamic, Jena, 48:1-10.
- Modoni G., Darini G., Spacagna R.L., Saroli M., Russo G., Croce P. (2013). Spatial analysis of land subsidence induced by groundwater withdrawal. *Engineering Geology*, 167:59-71.
- Mohr J.J., Reeh N., Madsen S.N. (1998). Three-dimensional glacial flow and surface elevation measured with radar interferometry. *Nature*, 391(6664):273–276.
- Meisina C., Zucca F., Notti D, Colombo A., Cucchi A., Savio G., Giannico C. and Bianchi M.(2008). Geological Interpretation of PSInSAR Data at Regional Scale. *Sensors 2008*, 8:7469-7492; DOI: 10.3390/s8117469.
- Milone G., Scepti G. (2011). A clustering approach for studying ground deformation trends in Campania Region through PS-InSAR time series analysis. *Journal of Applied Sciences*, 2011 ISSN 1812/ DOI: 10.3923/jas.
- Milutinovic Z. and Trendafiloski G. (2003). WP4: vulnerability of current buildings. *Tech rep, Risk-UE: an advanced approach to earthquake risk scenarios with applications to different European towns*, European Commission.
- Ministerial Circular n. 617 of 2th February (2009). Istruzioni per l'applicazione delle Nuove norme tecniche per le costruzioni, D.M. 14 gennaio 2008. Italian Ministry of Infrastructure and Transport, pp.447,(in Italian).
- Moore D.P., Watson A.D., Martin C.D. (2006). Deformation mechanism of a large rockslide inundated by a reservoir. *Workshop on the Mechanics and Velocity of Large Landslides*. Technical Report, Italy.
- Mora O., Mallorqui J.J., Broquetas A. (2003). Linear and nonlinear terrain deformation maps from a reduced set of interferometric SAR images. *IEEE Transactions on Geoscience and Remote Sensing*, 41:2243–2253.
- Moreira M., Prats-Iraola P., Younis M., Krieger G., Hajnsek I., Papathanass K. P. (2013). A Tutorial on Synthetic Aperture Radar. *IEEE Geoscience and remote sensing magazine*, pp 6-43, doi 10.1109/MGRS.2013.2248301.
- National Coal Board, (1975). Subsidence Engineers Handbook. *National Coal Board Production Dept.*, U.K.

- Negulescu C. and Foerster E. (2010). Parametric studies and quantitative assessment of the vulnerability of a RC frame building exposed to differential settlements. *Natural Hazards and Earth System Science*, 10(9):1781-1792.
- Negulescu C., Ulrich A., Seyedi D.M. (2014). Fragility curves for masonry structures submitted to permanent ground displacements and earthquakes. *Natural Hazards*, 74: 1461–1474. <http://dx.doi.org/10.1007/s11069-014-1253-x>.
- Nichol D. and Lowman R. D. W. (2000). Stabilisation and remediation of a minor landslide affecting the A5 Trunk Road at Llangollen, North Wales. In: Bromhead et al (eds), *Landslides in research, theory and practice. Proceedings, 8th International Symposium on Landslides*, Cardiff, UK, 3:1099–1104.
- Nicodemo G., Ferlisi S., Peduto D., Cascini L., Gullà G., Borrelli G., Fornaro G. (2014). Analisi di livello preliminare delle conseguenze indotte agli edifici da frane a cinematica lenta. In: *Atti dell'Incontro Annuale dei Ricercatori di Geotecnica – LARG 2014*, Chieti 14-16 Luglio 2014, pp. 1-6 (in Italian).
- Nicodemo G., Peduto D., Ferlisi S., Maccabiani J. (2016). Investigating building settlements via very high resolution SAR sensors. In: Bakker, J., Frangopol, D.M., van Breugel, K. (Eds.), *Life-Cycle of Engineering Systems: Emphasis on Sustainable Civil Infrastructure. Proceedings of the Fifth International Symposium on Life-Cycle Civil Engineering (LALCCE 2016)*, 16–19 October 2016, Delft, The Netherlands. Taylor & Francis Group, London, pp. 2256–2263, (ISBN 978-1-138-02847-0).
- Notti D., Davalillo J. C., Herrera G. Mora O. (2010). Assessment of the performance of X-band satellite radar data for landslide mapping and monitoring: Upper Tena Valley case study. *Natural Hazards and Earth System Sciences*, 10:1865–1875, doi:10.5194/nhess-10-1865-2010.
- Notti D., Herrera G., Bianchini S., Meisina C., García-Davalillo J.C., Zucca F. (2014). A methodology for improving landslide PSI data analysis. *International Journal of Remote Sensing*, 35.
- NTC (2008). Nuove norme tecniche per le costruzioni, D.M. 14 gennaio 2008 (in Italian).
- Ortiz J.A., Hernández A., Hernández M., Pacheco J., Zermeño E., Salinas R. (2015). Full-scale experimental and numerical study about structural behavior of thin-walled cold-formed steel building

- affected by ground settlements due to land subsidence. *In Proc. LAHS, 372, Prevention and mitigation of natural and anthropogenic hazards due to land subsidence*, pp. 141-144. Copernicus Publications.
- Osmanoglu B., Dixon T. H., Wdowinski S., Cabral-Cano E., & Jiang Y. (2011). Mexico City subsidence observed with persistent scatterer InSAR. *International Journal of Applied Earth Observation and Geoinformation*, 13(1):1–12.
- Okumura T. (1969). Analysis of land subsidence in Nigata. *In: Proceeding of the International Symposium on Land Subsidence, Vol. 1*, Tokyo, Japan, pp. 130-143.
- Ovando-Shelley E., Romo M.P., Contreras N., Giralt A. (2003). Effects on soil properties of future settlements in downtown Mexico City due to ground water extraction. *Geofisica International*, Vol. 2, no.2, pp. 185-204.
- Palmisano F., Vitone C., Cotecchia F., (2016). Landslide damage assessment at the intermediate to small scale. *Aversa et al. (eds.), Landslides and Engineered Slopes Experience, Theory and Practice*, Vol. 1, pp. 1549-1557.
- Peck R.B. (1969). Deep excavations and tunneling in soft ground. A thickness of the tail piece. *In: Proceedings of 7<sup>th</sup> International Conference on Soil Mechanics and Foundation Engineering*, Mexico City, pp. 225-290.
- Pedersen R., Sigmundsson F., Feigl K.L., Árnadóttir T. (2001). Coseismic interferograms of two Ms=6.6 earthquakes in the South Iceland Seismic Zone, June 2000. *Geophysical Research Letters*, 28 (17):3341-3344.
- Peduto D. (2008). Analysis of ground deformations related to subsidence and landslide phenomena via DInSAR techniques. *PhD Thesis*, pp. 258.
- Peduto D., Cascini L., Arena L., Ferlisi S., Fornaro G., Reale D. (2015). A general framework and related procedures for multi scale analyses of DInSAR data in subsiding urban areas. *ISPRS Journal of Photogrammetry and Remote Sensing*, Vol. 105: 186-210, ISSN 0924-2716, <http://dx.doi.org/10.1016/j.isprsjprs.2015.04.001>.
- Peduto D., Nicodemo G., Maccabiani J., Ferlisi S., D'Angelo R., Marchese A. (2016a). Investigating the behaviour of buildings with different foundation types on soft soils: two case studies in The Netherlands. VI Italian Conference of Researchers in Geotechnical Engineering, CNRIG2016, 22-23 Sept. 2016, Bologna (Italy).

- Procedia Engineering*, Vol 158, 2016, pp. 529–534, <http://dx.doi.org/10.1016/j.proeng.2016.08.484>.
- Peduto D., Nicodemo G., Maccabiani J., Ferlisi S. (2017). Multi-scale analysis of settlement-induced building damage using damage surveys and DInSAR data: A case study in The Netherlands. *Engineering Geology*, 218:117–133.
- Peduto D, Pisciotta G, Nicodemo G, Arena L, Ferlisi S, Gullà G, Borrelli L, Fornaro G, Reale D, (2016b) A procedure for the analysis of building vulnerability to slow-moving landslides. *Proceedings of 1st IMEKO TC4 International Workshop on Metrology for Geotechnics*, 17-18 March 2016. Benevento, Italy. pp. 248-254. ISBN 978-92-990075-0-1.
- Pellegrino A., Ramondini M., Urciouli G. (2004). Interplay between the morphology and mechanism of mudslides: field experiences from Southern Italy. *Lacerda W. (eds.), Proceedings of the 9th International Symposium on Landslides*, Rio de Janeiro, Vol.2 Balkema, Rotterdam, pp. 1403-1409.
- Peltzer G., Rosen P. (1995). Surface displacement of the 17 May 1993 Eureka Valley, California earthquake observed by SAR interferometry. *Science*, 268:1333-1336.
- Peltzer G., Rosen P., Rogez F., Hudnut K. (1996). Post seismic rebound in fault step-overs caused by pore fluid flow. *Science*, 273:1202-1204.
- Peltzer G., Crampé F., King G. (1999). Evidence of the nonlinear elasticity of the crust from Mw 7.6 Manyi (Tibet) earthquake. *Science*, 286(5438):272-276.
- Penna A., Lagomarsino S., Galasco A. (2013). A nonlinear macro-element model for the seismic analysis of masonry buildings. *Earthquake Engineering & Structural Dynamics*, <http://dx.doi.org/10.1002/eqe.2335>.
- Perissin D. and Wang T. (2011). Time-series InSAR applications over urban areas in China. *IEEE Journal of Selected Topics in Applied Earth Observations and Remote Sensing*, 4(1):92-100.
- Perissin D., Prati C., Rocca F. (2009). PSInSAR analysis over the three gorges dam and urban areas in China. *Urban Remote Sensing Joint Event*, 2009 Joint, pp. 1–5.
- Phien-Wej N., Giao P.H., Nutalaya P. (2006). Land subsidence in Bangkok, Thailand. *Engineering Geology*, 82:187-201.
- Pitilakis K. D. and Fotopoulou S. D. (2015). Vulnerability assessment of buildings exposed to co-seismic permanent slope displacements.

- Proceedings of the XVI ECSMGE – Geotechnical Engineering for Infrastructure and Development*, 151-173.
- Pickhaver J. A., (2006). Numerical modelling of building response to tunnelling. *PhD thesis*, Department of Engineering Science, University of Oxford.
- Poland, J.F. (1984). Guidebook to Studies of Land Subsidence Due to Ground-Water Withdrawal, prepared for the International Hydrological Programme, Working Group 8.4, UNESCO, Book Crafters, Chelsea, Massachusetts, pp. 16.
- Polshin D. E. and Tokar R. A., (1957). Maximum Allowable Non-uniform Settlement of Structures. *Proc. 4th Int. Conference Soil Mechanics and Foundation Engineering*, London, Butterworths Scientific Publications, 402–405.
- Potts D. M. and Addenbrooke, (1997). A structure's influence on tunneling-induced ground movements. *Proc. Instn. Civ. Engrs. Geotechn. Engng.*, Vol 125, 109-125.
- Pratesi, F., Tapete, D., Terenzi, G., Del Ventisette C., Moretti, S., 2015. Structural Assessment of Case Study Historical and Modern Buildings in the Florentine Area Based on a PSI-Driven Seismic and Hydrogeological Risk Analysis. G. Lollino et al. (eds.), *Engineering Geology for Society and Territory – Vol. 8*, DOI 10.1007/978-3-319-09408-3\_60, Springer International Publishing Switzerland 2015.
- Prati C., Ferretti A., Perissin D. (2010). Recent advances on surface ground deformation measurement by means of repeated space-borne SAR observations. *Journal of Geodynamics*, 49:161–170.
- Prokopovich N.P., Marriott M.J. (1983). Cost of Subsidence to the Central Valley Project, California. *Association of Engineering Geologist Bulletin*, 20(3):325-332.
- Professional Broking (2007). Subsidence costs sinking. *Professional Broking*, January 2007.
- Raucoles D., Maisons C., Carnec C., Le Mouelic S., King C., Hosford S. (2003). Monitoring of slow ground deformation by ERS radar interferometry on the Vauvert salt mine (France). Comparison with ground-based measurement. *Remote Sensing of Environment*, 88:468–478.
- Reale D., Fornaro G., Pauciuolo A., Zhu X., Bamler R. (2011a). Tomographic imaging and monitoring of buildings with very high resolution SAR data. *IEEE Geoscience and Remote Sensing Letters*, 8:661–665.

- Reale D, Nitti D O, Peduto D, Nutricato R, Bovenga F and Fornaro G (2011b). Post-seismic deformation monitoring with the COSMO/SKYMED constellation. *IEEE Geoscience and Remote Sensing Letters*, 8:696–700.
- Reilinger R.E., Ergintav S., Bürgmann S., McClusky S., Lenk O., Barka A., Gurkan O., Hearn L., Feigl K.L., Cakmak R., Aktug B., Ozener H., Töksoz M.N. (2000). Coseismic and postseismic fault slip for the 17 August 1999, M=7.5, Izmit, Turkey earthquake. *Science*, 289(5484):1519-1524.
- Remondo J., Bonachea J., Cendrero A., (2005). A statistical approach to landslide risk modelling at basin scale: from landslide susceptibility to quantitative risk assessment. *Landslides*, 2:321-328.
- Remondo J., Bonachea J., Cendrero A., (2008). Quantitative landslide risk assessment and mapping on the basis of recent occurrences. *Geomorphology*, 94:496–507.
- Ricceri G. (2007). Il futuro di Venezia tra subsidenza ed eustatismo. *Rivista Italiana di Geotecnica*, 3, Patron Editore (BO), (in Italian).
- Rignot E.J., Gogineni S.P., Krabill W.B., Ekholm S. (1997). North and northeast Greenland ice discharges from satellite radar interferometry. *Science*, 276:934-937.
- Rocca F. (2003) 3D motion recovery with multi-angle and/or left right Interferometry. In: Proceedings 3rd international workshop on ERS SAR interferometry, *FRINGE 2003*, Frascati, 2–5 Dec 2003. ESA SP-550.
- Rosen P., Werner C., Fielding E., Hensley S., Buckley S., Vincent, P. (1998). A seismic creep along the San Andreas fault northwest of Parkfield, CA measured by radar interferometry. *Geophysical Research Letters*, 25(6):825-828.
- Rossetto T., Elnashai A., (2003). Derivation of vulnerability functions for European-type RC structures based on observational data. *Engineering Structures*, 25:1241–1263.
- Rota M., Penna A., Strobbia C., (2006). Typological fragility curves from Italian earthquake damage data. *Proceedings 1st European conference on earthquake engineering and seismology*, Geneva, paper (No. 386).
- Rott H., Scheuchl B., Siegel A., Grasemann B. (1999). Monitoring very slow slope movements by means of SAR interferometry: A case study from a mass waste above a reservoir in the Ötztal Alps, Austria. *Geophysical Research Letters*, 26(11): 1629–1632.



- Rüsch H. and Mayer H., (1964). Bauschaden als Folge der Durchbiegung von Stahlbeton-Bauteilen, *Deutscher Ausschuss für Stahlbeton*, Berlin, No. 10. (in German).
- Sabetta F., Goretti A. and A. Lucantoni, (1998). Empirical fragility curves from damage surveys and estimated strong ground motion. *11th European Conference on Earthquake Engineering, Paris*, CD-ROM, ISBN 90 5410 982 3, Balkema.
- Saeidi A., Deck O. and Verdel, T. (2009). Development of building vulnerability functions in subsidence regions from empirical methods. *Engineering Structures*, 31, 10:2275–2286.
- Saeidi A., Deck O., Verdel T. (2012). Development of building vulnerability functions in subsidence regions from analytical methods. *Geotechnique*, 62 (2):107–120.
- Safeland Deliverable 2.5, (2011). Physical vulnerability of elements at risk to landslides: Methodology for evaluation, fragility curves and damage states for buildings and lifelines. Edited for the SafeLand European project by: Stumpf, A., Malet, J.-P., and Kerle, N., available at: <http://www.safeland-fp7.eu>.
- Salvi S., Atzori S., Tolomei C., Allievi J., Ferretti A., Rocca F., Prati C., Stramondo S., Feuillet N. (2004). Inflation rate of the Colli Albani volcanic complex retrieved by the permanent scatterers SAR interferometry technique. *Geophysical Research Letters*, 31(12), L12606.
- Sanabria M.P., Guardiola-Albert C., Tomas R., Herrera G., Prieto A., Sanchez H., Tessitore S. (2014). Subsidence activity maps derived from DInSAR data: Orihuela case study. *Natural hazards and earth system sciences*, 14:1341–1360.
- Scavia C. and Castelli M. (2003). The IMIRILAND project-Impact of Large Landslides in the Mountain Environment: identification and Mitigation of Risk. In: *Seismic and Landslide Risk in the European Union*, edited by: Yeroianni, M., *Workshop Proceedings*, 12–13 November 2002, pp. 82–91.
- Schack L., Soergel U. (2014). Exploiting regular patterns to group persistent scatterers in urban areas. *IEEE Journal of Selected Topics in Applied Earth Observations and Remote Sensing*, 7 (10), 4177–4183.
- Shi X., Wu J., Ye S., Zhang Y., Xue Y., Wei, Z. and Yu, J. (2008). Regional land subsidence simulation in Su-Xi-Chang area and Shanghai City, China. *Engineering Geology*, 100(1):27-42.

- Skempton A.W. (1953). The colloidal activity of clays. *Proc. 3rd International Conference on Soil Mechanics and Foundation Engineering*, Zurich, pp. 7-61.
- Skempton A. W. and MacDonald D. H., (1956). Allowable Settlement of Buildings. *P. I. Civil Eng.*, 5, Part III, 727–768.
- Son M. and Cording J., (2007). Evaluation of Building Stiffness for Building Response Analysis to Excavation-Induced Ground Movements. *Journal of Geotechnical and Geoenvironmental Engineering-ASCE*, 995–1002.
- Sowers G. F., (1962). Shallow Foundations. *Foundation Engineering*, G. A. Leonards (eds.), *McGraw-Hill Book Co.*, New York, NY, USA, 525–632, 1962.
- Stafleu J., Maljers D., Gunnink J.L., Menkovic A., Busschers F.S. (2011). 3D modeling of the shallow subsurface of Zeeland, the Netherlands. *Netherlands Journal of Geosciences-Geologie en Mijnbouw*, 90-4:293–310.
- Stramondo S., Bozzano F., Marra F., Wegmüller U., Cinti F.R., Moro M., Saroli M. (2008). Subsidence induced by urbanisation in the city of Rome detected by advanced InSAR technique and geotechnical investigations. *Remote Sensing of Environment*, 112:3160–3172, doi:10.1016/j.rse.2008.03.008.
- Stramondo S., M. Saroli C., Tolomei M., Moro F., Doumaz A., Pesci F., Loddo P., Baldi, and Boschi E. (2007). Surface movements in Bologna (Po Plain-Italy) detected by multitemporal DInSAR. *Remote Sensing of Environment*, 110:304–316.
- Strozzi T., Farina P., Corsini A., Ambrosi C., Thüning M., Zilger J., Wilesmann A., Wegmüller U., Werner C. (2005). Survey and monitoring of landslide displacements by means of L-band satellite SAR interferometry. *Landslide*, 2(3):193–201.
- Strozzi T., Wegmüller U., Tosi L., Bitelli G. and Spreckels V. (2001). Land subsidence monitoring with differential SAR interferometry. *PE&RS*, 67(11):1261-1270.
- Squarzonì C., Delacourt C., Allemand P. (2003). Nine years of spatial and temporal evolution of the LaVallette landslide observed by SAR interferometry. *Engineering Geology*, 68:53–66.
- Swiss RE (2011). The hidden risks of climate change: An increase in property damage from soil subsidence in Europe. [http://media.swissre.com/documents/Soil Subsidence Publication en 0718.pdf](http://media.swissre.com/documents/Soil%20Subsidence%20Publication%20en%200718.pdf).

- Syvitski J.P.M., Kettner A.J., Overeem I., Hutton E.W.H., Hannon M.T., Brakenridge R.G., Day J., Vörösmarty C., Saito Y., Giosam L., Nicholls R.J. (2009). Sinking deltas due to human activities. *Nature Geoscience*, 2(10):681–686. <http://dx.doi.org/10.1038/ngeo629>.
- Terzaghi K. (1950). Mechanism of landslides. Paige, S., Editor, 1950. *Application of Geology to Engineering Practice Geol. Soc. Am.*, Berkeley Vol., pp. 83–123.
- The Institution of Structural Engineers, (1994). Subsidence of low rise buildings. *The Institution of Structural Engineers*, London, pp. 106.
- Timoshenko S. P., (1955). *Vibration Problems in Engineering*, 3rd edn. Toronto, New York, London: D. van Nostrand Co.
- Tofani V., Raspini F., Catani F., Casagli N. (2014). Persistent scatterer interferometry (PSI) technique for landslide characterization and monitoring. In: Sassa, K., Canuti, P., Yueping, Y. (Eds.), *Landslide Science for a Safer Geoenvironment*, Vol. 2: Methods of Landslide Studies. Springer International Publishing. ISBN: 9783319050492, pp. 351–357.
- Tomás, R., Cano, M., Garcia-Barba, J., Vicente, F., Herrera, G., Lopez-Sanchez, J.M., 2013. Monitoring an earthfill dam using differential SAR interferometry: La Pedrera dam, Alicante, Spain. *Engineering Geology*, 157.
- Tomas R., Herrera G., Delgado J., Lopez-Sanchez J.M., Mallorqui J., Mulas J. (2010). A ground subsidence study base on DInSAR data: calibration of soil parameters and subsidence prediction in Murcia City (Spain). *Engineering Geology*, 111:19–30.
- Tomas R., Romero R., Mulas J., Marturia J.J., Mallorqui J.J., Lopez-Sanchez J.M., Herrera G., Gutierrez F., Gonzalez P.J., Fernandez Torres J., Duque S., Concha-Dimas A., Cocksley G., Castaneda del Alamo C., Carrasco D., Blanco P. (2014). Radar interferometry techniques for the study of ground subsidence phenomena: a review of practical issues through cases in Spain. *Environmental Earth Sciences*, 71(1): 163–181.
- Tommasi P., Pellegrini P., Boldini D., Ribacchi R. (2006). Influence of rainfall regime on hydraulic conditions and movement rates in the overconsolidated clayey slope of the Orvieto hill (central Italy). *Canadian Geotechnical Journal*, 43:70-86.
- Topal T. and Akin M. (2008). Investigation of a landslide along a natural gas pipeline (Karacabey-Turkey). In Chen et al (eds), *Proceedings, 10th*

- International Symposium on Landslides and Engineered Slopes*, Xi'an, China, 2:1647–1652.
- Tosi L., Teatini P., Strozzi T. (2013). Natural versus anthropogenic subsidence of Venice. *Scientific Reports*, 3:2710.
- Triggiani M. (2011). Le tecniche di interferometria radar applicate allo studio della subsidenza nel Golfo di Manfredonia. *Digilabs*, 2011, pp. 92, ISBN 8875220395, 9788875220396.
- UNEP - United Nations Environment Programme. (1997). World Atlas of Desertification. Second Edition, Nairobi, pp. 182 – ISBN: 0340691662.
- UNESCO - United Nations Educational, Scientific and Cultural Organization. <http://landsubsidence-unesco.org/> (last access, 21.02.2017).
- USGS, 2016. <http://dds.cr.usgs.gov/srtm/> (accessed 28.10.2016).
- van Asselen S., Stouthamer E., Smith N.D. (2010). Factors controlling peat compaction in alluvial floodplains – a case study in the cold-temperature Cumberland Marshes. *Canada. J. Sediment. Res.*, 80:155–166.
- van der Meulen M.J., Doornenbal J.C., Gunnink J.L., Stafleu J., Schokker J., Varnes R.W., van Geer F.C., van Gessel S.F., van Heteren S., van Leeuwen R.J.W., Bakker M.A.J., Bogaard P.J.F., Busschers F.S., Griffioen J., Gruijters S.H.L.L., Kiden P., Schroot B.M., Simmelink H.J., van Berkel W.O., van der Krogt R.A.A., Westerhoff W.E., van Daalen T.M. (2013). 3D geology in a 2D country: perspectives for geological surveying in the Netherlands. *Netherlands Journal of Geosciences-Geologie en Mijnbouw*, 92-4:217–241.
- van Rooy J.L., (1989). A proposed classification system for dolomitic areas south of Pretoria. *Contributions to Engineering Geology*, 1:57-65.
- van Rummelen F.F.F.E. (1965). Zeeuwsch Vlaanderen, Bladen Zeeuwsch Vlaanderen, West en Oost, Toelichtingbij de Geologische Kaart van Nederland, 1:50.000. *Rijks Geologische Dienst Haarlem*, pp. 79 (in Dutch).
- van Rummelen F.F.F.E. (1972). Blad Walcheren, Toelichtingbij de Geologische kaart van Nederland 1:50.000. *Rijks Geologische Dienst, Haarlem*, pp. 120 (in Dutch).
- van Westen C. J., (2004). Geo-information tools for landslide risk assessment: an overview of recent developments. Landslides: evaluation and stabilization - glissement de terrain: Evaluation et Stabilisation: proceedings of the 9th Int. Symp on Landslides, ed. by

- W. Lacerda, M. Erlich, S.A.B. Fontoura, A.S.F. Sayao. Balkema, pp. 39-56.
- van Westen, C.J., Castellanos Abella E.A., Sekhar L.K., (2008). Spatial data for landslide susceptibility, hazards and vulnerability assessment: an overview. *Engineering Geology*, 102, 3-4:112-131.
- Varnes D.J. (1958). Landslide Types and Processes. In *Special Report 29: Landslide and Engineering Practice* (E.B. Eckel, ed.), HRB, National Research Council, Washington, D.C., pp. 20-47.
- Varnes D. J. (1978). Slope Movement Types and Processes. Special Report 176: Landslides: Analysis and Control, edited by: Schuster, R. L. and Krizek, R. J., TRB, National Research Council, Washington, DC, 11–33, 1978.
- Varnes D.J., (1984). Landslide hazard zonation: a review of principles and practice. *Natural Hazards 3*, UNESCO, Paris, pp. 63.
- Vilardo G., Ventura G., Terranova C., Matano F. and Nardo S. (2009). Ground deformation due to tectonic, hydrothermal, gravity, hydrogeological, and anthropic processes in the Campania Region (Southern Italy) from permanent scatterers synthetic aperture radar interferometry. *Remote Sensing of Environment*, 113:197–212.
- Vos P.C. and Van Heeringen R.M. (1997). Holocene geology and occupation history of the Province of Zeeland. In: Fischer, M.M. (Eds.), *Holocene Evolution of Zeeland* (SW Netherlands), pp. 5–110.
- Wang Y., Zhu X., Shi Y., Bamler R. (2012). Operational TomoSAR processing using TerraSAR-X high resolution spotlight stacks from multiple view angles. In: *Proceedings IEEE 2012 IGARSS Conference*, (Munich, Germany), pp. 7047–7050.
- Wang Z., Liu G., Cui Q. (2009). Monitoring the coal mining subsidence in Jibei mine area using DInSAR technique. ICIECS'09, *Inform. Eng. Comput. Science*, 1–4.
- Wasowki J., Bovenga F. (2014). Investigating landslides and unstable slopes with satellite multi temporal interferometry: current issues and future perspectives. *Engineering Geology*, 174:103–138.
- Wegmüller U., Werner C., Strozzi T., Wiesman A. (2005). ERS\_ASAR Integration in the Interferometric Point Target Analysis. In: *Proceedings Fringe 2005 Workshop*, Frascati, Italy, 28 November–2 December.
- Wright T., Parsons B., Fielding E. (2001). Measurement of interseismic strain accumulation across the North Anatolian Fault by satellite radar interferometry. *Geophysical Research Letters*, 28(10):2117-2120.

- Worawattanamateekul J., Hoffmann J., Adam N., Kampes B. (2003). Urban deformation monitoring in Bangkok metropolitan (Thailand) using differential interferometry and the permanent scatterer technique. *FRINGE 2003 workshop*, Frascati, Italy.
- Zhang L.M., Ng A.M.Y. (2005). Probabilistic limiting tolerable displacements for serviceability limit state design of foundations. *Geotéchnique*, 55 (2):151–161.
- Zebker H.A., Goldstein R.M. (1986). Topographic mapping from interferometric synthetic aperture radar observations. *Journal of Geophysical Research*, 91(B5): 4993–4999.
- Zebker H. A., Rosen P. A., Hensley S. (1997). Atmospheric effects in interferometric synthetic aperture radar surface deformation and topographic map. *Journal of Geophysical Research*, 102(B4):7547–7563.
- Zhu X., Bamler R. (2010). Very high resolution spaceborne SAR tomography in urban environment. *IEEE Transactions on Geoscience and Remote Sensing*, 48:4296–4308.
- Zhou Y. (2000). Research and treatment of Shazhou Landslide, Sichuan. In: Bromhead et al (eds), *Landslides in research, theory and practice. Proceedings, 8th International Symposium on Landslides*, Cardiff, UK, 3:1647–1652.
- Zuccaro G., Cacace F., (2015). Seismic vulnerability assessment based on typological characteristics. The first level procedure “SAVE”. *Soil Dynamics and Earthquake Engineering*, 69:262-269.

## APPENDIX A

### **Validation of PSInSAR data accuracy: cross-comparison with leveling data.**

This Appendix concerns the validation of PSInSAR data accuracy used in Chapter 6 to derive the displacement suffered by buildings in subsidence-affected areas with ground measurements collected via topographic leveling techniques.

The availability of these measures allowed carrying out both qualitative and quantitative cross-comparisons with PSInSAR data.

As for the leveling data, the analyzed dataset includes a total of 180 bolts, identifiers of the leveling points (Figure A.1), which the municipality of Schiedam placed on the façades of the buildings composing the row houses in Figure A.1 in order to detect possible critical situations at the building foundation level due to ground settlements in the period 2004-2014.<sup>6</sup>

As for PSInSAR data, in order to better appreciate the building response to ground movements and to carry out a proper cross-comparison with the leveling data, only the PSInSAR data at the top of the buildings (Figure A.2) were used for the analysis.

In particular, for a given portion of each monitored building, the qualitative comparison dealt with the annual average velocity exhibited by the leveling point on the building and the mean PS velocity value computed as the mean of the yearly velocity values of PS located in the same portion of the building. For this purpose, the yearly average velocities exhibited by each leveling point placed on the façade of the buildings (Figure A.1) were calculated in the same period of PSInSAR acquisitions (2009- 2014), and compared with the PSInSAR velocities on the top of buildings (Figure A.2).

---

The contents of Appendix A are published in:

Nicodemo G., Peduto D., Ferlisi S., Maccabiani J. (2016). Investigating building settlements via very high resolution SAR sensors. In: *Life-Cycle of Engineering Systems: Emphasis on Sustainable Civil Infrastructure*. Delft (The Netherlands) 16-19 October 2016, Londra CRC Press/Balkema, Taylor & Francis Group, pp. 2256-2263.

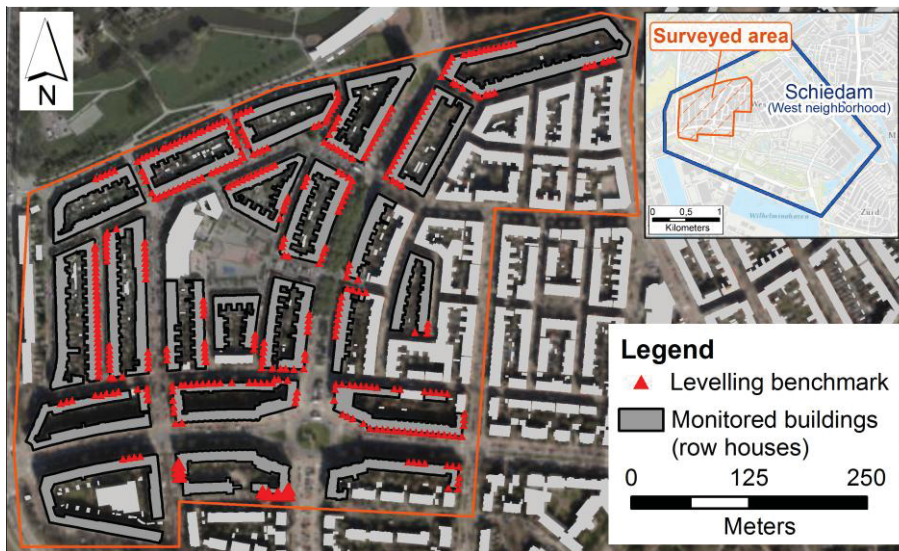


Figure A.1 Map of topographic leveling benchmarks provided by Schiedam municipality (period 2004-2014).

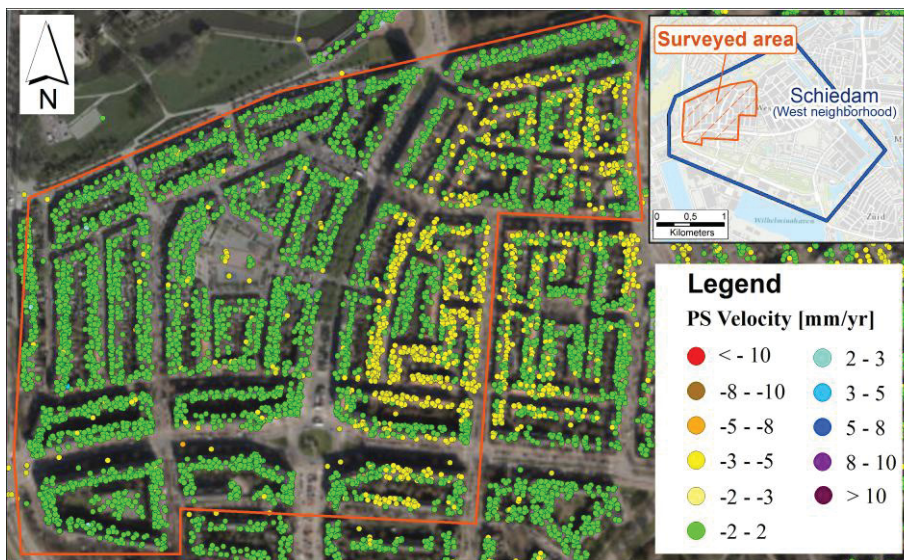


Figure A.2 Spatial distribution of ascending and descending orbit TerraSAR-X PS-InSAR data projected along the vertical direction (period 2009-2014) located on top of the buildings.



The results of the comparison are synthesized in the contingency table of Figure A.3. In particular, a movement threshold of 2 mm/yr (i.e. conservative on the PSInSAR accuracy) was set in order to identify buildings (or part of these) that are: *i*) moving for both measurement techniques; *ii*) not moving for both measurement techniques; *iii*) moving for leveling data and not moving for PSInSAR data and *iv*) vice-versa. Therefore, assuming that the true condition is the one for which the leveling velocities correctly identify the possibility that a building is moving (positive condition) or not moving (negative condition), the comparison with the recorded PSInSAR velocities allowed to identify the true positives (TP) and true negatives (TN) which represent consistent information on both datasets, and similarly the false positives (FP) and false negatives (FN) which instead represent the inconsistent information.

		PS-InSAR velocity	
		Positive (moving)	Negative (not moving)
Topographic leveling velocity	Positive (moving)	<b>TP</b>	<b>FN</b>
	Negative (not moving)	<b>FP</b>	<b>TN</b>

Figure A.3 PSInSAR-leveling contingency table with indication of the correct (green cells) and incorrect (red cells) rates.

The results of the comparison for 180 available leveling benchmarks (Table A.1) show a good fitting between leveling measurements and PSInSAR data (about 80%) for the monitored buildings. On the other hand, the occurrence of False negatives (FN) requires further investigation.

**Table A.1 Results of the PSInSAR-leveling contingency table.**

		PSInSAR velocity	
		Positive	Negative
Leveling velocity	Positive	12	37
	Negative	0	131

For this purpose, a quantitative comparison between the cumulative settlements recorded by leveling and PSInSAR benchmarks over a period of about 5 years was performed.

An example for two buildings is shown in Figure A.4a and b, for which the leveling-derived cumulative settlements were compared with the ones recorded by the closest PS. It is worth noting that the leveling benchmarks are located in the façade of the buildings, while the PS are located on the roofs. In the first case (Figure A.4a), assuming a linear trend in the period 2009-2014, PS recorded a cumulative settlement equal to 16.07 mm and the leveling point recorded a value of 17.2 mm with a difference of 1.13 mm. In the second case (Figure A.4b), the difference between 5-year PS cumulative settlement (2.06 mm) and the one pertaining to the closest leveling benchmark (3.44 mm) is 1.38 mm.

Extending the analysis to all 180 leveling points, the comparison of the yearly average velocity derived from leveling and PSInSAR data revealed an average difference of about 0.67 mm/yr with a standard deviation equal to 0.48 mm/yr.

The results further confirm the capability of the InSAR techniques of appreciating with high accuracy the settlements suffered by structures (e.g. buildings), with a good agreement between the different measurements and an accuracy up to the order of 1 mm/year for the average displacement velocity when, as in this case, data provided by very-high resolution radar sensors are used.

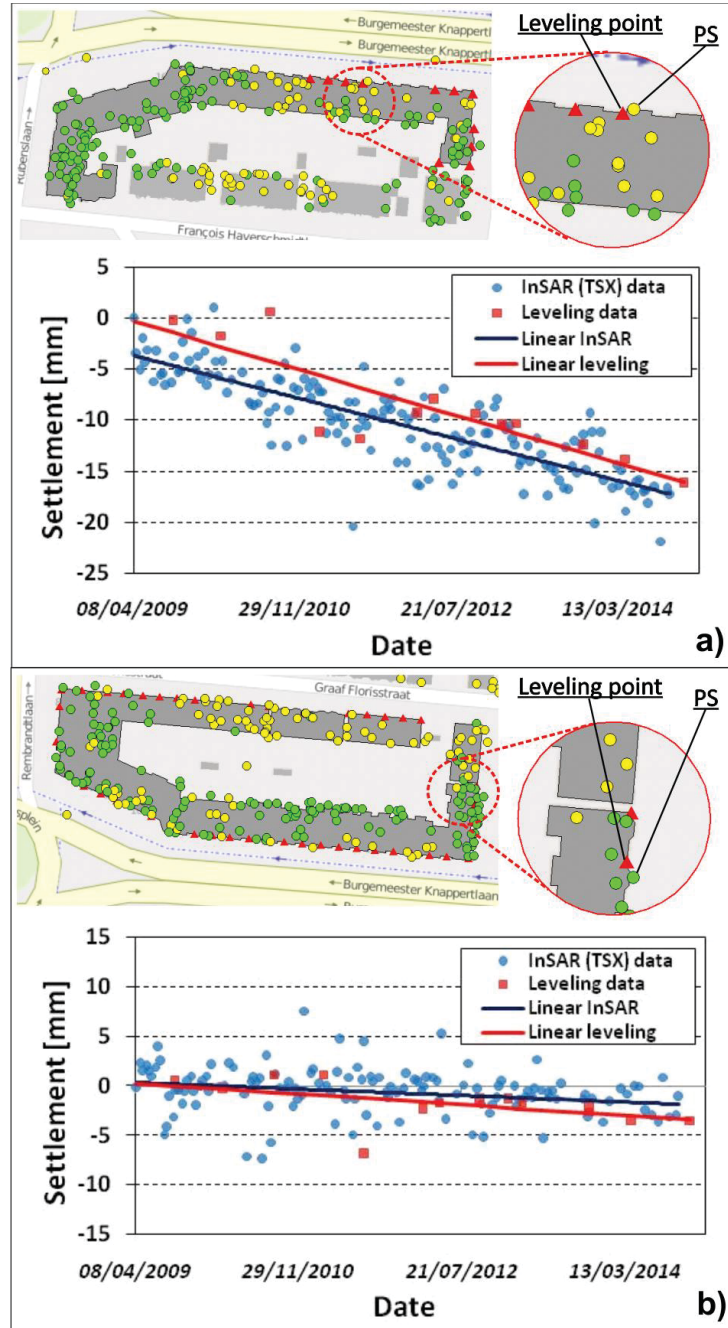


Figure A.4 Comparison between settlements derived from PSInSAR and leveling measurements in the period 2009-2014.

## APPENDIX B

### **Reliability assessment of the cumulative log-normal distribution function using the Kolmogorov-Smirnov (K-S) goodness-of-fit test.**

This appendix is devoted to show the results of the Kolmogorov-Smirnov (K-S) goodness-of-fit test that was performed in order to check the work hypothesis of using the cumulative lognormal distribution to describe the probability of reaching/exceeding a given damage level within the fragility curve construction.

The Kolmogorov-Smirnov goodness-of-fit test is a nonparametric test that allows verifying the fit of a cumulative distribution function of continuous variables. The test statistic is the maximum absolute difference “Dmax” (that is, usually the vertical distance) between the empirical and hypothetical cumulative distribution functions. This latter, must be always lower than a critical value “Dcrit” that is tabulated by the Authors for a small sample sizes ( $n < 35$ ), or can be computed using the proper equation in the case of large samples ( $n > 35$ ).

Figure B.1 shows the K-S test carried out on fragility curves derived for buildings in subsiding-affected area with shallow (Figure B.1a) and piled (Figure B.1b) foundations falling within of the neighborhood of Schiedam municipality (see Chapter 6 – Section 6.2.3).

The results confirm that the above work hypothesis is acceptable since the values (Table B.1) of the maximum distances (Dmax) between the considered log-normal distribution function for each damage level and the related empirical distribution function – defined according to the K-S test – are always lower than the critical values (Dcrit) provided by Kolmogorov–Smirnov for all significance levels ( $\alpha$ ) taken into account.

---

The contents of Appendix B are published in:

Peduto D., Nicodemo G., Maccabiani J., Ferlisi S. (2017). Multi-scale analysis of settlement-induced building damage using damage surveys and DInSAR data: A case study in The Netherlands. *Engineering Geology*, 218:117-133.

Peduto D., Ferlisi S., Nicodemo, G., Reale D., Pisciotta G., Gullà, G. (2017). Empirical fragility and vulnerability curves for buildings exposed to slow-moving landslides at medium and large scales. *Landslides* (in press), DOI: 10.1007/s10346-017-0826-7.

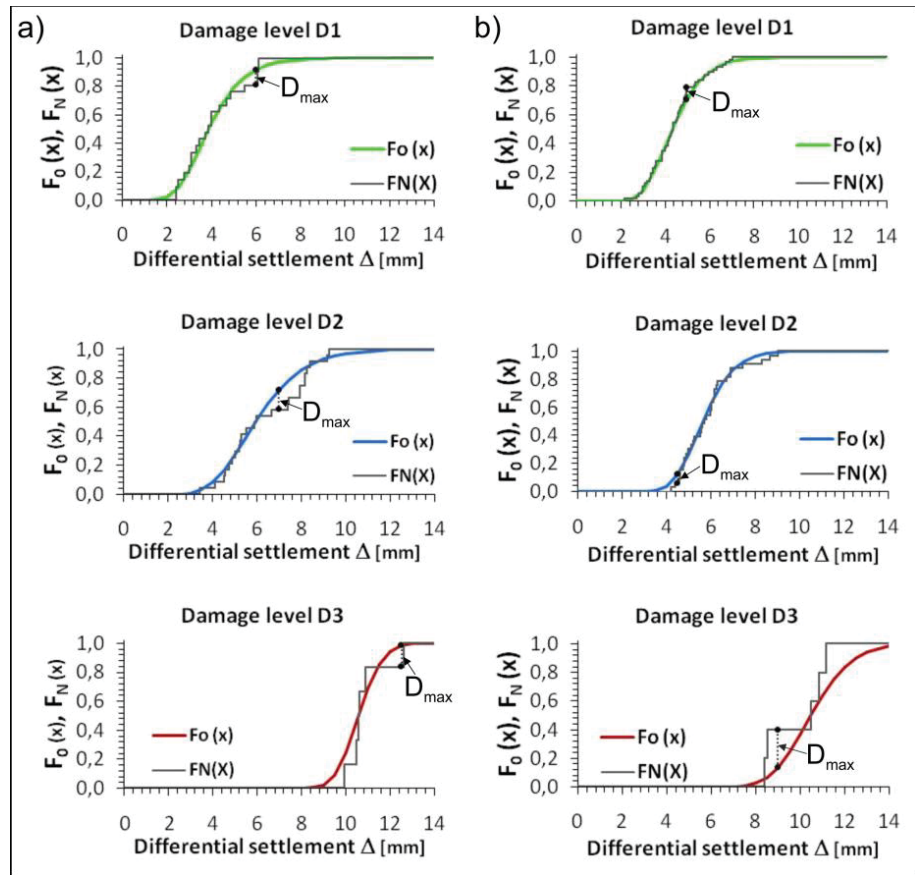


Figure B.1  $D_{max}$  estimation for the K-S goodness-of-fit test of the log-normal distribution function used for the generation of fragility curves for buildings with a) shallow and b) piled foundations within the Schiadam area.

Table B.1 Results of K-S test of derived fragility curves for buildings with shallow and piled foundations within the Schiadam area.

Damage level	Shallow foundation						Test $D_{max} < D_{crit}$
	$D_{max}$	$D_{crit}$	$D_{crit}$	$D_{crit}$	$D_{crit}$	$D_{crit}$	
		$\alpha=0.01$	$\alpha=0.05$	$\alpha=0.10$	$\alpha=0.15$	$\alpha=0.20$	
D1 (Very slight)	<b>0.108</b>	0.356	0.294	0.264	0.246	0.231	ok

D2 (Slight)	<b>0.137</b>	0.320	0.27	0.240	0.220	0.210	ok
D3 (Moderate)	<b>0.147</b>	0.618	0.521	0.470	0.436	0.410	ok
<b>Piled foundation</b>							
D1 (Very slight)	<b>0.083</b>	0.216	0.180	0.162	0.151	0.142	ok
D2 (Slight)	<b>0.063</b>	0.275	0.235	0.215	0.195	0.185	ok
D3 (Moderate)	<b>0.265</b>	0.669	0.454	0.510	0.424	0.446	ok

Similarly to the analysis carried out at detailed scale for buildings in subsiding-affected area, the reliability of the used cumulative lognormal distribution function was also checked using the K-S test for the fragility curves derived for the buildings in slow-moving landslide-affected areas within the Lungro municipality (see Chapter 7 – Section 7.2.4).

Also in such a case, the obtained results (Figure B.2) confirm the validity of the adopted work hypothesis since, as show in Table B.2, the critical values ( $D_{crit}$ ) provided by Kolmogorov–Smirnov for all significance levels ( $\alpha$ ) are always higher than ( $D_{max}$ ) value for all computed fragility functions relating to each considered damage level.

**Table B.2 Results of K-S test of derived fragility curves for masonry buildings within the Lungro area.**

Damage level	Shallow foundation						Test $D_{max} < D_{crit}$
	$D_{max}$	$D_{crit}$ $\alpha=0.01$	$D_{crit}$ $\alpha=0.05$	$D_{crit}$ $\alpha=0.10$	$D_{crit}$ $\alpha=0.15$	$D_{crit}$ $\alpha=0.20$	
	D1 (Very slight)	<b>0.350</b>	0.669	0.454	0.510	0.424	
D2	<b>0.182</b>	0.490	0.410	0.368	0.342	0.322	ok

Reliability assessment of the cumulative log-normal distribution function using the Kolmogorov-Smirnov (K-S) goodness-of-fit test

(Slight)							
D3 (Moderate)	<b>0.322</b>	0.577	0.486	0.436	0.405	0.381	ok
D4 (Severe)							
	<b>0.276</b>	0.733	0.624	0.564	0.575	0.494	ok
D5 (Very Severe)							
	<b>0.251</b>	0.929	0.842	0.776	0.726	0.684	ok

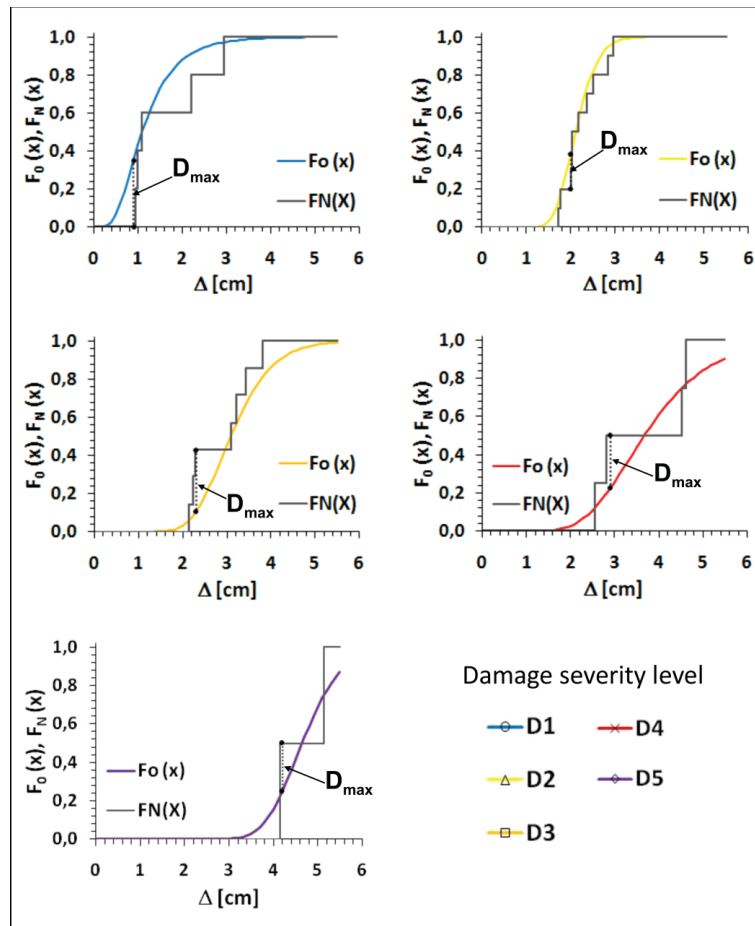


Figure B.2  $D_{max}$  estimation for the K-S goodness-of-fit test of the log-normal distribution function used for the generation of fragility curves for masonry buildings within the Lungro area.

# APPENDIX C

## Results of the numerical analysis in terms of damage exhibited by the masonry walls of a building subjected to differential settlements.

This Appendix presents the numerical results in terms of damage evolution exhibited by the masonry macro-elements (piers and spandrels) carried out, using a FME (Frame by macro elements) method, for a masonry building subjected to differential settlements. The analysis was performed for all the walls of the structure (exterior and interior), considering ten soil-foundation-structural models (see Chapter 8 - section 8.2), each of them subjected to differential settlements applied at the base of the foundation level with an increasing intensity ranging from 0 to 50 cm and four deformation modes (Figure C.1). The results for a total of forty simulations are shown in Figures C.2-C.41.

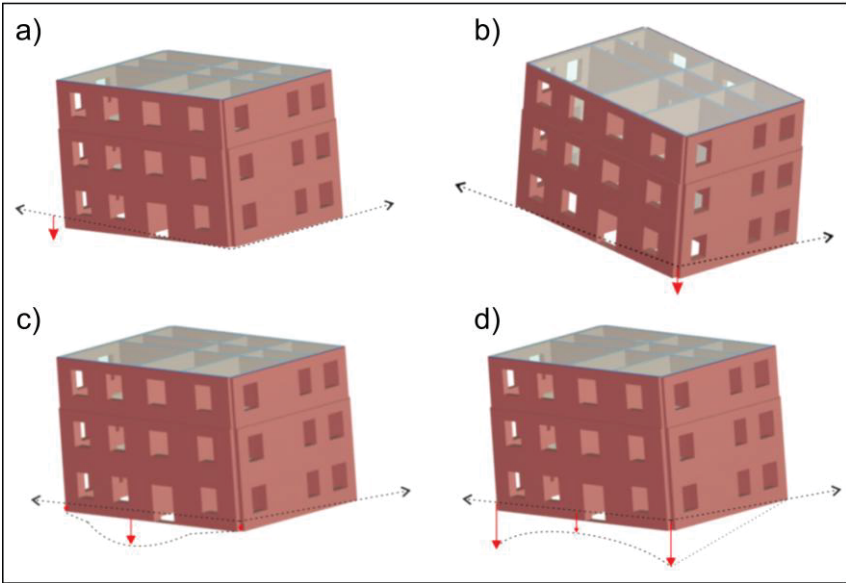


Figure C.1 Deformation modes considered for the parametric analysis: a) bilinear left; b) bilinear right; c) sagging; d) hogging.



Result of the numerical analysis in terms of damage exhibited by the masonry walls of a building subjected to differential settlements

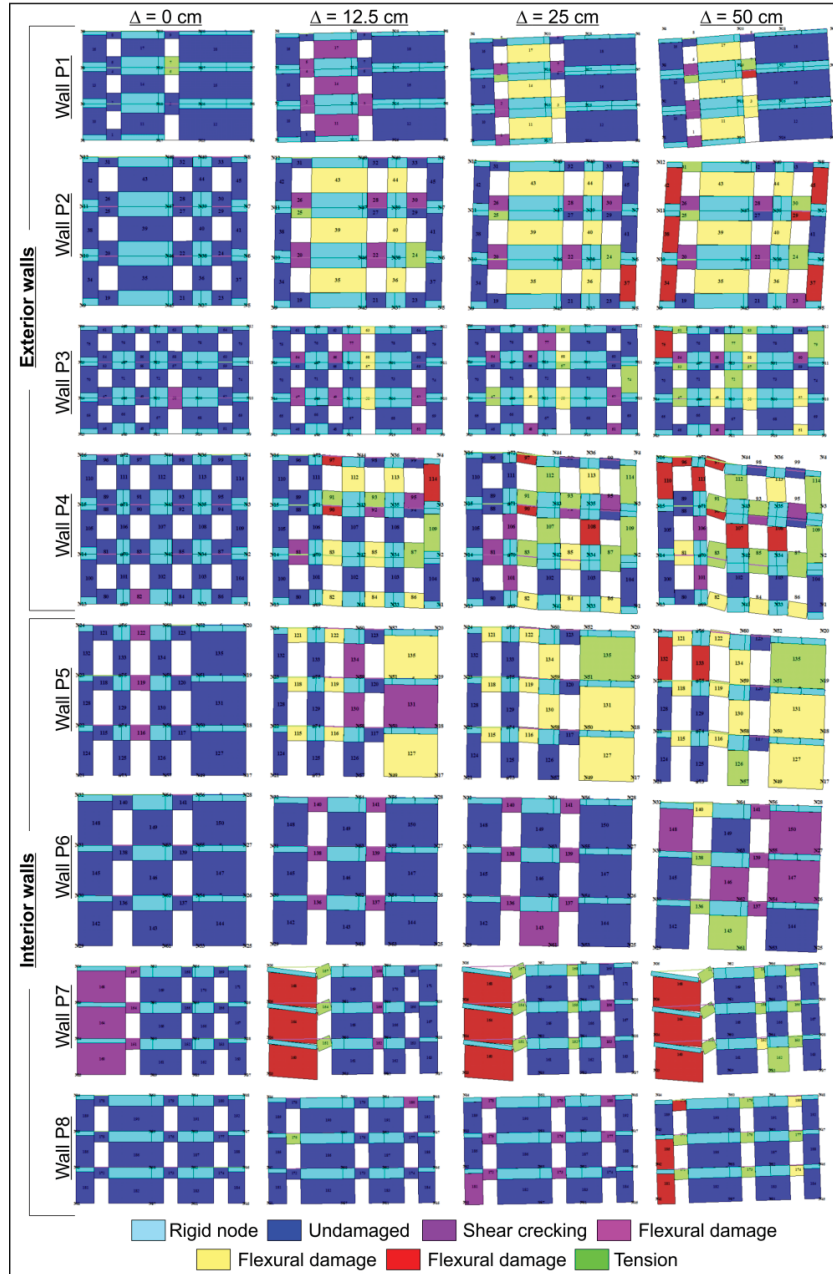


Figure C.2 Damage evolution of the exterior (P<sub>1</sub>, P<sub>2</sub>, P<sub>3</sub>, P<sub>4</sub>) and interior (P<sub>5</sub>, P<sub>6</sub>, P<sub>7</sub>, P<sub>8</sub>) walls of the masonry building M1 resting on soft soil (S1), during the progressive increase of the differential settlements from 0 to 50 cm applied with a bi-linear trend and a maximum value in the left corner.

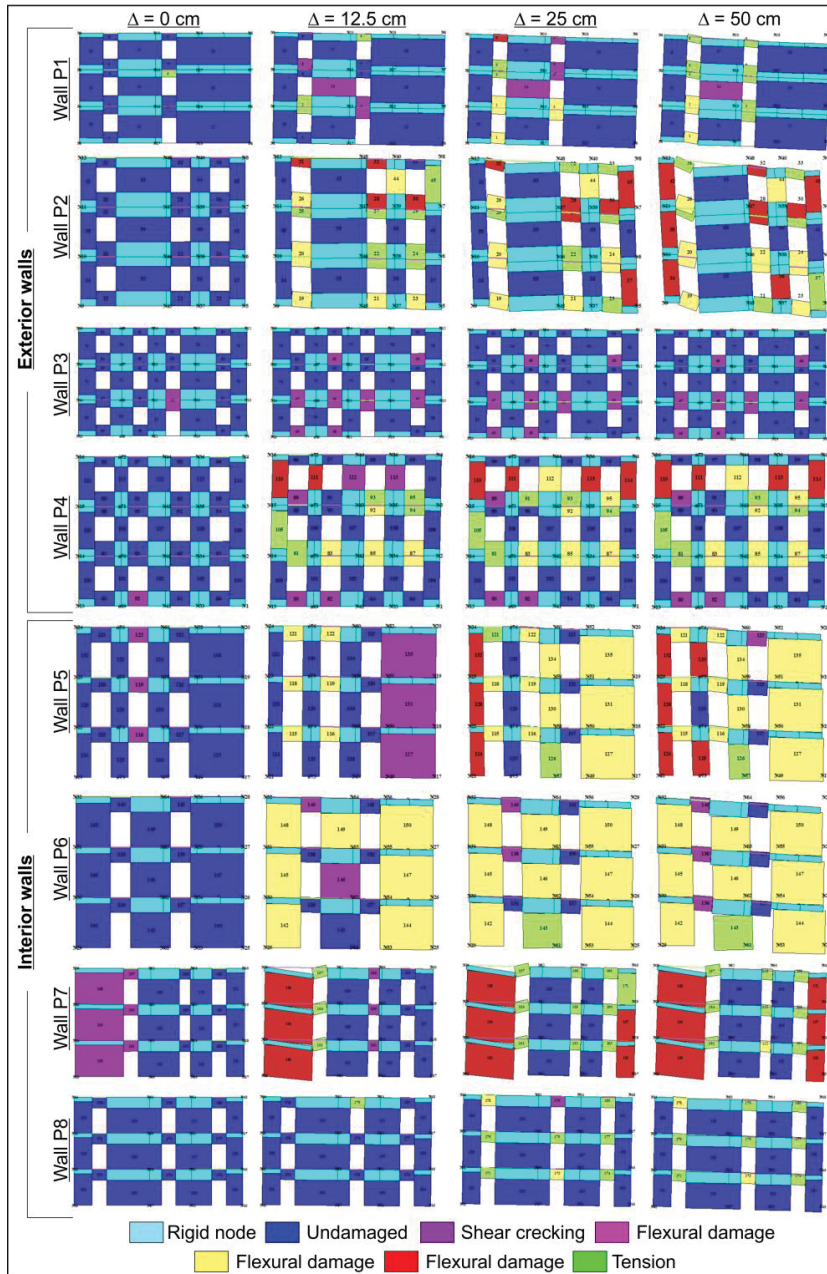


Figure C.3 Damage evolution of the exterior (P<sub>i</sub>, P<sub>2</sub>, P<sub>3</sub>, P<sub>4</sub>) and interior (P<sub>5</sub>, P<sub>6</sub>, P<sub>7</sub>, P<sub>8</sub>) walls of the masonry building M1 resting on soft soil (S1), during the progressive increase of the differential settlements from 0 to 50 cm applied with a bi-linear trend and a maximum value in the right corner.

Result of the numerical analysis in terms of damage exhibited by the masonry walls of a building subjected to differential settlements

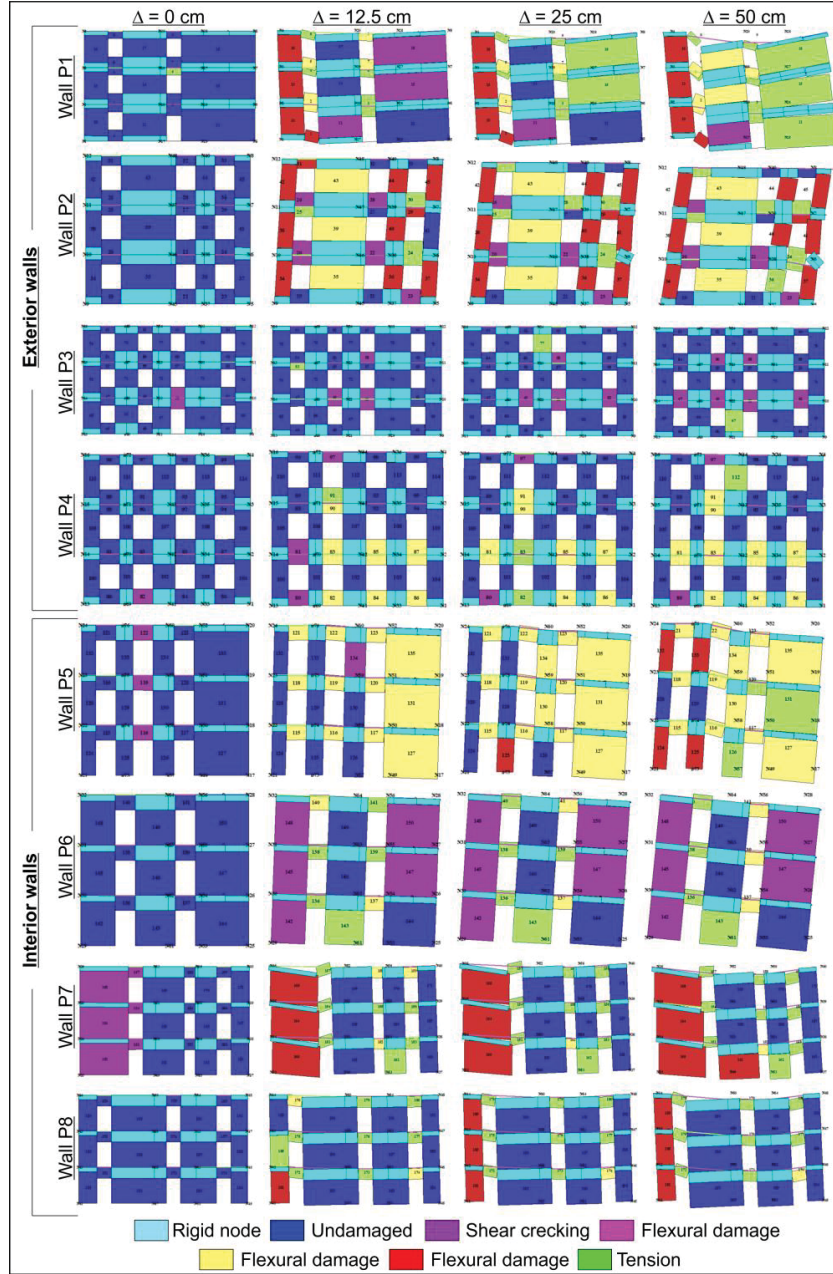


Figure C.4 Damage evolution of the exterior (P<sub>1</sub>, P<sub>2</sub>, P<sub>3</sub>, P<sub>4</sub>) and interior (P<sub>5</sub>, P<sub>6</sub>, P<sub>7</sub>, P<sub>8</sub>) walls of the masonry building M1 resting on soft soil (S1), during the progressive increase of the differential settlements from 0 to 50 cm applied according to a sagging configuration.

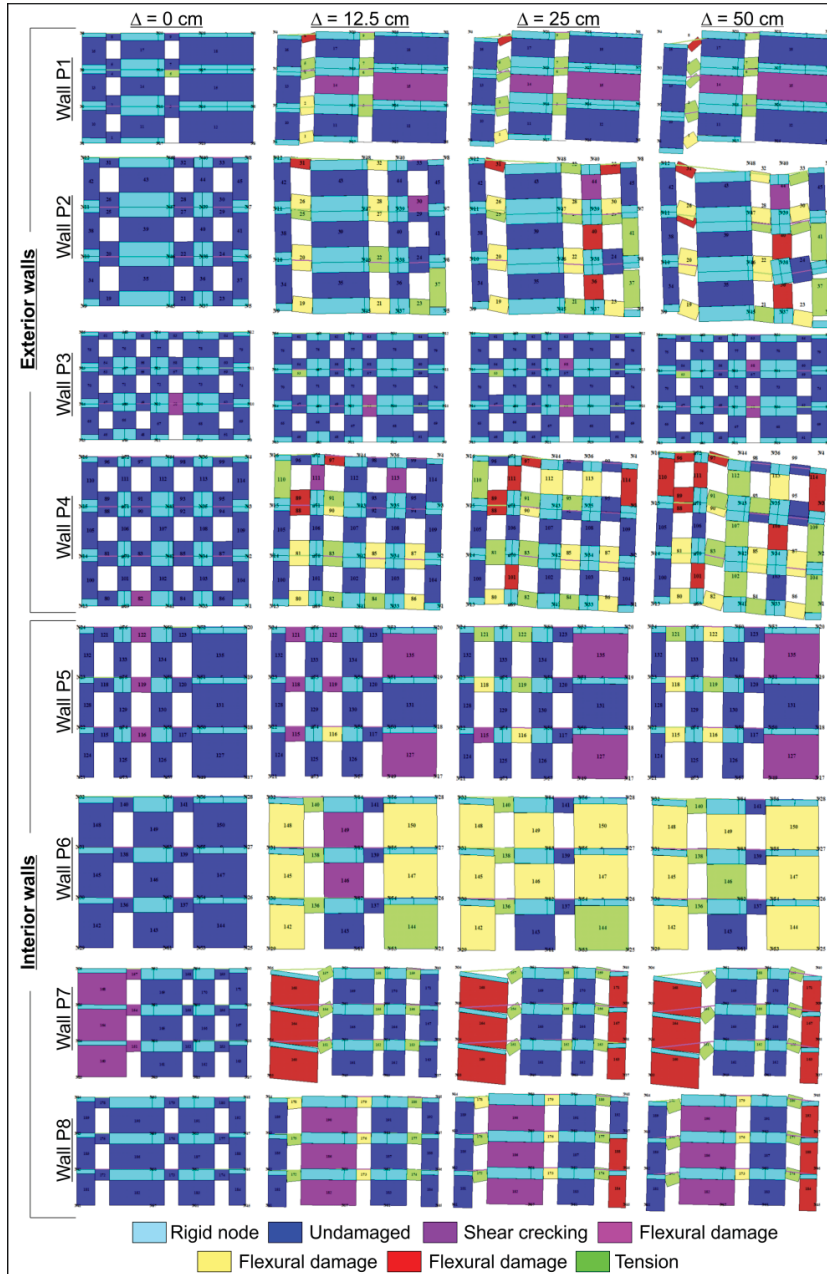


Figure C.5 Damage evolution of the exterior (P<sub>i</sub>, P<sub>2</sub>, P<sub>3</sub>, P<sub>4</sub>) and interior (P<sub>5</sub>, P<sub>6</sub>, P<sub>7</sub>, P<sub>8</sub>) walls of the masonry building M1 resting on soft soil (S<sub>1</sub>), during the progressive increase of the differential settlements from 0 to 50 cm applied according to a hogging configuration.

Result of the numerical analysis in terms of damage exhibited by the masonry walls of a building subjected to differential settlements

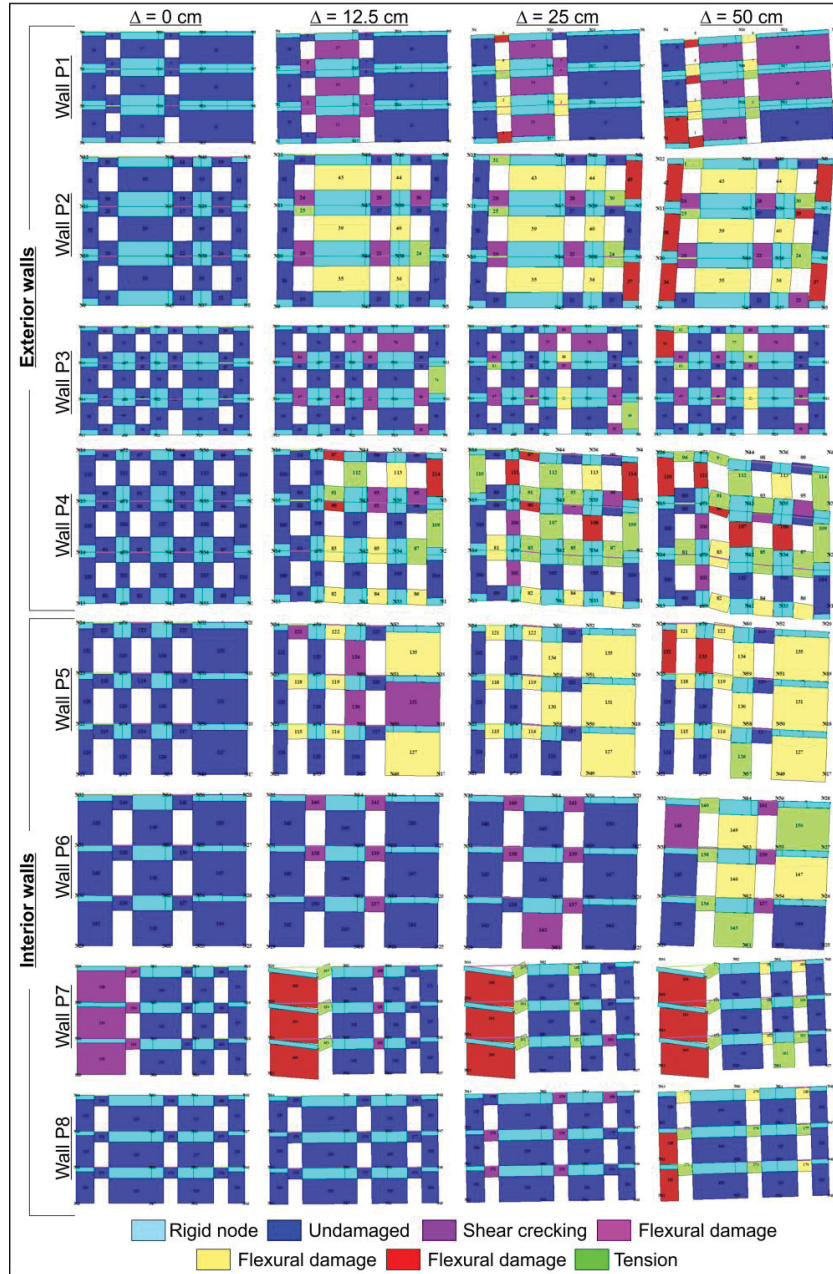


Figure C.6 Damage evolution of the exterior (P<sub>1</sub>, P<sub>2</sub>, P<sub>3</sub>, P<sub>4</sub>) and interior (P<sub>5</sub>, P<sub>6</sub>, P<sub>7</sub>, P<sub>8</sub>) walls of the masonry building M1 resting on soft clay (S2\_1), during the progressive increase of the differential settlements from 0 to 50 cm applied with a bi-linear trend and a maximum value in the left corner.

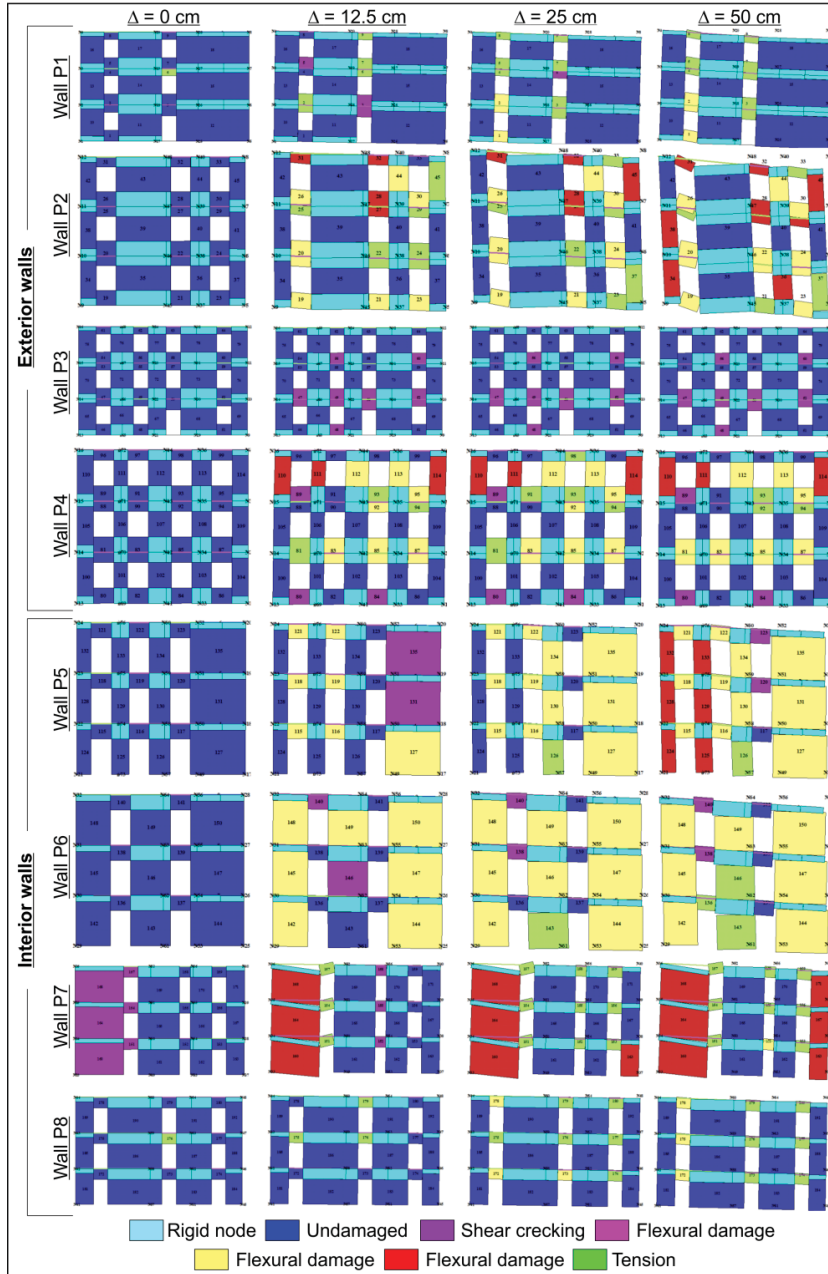


Figure C.7 Damage evolution of the exterior (P<sub>i</sub>, P<sub>2</sub>, P<sub>3</sub>, P<sub>4</sub>) and interior (P<sub>5</sub>, P<sub>6</sub>, P<sub>7</sub>, P<sub>8</sub>) walls of the masonry building M1 resting on soft clay (S2\_1), during the progressive increase of the differential settlements from 0 to 50 cm applied with a bi-linear trend and a maximum value in the right corner.

Result of the numerical analysis in terms of damage exhibited by the masonry walls of a building subjected to differential settlements

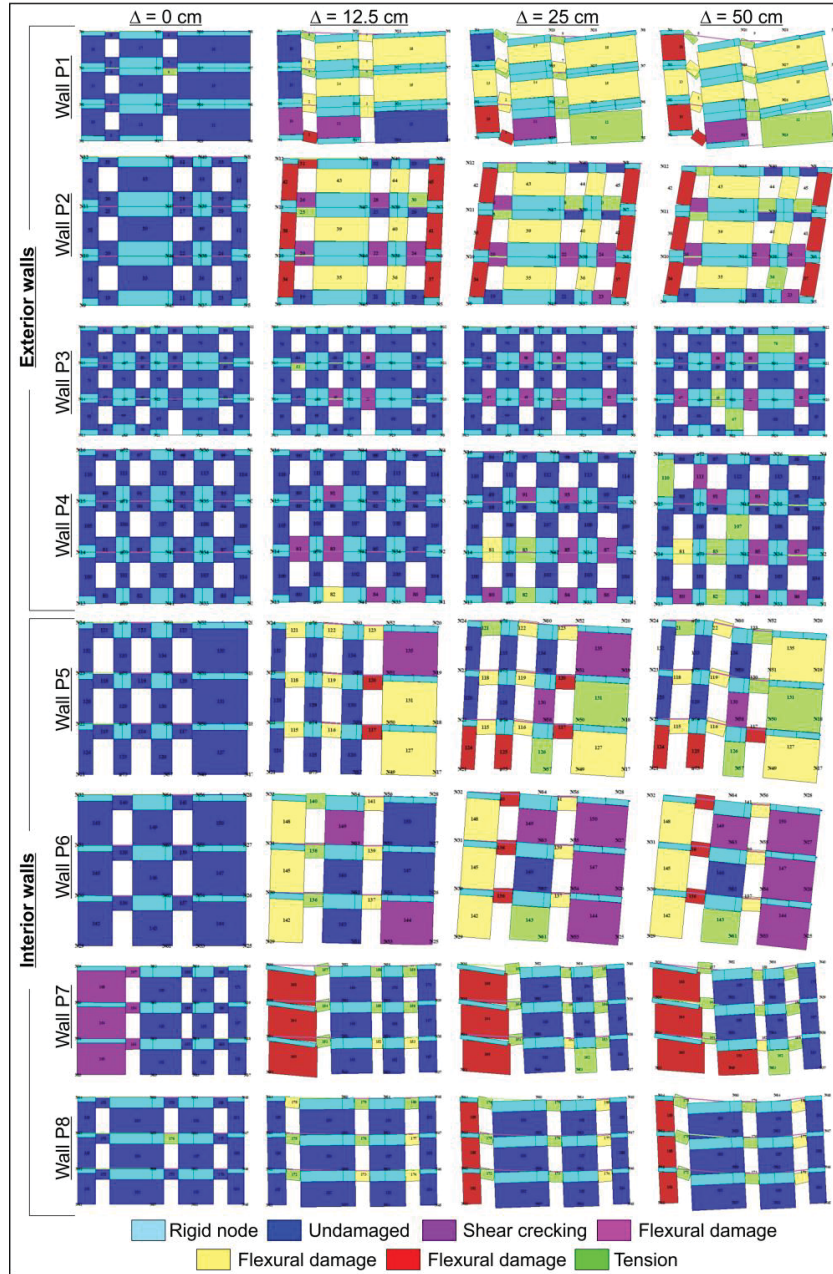


Figure C.8 Damage evolution of the exterior (P<sub>1</sub>, P<sub>2</sub>, P<sub>3</sub>, P<sub>4</sub>) and interior (P<sub>5</sub>, P<sub>6</sub>, P<sub>7</sub>, P<sub>8</sub>) walls of the masonry building M1 resting on soft clay (S2\_1), during the progressive increase of the differential settlements from 0 to 50 cm applied according to a sagging configuration.

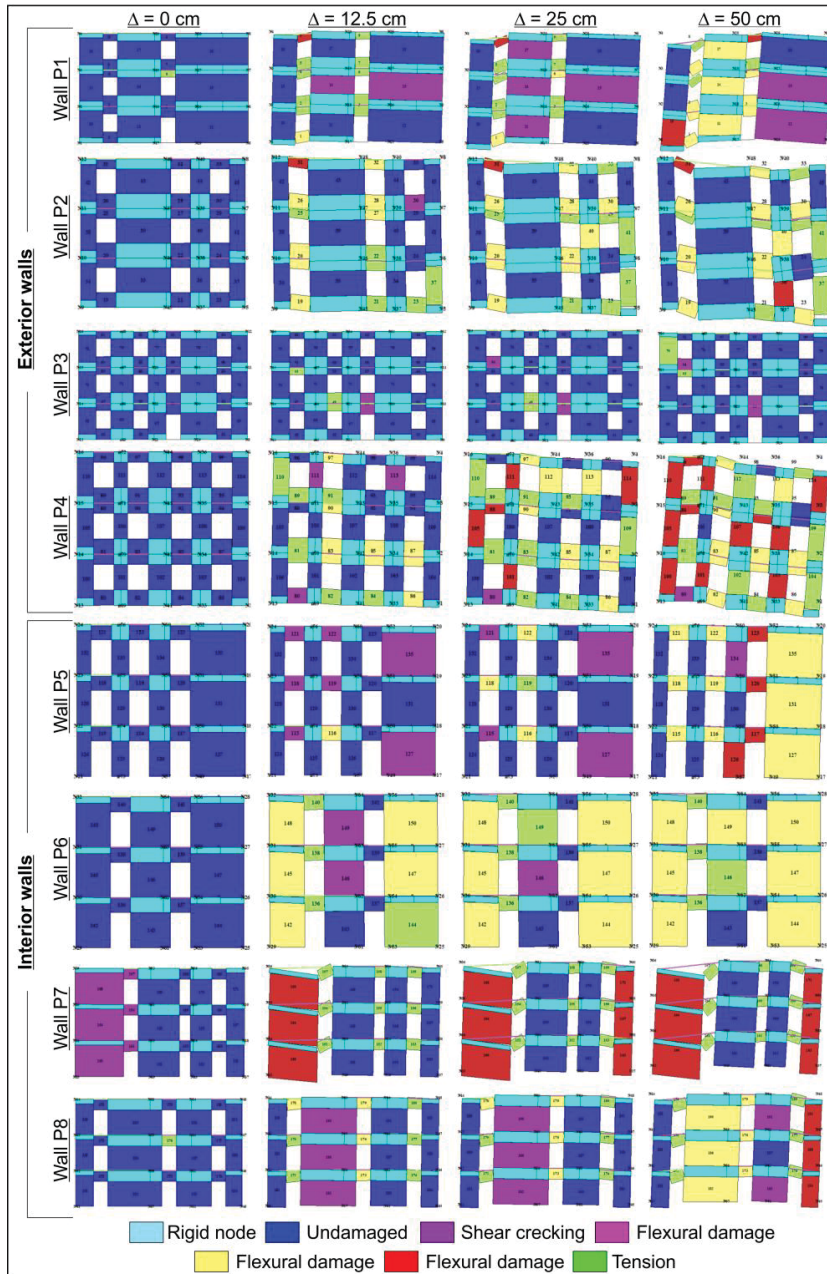


Figure C.9 Damage evolution of the exterior (P<sub>i</sub>, P<sub>2</sub>, P<sub>3</sub>, P<sub>4</sub>) and interior (P<sub>5</sub>, P<sub>6</sub>, P<sub>7</sub>, P<sub>8</sub>) walls of the masonry building M1 resting on soft clay (S<sub>2\_1</sub>), during the progressive increase of the differential settlements from 0 to 50 cm applied according to a hogging configuration.



Result of the numerical analysis in terms of damage exhibited by the masonry walls of a building subjected to differential settlements

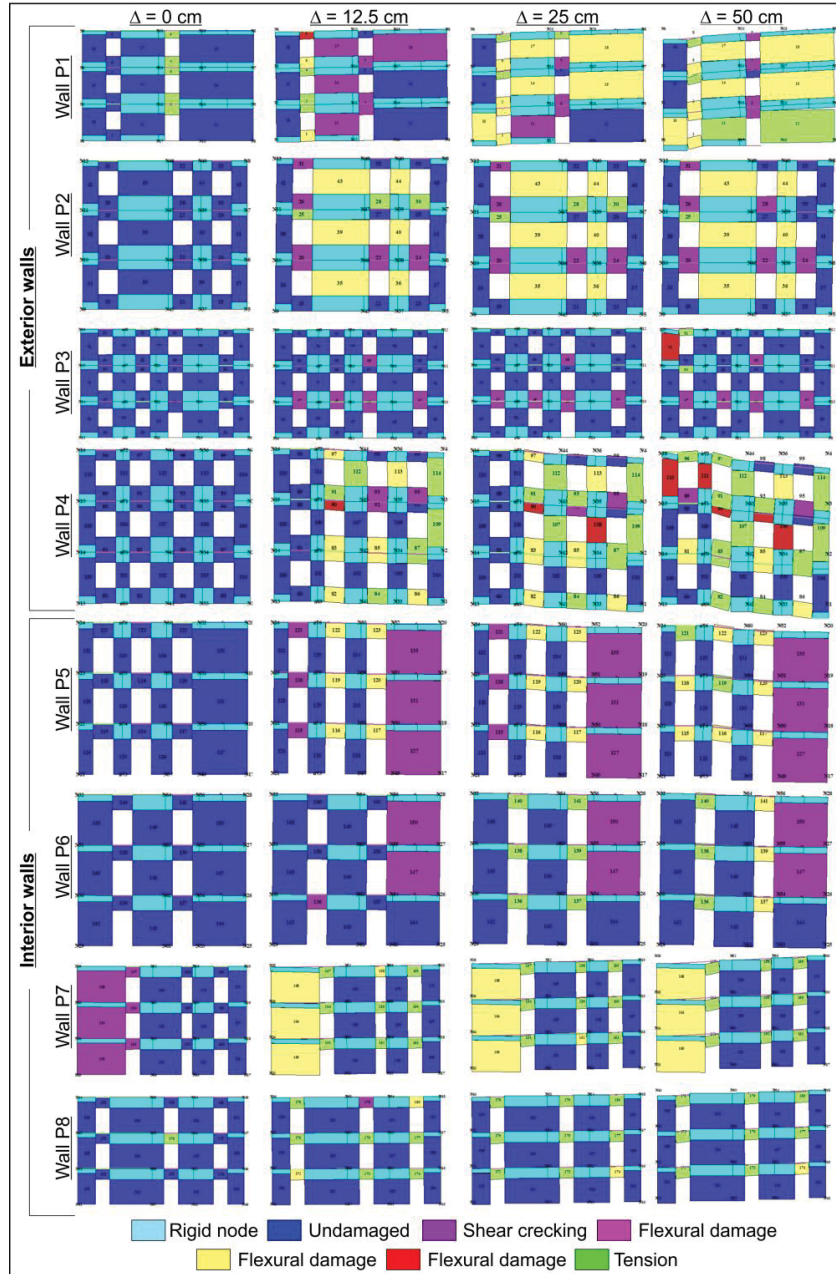


Figure C.10 Damage evolution of the exterior (P<sub>i</sub>, P<sub>2</sub>, P<sub>3</sub>, P<sub>4</sub>) and interior (P<sub>5</sub>, P<sub>6</sub>, P<sub>7</sub>, P<sub>8</sub>) walls of the masonry building M1 resting on medium/ hard clay (S2\_2), during the progressive increase of the differential settlements from 0 to 50 cm applied with a bi-linear trend and a maximum value in the left corner.

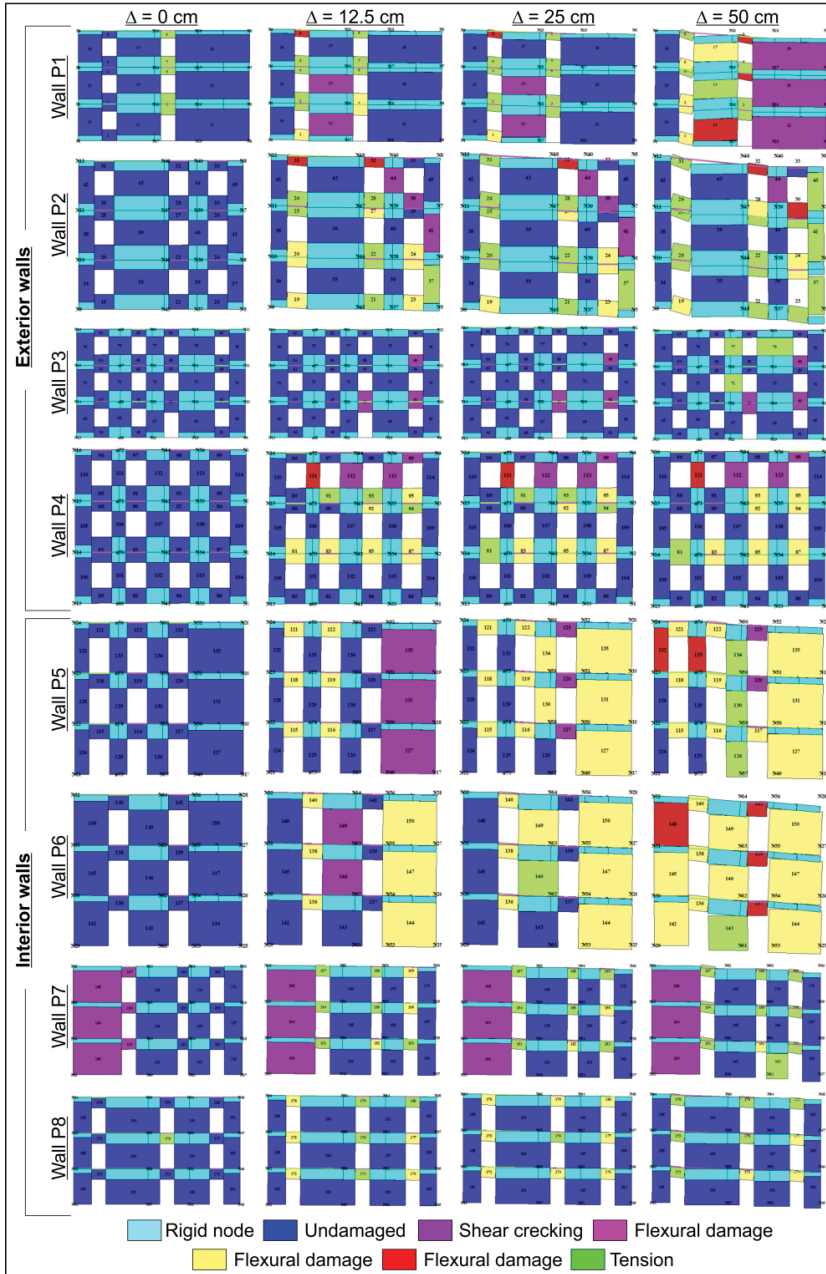


Figure C.11 Damage evolution of the exterior (P<sub>i</sub>, P<sub>2</sub>, P<sub>3</sub>, P<sub>4</sub>) and interior (P<sub>5</sub>, P<sub>6</sub>, P<sub>7</sub>, P<sub>8</sub>) walls of the masonry building M1 resting on medium/ hard clay (S2\_2), during the progressive increase of the differential settlements from 0 to 50 cm applied with a bi-linear trend and a maximum value in the right corner.

Result of the numerical analysis in terms of damage exhibited by the masonry walls of a building subjected to differential settlements

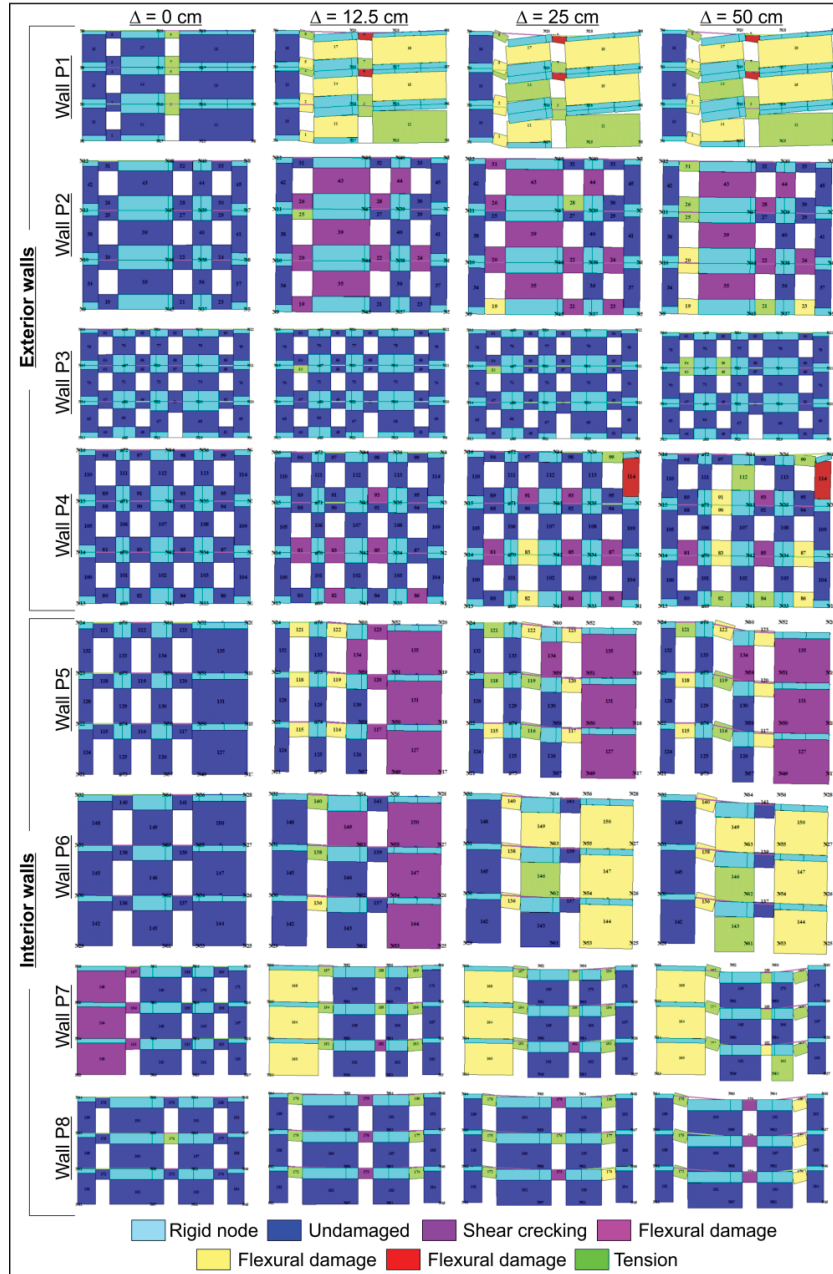


Figure C.12 Damage evolution of the exterior (Pi, P2, P3, P4) and interior (P5, P6, P7, P8) walls of the masonry building M1 resting on medium/ hard clay (S2\_2), during the progressive increase of the differential settlements from 0 to 50 cm applied according to a sagging configuration.

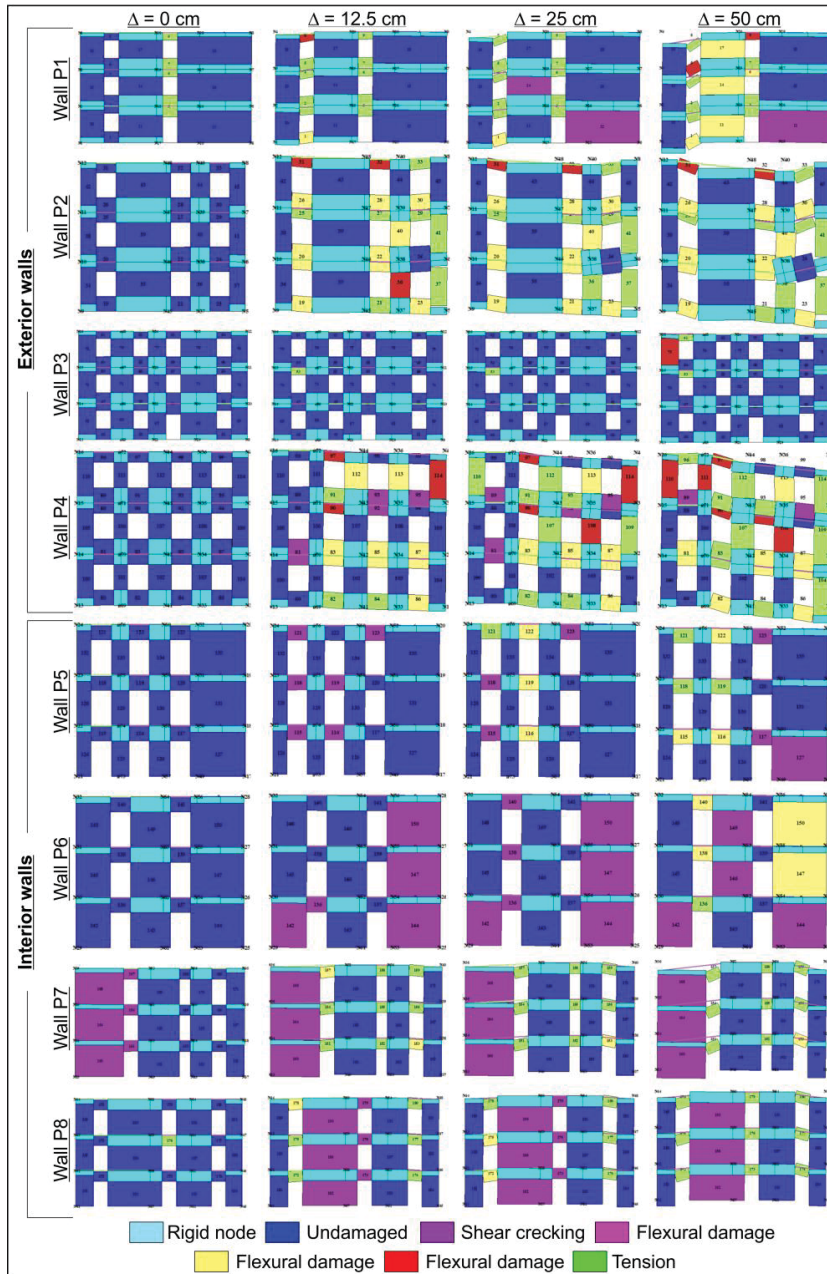


Figure C.13 Damage evolution of the exterior (P<sub>i</sub>, P<sub>2</sub>, P<sub>3</sub>, P<sub>4</sub>) and interior (P<sub>5</sub>, P<sub>6</sub>, P<sub>7</sub>, P<sub>8</sub>) walls of the masonry building M1 resting on medium/ hard clay (S2\_2), during the progressive increase of the differential settlements from 0 to 50 cm applied according to a hogging configuration.

Result of the numerical analysis in terms of damage exhibited by the masonry walls of a building subjected to differential settlements

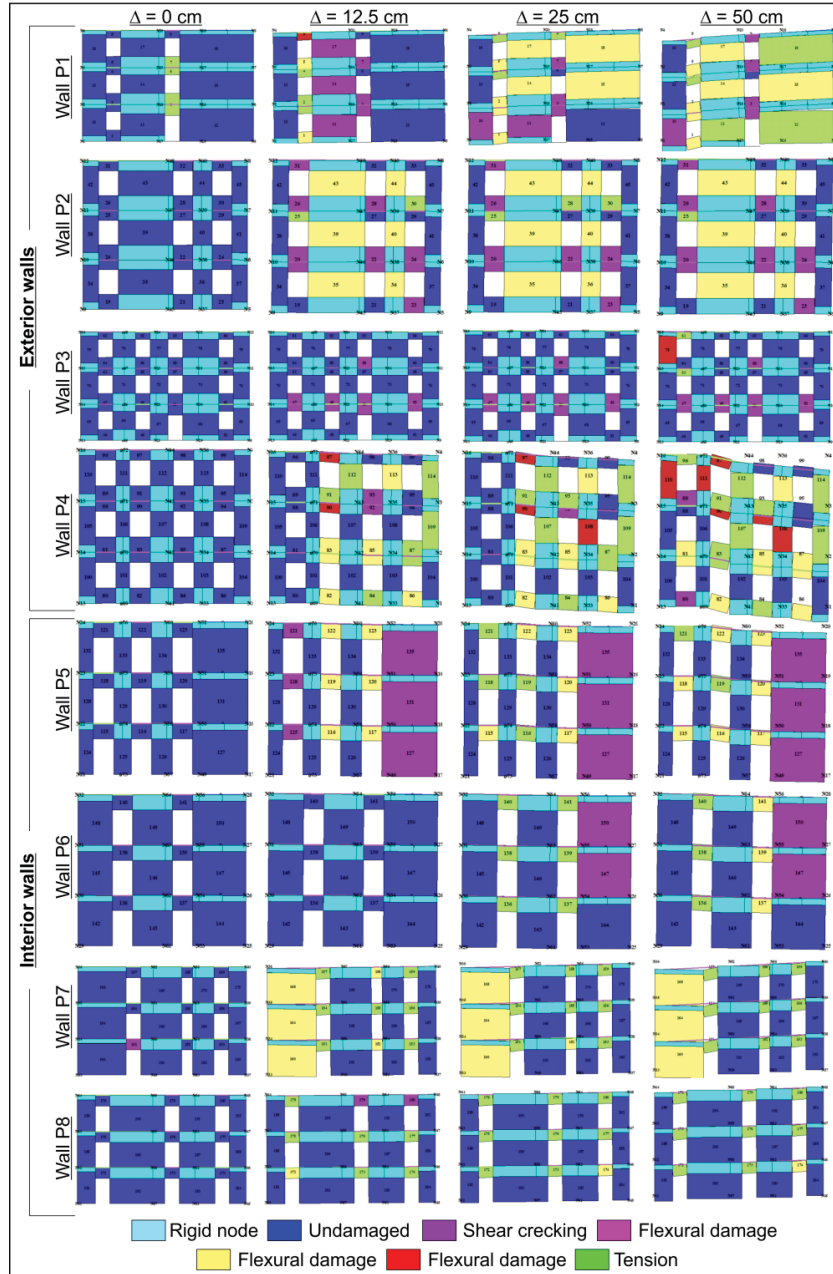


Figure C.14 Damage evolution of the exterior (P<sub>i</sub>, P<sub>2</sub>, P<sub>3</sub>, P<sub>4</sub>) and interior (P<sub>5</sub>, P<sub>6</sub>, P<sub>7</sub>, P<sub>8</sub>) walls of the masonry building M1 resting on loose sand (S3\_1), during the progressive increase of the differential settlements from 0 to 50 cm applied with a bi-linear trend and a maximum value in the left corner.

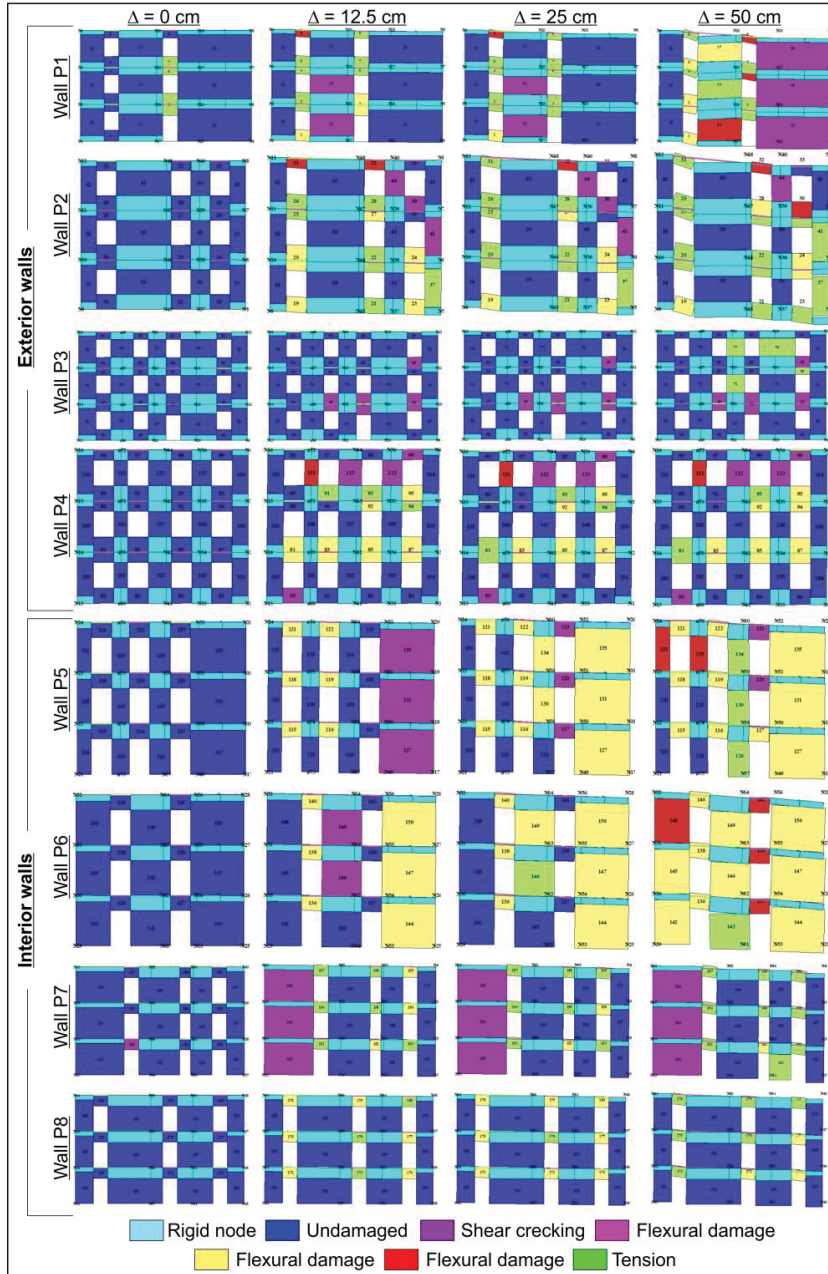


Figure C.15 Damage evolution of the exterior (P<sub>i</sub>, P<sub>2</sub>, P<sub>3</sub>, P<sub>4</sub>) and interior (P<sub>5</sub>, P<sub>6</sub>, P<sub>7</sub>, P<sub>8</sub>) walls of the masonry building M1 resting on loose sand (S<sub>3\_1</sub>), during the progressive increase of the differential settlements from 0 to 50 cm applied with a bi-linear trend and a maximum value in the right corner.

Result of the numerical analysis in terms of damage exhibited by the masonry walls of a building subjected to differential settlements

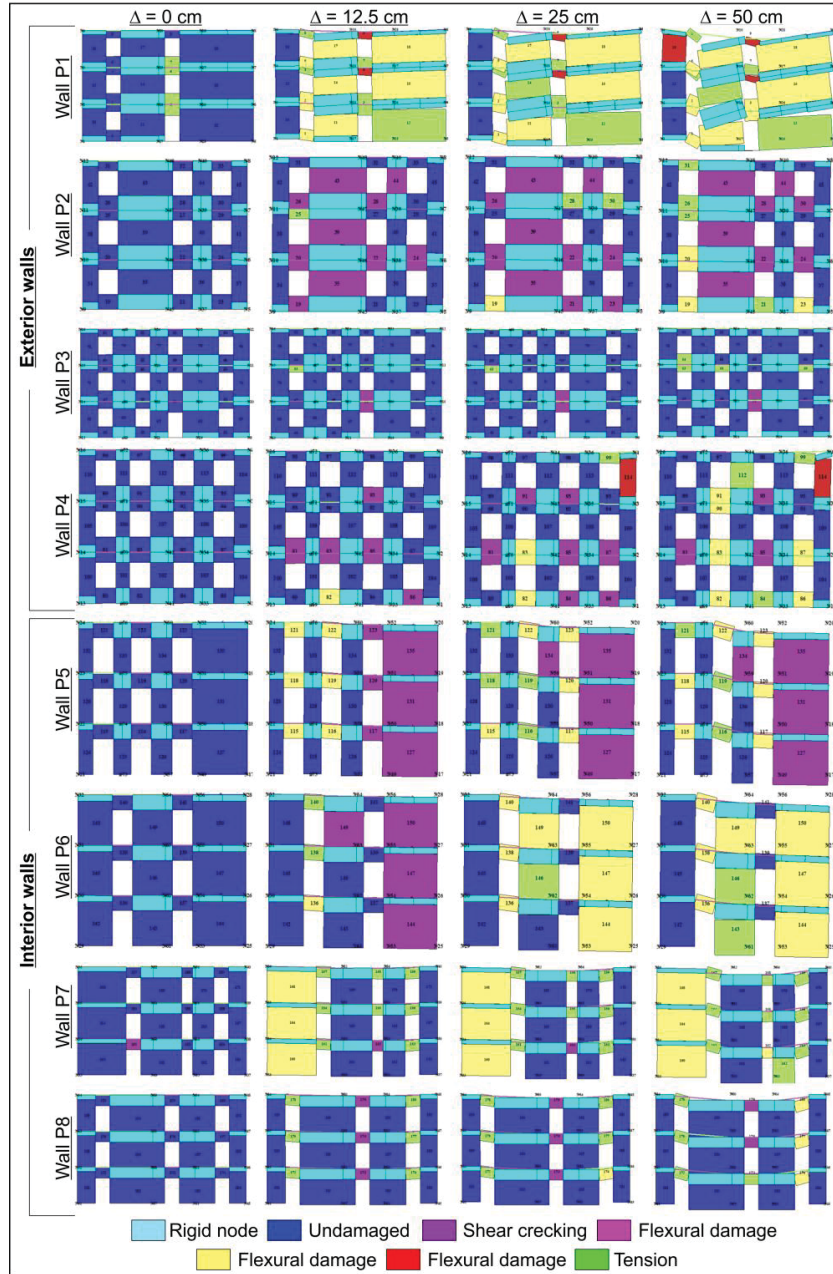


Figure C.16 Damage evolution of the exterior (P<sub>i</sub>, P<sub>2</sub>, P<sub>3</sub>, P<sub>4</sub>) and interior (P<sub>5</sub>, P<sub>6</sub>, P<sub>7</sub>, P<sub>8</sub>) walls of the masonry building M1 resting on loose sand (S3\_1), during the progressive increase of the differential settlements from 0 to 50 cm applied according to a sagging configuration.

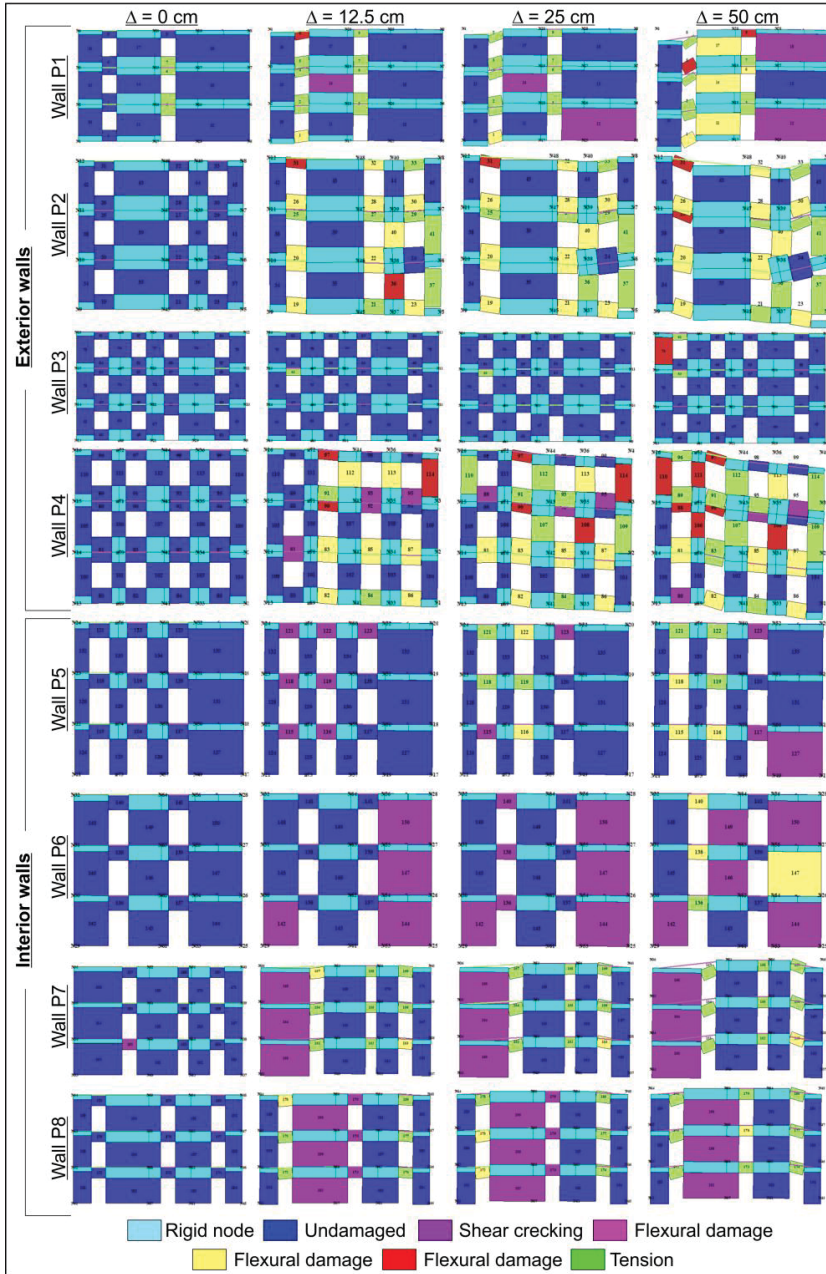


Figure C.17 Damage evolution of the exterior (P<sub>i</sub>, P<sub>2</sub>, P<sub>3</sub>, P<sub>4</sub>) and interior (P<sub>5</sub>, P<sub>6</sub>, P<sub>7</sub>, P<sub>8</sub>) walls of the masonry building M1 resting on loose sand (S3\_1), during the progressive increase of the differential settlements from 0 to 50 cm applied according to a hogging configuration.



Result of the numerical analysis in terms of damage exhibited by the masonry walls of a building subjected to differential settlements

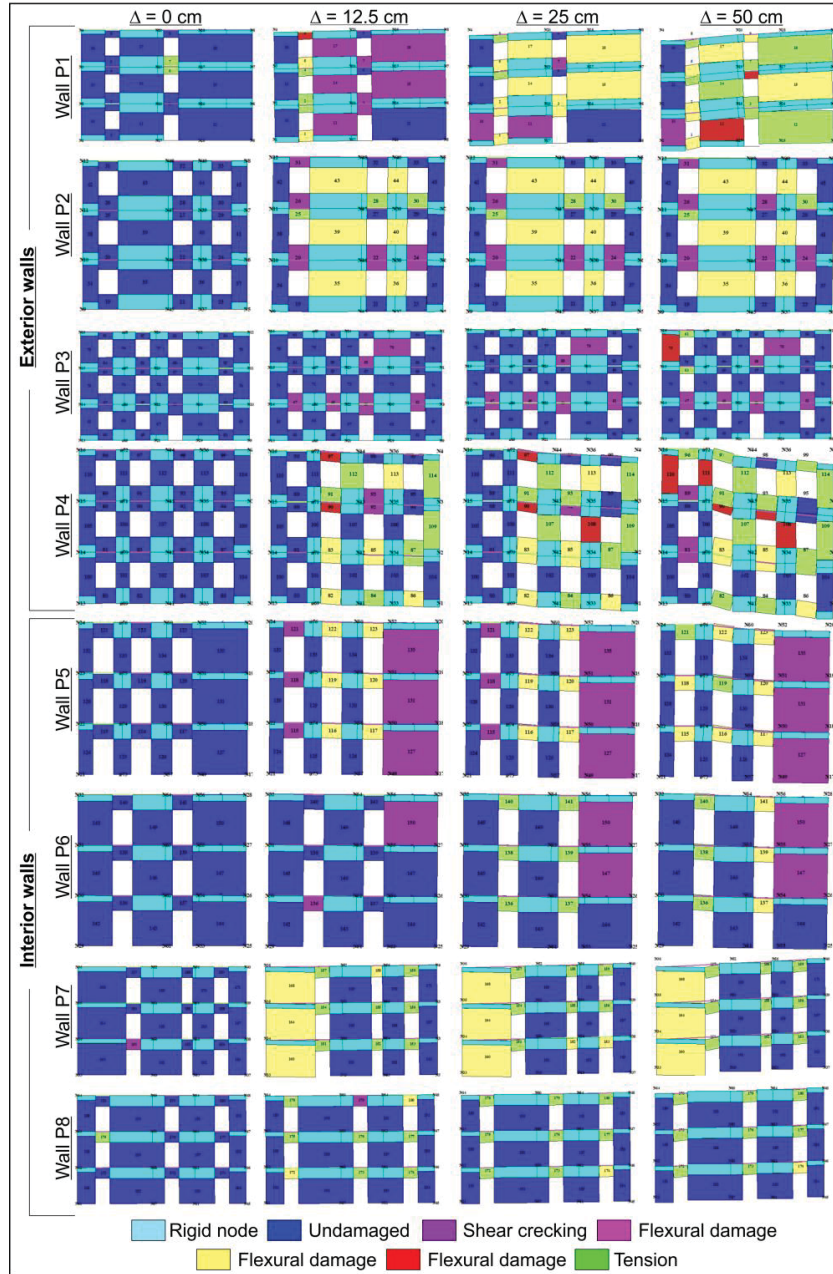


Figure C.18 Damage evolution of the exterior (Pi, P2, P3, P4) and interior (P5, P6, P7, P8) walls of the masonry building M1 resting on dense sand (S3\_2), during the progressive increase of the differential settlements from 0 to 50 cm applied with a bi-linear trend and a maximum value in the left corner.

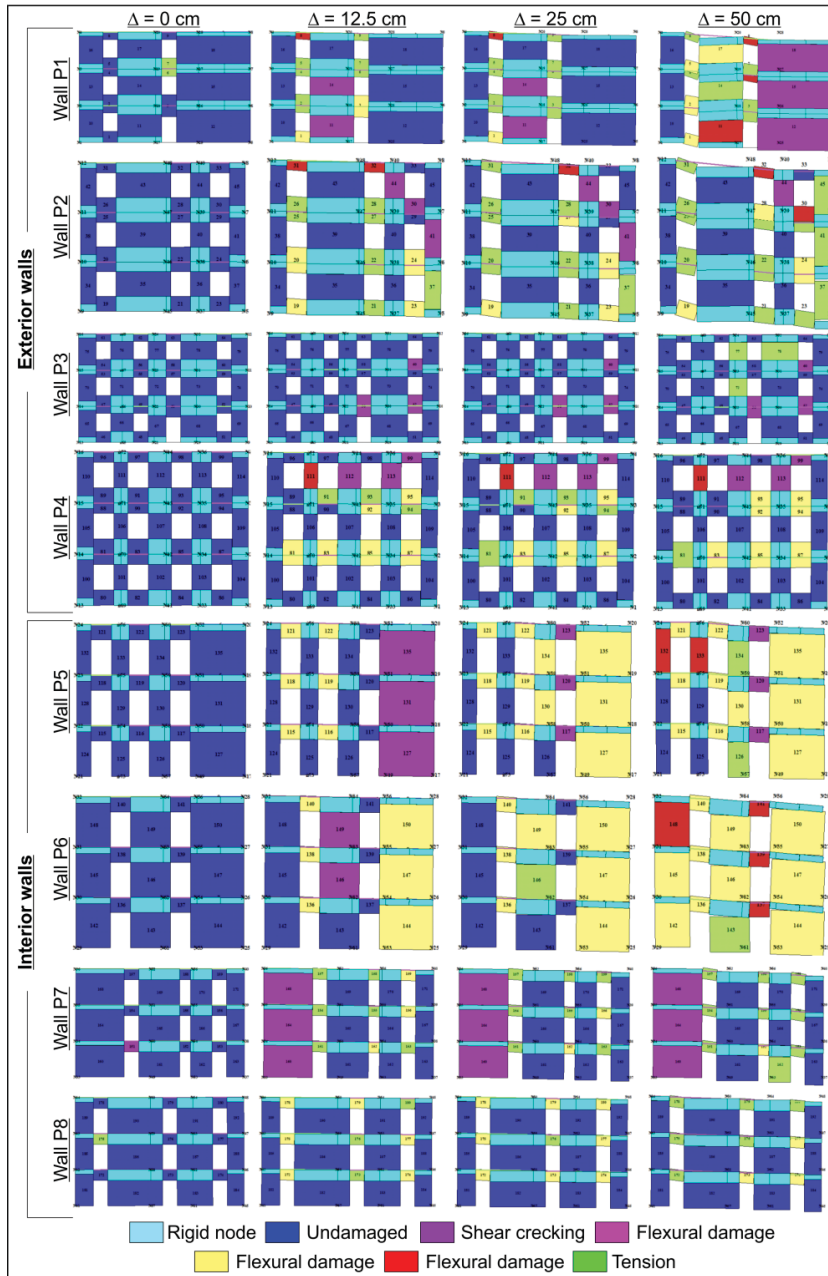


Figure C.19 Damage evolution of the exterior (P<sub>i</sub>, P<sub>2</sub>, P<sub>3</sub>, P<sub>4</sub>) and interior (P<sub>5</sub>, P<sub>6</sub>, P<sub>7</sub>, P<sub>8</sub>) walls of the masonry building M1 resting on dense sand (S3\_2), during the progressive increase of the differential settlements from 0 to 50 cm applied with a bi-linear trend and a maximum value in the right corner.

Result of the numerical analysis in terms of damage exhibited by the masonry walls of a building subjected to differential settlements

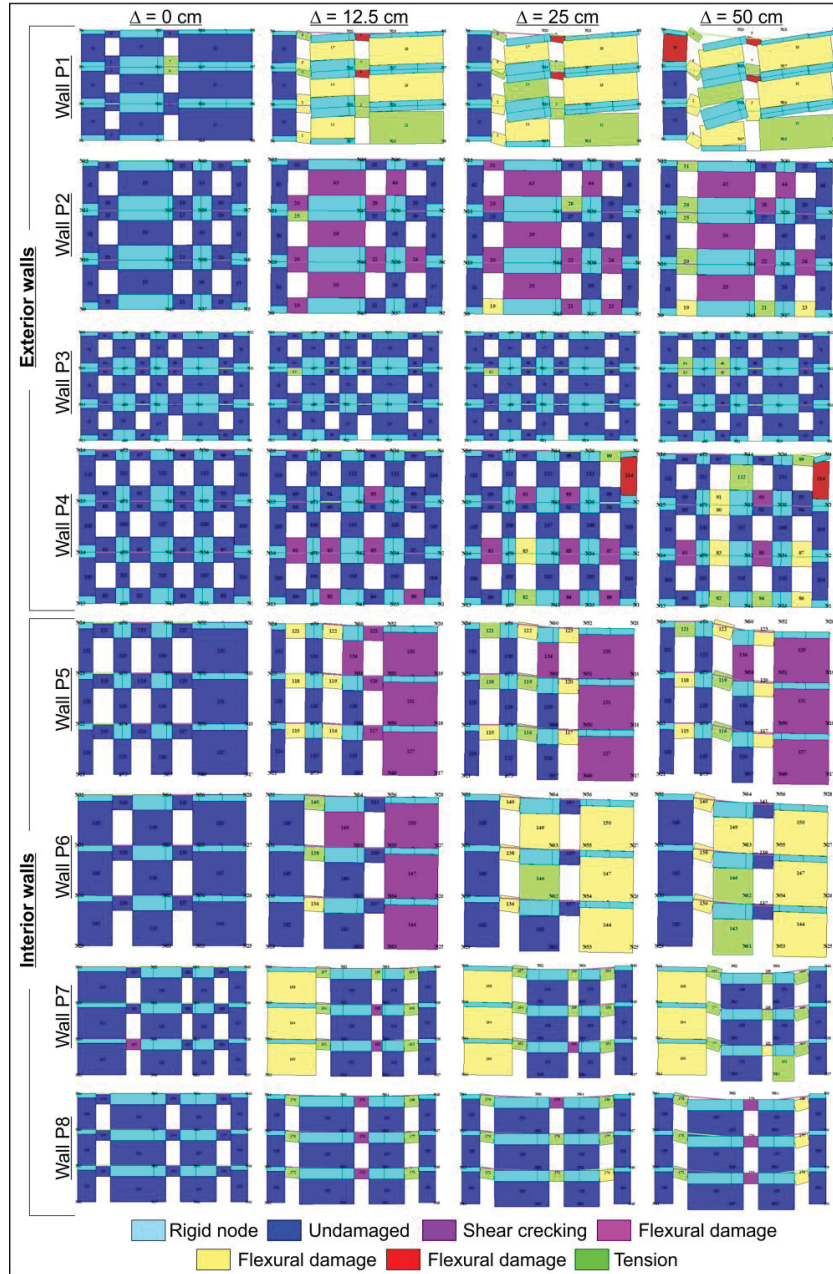


Figure C.20 Damage evolution of the exterior (P<sub>i</sub>, P<sub>2</sub>, P<sub>3</sub>, P<sub>4</sub>) and interior (P<sub>5</sub>, P<sub>6</sub>, P<sub>7</sub>, P<sub>8</sub>) walls of the masonry building M1 resting on dense sand (S<sub>3\_2</sub>), during the progressive increase of the differential settlements from 0 to 50 cm applied according to a sagging configuration.

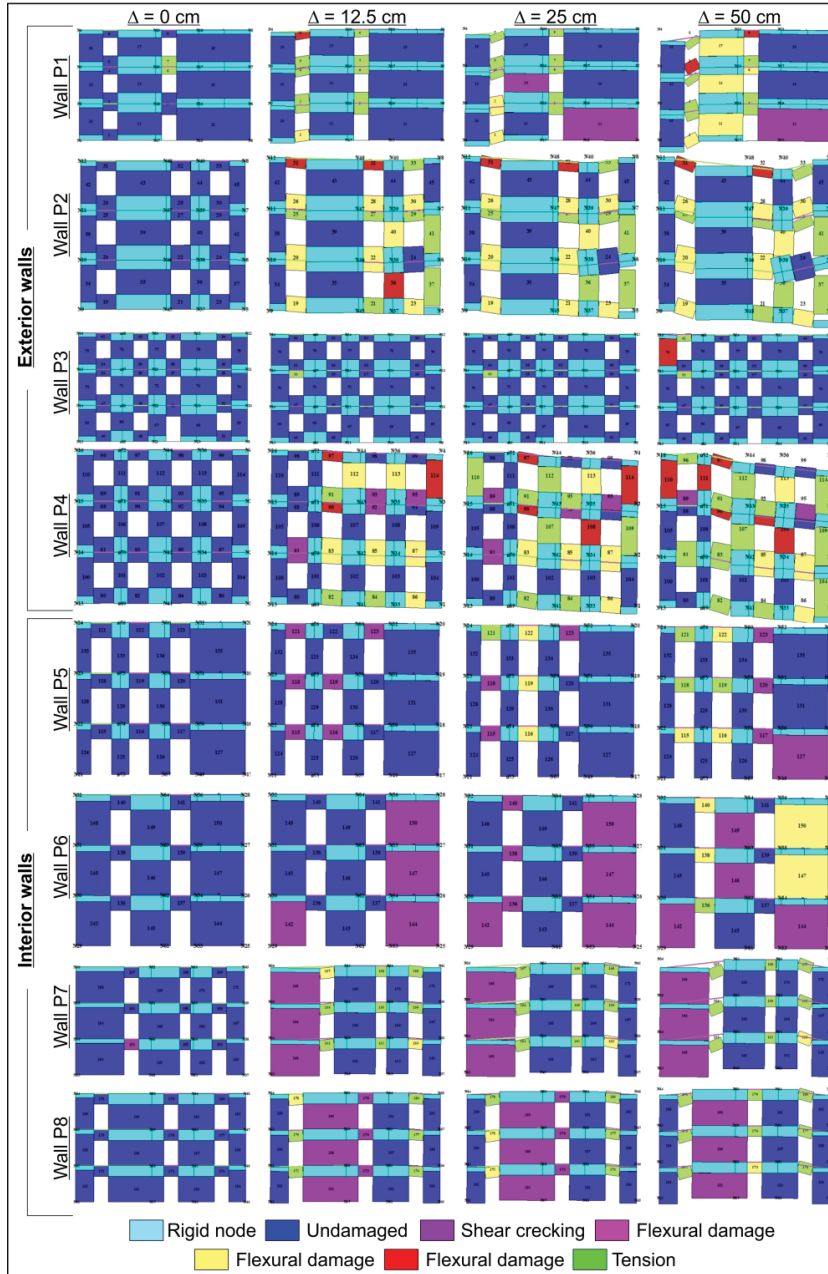


Figure C.21 Damage evolution of the exterior (P<sub>i</sub>, P<sub>2</sub>, P<sub>3</sub>, P<sub>4</sub>) and interior (P<sub>5</sub>, P<sub>6</sub>, P<sub>7</sub>, P<sub>8</sub>) walls of the masonry building M1 resting on dense sand (S3\_2), during the progressive increase of the differential settlements from 0 to 50 cm applied according to a hogging configuration.

Result of the numerical analysis in terms of damage exhibited by the masonry walls of a building subjected to differential settlements

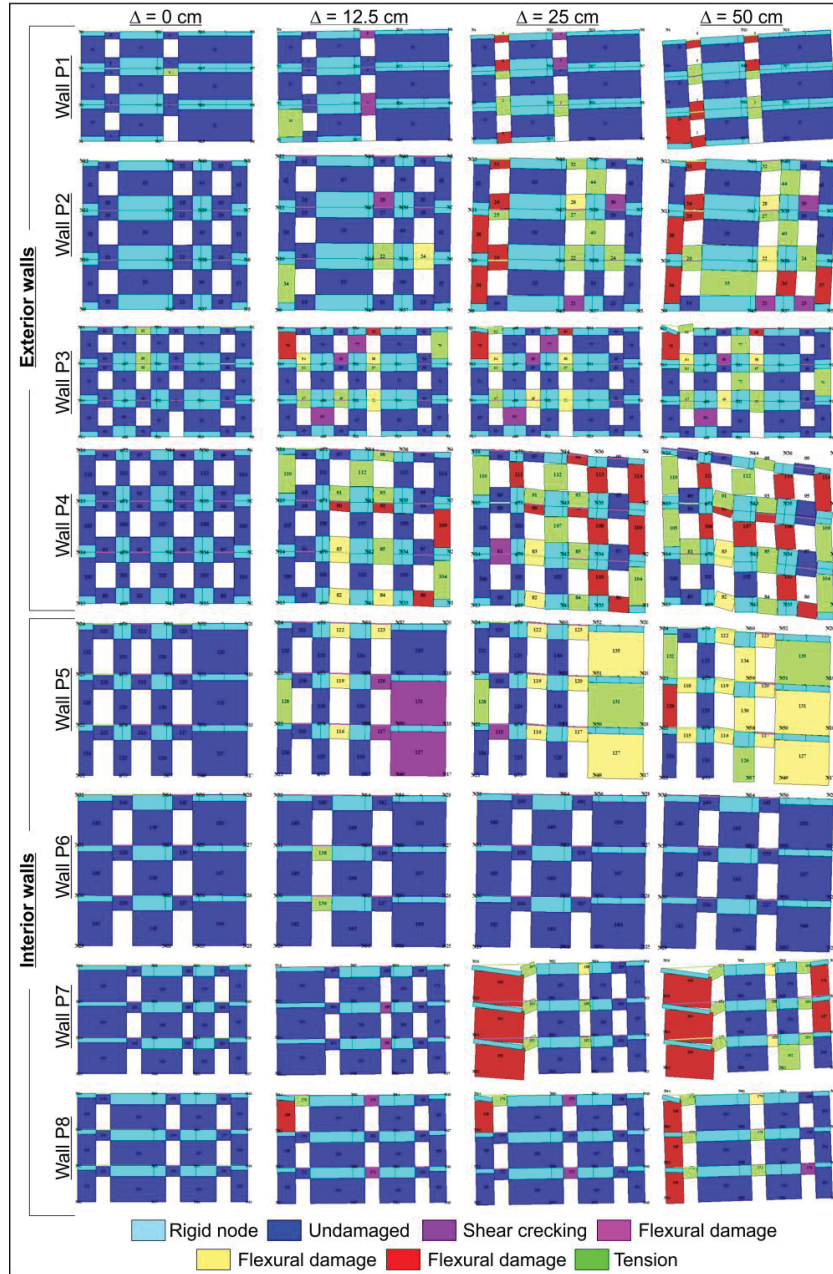


Figure C.22 Damage evolution of the exterior (P<sub>1</sub>, P<sub>2</sub>, P<sub>3</sub>, P<sub>4</sub>) and interior (P<sub>5</sub>, P<sub>6</sub>, P<sub>7</sub>, P<sub>8</sub>) walls of the masonry building M2 resting on soft soil (S1), during the progressive increase of the differential settlements from 0 to 50 cm applied with a bi-linear trend and a maximum value in the left corner.

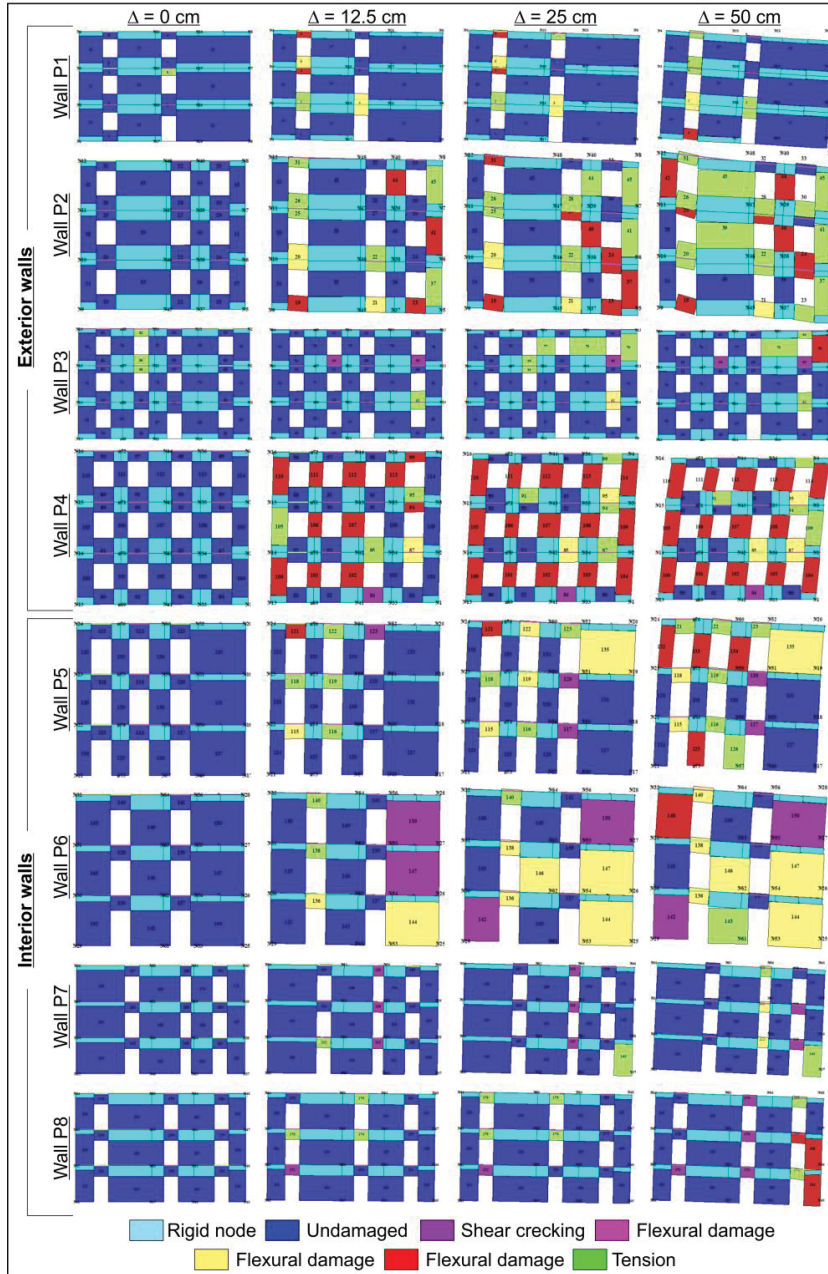


Figure C.23 Damage evolution of the exterior (P<sub>i</sub>, P<sub>2</sub>, P<sub>3</sub>, P<sub>4</sub>) and interior (P<sub>5</sub>, P<sub>6</sub>, P<sub>7</sub>, P<sub>8</sub>) walls of the masonry building M2 resting on soft soil (S<sub>1</sub>), during the progressive increase of the differential settlements from 0 to 50 cm applied with a bi-linear trend and a maximum value in the right corner.

Result of the numerical analysis in terms of damage exhibited by the masonry walls of a building subjected to differential settlements

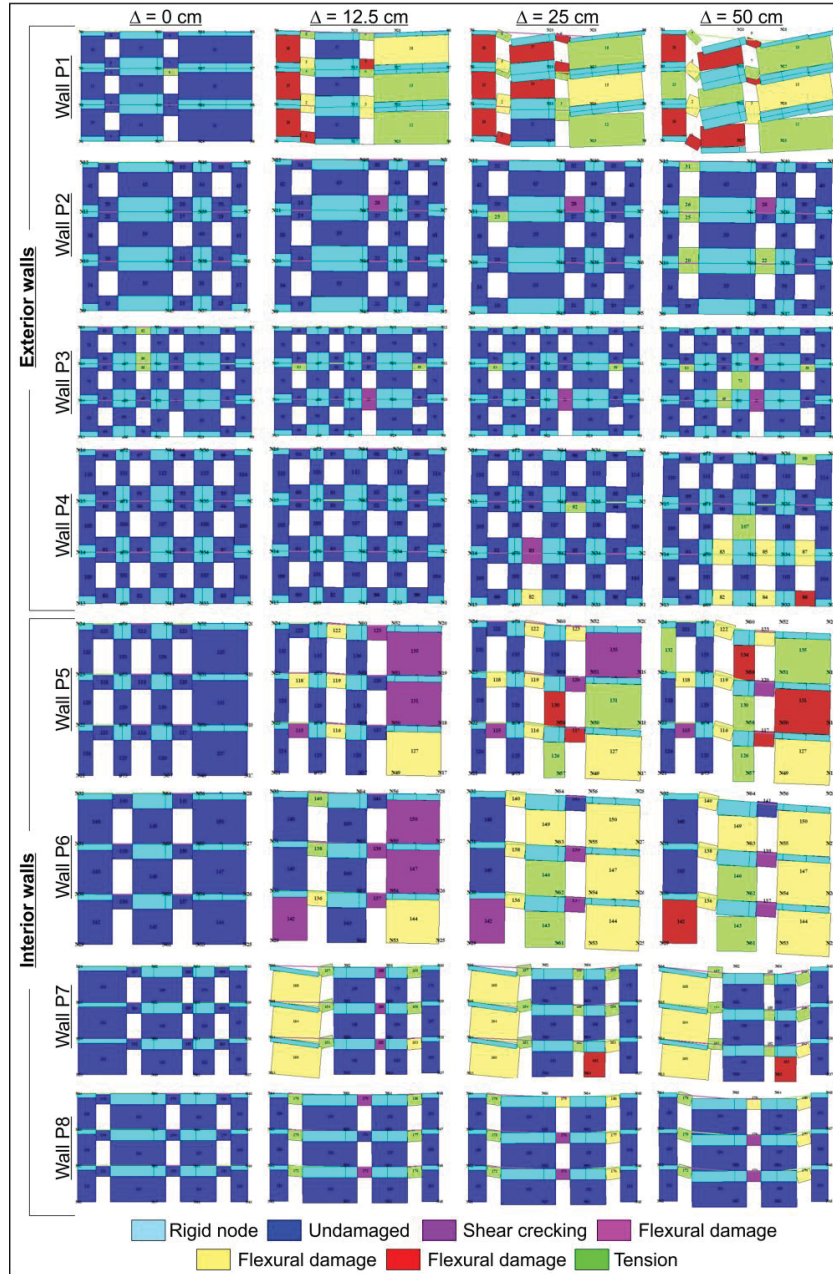


Figure C.24 Damage evolution of the exterior (P<sub>i</sub>, P<sub>2</sub>, P<sub>3</sub>, P<sub>4</sub>) and interior (P<sub>5</sub>, P<sub>6</sub>, P<sub>7</sub>, P<sub>8</sub>) walls of the masonry building M2 resting on soft soil (S1), during the progressive increase of the differential settlements from 0 to 50 cm applied according to a sagging configuration.

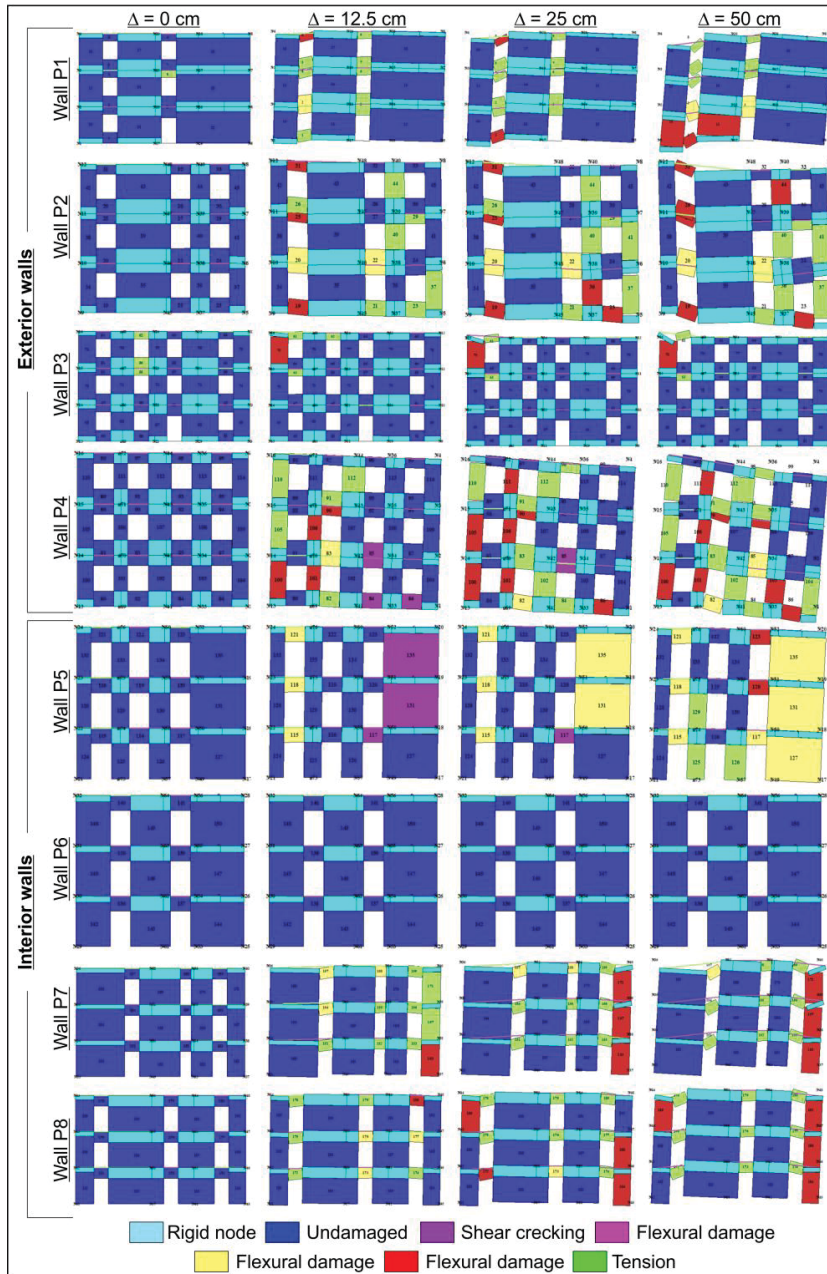


Figure C.25 Damage evolution of the exterior (P<sub>i</sub>, P<sub>2</sub>, P<sub>3</sub>, P<sub>4</sub>) and interior (P<sub>5</sub>, P<sub>6</sub>, P<sub>7</sub>, P<sub>8</sub>) walls of the masonry building M2 resting on soft soil (S<sub>1</sub>), during the progressive increase of the differential settlements from 0 to 50 cm applied according to a hogging configuration.



Result of the numerical analysis in terms of damage exhibited by the masonry walls of a building subjected to differential settlements

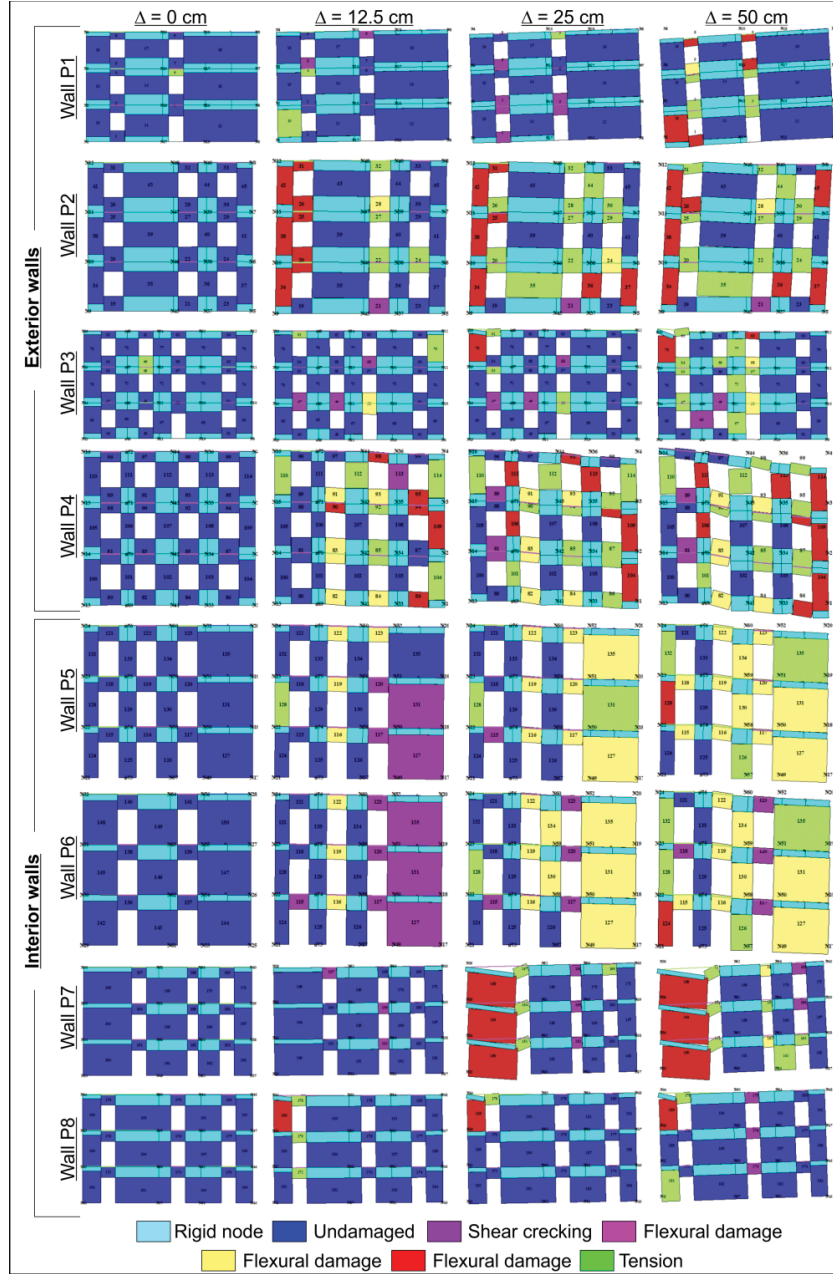


Figure C.26 Damage evolution of the exterior (P1, P2, P3, P4) and interior (P5, P6, P7, P8) walls of the masonry building M2 resting on soft clay (S2\_1), during the progressive increase of the differential settlements from 0 to 50 cm applied with a bi-linear trend and a maximum value in the left corner.

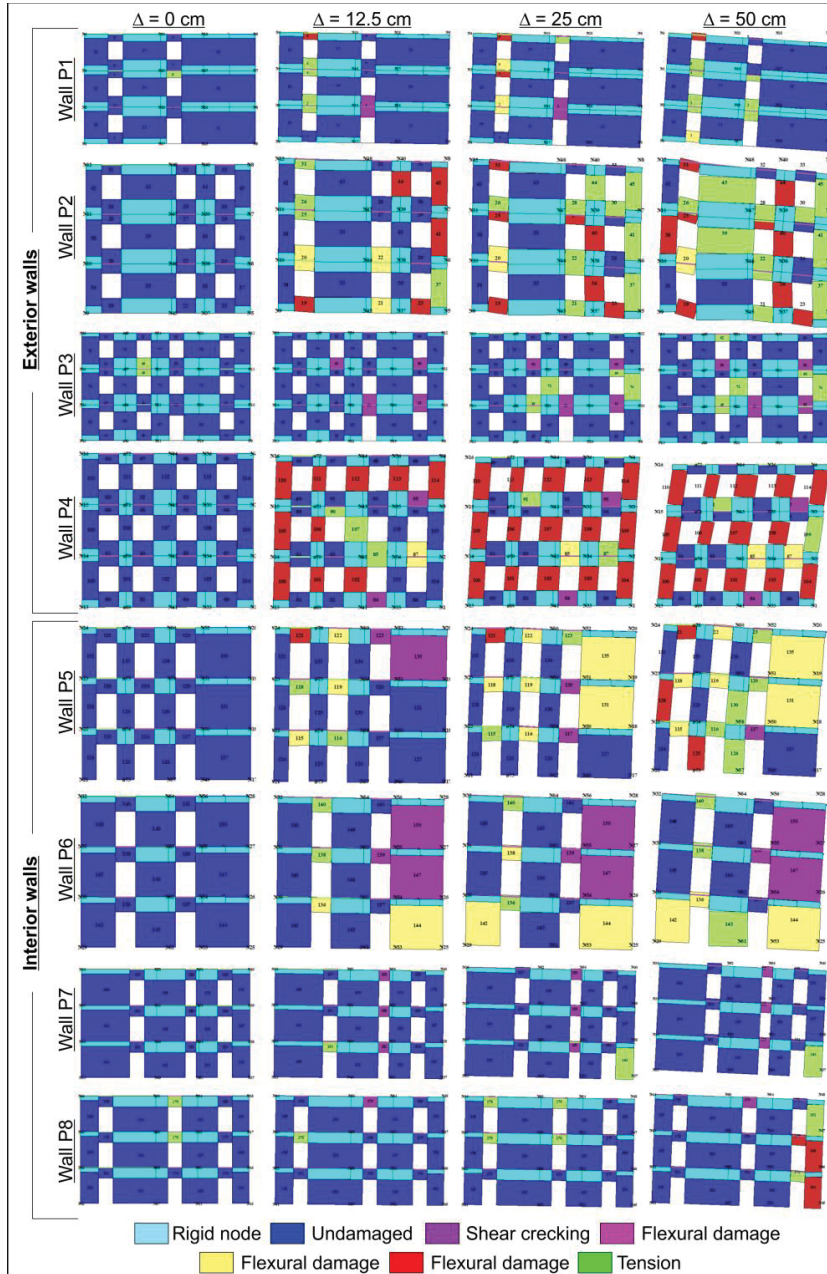


Figure C.27 Damage evolution of the exterior (P<sub>i</sub>, P<sub>2</sub>, P<sub>3</sub>, P<sub>4</sub>) and interior (P<sub>5</sub>, P<sub>6</sub>, P<sub>7</sub>, P<sub>8</sub>) walls of the masonry building M2 resting on soft clay (S<sub>2\_1</sub>), during the progressive increase of the differential settlements from 0 to 50 cm applied with a bi-linear trend and a maximum value in the right corner.

Result of the numerical analysis in terms of damage exhibited by the masonry walls of a building subjected to differential settlements

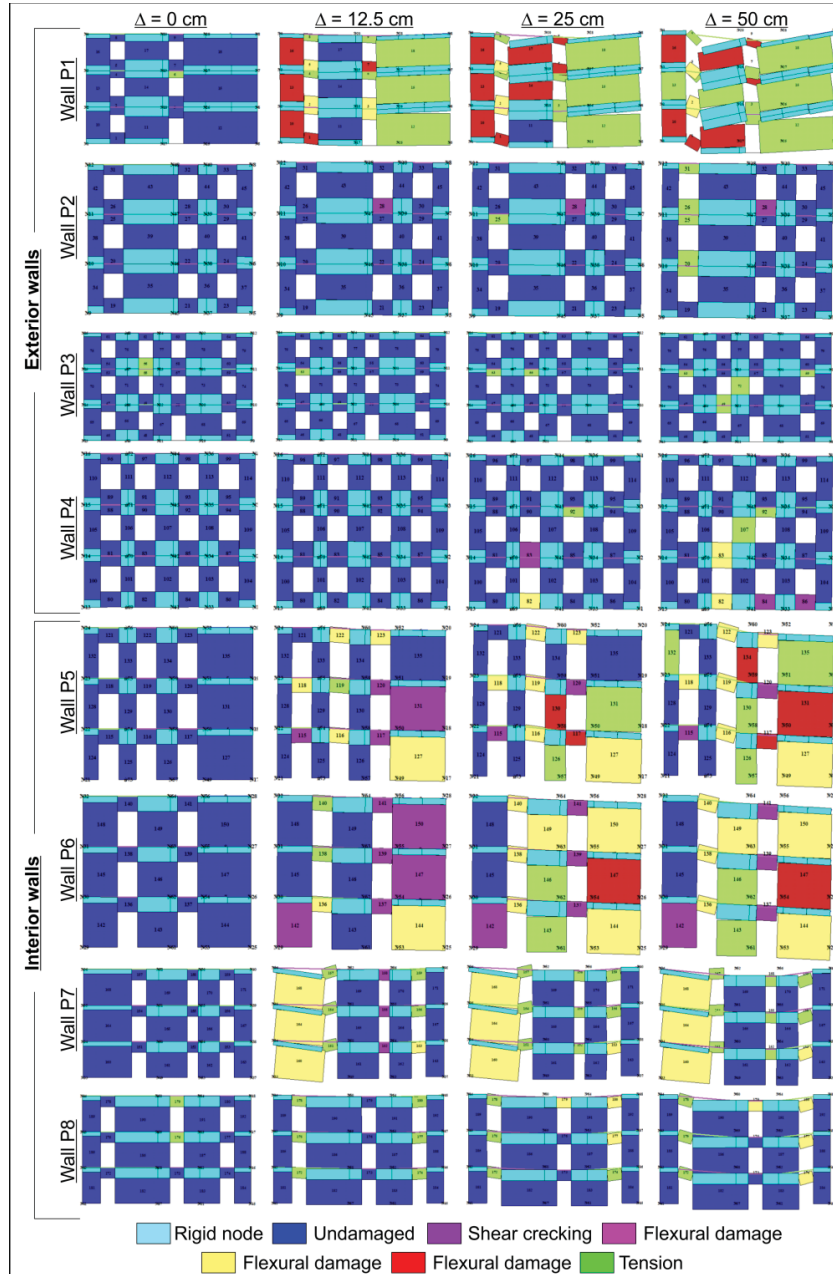


Figure C.28 Damage evolution of the exterior (P1, P2, P3, P4) and interior (P5, P6, P7, P8) walls of the masonry building M2 resting on soft clay (S2\_1), during the progressive increase of the differential settlements from 0 to 50 cm applied according to a sagging configuration.

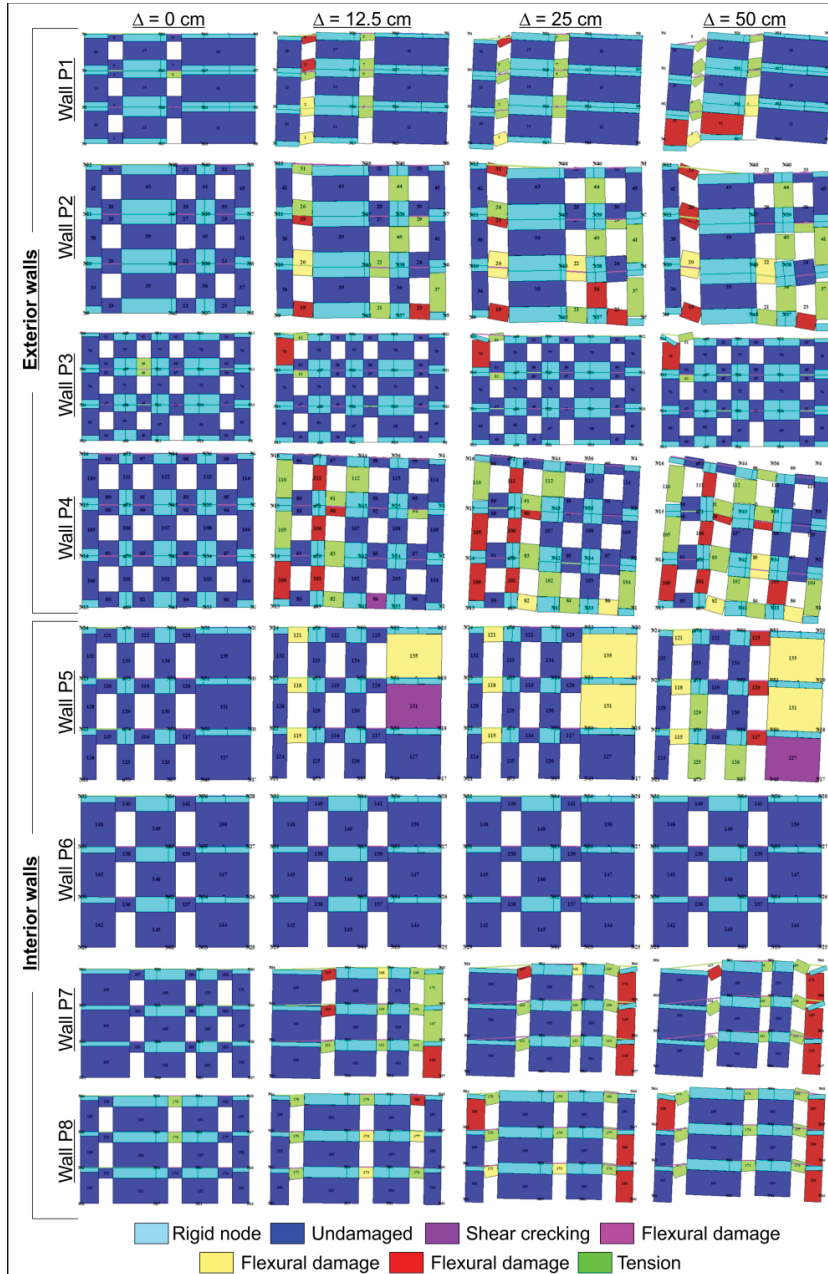


Figure C.29 Damage evolution of the exterior (P<sub>i</sub>, P<sub>2</sub>, P<sub>3</sub>, P<sub>4</sub>) and interior (P<sub>5</sub>, P<sub>6</sub>, P<sub>7</sub>, P<sub>8</sub>) walls of the masonry building M2 resting on soft clay (S<sub>2\_1</sub>), during the progressive increase of the differential settlements from 0 to 50 cm applied according to a hogging configuration.

Result of the numerical analysis in terms of damage exhibited by the masonry walls of a building subjected to differential settlements

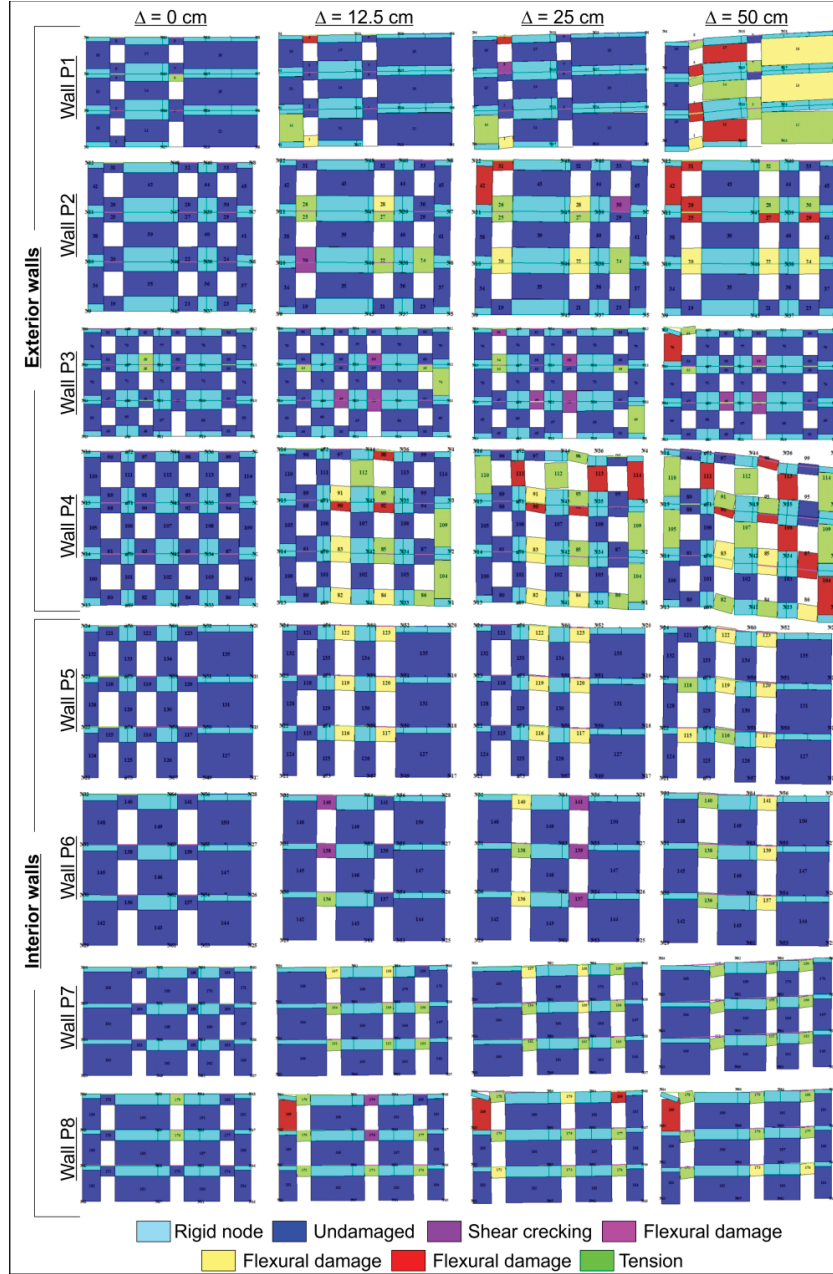


Figure C.30 Damage evolution of the exterior (P1, P2, P3, P4) and interior (P5, P6, P7, P8) walls of the masonry building M2 resting on medium/hard clay (S2\_2), during the progressive increase of the differential settlements from 0 to 50 cm applied with a bi-linear trend and a maximum value in the left corner.

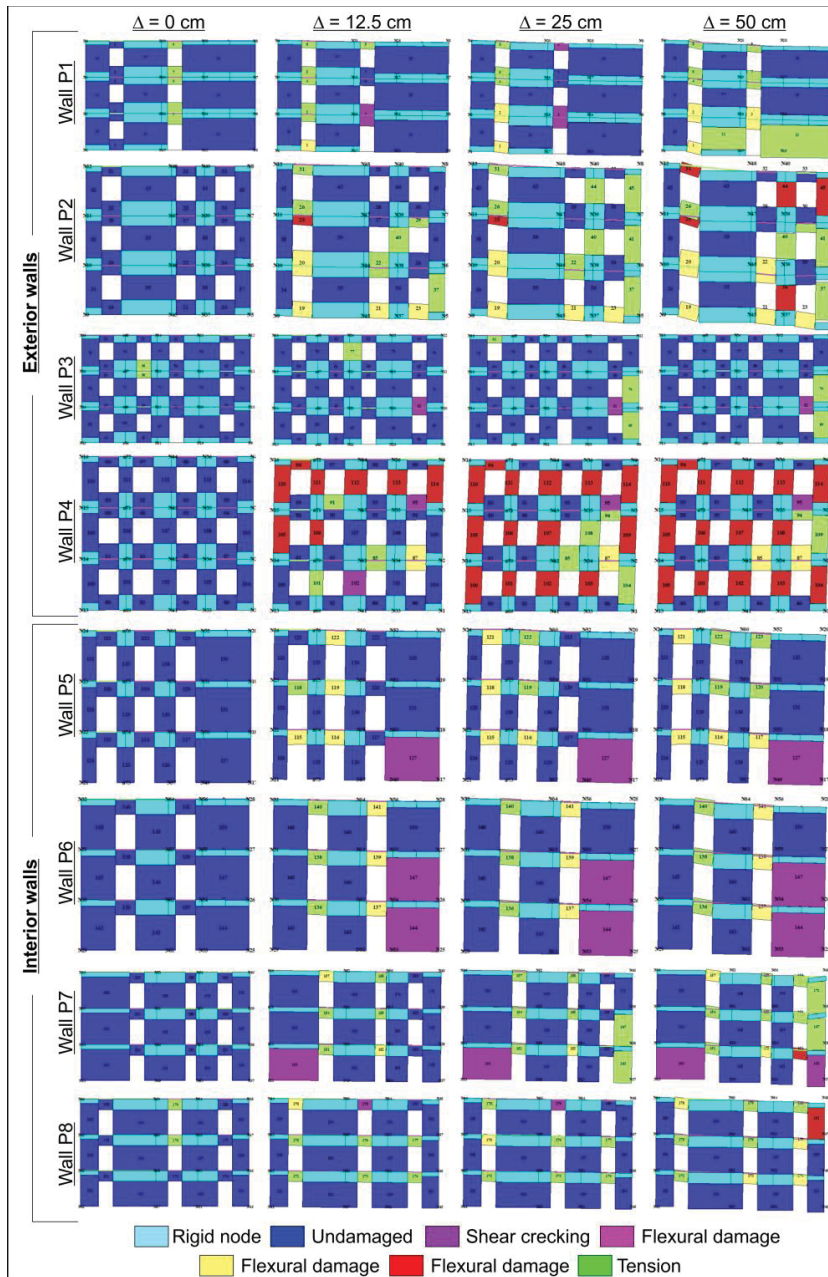


Figure C.31 Damage evolution of the exterior (P<sub>i</sub>, P<sub>2</sub>, P<sub>3</sub>, P<sub>4</sub>) and interior (P<sub>5</sub>, P<sub>6</sub>, P<sub>7</sub>, P<sub>8</sub>) walls of the masonry building M2 resting on medium/hard clay (S2\_2), during the progressive increase of the differential settlements from 0 to 50 cm applied with a bi-linear trend and a maximum value in the right corner.

Result of the numerical analysis in terms of damage exhibited by the masonry walls of a building subjected to differential settlements

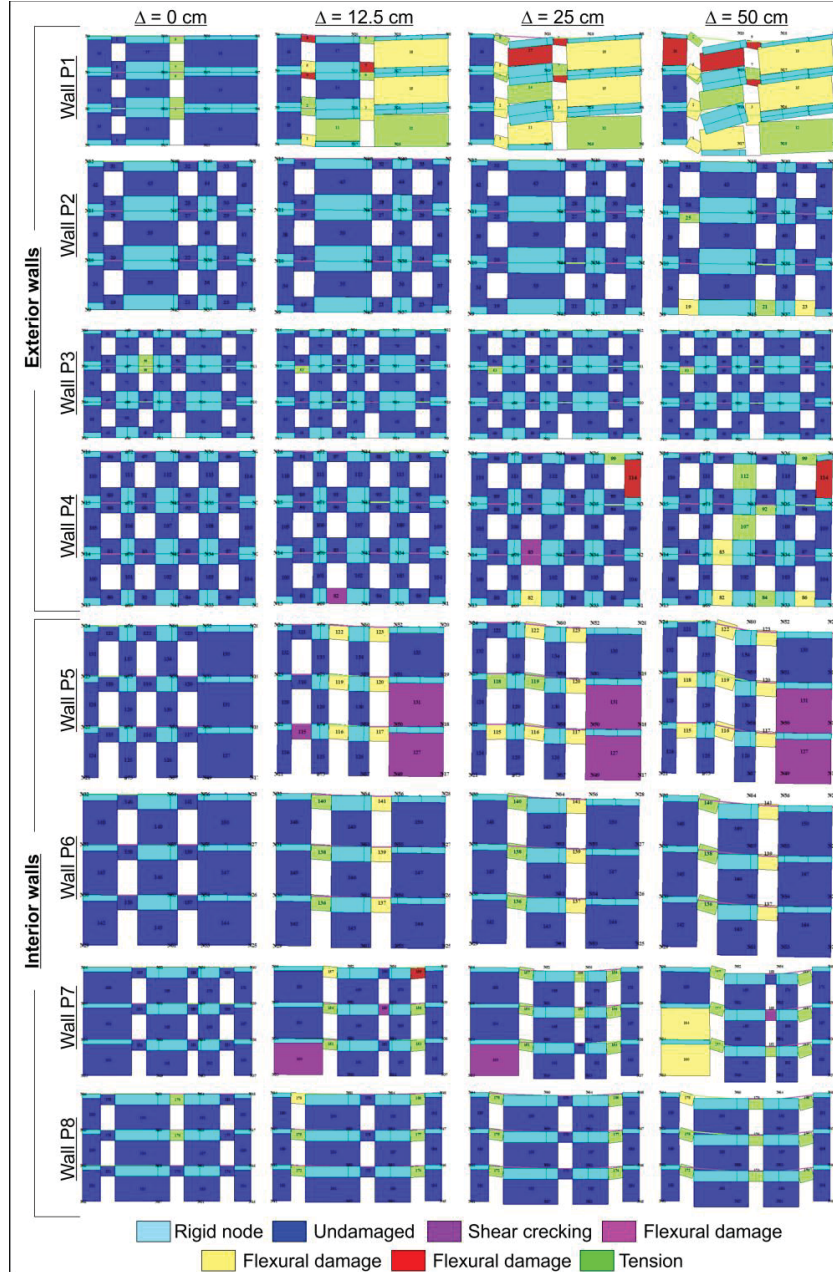


Figure C.32 Damage evolution of the exterior (P1, P2, P3, P4) and interior (P5, P6, P7, P8) walls of the masonry building M2 resting on medium/hard clay (S2\_2), during the progressive increase of the differential settlements from 0 to 50 cm applied according to a sagging configuration.

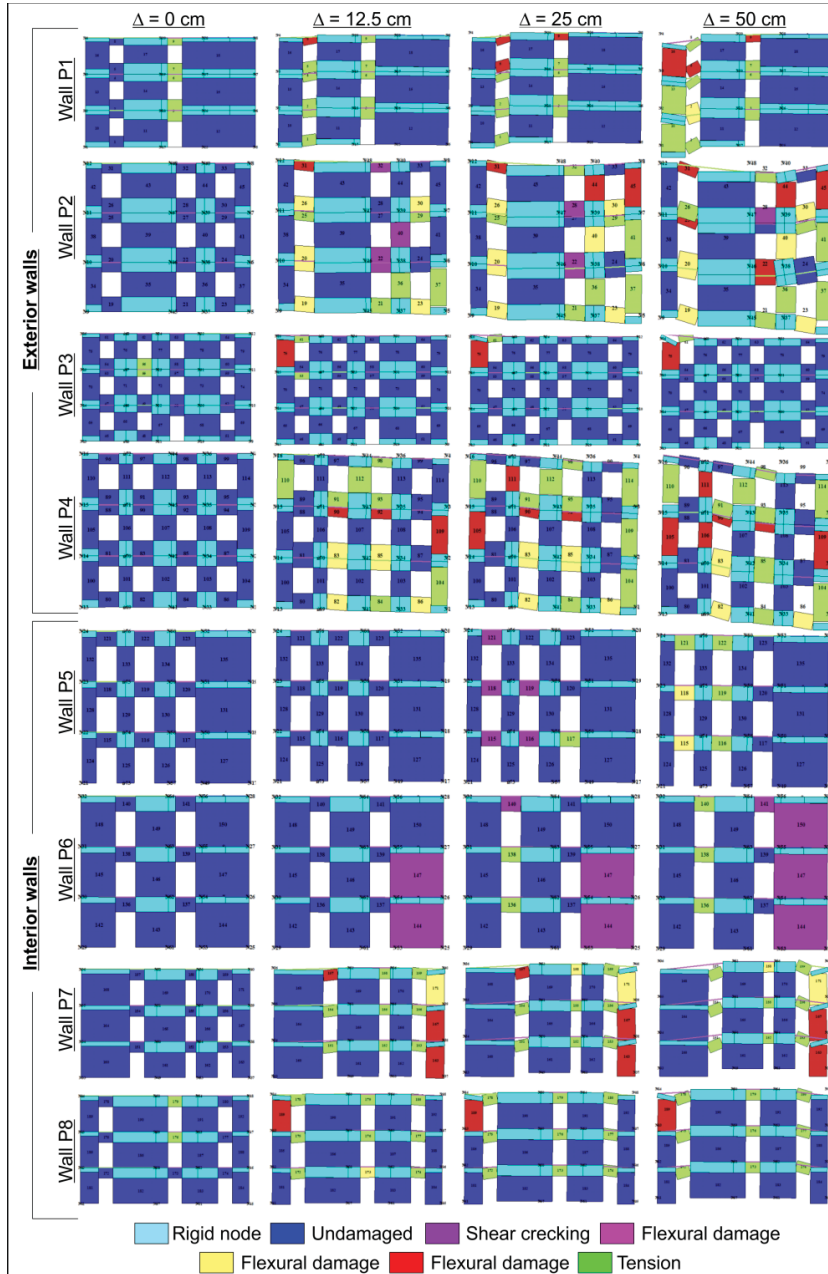


Figure C.33 Damage evolution of the exterior (P<sub>i</sub>, P<sub>2</sub>, P<sub>3</sub>, P<sub>4</sub>) and interior (P<sub>5</sub>, P<sub>6</sub>, P<sub>7</sub>, P<sub>8</sub>) walls of the masonry building M2 resting on medium/hard clay (S2<sub>2</sub>), during the progressive increase of the differential settlements from 0 to 50 cm applied according to a hogging configuration.



Result of the numerical analysis in terms of damage exhibited by the masonry walls of a building subjected to differential settlements

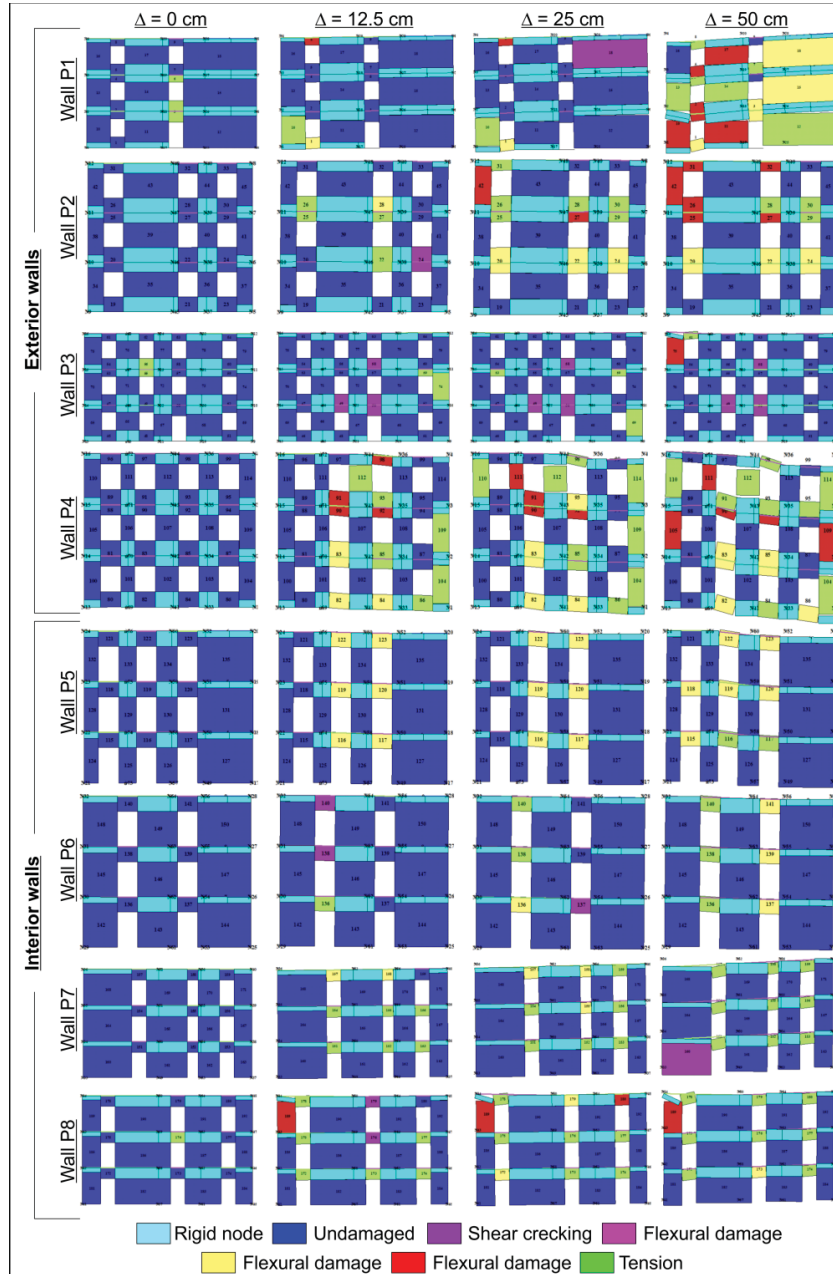


Figure C.34 Damage evolution of the exterior (P<sub>1</sub>, P<sub>2</sub>, P<sub>3</sub>, P<sub>4</sub>) and interior (P<sub>5</sub>, P<sub>6</sub>, P<sub>7</sub>, P<sub>8</sub>) walls of the masonry building M2 resting on dense sand (S3\_1), during the progressive increase of the differential settlements from 0 to 50 cm applied with a bi-linear trend and a maximum value in the left corner.

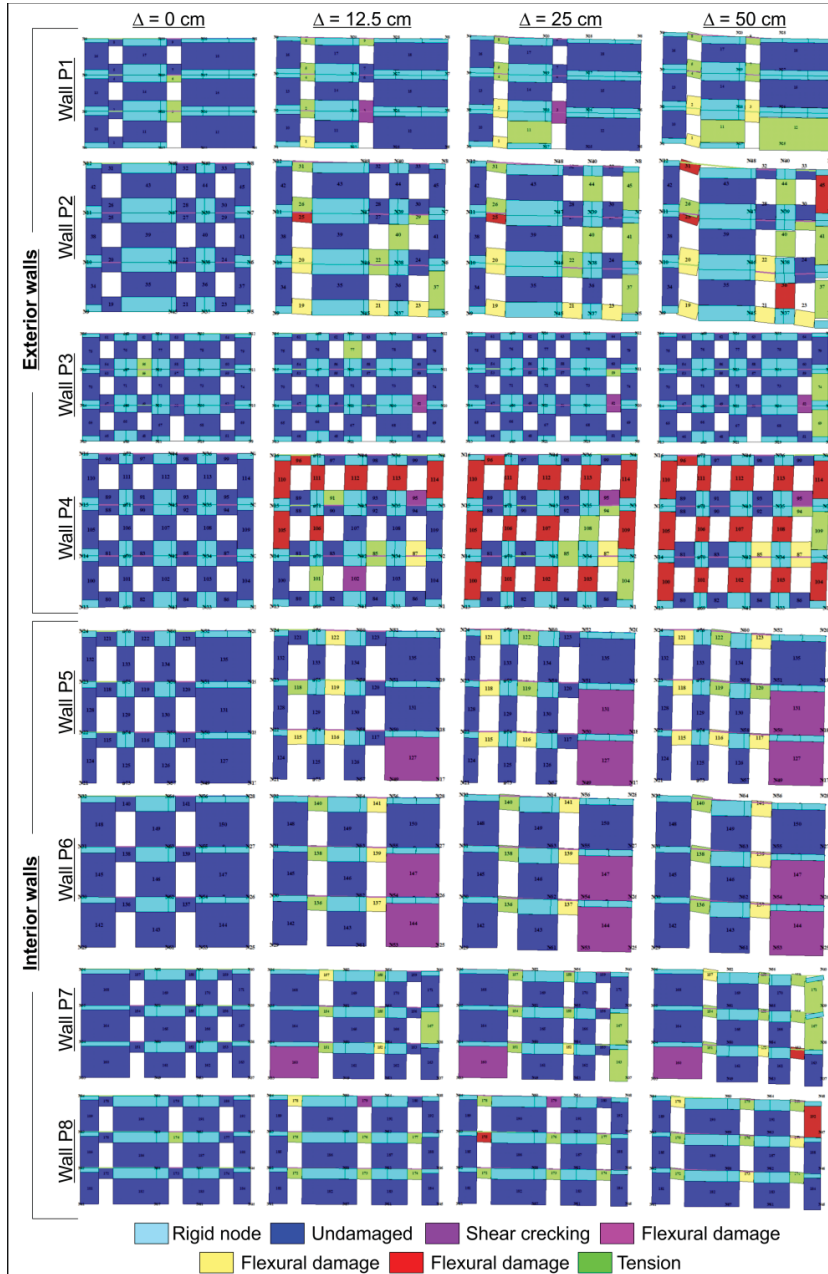


Figure C.35 Damage evolution of the exterior (P<sub>i</sub>, P<sub>2</sub>, P<sub>3</sub>, P<sub>4</sub>) and interior (P<sub>5</sub>, P<sub>6</sub>, P<sub>7</sub>, P<sub>8</sub>) walls of the masonry building M2 resting on dense sand (S3\_1), during the progressive increase of the differential settlements from 0 to 50 cm applied with a bi-linear trend and a maximum value in the right corner.

Result of the numerical analysis in terms of damage exhibited by the masonry walls of a building subjected to differential settlements

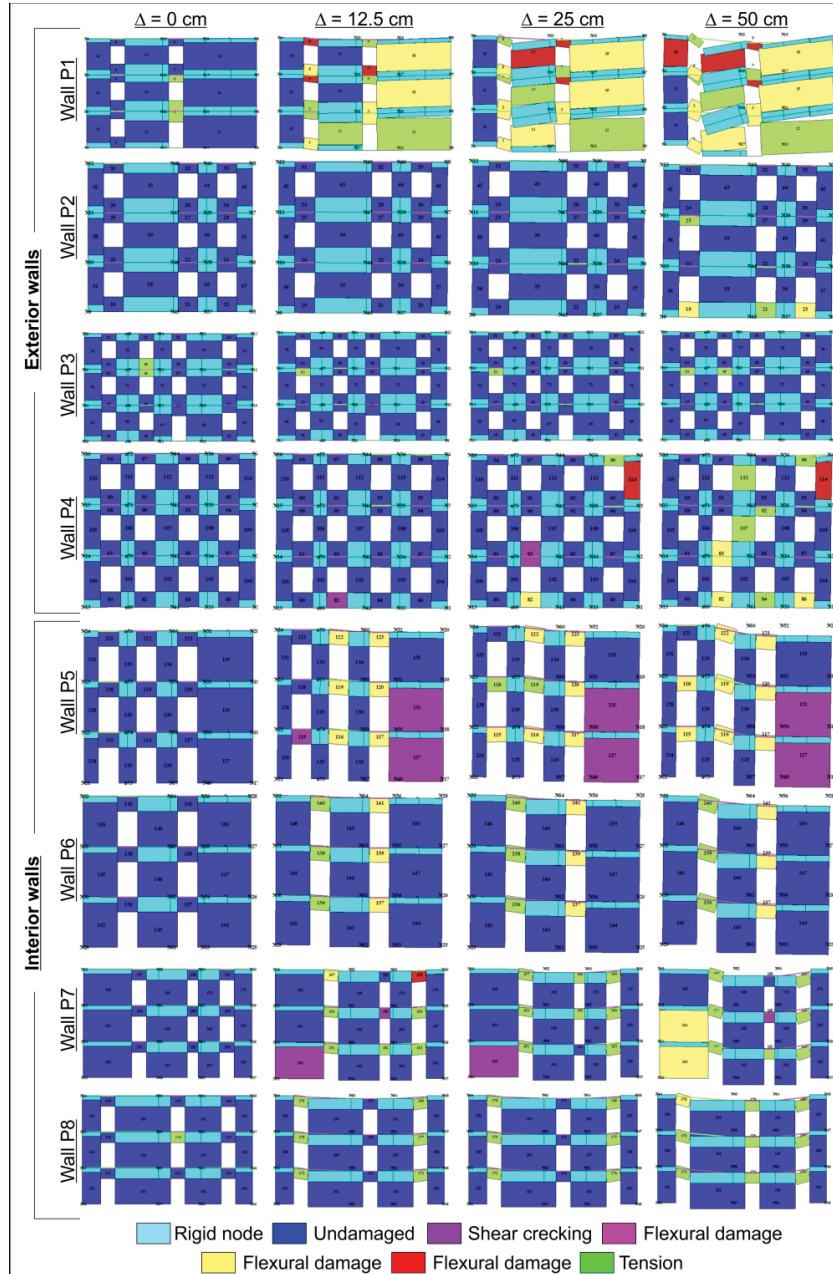


Figure C.36 Damage evolution of the exterior (P<sub>i</sub>, P<sub>2</sub>, P<sub>3</sub>, P<sub>4</sub>) and interior (P<sub>5</sub>, P<sub>6</sub>, P<sub>7</sub>, P<sub>8</sub>) walls of the masonry building M2 resting on dense sand (S3\_1), during the progressive increase of the differential settlements from 0 to 50 cm applied according to a sagging configuration.

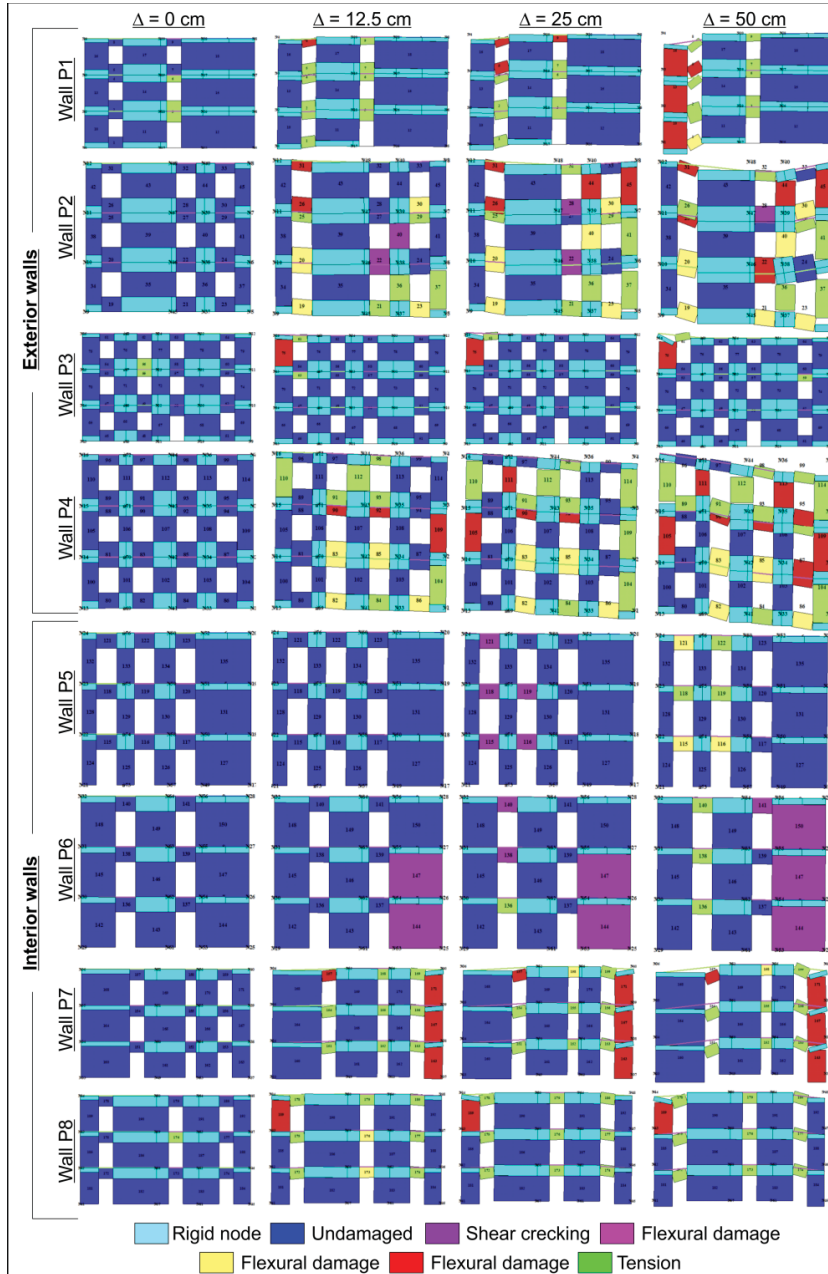


Figure C.37 Damage evolution of the exterior (P<sub>i</sub>, P<sub>2</sub>, P<sub>3</sub>, P<sub>4</sub>) and interior (P<sub>5</sub>, P<sub>6</sub>, P<sub>7</sub>, P<sub>8</sub>) walls of the masonry building M2 resting on dense sand (S3\_1), during the progressive increase of the differential settlements from 0 to 50 cm applied according to a hogging configuration.

Result of the numerical analysis in terms of damage exhibited by the masonry walls of a building subjected to differential settlements

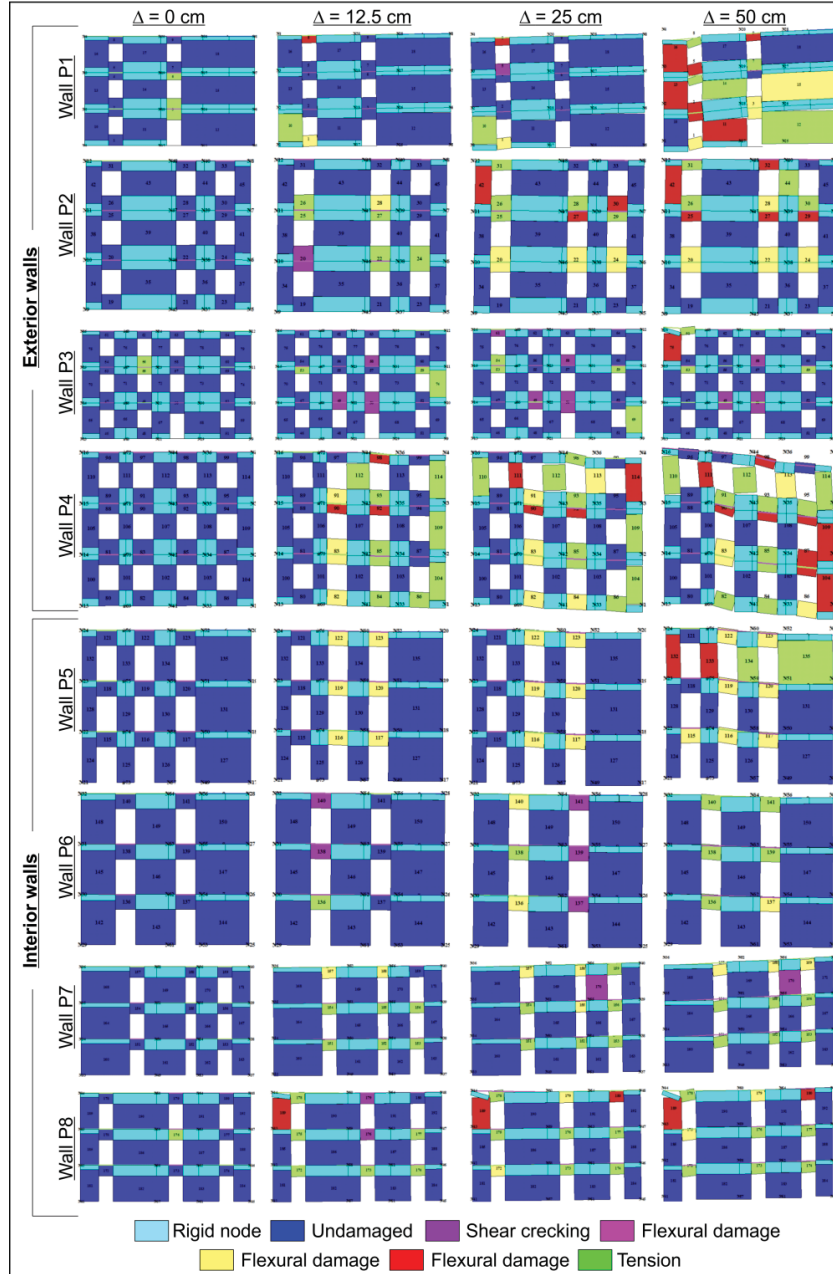


Figure C.38 Damage evolution of the exterior (P1, P2, P3, P4) and interior (P5, P6, P7, P8) walls of the masonry building M2 resting on loose sand (S3\_2), during the progressive increase of the differential settlements from 0 to 50 cm applied with a bi-linear trend and a maximum value in the left corner.

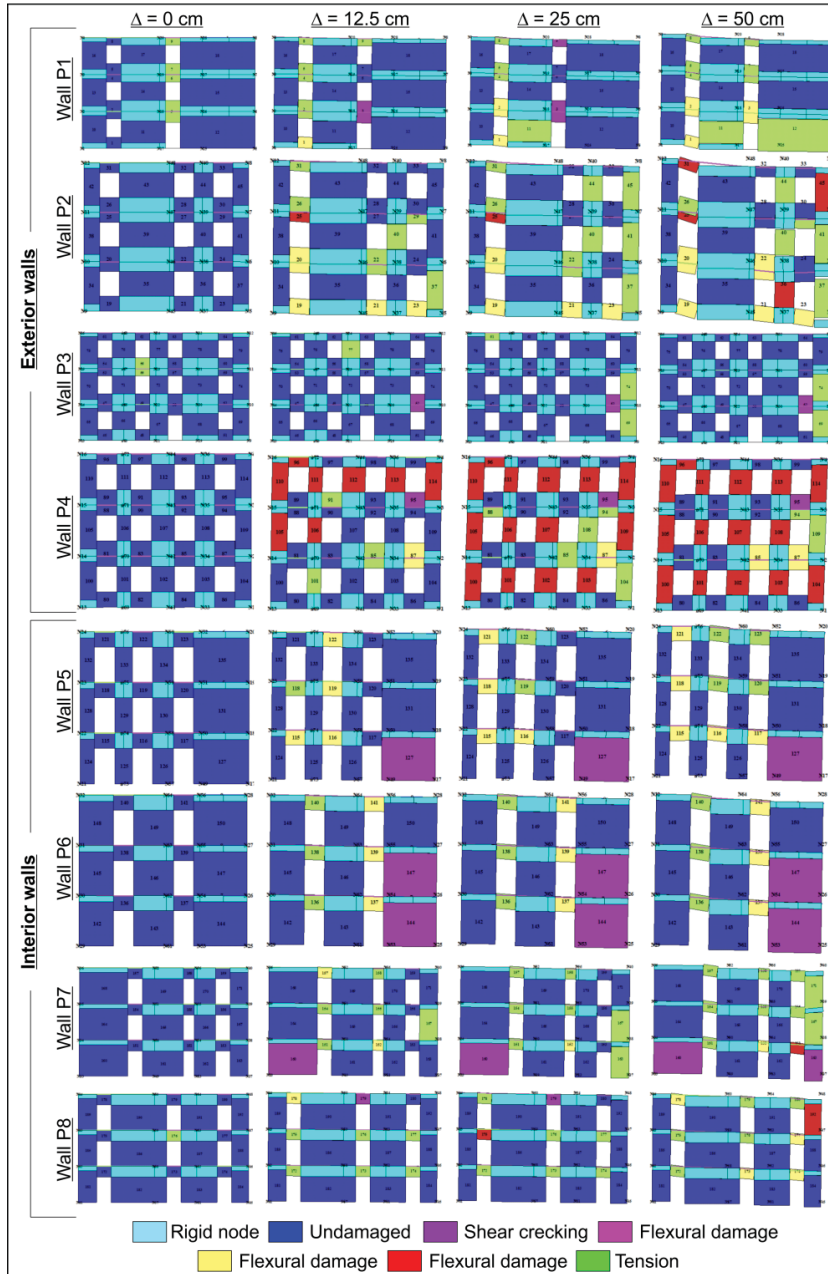


Figure C.39 Damage evolution of the exterior (P<sub>i</sub>, P<sub>2</sub>, P<sub>3</sub>, P<sub>4</sub>) and interior (P<sub>5</sub>, P<sub>6</sub>, P<sub>7</sub>, P<sub>8</sub>) walls of the masonry building M2 resting on loose sand (S3\_2), during the progressive increase of the differential settlements from 0 to 50 cm applied with a bi-linear trend and a maximum value in the right corner.

Result of the numerical analysis in terms of damage exhibited by the masonry walls of a building subjected to differential settlements

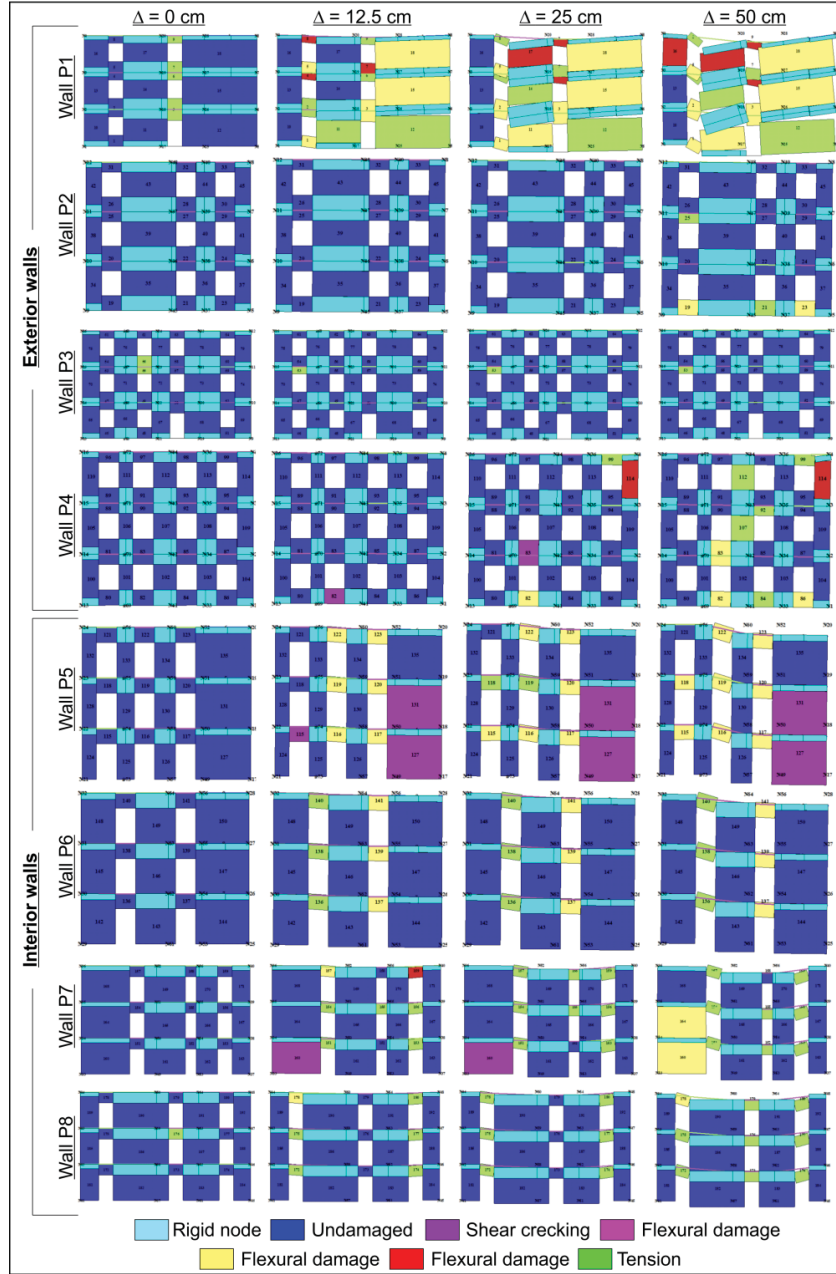


Figure C.40 Damage evolution of the exterior (P<sub>i</sub>, P<sub>2</sub>, P<sub>3</sub>, P<sub>4</sub>) and interior (P<sub>5</sub>, P<sub>6</sub>, P<sub>7</sub>, P<sub>8</sub>) walls of the masonry building M2 resting on loose sand (S3\_2), during the progressive increase of the differential settlements from 0 to 50 cm applied according to a sagging configuration.

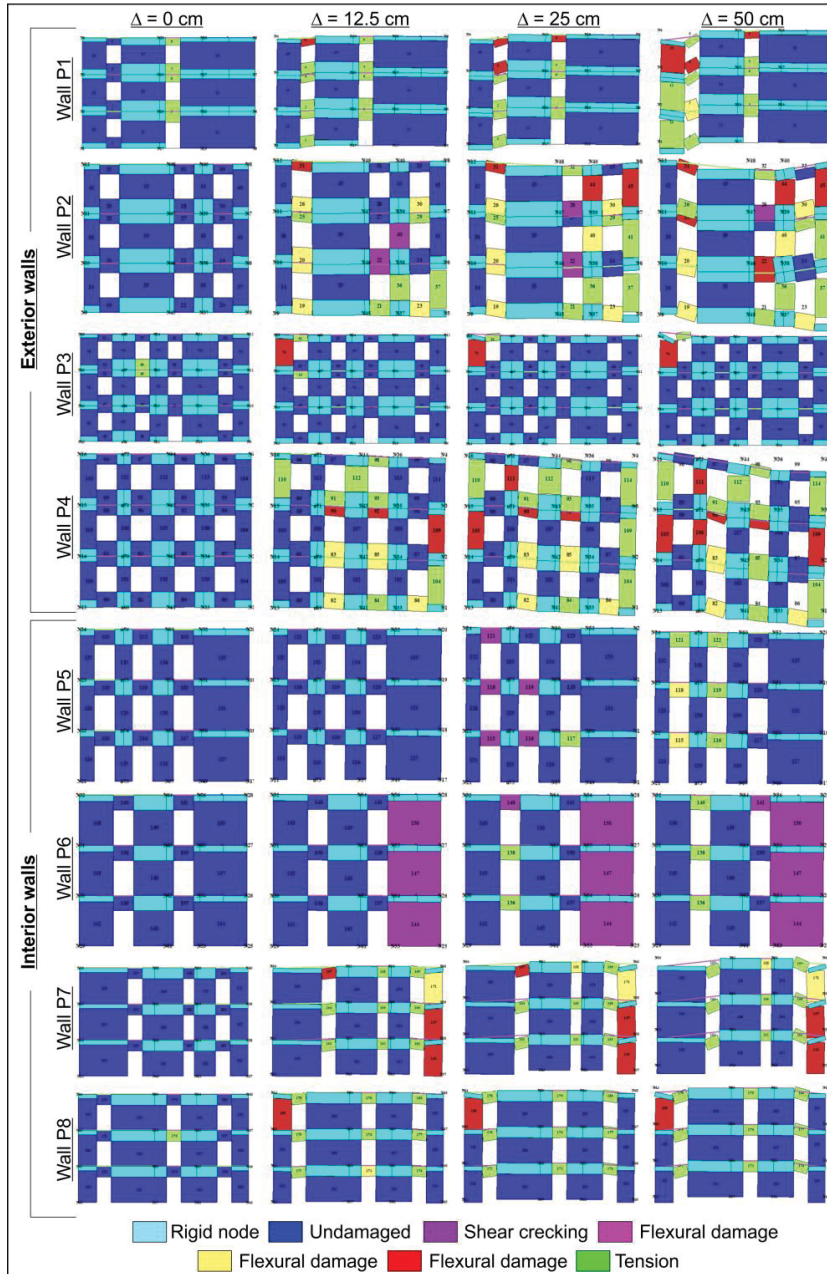


Figure C.41 Damage evolution of the exterior (P<sub>i</sub>, P<sub>2</sub>, P<sub>3</sub>, P<sub>4</sub>) and interior (P<sub>5</sub>, P<sub>6</sub>, P<sub>7</sub>, P<sub>8</sub>) walls of the masonry building M2 resting on loose sand (S3\_2), during the progressive increase of the differential settlements from 0 to 50 cm applied according to a hogging configuration.